ABSTRACT

Title of thesis: BIOMIMETIC INSECT FLAPPING WING AERODYNAMICS AND CONTROLS FOR MICRO AIR VEHICLES

Pranay Seshadri, Master of Science, 2011

Thesis directed by: Professor Inderjit Chopra
Department of Aerospace Engineering

The goal of the current research is to develop a hover capable, fully autonomous, flapping wing micro air vehicle with a thorough understanding of the associated aerodynamics and aeroelasticity. The approach followed in this work is to look at this problem from three different perspectives: 1) Instantaneous Rigid Wing Aerodynamics, 2) Time Averaged Flexible Wing Aerodynamics, and 3) Vehicle Integration and Control

Unlike prior studies that have focused on one of these aspects, this study will encompass each aspect using a different methodology. The commonality between these three elements in this study is the flapping mechanism. At the core of this work is a simplified, elegant flapping actuation system that is capable of emulating insect wing kinematics in all its degrees of freedom. The mechanism is shown to be novel compared to existing flapping mechanisms and is easily scalable.

BIOMIMETIC INSECT FLAPPING WING AERODYNAMICS AND CONTROLS FOR MICRO AIR VEHICLES

by

Pranay Seshadri

Thesis submitted to the Faculty of the Graduate School of the
University of Maryland, College Park in partial fulfillment
of the requirements for the degree of
Master of Science
2011

Advisory Committee:
Professor Inderjit Chopra, Chair
Dr. Moble Benedict
Associate Professor James Baeder
Associate Professor James Sean Humbert

Dedication

To my parents

Acknowledgments

I begin by extending my sincere gratitude to my advisor Inderjit Chopra. Throughout my years working at the Alfred Gessow Rotorcraft Center, Dr. Chopra has provided an environment with the highest level of professionalism and expectation. Despite numerous setbacks both professional and personal he has provided unwavering support and benevolence. I admire his contagious exuberance for quality research and his technical prowess. It has been a true learning experience being his student for these years.

I would like to thank Moble Benedict for being a very encouraging mentor and a patient teacher. Working alongside Moble has been an enriching experience, one that has taught me lessons that go well beyond the walls of any laboratory. His technical brilliance, resourceful creativity and diligence form an ethos that every researcher should strive to achieve. I am indebted by his belief in my abilities and humbled to have worked under his tutelage.

Without the support of my family and friends, this work would have been extremely insipid and mundane. I ask forgiveness for the missed calls, no reply emails and the shear brevity of my responses when betided. I am also thankful for the kinship from my numerous colleagues at the Rotorcraft Center. Their astute scholarship and light-hearted disposition were crucial in shaping the research and methods behind this work.

Lastly I want to thank you, the reader, for giving this work true meaning.

Table of Contents

List of Tables

List of Figures

List of Abbreviations

α	angle of attack
β	coning angle
Φ	stroke angle
Θ	pitch angle
ψ	phase angle
C_l	wing lift coefficient
C_d	wing drag coefficient
c_l	wing sectional lift coefficient

MAV	Micro Air Vehicle
FMAV	Flapping Wing Micro Air Vehicle
DARPA	Defense Advanced Research Projects Agency
CFD	Computational Fluid Dynamics
LEV	Leading Edge Vortex
PIV	Particle Image Velocimetry
DAQ	Data Acquisition
NI	National Instruments
SC	Signal Conditioning
FFT	Fast Fourier Transform

Chapter 1

Introduction

1.1 Overview

The need for small autonomous aerial vehicles to perform a myriad of operations has fostered tremendous research and development activities in the emerging field of micro air vehicles (MAVs). A MAV can be broadly classified as a flying vehicle having a maximum wing span of 15 cm and weighing from 100 – 200 grams [7]. While MAVs can be extremely useful assets to the military especially for operations in highly populated urban environments, they can also be used for civilian applications such as traffic monitoring, biochemical sensing, border surveillance, fire and rescue operations, wildlife surveys, etc. Many of these scenarios are extremely challenging and would require the vehicle to operate outdoors in gusty environments and also within confined spaces such as buildings, caves, etc. In order to be able to successfully execute these missions, MAVs should be capable of efficient hover and also be extremely maneuverable.

Many fixed wing MAVs have been successfully flight tested. They are extremely efficient with endurance close to over 30 minutes [12]. However, they lack the ability to hover, and therefore cannot operate in highly constrained environments. Rotary-wing MAVs, on the other hand, have the capability to hover, but their efficiency is significantly lower compared to their fixed-wing counterparts [7];

also they have limited maneuverability, making them less effective in gusty environments. This means that scaling down full-scale concepts such as fixed-wings and helicopters may not be the right approach for operating in a completely different aerodynamic regime. Therefore, it is important to investigate alternate solutions such as flapping wings, which have been proven in nature to perform extraordinarily well at low Reynolds numbers. However, the greatest challenge in utilizing the flapping wing concept for MAVs lies in emulating their wing kinematics and understanding their associated complex aerodynamics.

The regime of low Reynolds numbers ($10^3 - 10^5$) is characterized by higher relative viscous losses and lower aerodynamic efficiencies compared to higher Reynolds numbers. The flow environment manifests itself in the form of high drag coefficients and therefore low values of power loading (thrust / power) [24]. In order to develop efficient and maneuverable vehicles, it is necessary to obtain a complete understanding of the flow environment. The nature of flapping flight introduces an additional level of complexity, as the unsteady wing kinematics employed by natural flyers can lead to the generation of a large number of unconventional and unsteady flow phenomena, which contributes significantly to the resultant forces and moments on the wing. It is because the traditional quasi-steady or even unsteady aerodynamic theories fail to explain the flow phenomena or the forces experienced by these flapping wings. The introduction of wing aeroelasticity also adds another dimension to this already multifarious problem.

1.2 Avian and Insect Based Flapping Flight

Before delving into the aerodynamics of flapping flight, it is first necessary to distinguish between the two main modes of flapping flight in nature: insect and avian. Thus, a brief morphology of each of these species is provided here. The insect body comprises of three main elliptical sacs namely the head, thorax and abdomen. Attached to these sacs are the wings, antennas, legs and halteres. The wings comprise of a translucent membrane stretched over a network of hollow tubes; concentrated towards the wing root and dispersing towards the tip . This in effect leads to the greatest lightness to strength ratio. Unlike insects, that possess no muscular or skeletal system in their wings, birds have a network of bones within their wings along with an extensive muscular web. The wing bones here are directly connected to the central vertebrae [32].

There is also a difference in the nature of flapping between birds and insects. While birds distinctly beat their wings in the vertical plane, insect restrict their motion to the horizontal plane, which would be tilted forward depending on the forward speed (see Figure 1.1). The overall stroke trajectory of an insect wing is a figure of eight ring, while that of a bird is an ellipse with a pointed summit [32]. The frequency of flapping is also different with insect flapping up to 200 Hz, while birds flapping more close to 5 Hz. While birds are actively able to change the twist, camber and aspect ratio with their muscles, insect can only control wing motions at the root. Thus, insects depend on the large aeroelastic couplings to obtain the required twist and camber. The most significant and relevant difference however

is the ability to hover. While most insects are capable of hovering, in birds it is restricted to a few species such as hummingbirds. Interestingly the wing motion of a hummingbird bears a greater resemblance to insect motion than avian motion.

Avian based flapping is characterized by flapping mostly in a vertical plane with small changes in pitch and this type of flapping cannot generate the required lift to support the weight of the bird in the absence of any forward speed. From the perspective of developing an efficient and maneuverable MAV, hover capability is extremely advantageous and it forms one of the primary tenets of this study.

1.3 Insect Wing Kinematics

Insect wing kinematics consists of a combination of different active modes as shown in Figure 1.2. In the course of a complete stroke, the wing translates from the abdomen towards the thorax, in what is termed the downstroke. Even during the translational phase, the angle of attack of the wing continuously changes due to a constantly varying pitch angle. Upon reaching the end of its flapping stroke, the wing rotates so as to have a positive pitch angle for the subsequent stroke backwards to the abdomen. This rotational phase is called supination. The translational phase that ensues is referred to as the upstroke. Finally, upon reaching the end of the upstroke the wing once again rotates through pronation back into the downstroke [28]. Insects can also tilt the reference plane of flapping; termed the stroke plane, thereby varying the net direction of the aerodynamic forces.

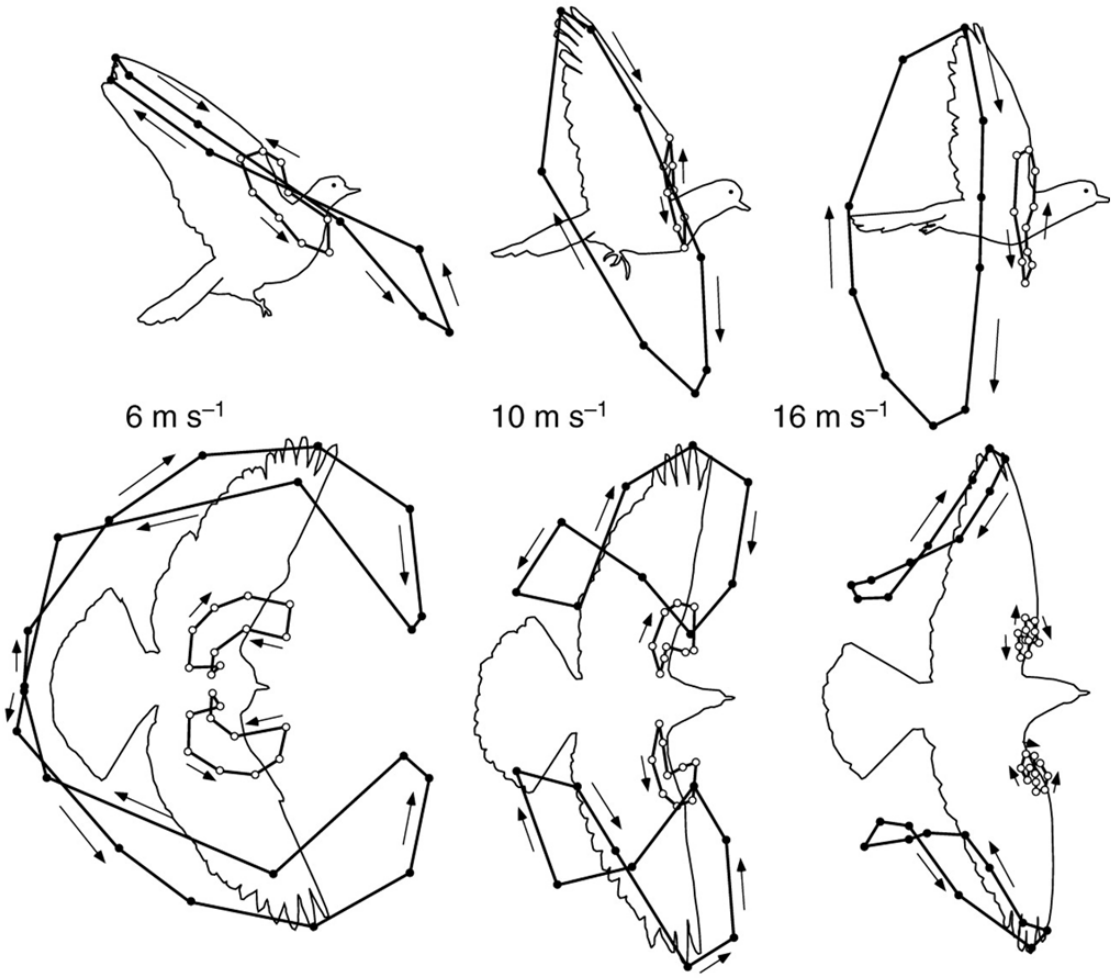

Figure 1.1: Avian wing kinematics for different forward velocities [33]

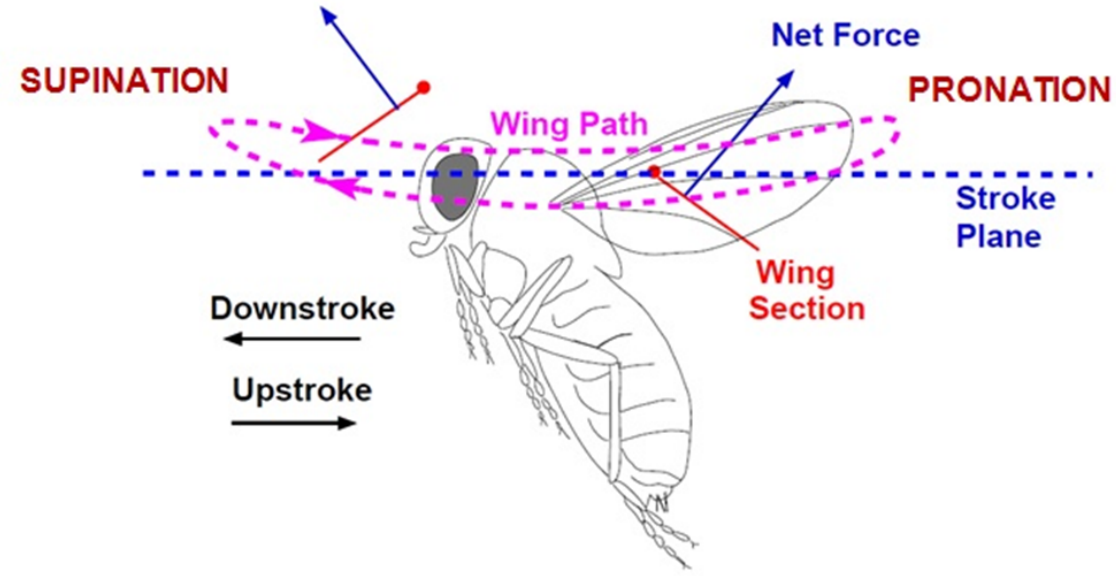

Figure 1.2: Insect wing kinematics

1.4 Experimental Studies

There have been several approaches followed by scientists and engineers to unravel the aerodynamics associated with insect flight. These studies have been motivated not just by a need to build next generation MAVs, but also to understand the unsteady mechanisms insects utilize to attain high instantaneous lift. Overall the approaches have been to either use real insects or complex mechanisms that accurately emulate insect wing kinematics. These two approaches will be discussed below.

For the purpose of capturing the wing kinematics of real insects, a system of three mutually orthogonal cameras is used to capture footage of insects flying within an enclosure. The video feed is post-processed to determine the stroke kinematics [11]. This technique has been used to provide insight insect into the insect kinematics

of the hawkmoth [10] and the fruit fly (*Drosophila Melanogaster*) [11]. While this technique provides tremendous insight into the wide range of motions, insect can adopt for a variety of maneuvers, they do not provide quantitative information on the in-flight forces and body torques. It is here that the second approach provides more insight.

Till date the primary source of experimental data for flight forces generated by an insect has come from a Reynolds number scaled model designed to emulate the wing kinematics of a fruit fly. Known as the Robofly, the setup features six computer-controlled stepper motors attached to a gearbox assembly with a series of timing belts and coaxial drive shafts (see Figure 1.3). The wings are capable of rotational motion about all three axis and are designed to flap at chord Reynolds numbers of 75-1500 [9]. Each wing has a force sensor attached to it in order to measure the lift and drag forces acting on the wing. Another source of experimental data has been a model hawkmoth developed by Ellington and Usherwood [34]. Here the authors tested different model hawkmoth wings on a rotor stand to examine the stability of the leading edge vortex. Parameters varied included camber, twist and leading edge characteristic (thick, sharp and sawtooth). Numerous qualitative studies on mechanisms that emulate both flapping and wing rotation motions have also been conducted. However these experiments were conducted with the intent of flow visualization rather than instantaneous force measurements [22].

All these prior studies have been strictly focus on the aerodynamics and have thus employed rigid wings only. In an effort to emulate insect flight more accurately, researchers have designed flapping wing mechanisms that are designed to

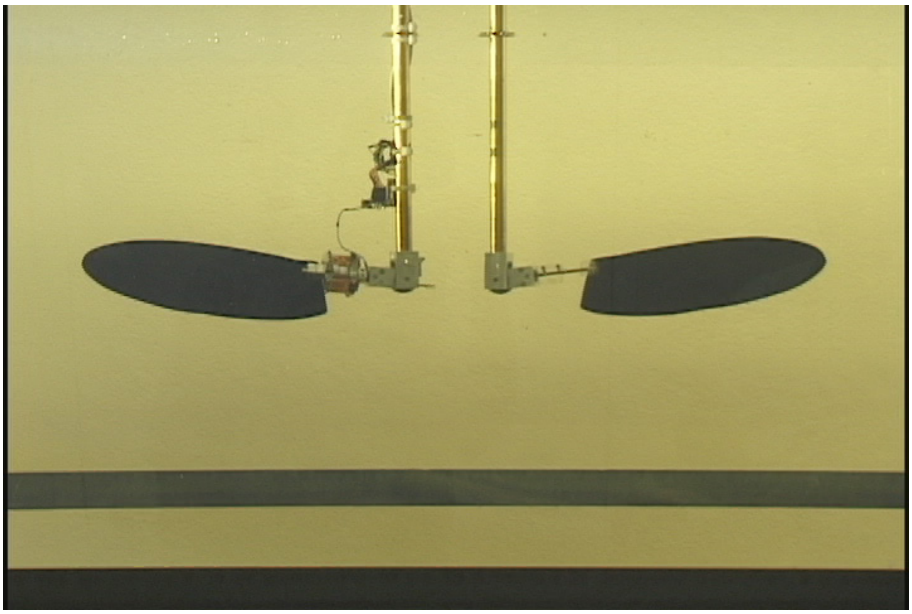

Figure 1.3: Robofly experimental apparatus

flap insect-based flexible wings. Aono et. al conducted an extensive computational and experimental study on a crank-slider based flapping mechanism (see Figure 1.4). The force transducer here is mounted to the body as oppose to the wings, thus it captures instantaneous body forces and moments in addition to those produced by the wing [4]

Both the approaches have facilitated and shaped our understanding of the aerodynamics of insect-based flapping flight. The results from these experiments and others alike are discussed below with the perspective of understanding the unsteady mechanisms insect adopt in flight.

1.5 Analytical Studies

While the lack of sufficient experimental data hinders the advancement of a complete theory of unsteady force generation of insect-based flapping wing flight, numerous studies have been conducted using different methodologies. These analytical studies may be grouped into quasi-steady analysis, indicial function-based reduced order models, unsteady vortex lattice models or computational fluid dynamics (CFD) [29]. Quasi-steady aerodynamics is a simple modelling tool that ignores the effects of the wake and takes in contributions to the aerodynamic forces from the horizontal air speed (U), the airfoil plunge speed ($h\dot{(}t)$), the pitch rate ($\alpha\dot{(}t)$) and the local induced velocity ($v_i(x,t)$). The disadvantage of quasi-steady aerodynamics being applied to insect-based flapping aerodynamics is that it requires experimentally determined lift and drag coefficients [35]. Singh [29] and Ansari [3] independently developed an unsteady indicial model and both showed good correlation with Dickinson's experimental data. Singh extended his analysis to include wing deformation through a comprehensive aeroelastic model [29]. The approach followed by researchers has been to decompose the aerodynamic forces into its individual components and then add them to the total force. For instance, Singh computed the translational and rotational circulation from thin airfoil theory and incorporated the effect of the leading edge vortex using Polhamu's leading edge suction analogy. He used the Wagner function for the implementation of a starting vortex and the Kussner function for the shed and tip vortex [29]. More details regarding these unsteady mechanisms are provided below.

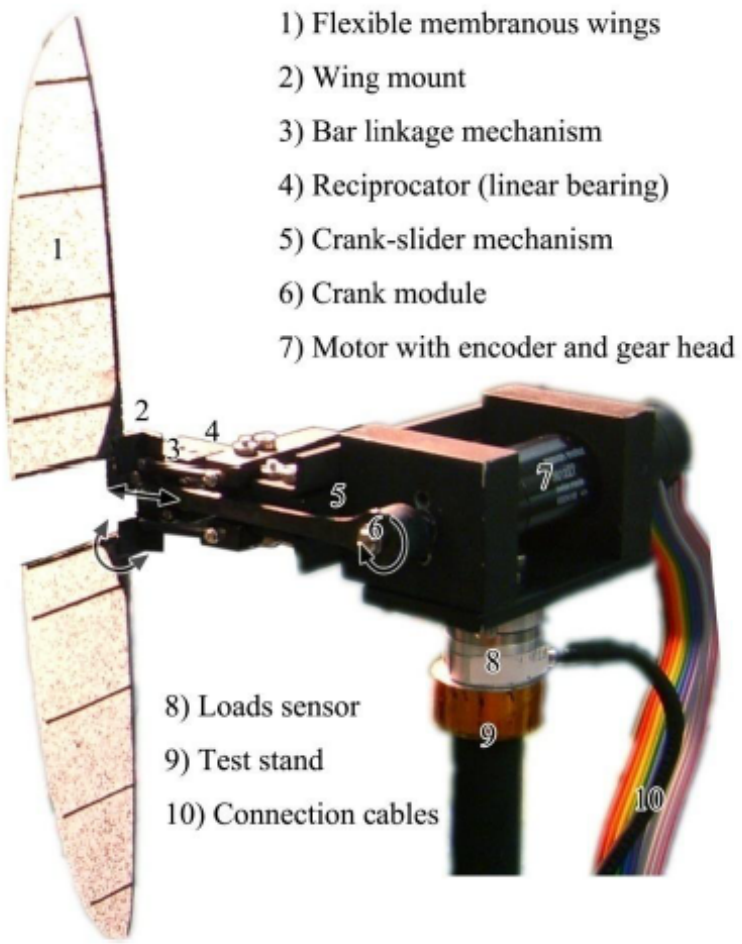

Figure 1.4: Flexible-wing flapping wing test rig [4]

1.6 Unsteady Mechanisms

Insect flight in its totality consists of a variety of unsteady mechanisms that augment the aerodynamic forces well in excess of those predicted by quasi-steady aerodynamics. A brief review of the unsteady mechanisms that have been captured through the various experimental approaches is given below.

1.6.1 Knoller-Betz Effect

During the early 1900s, Knoller and Betz conducted experiments where they showed individually that a flapping wing creates an effective angle of attack thus producing an aerodynamic force with both lift and thrust components [27]. This phenomenon, termed the Knoller-Betz effect, is an important unsteady aerodynamic effect that can provide insight into the lift and thrust variation seen in insects. Von Karman and Burgers provided the theoretical foundation for this lift and thrust production based off the nature of the wake. A wake which comprised of two rows of counter-rotating vortices, known later as the reverse Karman street, was observed behind lift and thrust generating airfoils [27]. Further experiments showed that the nature of these forces had a strong dependence to the Strouhal number, aspect ratio and the pitch angle [27].

1.6.2 Leading Edge Vortex

With advent of research in rotorcraft aeromechanics, tremendous research was conducted (and still is) towards understanding the nature of dynamic stall. Dynamic

stall in general can refer to a range of phenomena that occur on a lifting surface when it is subjected to time-dependent pitching, plunging or vertical translation, or any other type of unsteady motion, that causes a dynamic variation in the angle of attack. Dynamic stall effectively pushes the lifting surface beyond its static stall value [17]. Insects utilize a form of dynamic stall called the leading edge vortex for lift augmentation.

The most significant discovery towards understanding the nature of insect-based flapping has been that of the leading edge vortex (LEV). The existence of the LEV as a source of lift augmentation in insects was introduced by Ellington and is a well accepted theory [10]. There are two theories to explain this increase in lift, however both are inherently equivalent. The first - the circulation approach - states that the net circulation about the wing is increased due to the presence of the vortex. The second - the pressure approach - states that the presence of the leading edge vortex increases the low pressure region on the upper surface thereby introducing more suction, which increases the lift [10]- [2]. Research on model hawkmoth wings revealed that the LEV was stable throughout the translation phase of the stroke. Usherwood and Ellington postulated that the stability of the LEV was due to the strong spanwise flow from the vortex core. This in effect prevented the growth and the inevitable shedding of the LEV [24]. Dickinson in his experiments on the Robofly also noticed a stable spanwise LEV through the translation phase of flapping. He attributed the LEV's stability not to spanwise flow, but rather to the tip vortex and wake vorticity.

Extensive flow visualization studies were performed by Singh and Ramasamy

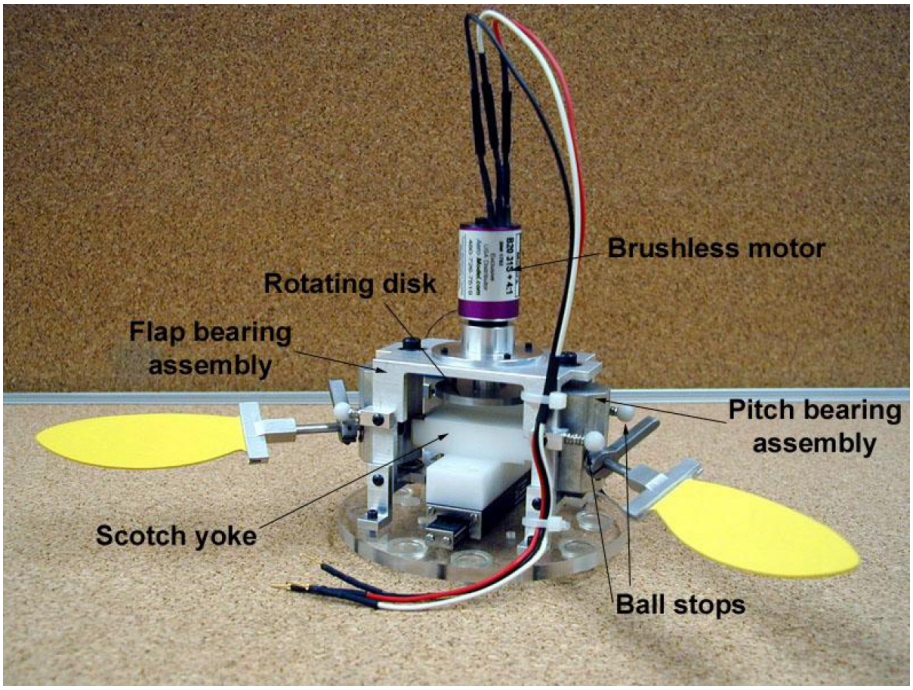

Figure 1.5: Flapping apparatus of Singh et. al [28]

[28], [22] on a MAV scale Reynolds number (15,500) flapping wing rig shown in Figure 1.5. Compared to prior studies that revealed the stability of the LEV throughout translation, their work showed that the LEV attached, grew in strength and then separated from the leading edge. This separation was followed by the appearance of another LEV which exhibited the same behavior of continual convection and shedding [24]. A representative result of their work is shown in Figure 1.6.

1.6.3 Rotational Circulation

Studies conducted by Dickinson et. al have also showed that during the supination and pronation phases, rotational lift can be generated. This lift which is generated towards the end of the halfstrokes is analogous to the Magnus effect on

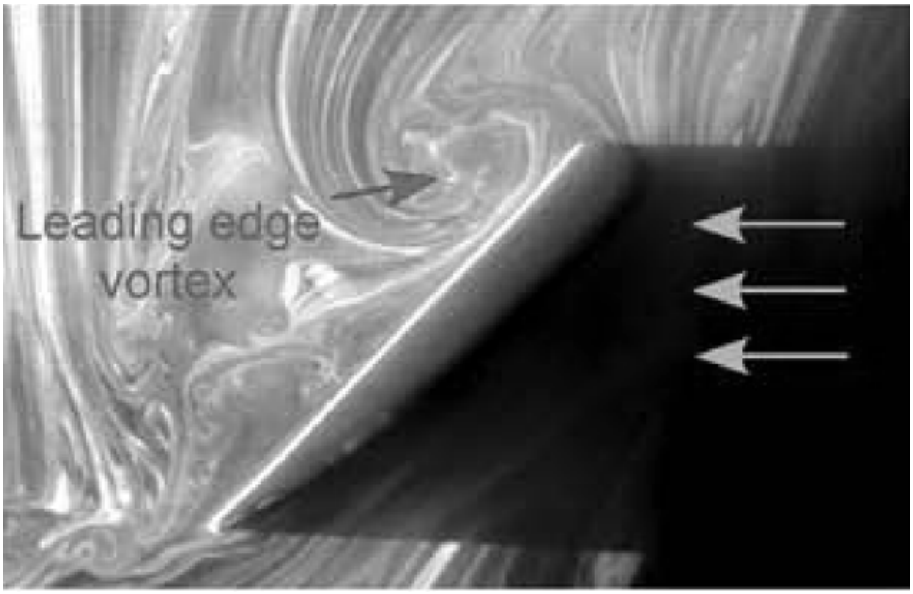

Figure 1.6: Leading edge vortex seen in flow visualization [22]

a spinning baseball [9], [18]. The Magnus effect is attributed to the asymmetric boundary layer separation between the two sides of the baseball. As the ball rotates with a forward velocity, the boundary layer on the advancing side is quickly tripped, while on the retreating side it is more gradual. In other words flow is much more turbulent on the advancing side as compared to the retreating side, and as a result separation is delayed on the retreating side. The overall difference in velocity profiles between these two sides causes a net circulation to be formed that leads to the generation of an axial force [19], [6]. This is known as rotational lift. The direction and magnitude of this rotational lift force is dependent on the pitch angle variation during rotation, the direction of the freestream velocity and the location of the pitching axis [9]. Figure 1.7 shows three different types of rotations termed as advanced, symmetric and delayed.

As seen from the figure, rotations are classified as advanced when the pitch

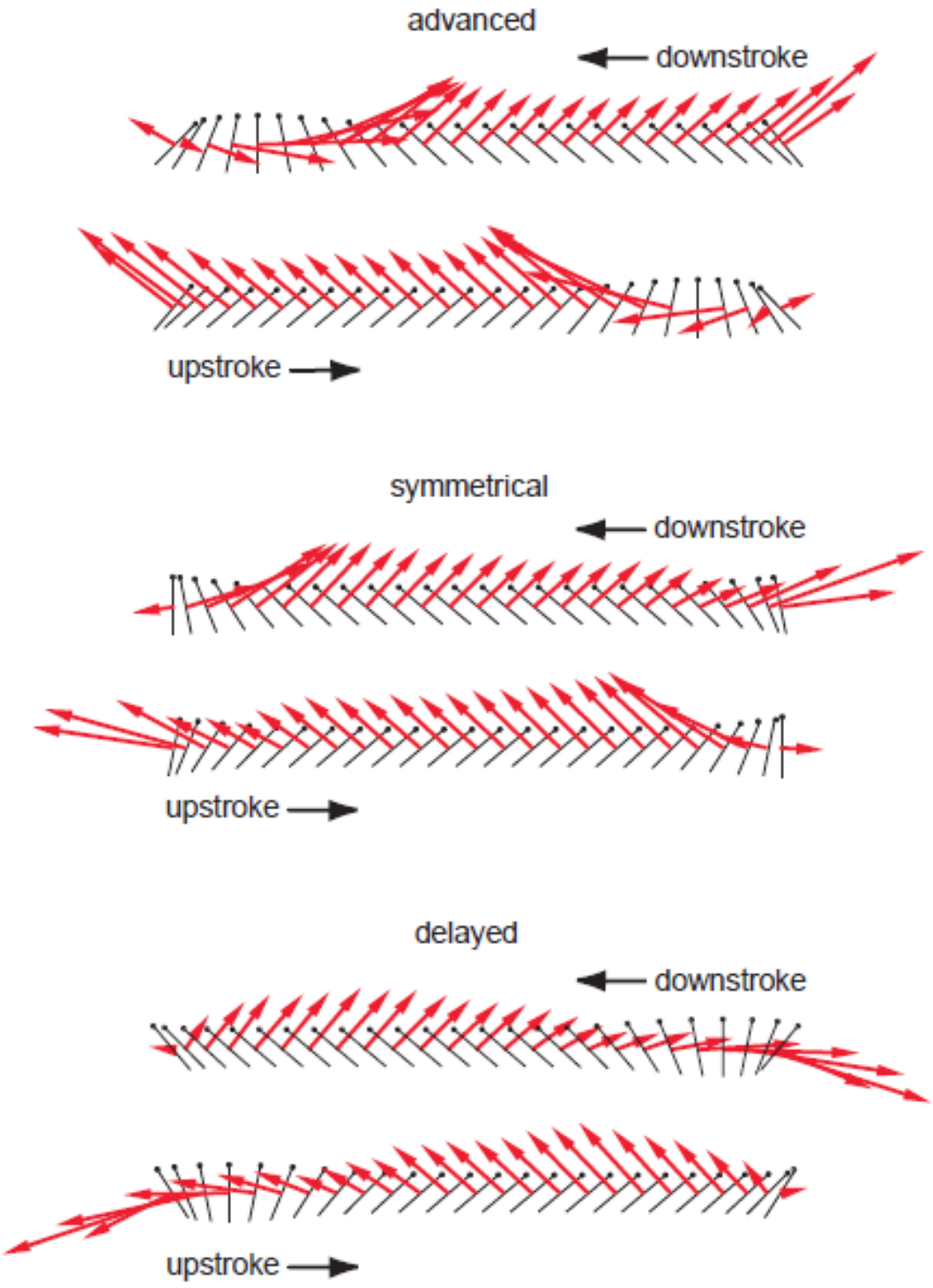

Figure 1.7: Three types of rotations with resultant force vectors [9]

angle at the end of the halfstroke is greater than 90^o with respect to the freestream velocity; that is the rotation is complete before the initiation of the next halfstroke. A delayed rotation is the opposite of an advanced one, that is pitch angle at the end of a halfstroke is below 90^o with respect to the freestream velocity. A symmetric rotation ensues when the pitch angle at the end of each halfstroke is exactly 90^o. Both computational and experimental studies have shown that while a positive lift peak is produced due to advanced rotations, negative lift is produced when the rotation is inherently delayed.

1.6.4 Wake Capture

The wing kinematics in insects comprises of a reciprocating flapping motion in the wake generated by previous strokes. Towards the end of the strokes at the supination and pronation phases, the wing directly encounters the wake shed from the previous halfstroke and this interaction may lead to the augmentation of the lift force. This mechanism is referred to as wake capture [24]. This force is different from rotational circulation as it is not dependent on the timing of rotation [9], but is dependent on the type of rotation (advanced, delayed or symmetric). Figure 1.8 shows PIV images for the three types of rotations at the end of a halfstroke, that show different circulations based on the type of rotation. The key difference between wake capture and rotational circulation is that while rotational circulation manifests as a force transient through rotation, wake capture always occurs after rotation; and is reflected as a force transient in the next halfstroke.

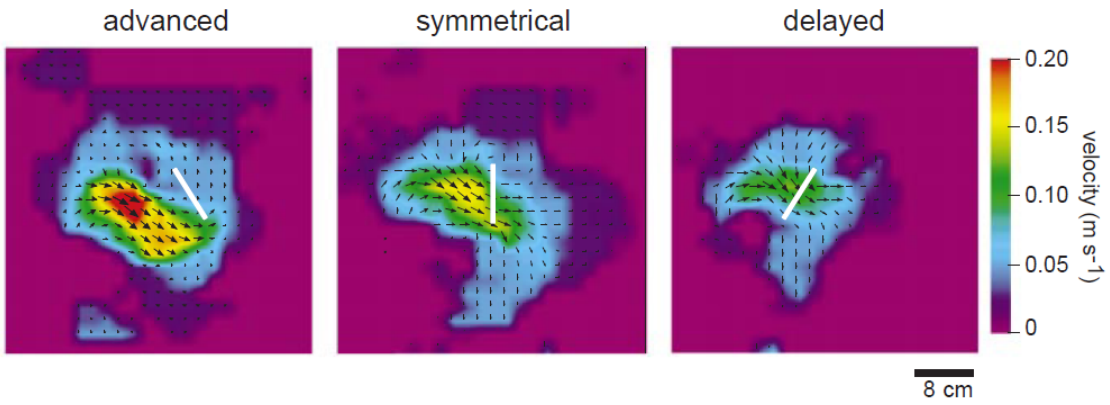

Figure 1.8: PIV evidence for wake capture mechanism [9]

Numerous computational studies have also been performed to investigate the nature of the wake capture mechanism. For instance, Tang et al [30] not only observed the wake capture phenomenon but also stated its ability to enhance lift was highly dependent on the chord Reynolds number.

1.7 Flapping Wing Micro Air Vehicles

Perhaps the most challenging facet of this research is to be able to design and develop vehicles that take full advantage of the unsteady aerodynamic phenomena, just as insects do. Even though the flapping mechanisms discussed earlier can emulate the insect kinematics very accurately, they are too cumbersome and heavy to be used on a flying vehicle. Furthermore, these mechanisms require either manual (not while flapping) change of the pitch and stroke angles, or an elaborate system of servos (while flapping) to produce different flapping kinematics. In other words, developing a suitable, quick response, control strategy is a significant challenge. In this regard there have been some successful flapping wing micro air vehicles, as

shown in Figure 1.9.

Even though many researchers have attempted to built hover-capable flapping wing MAVs, only four of them are capable of untethered hover, most notably Mentor (SRI/ Toronto), Harvard's Microfly and the Nano Scout (Aerovironment) [36], [1], [21]. All these vehicles are designed to emulate the wing kinematics of insects. Delfly, on the other hand is based on avian kinematics, and as a result can not hover. Mentor, which is the heaviest of all these vehicles at 580 grams has four wings providing lift and propulsion. It uses a set of four vanes for directional control (see Figure 1.9). It should be noted that both Mentor and DelFly use a single four-bar based mechanisms for flapping all the four wings. It is worthy to note that DelFly uses traditional fixed wing control sufaces; that is has an elevator and a rudder that are controlled by magnetic actuators [8]. The main disadvantage of the Mentor and Delfly is that they use four wings with fixed kinematics (no wing kinematics modulation) and incorporate vanes in the wing wake for stability and control. This may be one of the most practical and easy approaches to build a stable flapping-wing MAV. Insects and humming birds on the other hand are capable of performing remarkable aerial maneuvers primarily due to the large control forces and moments that they can generate by modulating their wing kinematics. Eliminating this capability from the design can severely impede the maneuvering ability of the vehicle.

At a much smaller scale; weighing 0.60 grams is Harvard's Microfly. The wings are flapped in an insect like manner by the action of a single piezoelectric actuator. A piezoelectric actuator is used because at this scale, it is not feasible to have an

Figure 1.9: Existing micro air vehicles

electric motor powering the wings through a system of gears. Due to the fact that these materials are typically brittle and have high operation frequencies and stresses, the microfly uses a minature transmission manufactured from carbon fiber flexures. The mechanism has demonstrated uncontrolled free flight in hover only with altitude control [21].

The vehicle that truly epitomizes the design and requirements of a flapping wing micro air vehicle is Aerovironment's Nano Scout. The wing kinematics of the Nano resembles that of a hummingbird, which as mentioned earlier has a greater resemblance to insect wing motions than birds. The Nano has successfully demonstrated hover, controlled flight, gust tolerance (up to five miles per hour), a variety of maneuvers and the capability to fly indoors and outdoors [1]. It has demonstrated a maximum endurance of eight minutes. The vehicle has a gross weight of 19 grams and this includes a video camera with a downlink. Controls are generated purely by wing kinematic modulation and not by using any external control surfaces [15].

1.8 Goals and Outlines

The goal of the current research is to develop a hover capable, fully autonomous, flapping wing micro air vehicle with a thorough understanding of the associated aerodynamics, aeroelasticity and efficiency. The approach proposed in this work is to look at this problem from three different perspectives:

1. Instantaneous Rigid Wing Aerodynamics

2. Time Averaged Flexible Wing Aerodynamics

3. Vehicle Integration and Control

Unlike prior studies that have focused on one of these aspects, this study will encompass each aspect using a different set of tools and analyses. The commonality between these three elements in thus study is the flapping mechanism. At the core of this work is a simplified, elegant flapping actuation system that is capable of emulating insect wing kinematics in all its degrees of freedom. The mechanism is shown to be novel compared to existing flapping mechanisms and easily scalable. Analytical studies into this mechanism and its operating principle are presented in Chapter 2. It is designed for producing a set of kinematics that are optimized and truly capture the nature of insect wing motions in a very simplistic manner.

In Chapter 3, this design is transformed into a working mechanism designed to flap up to frequencies of 20 Hz. Numerous flexible wings are fabricated and tested on this mechanism for the metrics of average lift and power. Particular focus is on the aeroelastic tailoring of these wings so as to emulate the passive wing motions seen on actual insects in addition to the actuated flapping and pitching motions. The primary experimental tools are force and power measurements, motion capture tests, high speed videography and flow visualization. Furthermore, this chapter sheds light on the aerodynamic efficiency of flapping wings at the micro air vehicle scale.

Instantaneous rigid wing aerodynamics are presented in Chapter 4. Here the motivation is to reveal the presence of unsteady flow structures at MAV scale Reynolds numbers. A rigid wing is used in these tests so as to negate the effects

of wing bending and flexing. The fundamental questions this chapter seeks to shed light on are the nature of the leading edge vortex for a variety of wing kinematics and the contribution of rotational lift in flapping. This study is substantiated with flapping tests, wind tunnel tests, 3-D motion capture tests and vacuum chamber tests. Detailed flow visualization and particle image velocimetry are also employed in addition to data from a six degree of freedom balance at the wing root.

The lessons learned from Chapters 3 and 4 culminate in Chapter 5; where the goal is to design and develop the vehicle. Numerous failed and successful vehicle design iterations are presented. Tethered hover tests are conducted on a vehicle employing the same flapping mechanism as used in the preceding chapters. Control methodologies are developed and implemented on this vehicle. The final integrated vehicle is presented with on board power and control capabilities.

Chapter 2

Flapping Mechanism Operating Principle

2.1 Overview

In this chapter, the underlying principle of a four-bar-based mechanism to emulate insect-based flapping kinematics is discussed. The present mechanism can be designed to output a variety of insect-based wing motions. Single four bar mechanisms have been implemented widely for actuating flapping wing platforms [**?**], [**?**]. In essence, the four bar mechanism is utilized to convert the rotary motion of a motor to linear flapping motion. However, a single four-bar mechanism can only emulate the flapping degree of freedom in the wing kinematics. In this chapter we present a novel approach of emulating insect kinematics using a dual-differential four-bar mechanism. By utilizing a dual-differential four-bar mechanism (two four bar mechanisms at a phase difference with respect to each other) the translation as well as rotation degrees of freedom in insect wing kinematics can be emulated accurately. The mechanisms developed in the previous studies [9], [10] to emulate insect wing kinematics were extremely complex and were primarily meant for experimental benchtop setups. Therefore, one of the main objectives of the present research was to develop a simplified mechanism to emulate insect wing kinematics accurately so that it could be utilized on a flight-capable flapping wing vehicle.

If examined carefully, the insect wing kinematics (translation and wing rota-

tion) can be interpreted as both leading and trailing edges undergoing a periodic motion with a phase difference with the trailing edge always trailing the leading edge. This periodic motion is shown in Figure 2.1.

For simplicity of explanation we can assume that the wing is flapped in a harmonic fashion in a two-dimensional space as shown in Figure 2.2. Then the motion of the leading edge can be expressed as $Asin(\omega t)$ and the motion of the trailing edge can be written as $Asin(\omega t - \psi)$ (Figure 2.1). The pitch angle of the wing (Θ), at a particular instant is given by:

$$\Theta = tan^{-1}\left(\frac{Asin(\omega t) - Asin(\omega t - \psi)}{h}\right) \tag{2.1}$$

Therefore, the pitch angle depends on two parameters, the phase difference (ψ) and the vertical separation (h) between the leading edge and the trailing edge.

2.2 Four-bar Kinematics

In the actual flapping mechanism, the leading and trailing edges move in three dimensional space using a four bar mechanism instead of simple harmonic motion. This will cause significant difference in the kinematics of the wing compared to the simple harmonic case depending upon the lengths of the four-bar mechanism (L_1, L_2, L_3, L_4), the phase lag (ψ) and the vertical separation (h) between the two four-bar mechanisms. It is important to understand the kinematics of a single four-bar mechanism in order to understand the kinematics of the complete flapping mechanism.

As shown in Figure 2.3, a four bar mechanism comprises of four distinct link-

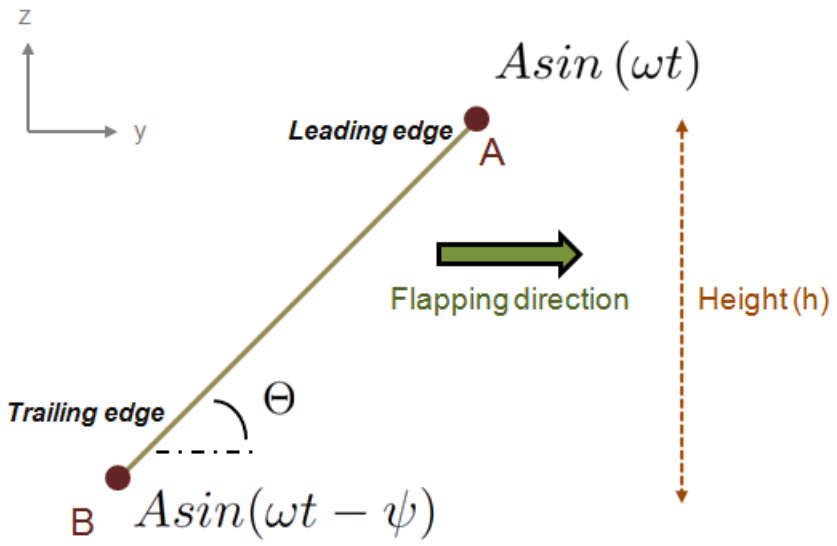

Figure 2.1: Schematic explaining the operating principle of the mechanism

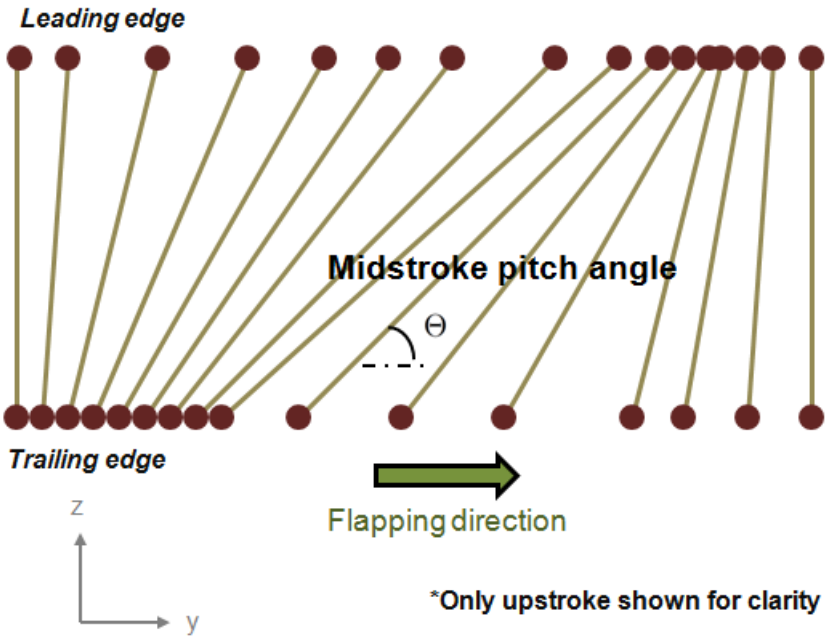

Figure 2.2: Variation of pitch angle through flapping stroke

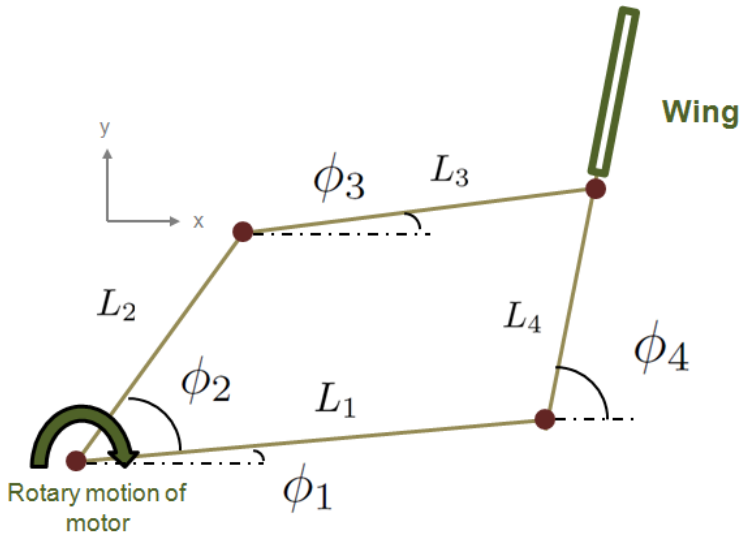

Figure 2.3: Four bar mechanism

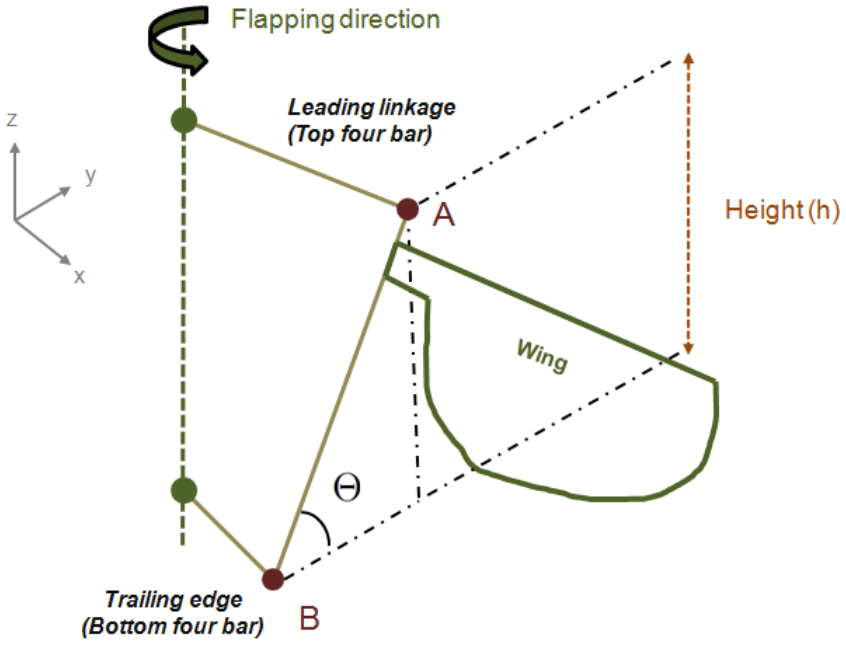

Figure 2.4: Schematic of proposed flapping mechanism

ages that are connected together using pin joints to convert the rotary motion of a motor into a flapping motion. The equations of motion of a four-bar mechanism can be derived as follows. The formulation begins with the four bar loop closure vector equation as shown in equation 2.2 and 2.3:

$$\overrightarrow{\mathbf{L_2}} + \overrightarrow{\mathbf{L_3}} = \overrightarrow{\mathbf{L_1}} + \overrightarrow{\mathbf{L_4}} \tag{2.2}$$

$$L_2 e^{(i\phi_2)} + L_3 e^{(i\phi_3)} = L_1 e^{(i\phi_1)} + L_4 e^{(i\phi_4)} \tag{2.3}$$

Where ϕ_1, ϕ_2, ϕ_3 and ϕ_4 are the angles the respective four-bar linkages make with horizontal axis (see Figure 2.3). Here the value of ϕ_2 is set to vary from 0 to 2π in order to emulate the rotary motion of the motor as shown in Figure 2.3, and ϕ_1 is set to 0. Thus we obtain:

$$L_2\left(sin(\phi_2), cos(\phi_2)\right) + L_3\left(sin(\phi_3), cos(\phi_3)\right) = L_1\left(0, 1\right) + L_4\left(sin(\phi_4), cos(\phi_4)\right) \tag{2.4}$$

Simplifying, we obtain two sets of equations:

$$L_3 sin(\phi_3) = L_4 sin(\phi_4) - L_2 sin(\phi_2) \tag{2.5}$$

$$L_3 cos(\phi_3) = L_1 + L_4 cos(\phi_4) - L_2 cos(\phi_2) \tag{2.6}$$

Adding the squares of both equations we have:

$$1 = \left(L_4 sin(\phi_4) + Y\right)^2 + \left(L_4 cos(\phi_4) + X\right)^2 \tag{2.7}$$

where

$$X = L_1 - L_2 cos(\phi_2) \tag{2.8}$$

$$Y = -L_2 sin(\phi_2) \tag{2.9}$$

Thus, from equation 2.7 we have:

$$\phi_4 = tan^{-1}\left(\frac{Y}{X}\right) - cos^{-1}\left(\frac{L_3^2 - L_4^2 - X^2 - Y^2}{2L_4\sqrt{X^2+Y^2}}\right) \tag{2.10}$$

For a more detailed derivation and discussion the reader is encouraged to see reference [3].

The velocities of the individual four-bar mechanisms can be obtained by differentiating the loop closure four bar vector equation (Equation 2.2 and 2.3), yielding:

$$\omega_4 = \frac{\omega_2 L_2 sin(\phi_3 - \phi_2)}{L_4 sin(\phi_3 - \phi_4)} \tag{2.11}$$

where

$$\phi_3 = \frac{-cos^{-1}(X + L_4 cos(\phi_4))}{L_3} \tag{2.12}$$

For simple translation motions with no pitching (no phase difference) the velocity profile of the four bar based flapping linkage (L_4) is such that for maximum and minimum values of ϕ_4, the angular velocity (ω_4) is zero. The angular velocity is maximum at the mean value of ϕ_4 which corresponds to the mid-stroke linkage location.

The acceleration kinematics for the flapping linkage can be derived in a similar fashion, by taking the second derivative of Equation 2.3. The angular acceleration of the top four bar linkage is given as:

$$\alpha_4 = \frac{L_2\alpha_2 sin(\phi_3 - \phi_2) - L_2\omega_2^2 cos(\phi_3 - \phi_2) + L_4\omega_4 cos(\phi_3 - \phi_4) - L_3\omega_3^2}{L_4 sin(\phi_3 - \phi_4)} \tag{2.13}$$

where the value of ω_3 can be obtained from the velocity kinematics analysis, and is found to be:

$$\omega_3 = \frac{-\omega_2 L_2 sin(\phi_2 - \phi_4)}{L_3 sin(\phi_3 - \phi_4)} \tag{2.14}$$

In equation 2.12, the value of α_2 is set to 0, as it is assumed that the motor operates at a constant angular velocity. With this understanding of the position, velocity and acceleration profiles of a single four bar mechanism, we now address the kinematics of a dual differential four bar mechanism.

2.3 Wing Kinematics Using Dual-Differential Four-Bar Mechanism

The prior section was devoted to obtaining an expression for the azimuthal location of the flapping linkage (L_4) for a four-bar mechanisms given the linkage lengths. In the proposed mechanisms, two such four-bars are utilized to generate wing flapping, pitching and coning motions.

2.3.1 Stroke Kinematics

The flapping kinematics, or wing azimuthal location is determined by the azimuthal locations of both the top and bottom L_4 locations. Assuming that the wing is halfway between these two four-bar mechanisms (at a height of $h/2$), its position is the average of the two four-bar azimuthal locations. It is given by:

$$W_\phi = \frac{1}{2}\left(tan^{-1}\left(\frac{Y}{X}\right) - cos^{-1}\left(\xi\right) + tan^{-1}\left(\frac{Y_T}{X_T}\right) - cos^{-1}\left(\xi_T\right)\right) \tag{2.15}$$

where

$$\xi = \left(\frac{L_3^2 - L_4^2 - X^2 - Y^2}{2L_4\sqrt{X^2+Y^2}}\right), \xi_T = \left(\frac{L_3^2 - L_4^2 - X_T^2 - Y_T^2}{2L_4\sqrt{X_T^2+Y_T^2}}\right)$$

Here the subscript T denotes the trailing edge. For increasing values of the phase angle (ψ), the amplitude of W_ϕ decreases. In other words the wing progressively devotes more of the stroke time to rotation than translation. To make this

more lucid, consider a wing during a downstroke - supination - upstroke motion. As the top linkage approaches the end of the halfstroke, the bottom linkage lags behind. Now, even before the bottom linkage has reached the end of the downstroke, the top linkage has started the upstroke. As a result, when the two linkages pass over each other (the wing attains a pitch of 90^o), the wing is not at the end of the stroke. Now as the bottom linkage reaches the end of the downstroke, the top linkage is well into the upstroke. Supination does not occur at the end of the stroke, but rather where the top and bottom linkages pass each other (which is not at the ends of the stroke). As a result, the overall amplitude seen by the wing (not the individual four-bar linkages) is reduced. Inputting large values of the phase difference into equation 2.25 yields this result.

2.3.2 Pitch Kinematics

The pitch kinematics are a function of the four-bar linkage locations as well. As shown in Figure 2.4, the angle subtended by the line connecting points A and B (tips of the leading and trailing linkages) with the horizontal plane is the pitch angle (Θ) of the wing at any instant of the flap. This is given by:

$$\Theta = sin^{-1}\left(\frac{h}{\sqrt{(X - X_T)^2 + (Y - Y_T)^2 + h^2}}\right) \tag{2.16}$$

where

$$X_T = L_1 - L_2 cos(\phi_2 - \psi) \tag{2.17}$$

$$Y_T = -L_2 sin(\phi_2 - \psi) \tag{2.18}$$

The subscript T denotes the trailing edge. It should be noted that for small values of the vertical distance h and small values of the phase difference, ψ, the wing flaps in an approximately horizontal stroke plane. However, significant increases in these values will lead to wing out of plane motions along with the wing pitching motion. This out of plane motion is characterized by the coning angle (β) which is defined along with the pitching angle in Figures 2.5 to 2.7.

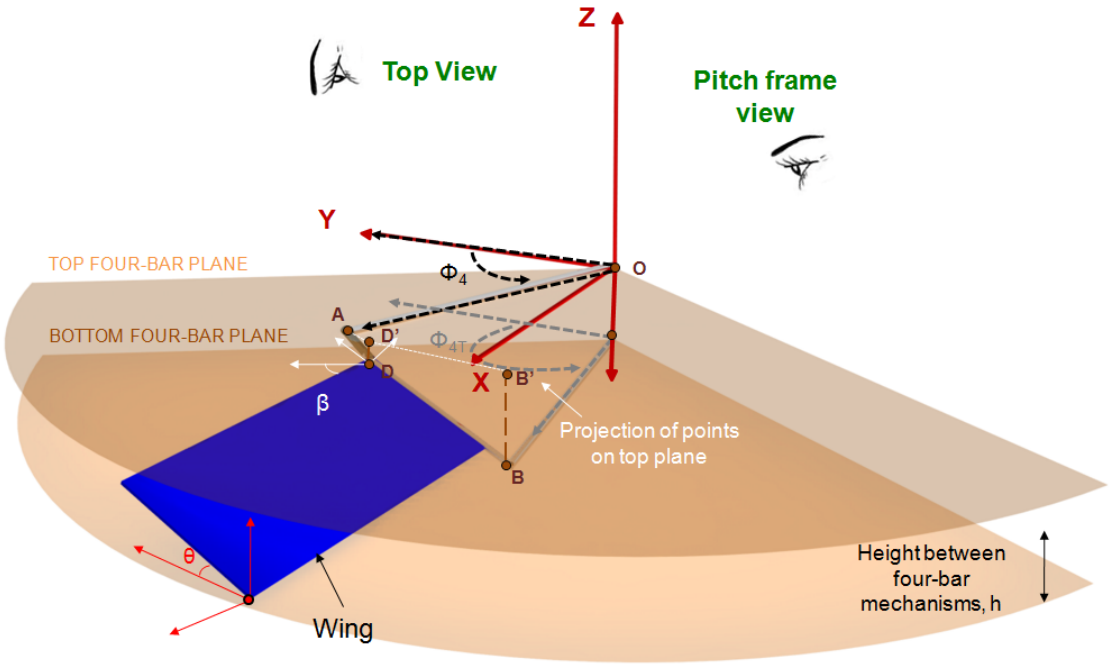

Figure 2.5: Isometric view of dual-differential four-bar with wing

2.3.3 Coning Kinematics

The isometric view of the dual-differential four-bar based flapping schematic in Figure 2.5 shows the stroke angles (ϕ_4, ϕ_{4_T}), the coning angle (β) and the pitch angle (θ). From the four-bar relations derived earlier the position of points A and B

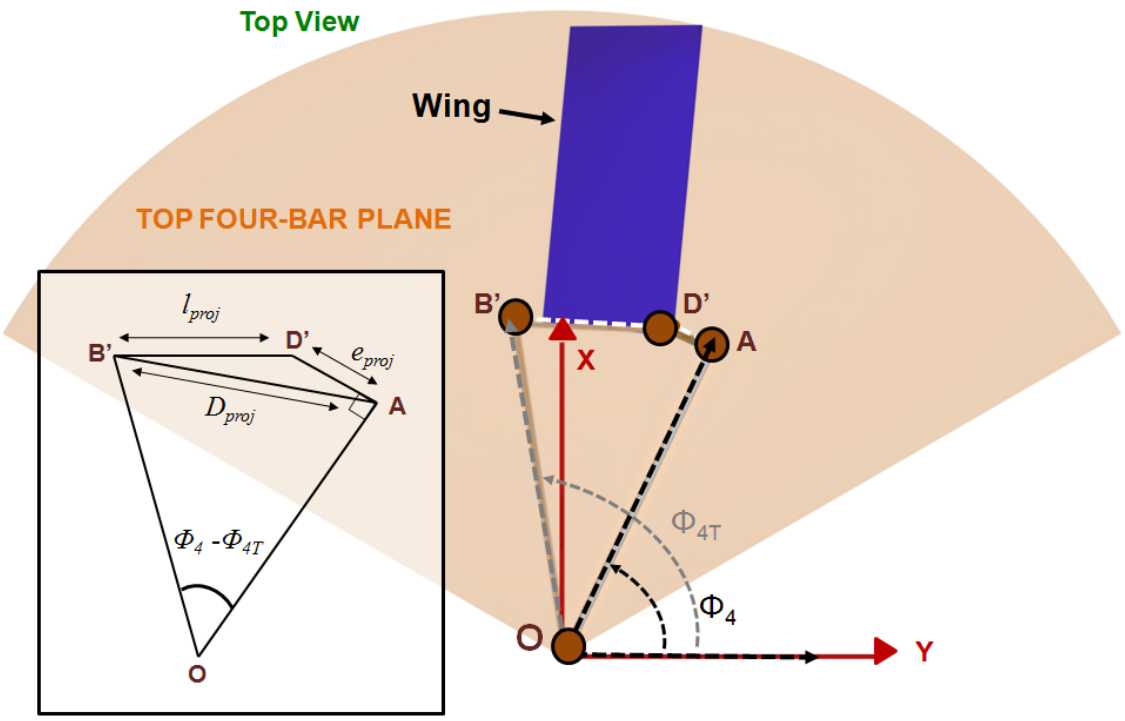

Figure 2.6: Top view of dual-differential four-bar with wing

throughout the stroke are known. The position of these points are governed by the subtended stroke angle and the offset arm AO. Segment AD is the offset from the pitch hinge and the coning hinge. Changing this distance will only affect the coning kinematics not the pitch angle variation. Segments AD' and D'B' are projections of segments AD and DB on the top four-bar stroke plane respectively. Depending on the spatial orientation of the 2-D plane on which these segments are viewed on, their apparent lengths may be different. Figure 2.6 illustrates these lengths as seen from the top. Here segments AD', B'D' and B'A are referred as to as e_{proj}, l_{proj} and D_{proj} respectively for simplicity. In this triangle (shown in the white box), D_{proj} is known, as it is the 2-D distance between the two L_4 linkage lengths (projection of D on the top four-bar plane; where D is the distance between the two L_4 linkages).

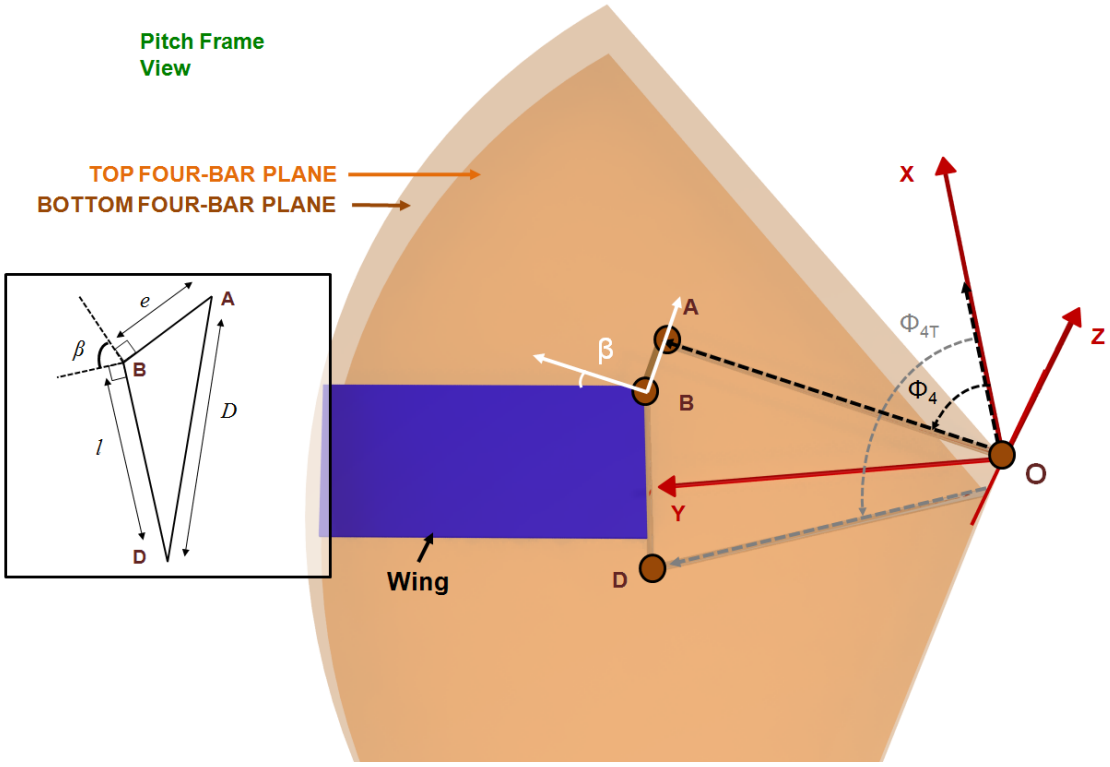

Figure 2.7: Pitching plane view of dual-differential four-bar with wing

Segment e_{proj} is the projection of e on the top four-bar plane and is thus $ecos(\Theta)$. Through simple trigonometric relations the value of l_{proj}; which is the only unknown length in triangle $B'D'A$, can be found to be:

$$l_{proj} = \sqrt{e_{proj}^2 + D_{proj} - 2e_{proj}D_{proj}cos\left(\frac{\phi_4 - \phi_{4_T}}{2}\right)} \tag{2.19}$$

This segment is now projected on the pitch plane (Figure 2.7) as length l, and is as $l_{proj}/cos(\Theta)$. In the triangle shown in Figure 2.7, the length D is the distance between points A and B (refer Figure 2.5). This can be determined easily as the spatial location of points A and B are known. Thus, all the lengths of this triangle ABD are known, and thus β can be determined to be:

$$\beta = \frac{\pi}{2} - cos^{-1}\left(\frac{D^2 - e^2 - l^2}{-2el}\right) \tag{2.20}$$

2.4 Mechanism Modeling and Simulation

Using the dual-differential four-bar schematic shown in Figure 2.5 as a baseline, a 3-D flapping wing model was designed as shown in Figure 2.8. The model was developed in CATIA V5 using the DMU Kinematics toolbox. There were three main reasons for pursuing the model:

- Firstly, demonstrate that the dual-differential four-bar mechanism was capable of generating complex figure of eight motions, as seen on insects.
- Implement the flapping, pitching and coning angles on a mechanisms in a simplistic manner, that can actually be fabricated and developed.

- Verify that the flapping, pitching and coning formulations (derived earlier) accurately predicted wing kinematics.

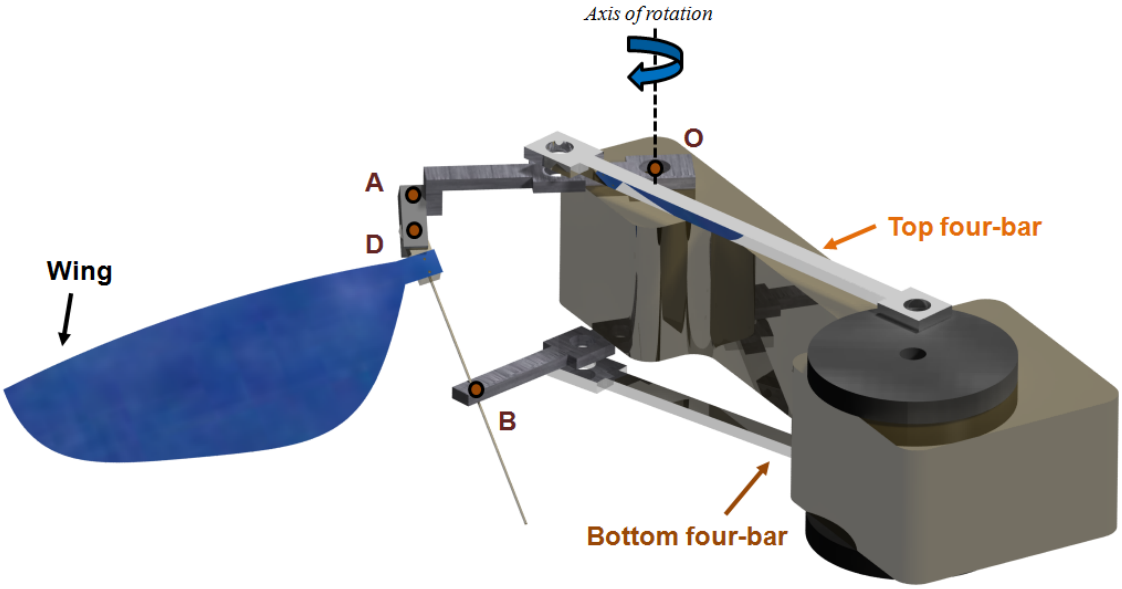

Figure 2.8: Isometric view of dual-differential four-bar flapping mechanism model

Figure 2.9 shows the top view of the model with the four-bar lengths labelled. It is vital when utilizing a four-bar mechanism to make sure that the four links can produce the required stroke kinematics. A slight increase or decrease in any one of the linkage lengths can adversely affect the stroke kinematics of the wing. This will be addressed in detail in the next section,as a parametric study was performed to obtain certain desired kinematics.

Figure 2.10 illustrates the view from the pitch frame of the wing. In order to permit both coning and pitching motions a double hinge was incorporated. This permits two degree of freedom motions, namely a rotation along the span of the wing, and a rotation along the chord of the wing as seen in Figure 2.10. As the wing flaps through the stroke amplitude, the distance between the leading and trailing

linkages varies as was discussed earlier. In order to permit this variation in the distance between the linkages through the stroke, a pin attached to the double hinge strokes through a clearance hole in the trailing linkage. If this distance variation was not permitted, the mechanism would not be feasible. A complete halfstroke is illustrated in Figure 2.11. Here the variation between the leading and trailing linkages through the stroke amplitude is clearly visible.

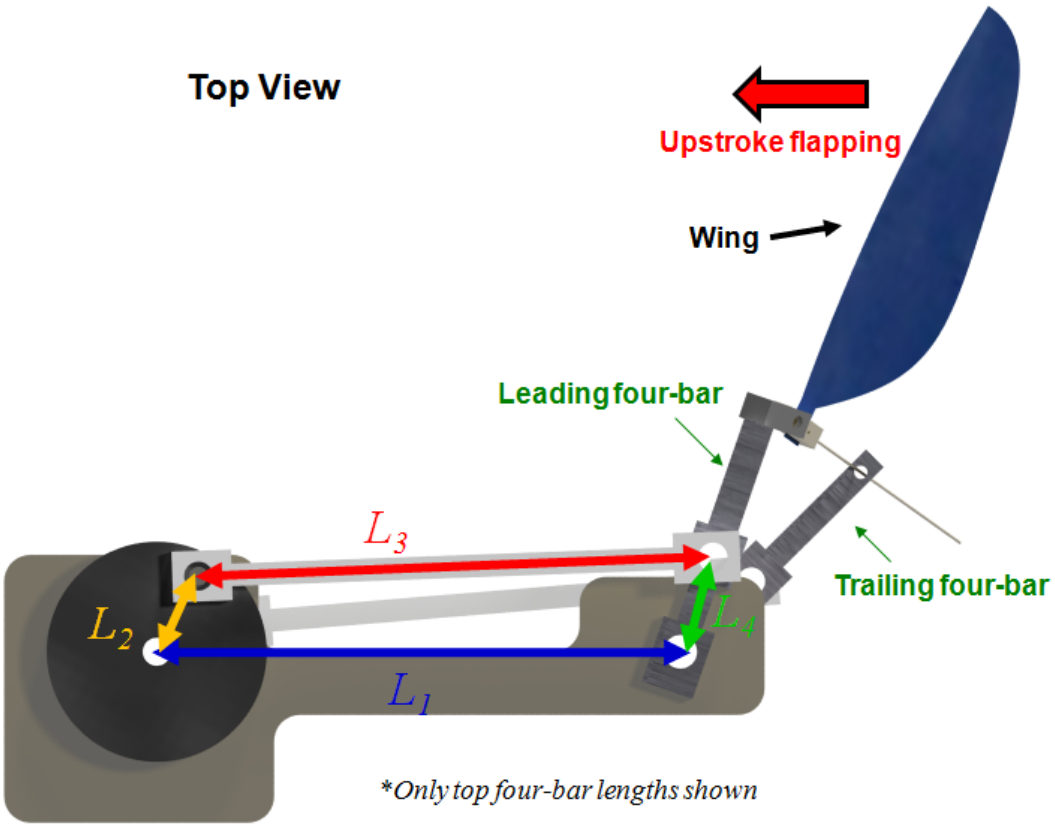

Figure 2.9: Top view of dual-differential four-bar flapping mechanism model

Figure 2.12 plots the wing stroke kinematics for both upstroke and downstroke motions, as predicted by the model. Here the wing is plotted as a series of lines (representative of the chord). Black dashed lines represent the upstroke flap, while

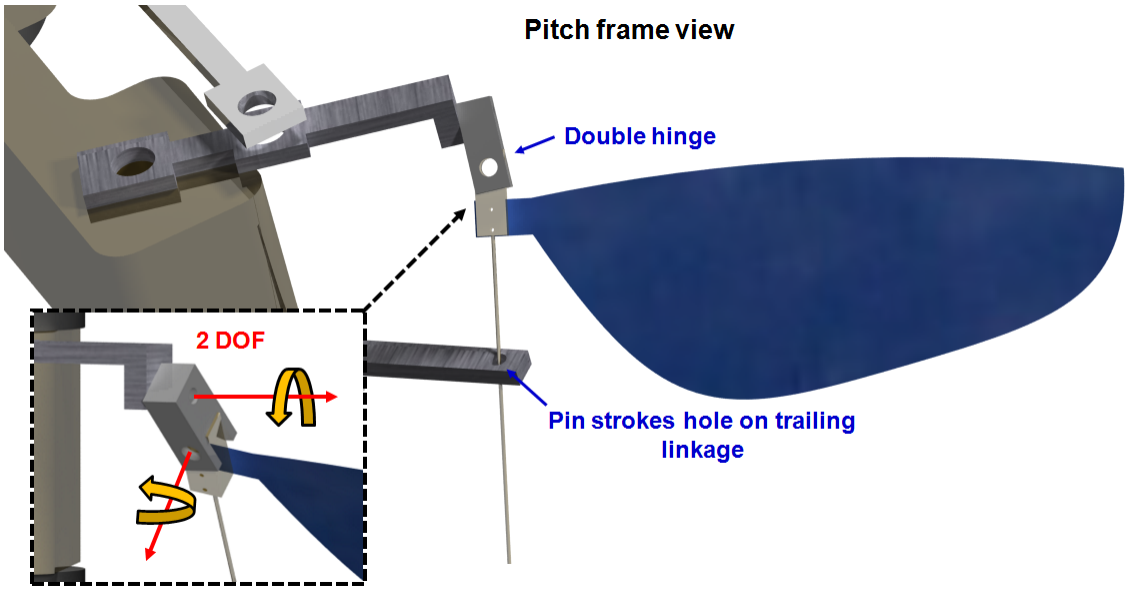

Figure 2.10: Pitch frame view of dual-differential four-bar flapping mechanism model

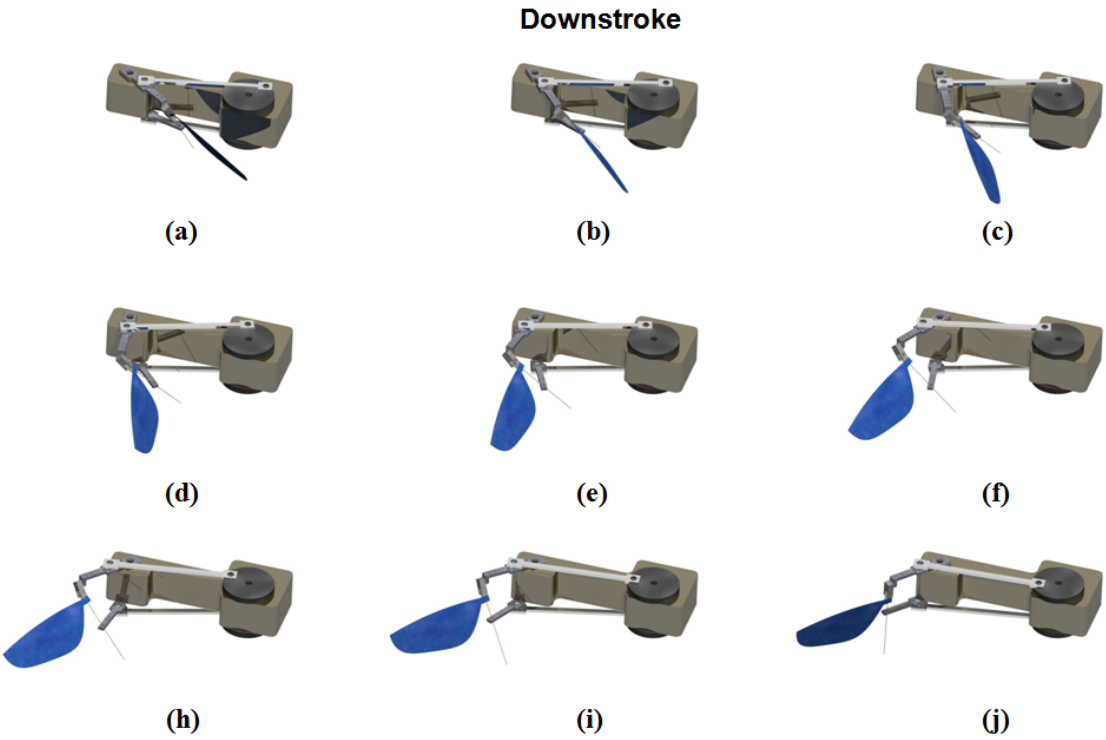

Figure 2.11: Model flapping in downstroke

red thick lines denote the downstroke flap. It was observed that for large values of the phase difference, (ψ), large coning and pitching angles together generated a figure of eight motion. Thus, despite the complex kinematics that can be generated from the model, the implementation of the various degrees of freedom has been done in a very simplistic manner as seen from the various illustrations.

The model was flapped for a variety of input kinematics and the wing and four-bar kinematics were recorded by placing sensors on various moving parts within the DMU Kinematics framework. Stroke angles of the top and bottom four-bar mechanisms were tracked along with the wing pitching and coning angles. Representative results are shown in Figure 2.13 and 2.14. The red circular markers in the graphs are from the CATIA simulation and the blue squared markers are from the derived formulas discussed earlier. Graphs that plot the stroke amplitude are analytical predicted by equation 2.10, the pitch angle is determined through equation 2.16 and the coning via equation 2.20. The x-axis of all the graphs corresponds to a one complete flap cycle. Overall there is an extremely good correlation between the two data set, thus validating the formulas for the stroke position, wing pitch and wing coning variations.

2.5 Mechanism Parametric Studies

It is essential to set the individual lengths of the four-bar mechanism such that they are optimized for maximum stroke amplitude. This is because prior studies have shown that a large stroke angle is advantageous from the perspective of lift

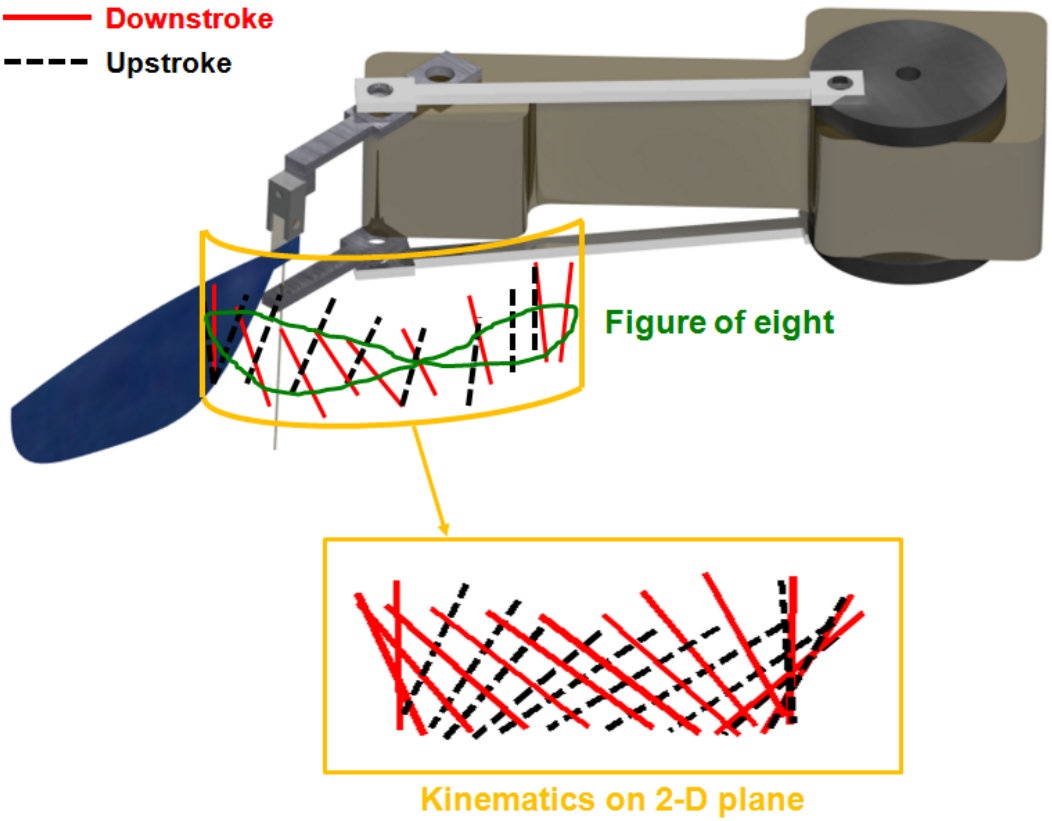

Figure 2.12: Model flapping in figure of eight motion

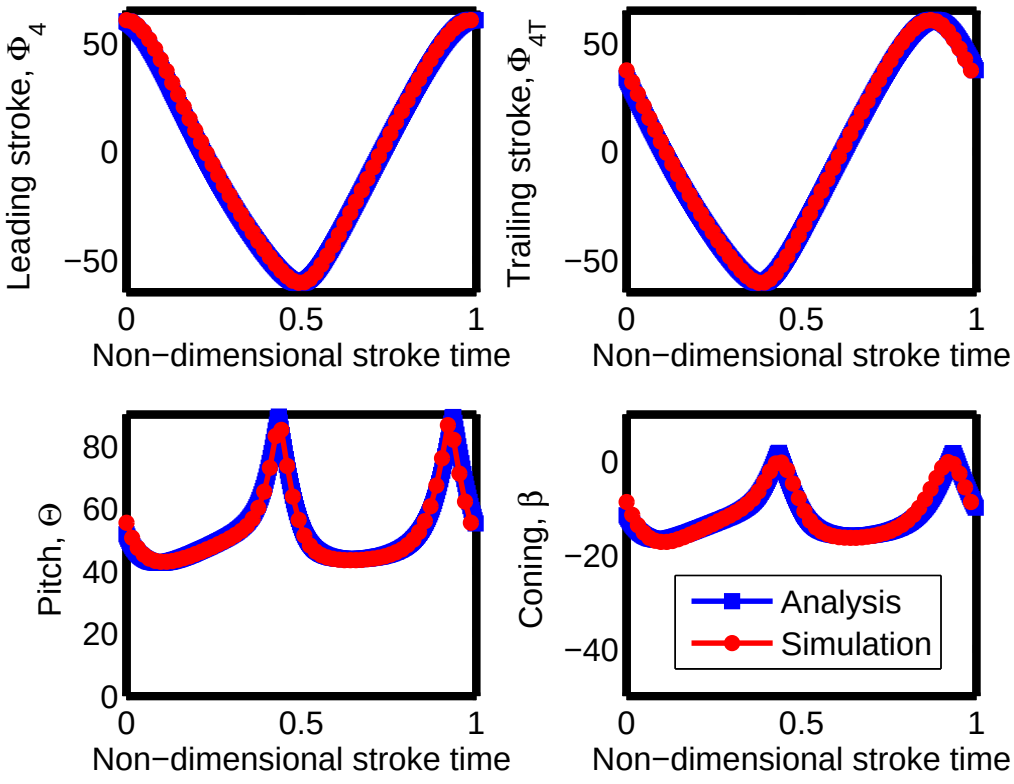

Figure 2.13: Comparison of kinematic angles at $\phi = 40^o$ and $h = 0.28$

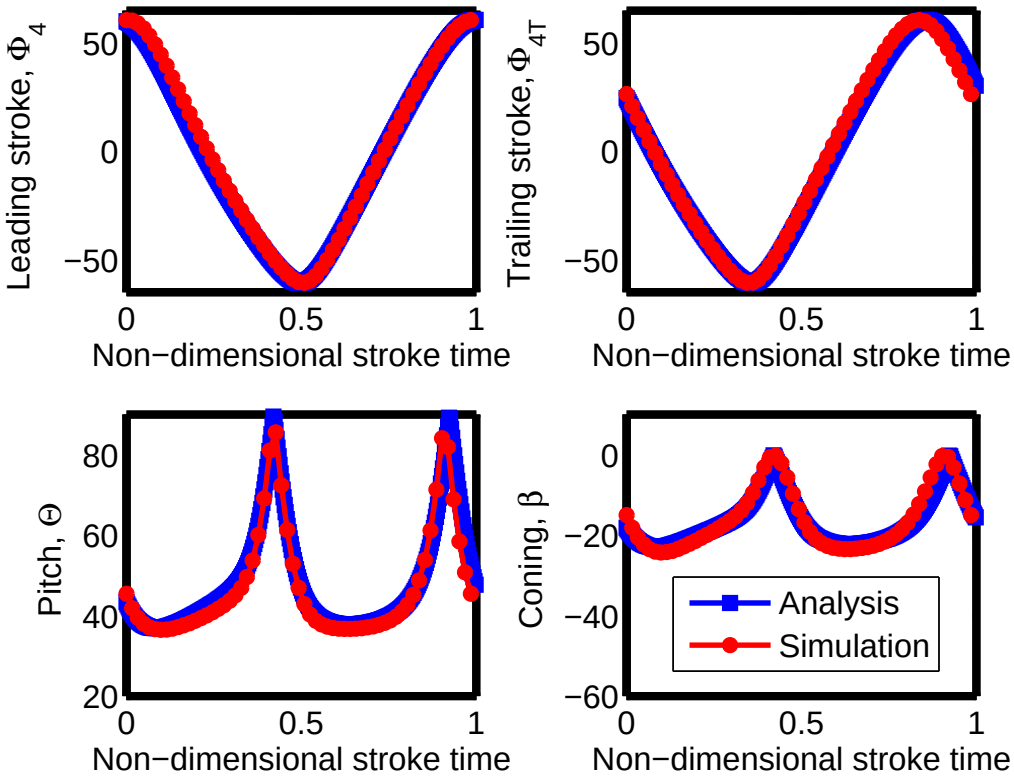

Figure 2.14: Comparison of kinematic angles at $\phi = 50^o$ and $h = 0.28$

production for a flapping wing system [9]. In this study the four-bar lengths are individually varied to understand their effect on the resultant kinematics. Thereafter, the pitching kinematics of the dual-differential mechanism are analyzed for different values of the phase angle and the height.

2.5.1 Single Four-Bar Studies

Baseline values for the four linkage lengths were selected, and then the values of each linkage length were varied in order to gauge their respective effect individually. Here the baseline values for the other lengths are $[L_2 = 0.16, L_3 = 0.98, L_4 = 0.19]$. The maximum and minimum L_1 lengths in the graph was determined by the feasibility of the four-bar mechanism. In other words, increasing or decreasing any four-bar length beyond a certain limit will result in a unworkable mechanism. Grashof's criterion regarding the length of linkages with respect to each other plays an important role in the feasibility of a four-bar. The linkage lengths were non-dimensionalized with respect to L_1, which was the longest length for the cases.

Figure 2.15 plots the effect of varying L_1 on the stroke angle while maintaining the lengths of the other lengths the same.The x axis plots the non-dimensional stroke time with respect to θ_2, which corresponds to the azimuth. It is evident that while a variation of L_1 does not have a significant effect on the stroke angle, it does cause a phase shift. That is increasing the value of L_1 shifts the stroke forwards with respect to the azimuthal angle.

The variation of the eccentric length L_2 is plotted in Figure 2.16 for the same

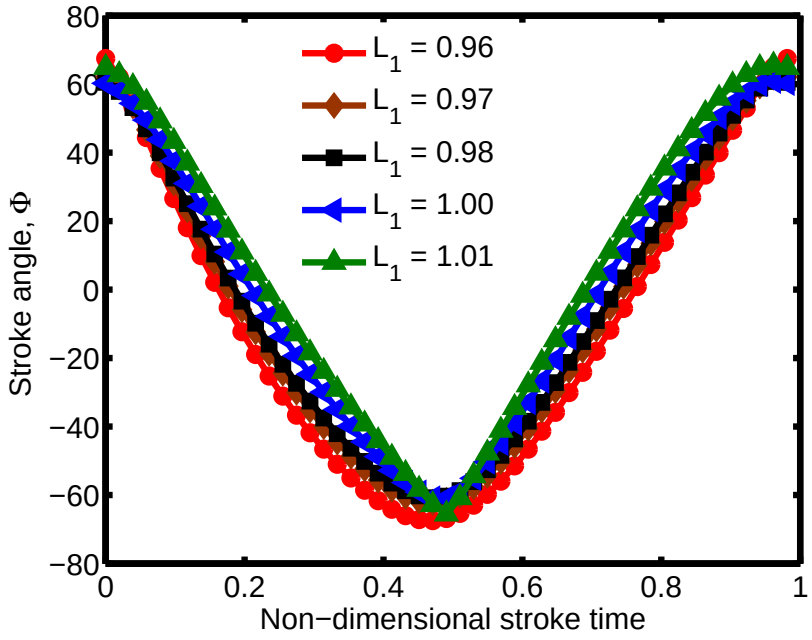

Figure 2.15: Stroke angle variation for different L_1

parameters shown in Figure 2.15. Increasing L_2 from 0.13 to 0.17 results in a large increase in the stroke angle from 85^o to 130^o respectively.

Figure 2.17 shows the effect of varying length L_3. It has the same effect as L_1, that is a very small change in the stroke angle and a movement of the stroke amplitude (phase shift). Interestingly, the effect is the converse of a variation in L_1; an increase in L_3 causes a backward shift in the phase with respect to the azimuth.

The variation of the wing linkage, L_4 is plotted in Figure 2.18. Values of L_4 range from 0.17 to 0.21. This graph shows two values of L_4 that do not producing working four-bar mechanisms in conjunction with the other baseline linkage lengths. As was discussed earlier there is a stringent requirement on the length of each four-bar length in order for the system to be mechanically feasible. In mathematical terms, with regard to the equations derived we observe the occurrence of complex

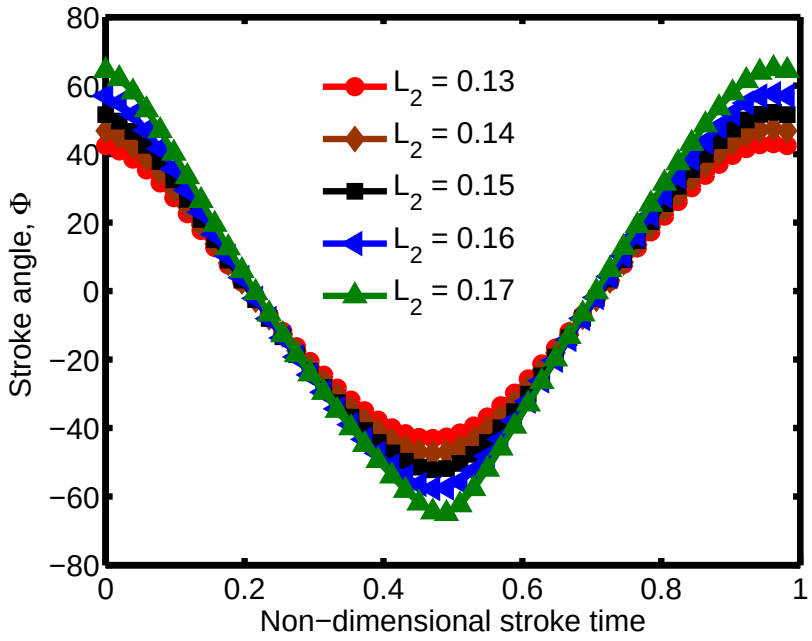

Figure 2.16: Stroke angle variation for different L_2

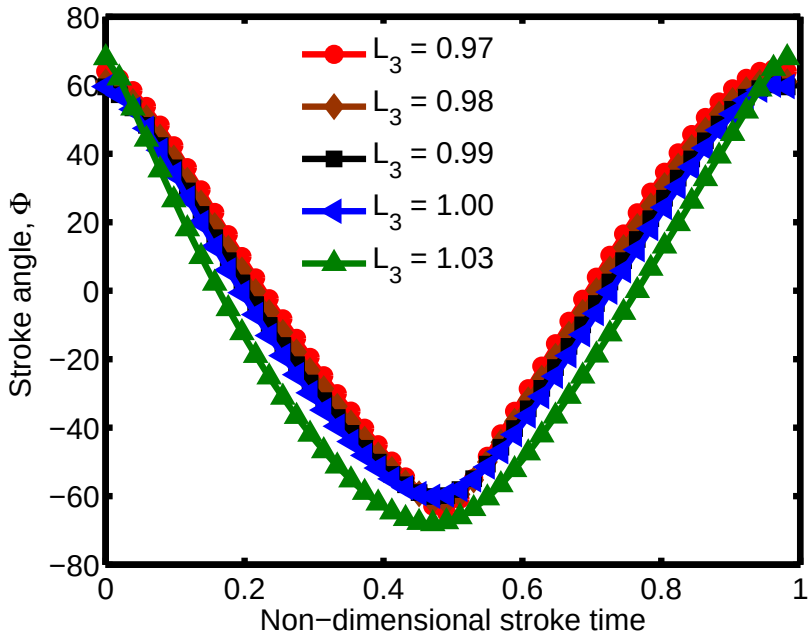

Figure 2.17: Stroke angle variation for different L_3

numbers in the stroke angle (θ_4). In Figure 2.18 for L_4 values of 0.17 and 0.18, the oddities in the stroke variations at a non-dimensional stroke time of 0.5 correspond to the presence of complex numbers. Like L_2, a variation in L_4 results in a significant change in the stroke amplitude. The effect though is the converse of the variation in L_2; increasing L_4 causes a decrease in the stroke amplitude. To summarize, lengths L_2 and L_4 (which are the eccentric lengths) have a greater influence on the stroke magnitude as compared to L_1 and L_3; which have a greater role in the location of the stroke angle.

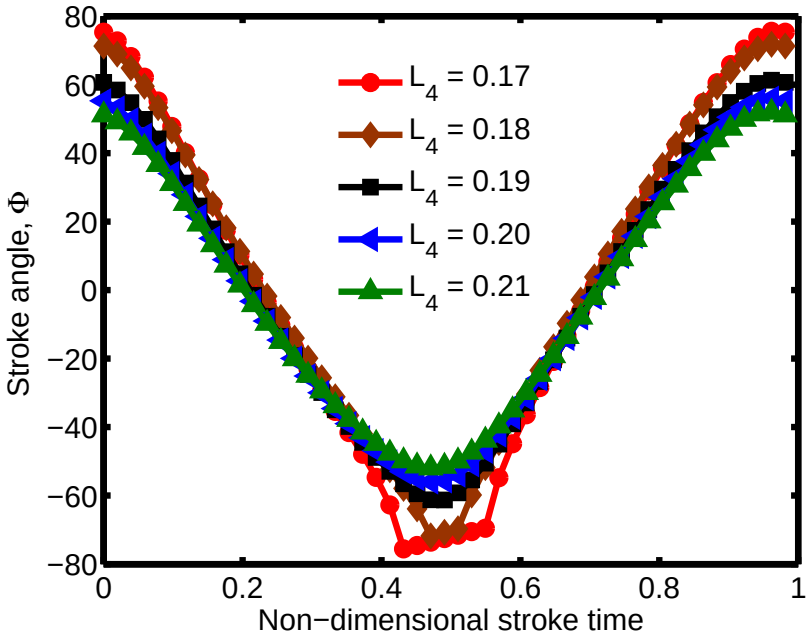

Figure 2.18: Stroke angle variation for different L_4

2.5.2 Dual-Differential Four-Bar Studies

As mentioned earlier there are two more parameters that govern the kinematics of the proposed dual-differential four-bar mechanism; the phase difference (ϕ)

and the height between the two four-bars (h). Figure 2.19 plots the pitch angle (Θ) variation as a function of the non-dimensional stroke time for varying phase difference (ψ)and Figure 2.20 plots the pitch variation with changing height. It is observed that for increasing values of the phase angle, the pitch angle gets reduced significantly. Decreasing the height between the two-four bars also has the same effect as shown in Figure 2.20.

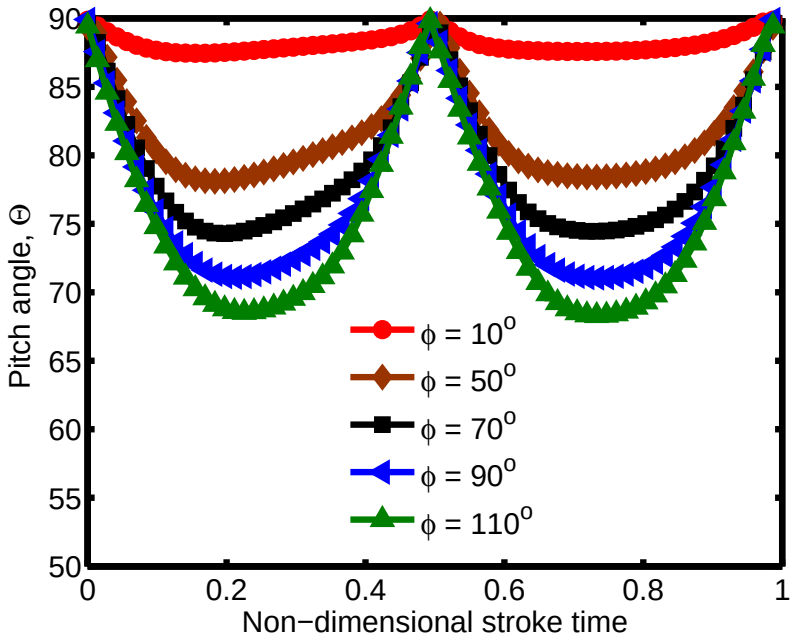

Figure 2.19: Stroke angle variation for different ϕ

2.6 Conclusions

In this chapter, a simple concept has been introduced capable of emulating all three degrees of freedom of insect kinematics. Unlike other flapping mechanisms that rely on passive wing kinematics to attain complex figure of eight rings, this

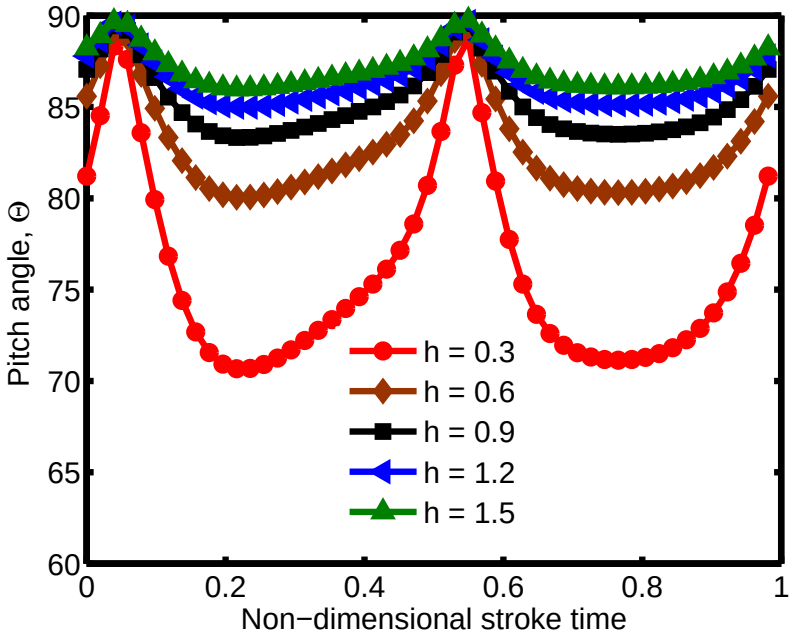

Figure 2.20: Stroke angle variation for different h

mechanism can produce such motions with a rigid wing. The following are the main conclusions of this chapter:

1. Kinematic relations for the wing stroke, pitch and coning angles were formulated using simple trigonometric relations for the dual-differential four-bar mechanism. The equations were derived using a four-bar linkage analysis.

2. A model was designed using DMU Kinematics toolbox within CATIA V5. The model was designed in a simplistic manner, while ensuring that the mechanism incorporated all proposed degrees of freedom. To this extent a novel double hinge and pin-hole arrangement were presented to accomodate the coning and pitching variations. When simulated, it was found that the model was able to generate a figure of eight motion.

3. The model was simulated for a variety of wing kinematics. Sensors used within the DMU Kinematics framework tracked the various kinematic angles. When compared with those generated via the analytical expression an extremely good correlation was observed.

Chapter 3

Results and Analysis: Mean Flapping Tests

3.1 Overview

One of the central goals of this work is to design and fabricate a hover-capable, flapping wing MAV. In this regard, importance must be given to the wings. The wings need to be aeroelastically tailored so as to produce as much lift as possible with the minimum weight. A benchtop setup that uses the dual-differential four-bar mechanism for emulating insect kinematics was designed and built. This benchtop setup was equipped with load cells to measure the lift and motor torque. Trying to measure these metrics on an actual vehicle would be tedious thus the test bed approach is pursed.

During the course of this research, numerous wings were designed, fabricated and tested (see Figure 3.1). The wing parameters varied during testing included: pitching kinematics, rib thickness, rib width, rib angle and the number of ribs. Average force and power measurements were made for these wings for numerous flapping frequencies. Wing deformations and geometric pitch angle variations were captured using a marker-tracking motion capture system (VICON®). A flow visualization study was carried out to get a qualitative idea of the unsteady air flow structures present while flapping.

Figure 3.1: Montage of aeroelastic wing designs

3.2 Benchtop Flapper

The flapping mechanism, which was built based on the four bar mechanisms is described in the previous chapter and is shown in Figure 3.2. In this mechanism, the phase difference between the top and bottom four-bar mechanisms can be changed by changing the phase of one of the flywheels relative to the other until the desired pitch angle variation of the wing is obtained. Therefore, using this mechanism, the wings can be tested at different geometric angles of attack. In order to keep the weights of the moving parts to a minimum, these are fabricated out of Delrin® (plastic).

To attach the wing, the ends of the flapping linkages are connected by a double hinge assembly (see Figure 3.3). Since the distance and the angle between the linkage ends are changing, a double hinge mechanism is installed between the leading and trailing linkages. This permits a two degree of freedom motion, as was discussed in Chapter 2. As the wing pitches through the stroke, the distance between the leading and trailing linkages are varying. In order to permit this motion a pin is attached

to the double hinge. As the wing flaps, the pin strokes a rod-end bearing as shown in Figure 3.3. The wing is connected to the attachment on the pin. The minimum pitch angle for the wing obtained by this mechanism is limited by the maximum swivel angle allowed by the rod-end bearing in the trailing linkage.

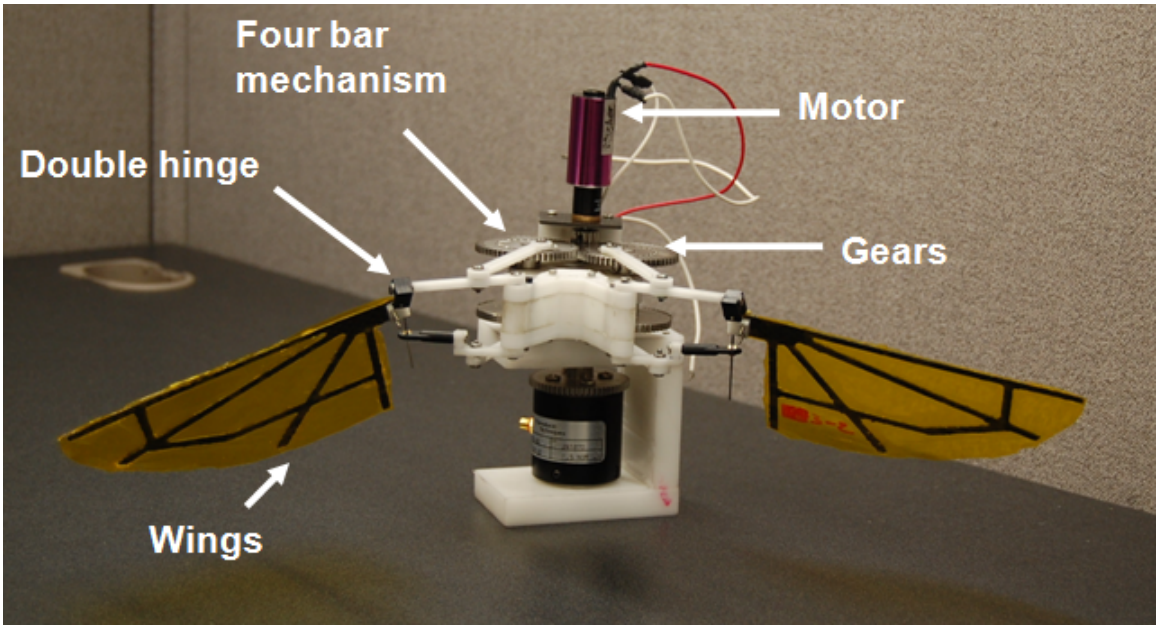

Figure 3.2: Benchtop flapping mechanism

The mechanism is flapped using a B-20 brushless Hacker motor, which has an internal planetary gear box. The overall gear reduction in two stages is 16:1. A high gear ratio is extremely important because it allows the motor to operate at the optimum RPM, which is much higher than the operating frequency of the flapping mechanism.

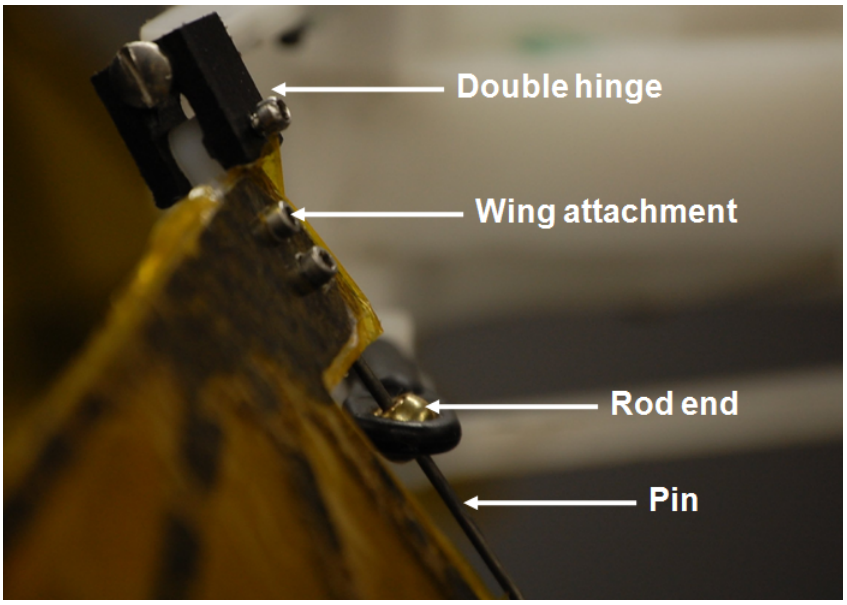

Figure 3.3: Double hinge and pin assembly

3.3 Lift Measurements

Lift values were obtained using a OHAUS Explorer Pro EP6102 mass balance. The balance has an accuracy of 0.01 g [1]. The lift values taken were averaged over a period of five seconds, and repeated several times in order to ensure repeatability. It is crucial to note that for the stroke average tests the inertial force contribution is assumed to average out to zero for each cycle. As a result, the average lift value over several strokes is reflective of the pure aerodynamic force. The focus of these tests were to measure the time averaged aerodynamic performance in terms of net thrust and power. For instantaneous force measurements, a different experimental setup is used as will be discussed later.

3.4 Power Measurements

The output mechanical power of the flapping mechanism is measured through a special arrangement of the motor and torque cell so that it only measures the torque provided by the motor to flap the wing and not any of the inertial body moments produced by the wing. The motor was mounted on four coaxial bearings so that all degrees of freedom except the rotation about the motor axis, is constrained. As a result, when the motor is connected to the torque sensor, it only registers the motor torque. The power consumed was obtained from the torque and frequency measurements. A close up of this arrangement is shown in Figure 3.4. A RTS-10 (10 oz-in) low capacity reaction torque sensor from Transducer Techniques was used to measured the torque from the motor.

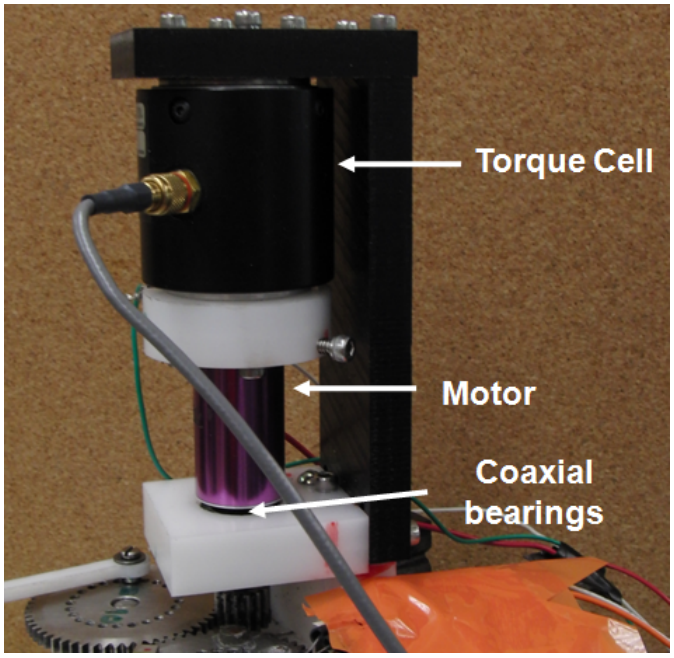

Figure 3.4: Arrangement for experimentally obtaining power

3.5 Frequency Measurements

A Hall effect sensor was mounted on the mechanism, in conjunction with magnets mounted on the flywheel, which were used to determine the flapping frequency. Totally eight magnets were used to provide a frequency measurement resolution of 0.125 Hz (see Figure 3.5).

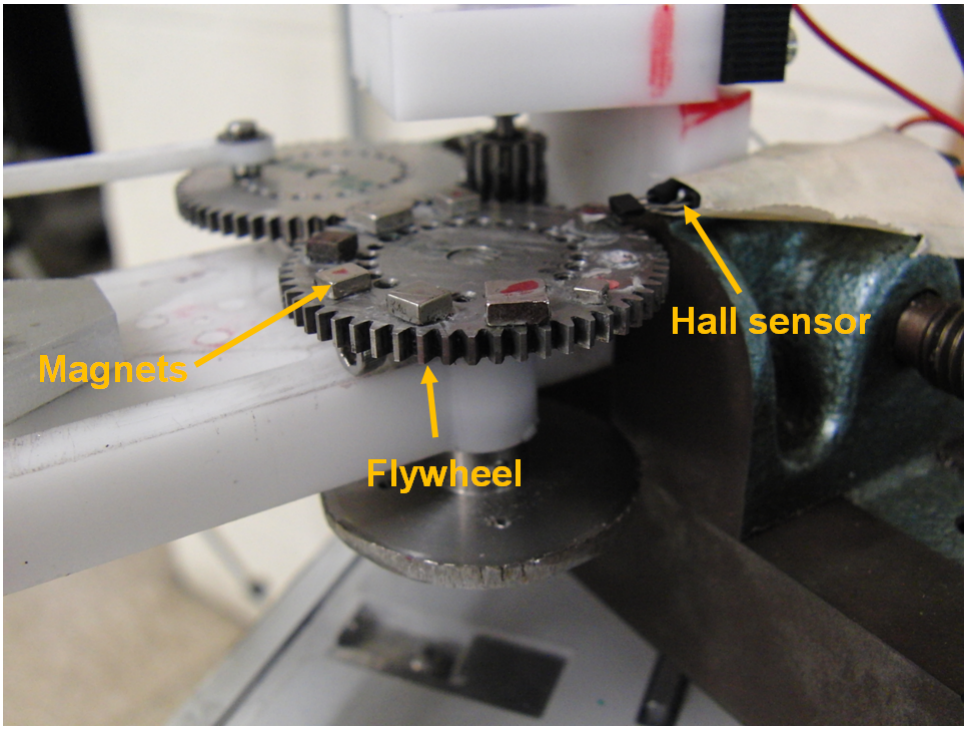

Figure 3.5: Hall sensor and magnets for measuring frequency

3.6 Wing Structure, Design and Fabrication

During the entire flapping cycle, the leading edge of the wing remains stiff in bending while there is significant torsional deformation (passive pitching) [13]. The design of all the aeroelastic wings fabricated followed this governing principle.

The schematic in Figure 3.6 outlines the wing fabrication procedure for a generic wing. As shown in step 1, the wing is placed on an aluminum plate that is has three coats of Frekote 700−NC releasing agent. This is used to prevent the carbon fiber from sticking onto the plate after the curing cycle. Thin strips of unidirectional carbon fiber sheets are used as the ribs of the wing. They are cut long enough so as to permit sufficient length for folding over a carbon rod. In order to simulate the stiff leading edge of an insect-based wing, a unidirectional carbon rod is placed along the leading edge of the wing. After the rod has been placed, the unidirectional fibers can be folded over the rod, such that they are cantilevered off the leading edge spar. At the root, layers of $0^o/90^o$ carbon fiber are used. This serves to clamp the wing; to attach it to the flapping mechanism. As a result they need to be strong in both longitudinal and lateral directions, which is the reason why unidirectional fiber is not utilized here. Once assembled, another aluminum plate is clamped over the first plate in the form of a sandwich structure (Step 2). The wing is cured in the oven at 250^oF for 75 minutes and then 350^oF for 90 minutes. Once the curing cycle is complete, the wing is removed from the aluminum plates, and a mylar film is applied to the wing (Step 3). Holes are drilled in the root carbon fiber piece for clamping on the flapping mechanism.

The generic wing outline is shown in Figure 3.7 with span, chord and rib separation measurements. It should be noted that the bending deformation of these chordwise spars manifest as the torsional deformation or passive pitching of the wing. Therefore, the passive pitching of the wing mainly depends on the bending stiffness and the orientation of these chordwise spars and to some extent on the

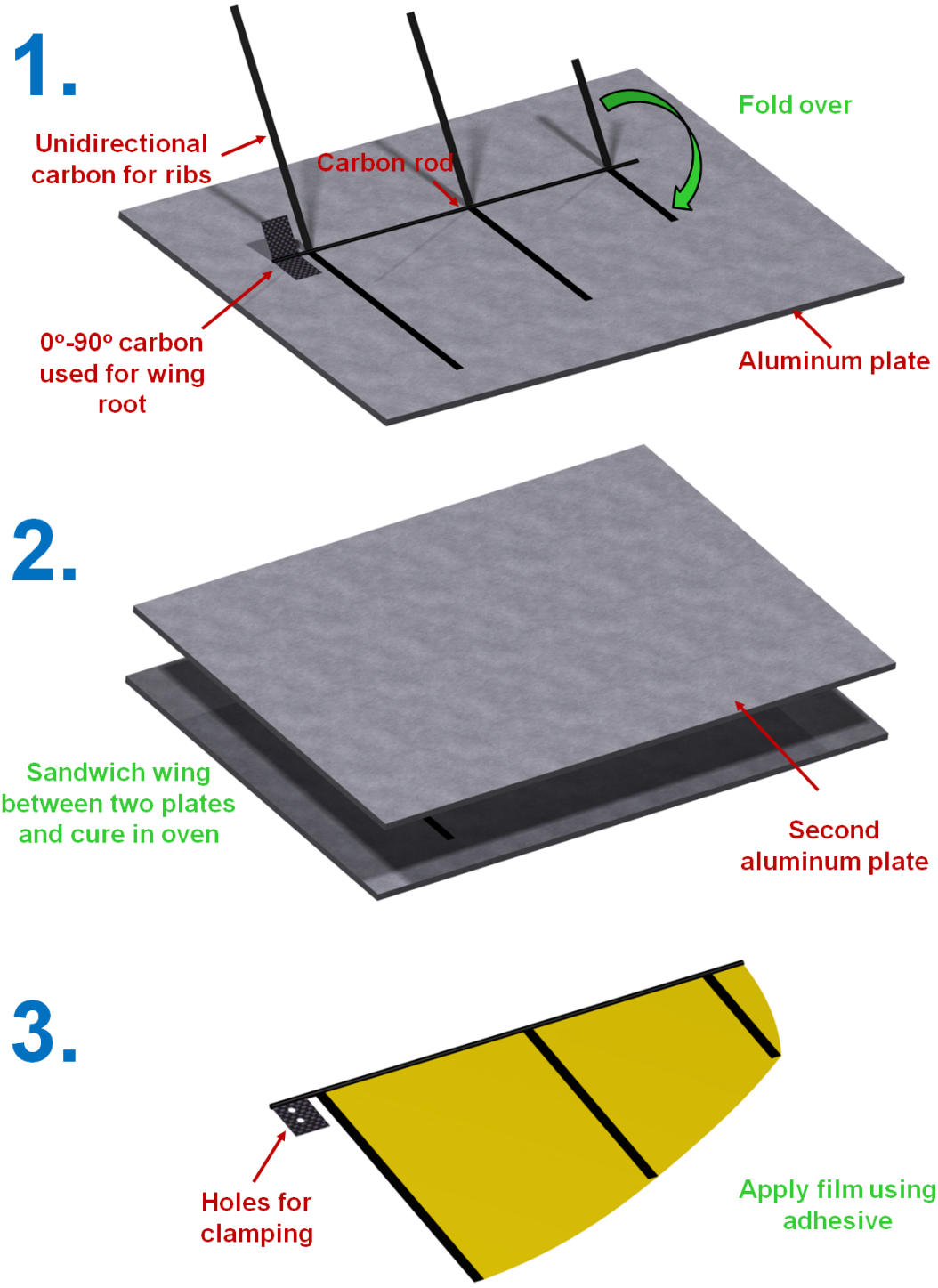

Figure 3.6: Wing fabrication procedure

torsional stiffness of the leading edge spar.

Each wing had the same planform, shape, chord and span dimensions. All the wings used a 1.5 mm diameter unidirectional carbon rod of circular cross-section as the leading edge spar with a span of 165 mm (6.5 inches). With the exception of Wings X and Y that had a chord length of 3.5 inches, all wings had a chord of 4 inches. The main differences in the construction of these wings were in the thickness, width, orientation, and the number of chordwise ribs. Three different mylar films with different thickness were also investigated for the wing skin. The nomenclature and the description of each of these wings tested are provided in Table 3.1.

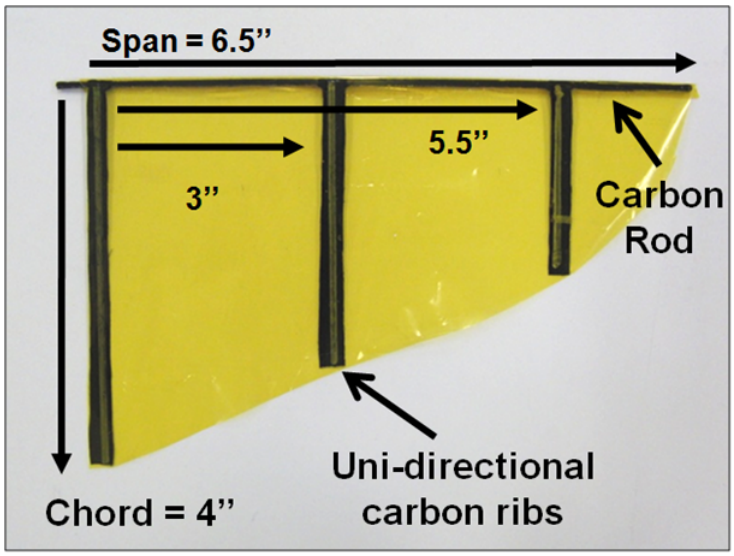

Figure 3.7: Aeroelastic wing outline

3.7 Lift Results

The main challenge in building a hover-capable flapping wing MAV lies in maximizing the lift produced for a fixed flapping frequency, while minimizing the

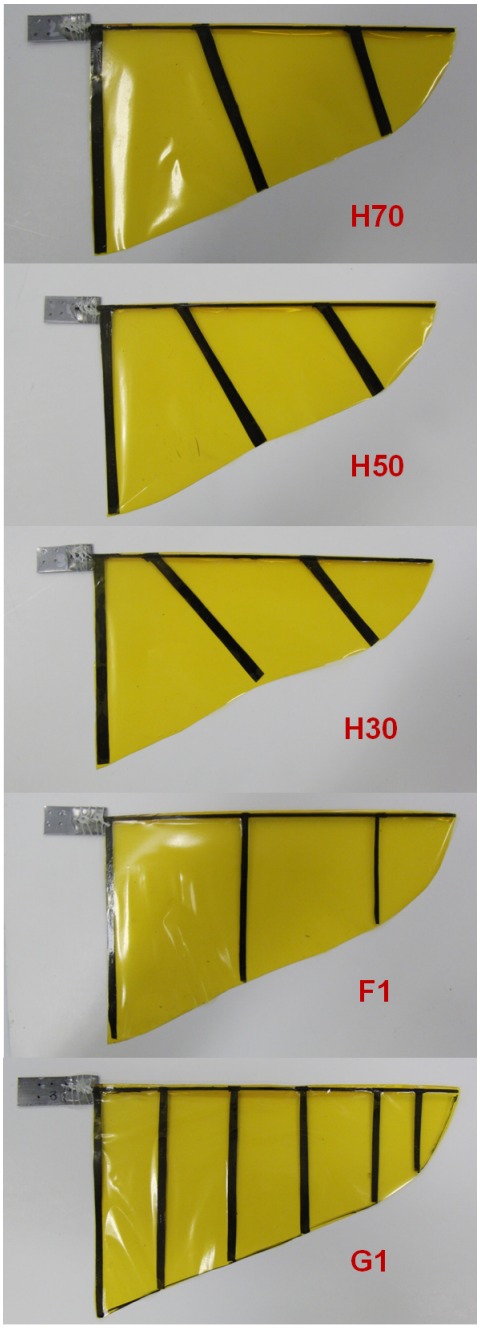

Figure 3.8: Wing designs for testing

weight of the wing. The wings need to have a certain bending stiffness and torsional flexibility in order to permit the attainment of the optimum pitch angle variations, thus maximizing the lift. At the same time, the mass has to be at a minimum so as to decrease the inertial forces. The goal of these experiments is to design light-weight wings (<2 grams) that can produce enough lift for a 100 gram flapping MAV to hover at relatively lower flapping frequencies (<15 Hz).

Utilizing the dual-differential four-bar mechanism numerous pitching variations can be generated based upon the phasing between the four-bar mechanisms. Thus as the wing flaps through its stroke, the pitch angle is changing at each instant. In order to classify a particular stroke variation, the angle at the mid-stroke is determined. This angle termed the midstroke angle, or θ_m, is the pitch angle of the wing at the midstroke. It is also the lowest angle the wing attains during one halfstroke. Figure 3.9 shows the midstroke pitch angle for a particular pitch variation through the stroke.

3.7.1 Effect of Pitching Kinematics

Figures 3.10 and 3.11 plot the lift variation for Wing Y and Wing X at three different midstroke pitch angles. Wing Y and Wing X have the same properties as Wing A1 and Wing A2, but with a smaller chord of 3.5 inches instead of 4 inches. From the graphs it is evident that at low frequencies, the lift values for all pitch angles are quite similar, however at higher frequencies the 90^o pitch case dominates. The occurrence of maximum lift at 90^o pitch may be attributed to the

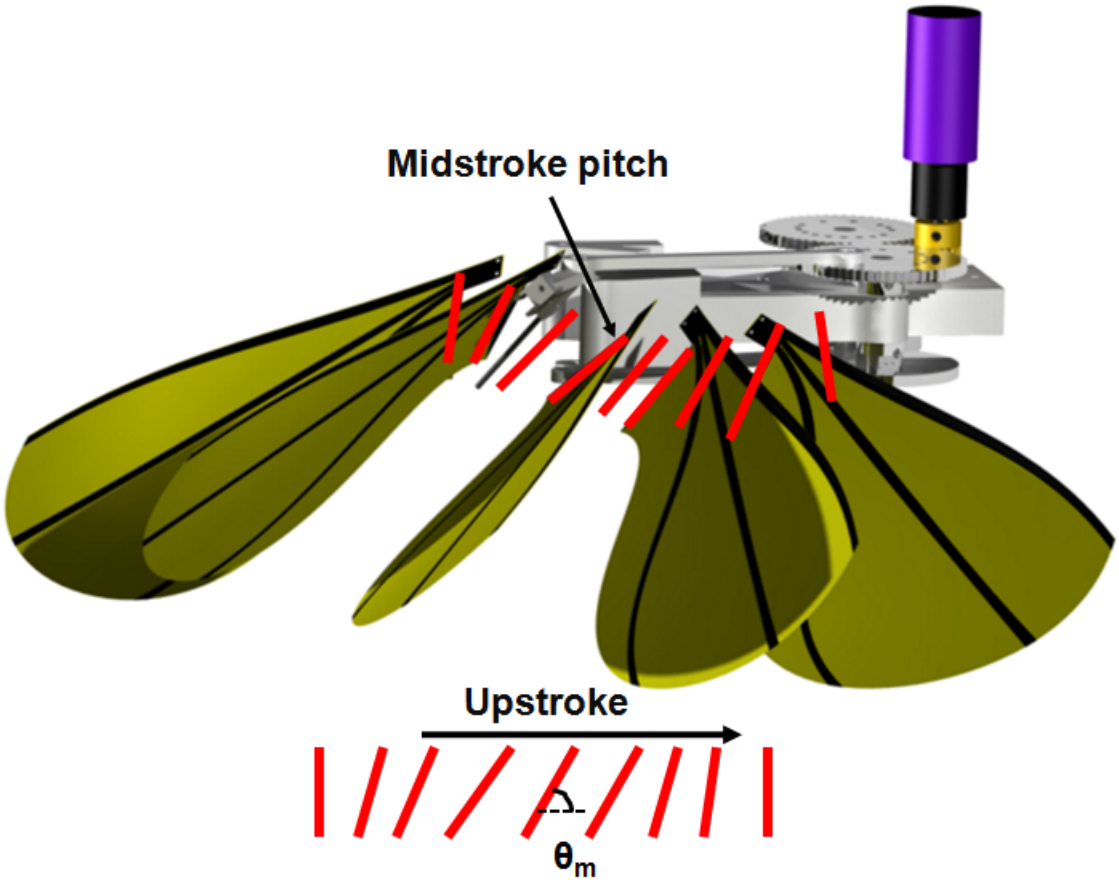

Figure 3.9: Definition of midstroke pitch angle

passive pitching of the wings at high frequencies, enabling the wing to operate at more favorable angles of attack.

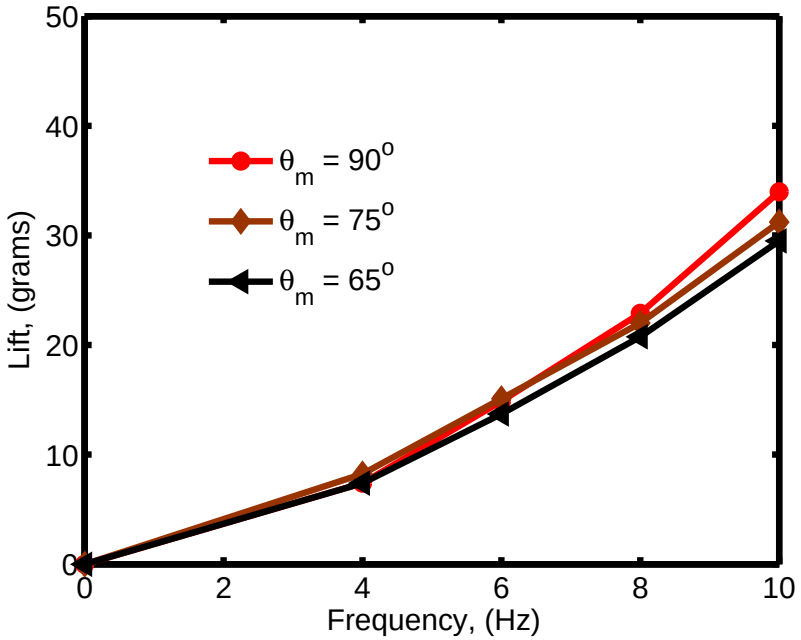

Figure 3.10: Lift variation for Wing Y with different midstroke pitch angle variations

The actual geometric angle of attack of the wing is a combination of the prescribed wing kinematics (pitch angle) and the torsional deformation (passive pitching). Thus, while the pitch is at 90^o, the angle of attack maybe markedly different.

In order to quantify the extent of torsional deformation and the corresponding angle of attack, a VICON® motion tracking system was utilized on the flapping wing system. Reflective markers were placed on the spars of the wings as shown in Figure 3.12. The idea was to track the motion of these individual markers with respect to time and thus obtain a quantitative measure of wing deflection distribution at high frequencies. The two points on each spar could be connected via a

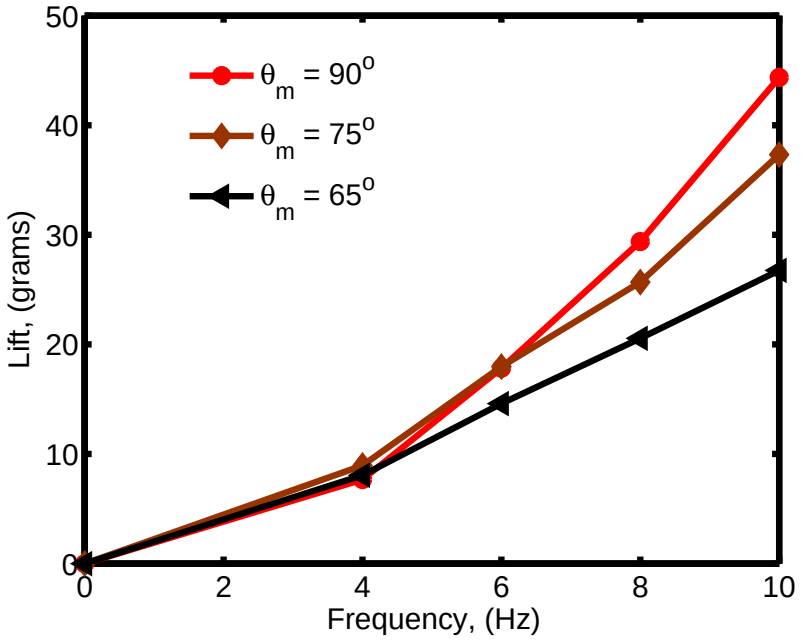

Figure 3.11: Lift variation for Wing X with different midstroke pitch angle variations

line, and thus the geometric angle of attack could be estimated. Additionally, the extent of wing deformation from root to tip could also be obtained, thus providing a quantitative insight into the aeroelasticity of the wing.

Utilizing the motion tracking system on Wing X for the different pitch angles at a frequency of 8 Hz, the geometric angle of attack variation measured during a flapping cycle is shown in Figures 3.12 to 3.14. The angle measured using VICON® is the net sectional pitch angle of the wing, which is a combination of the prescribed pitch variation by the mechanism and the wing elastic torsion. For the purpose of nomenclature, the spars are named A, B and C; with spar A being the most inboard or the root spar of the wing, spar B the middle spar and spar C being the outboard spar or the tip spar. Also presented is the prescribed wing pitch angle variation obtained using the dual-differential four-bar analysis, that represents the rigid wing

kinematics. From the results, it is evident that the wing twist of spar C (wing tip) was the highest and therefore the lowest geometric angle, followed by spar B and then by spar A. This trend is expected because the aerodynamic and inertial forces experienced by the wing increases from the root to the tip. For instance, in the 90^o pitch case (Figure 3.12), the geometric angle of attack at spar A averages between 65^o to 80^o, whereas that of spar C is 55^o to 65^o. Figure 3.13 and 3.14 plot the geometric angle variation for midstroke angles of θ_m of 75^o and 65^o. For a pitch angle of 90^o, the spar has an angle of attack of 60^o to 75^o, while at a pitch of 65^o, the angle lies between 40^o to 55^o.

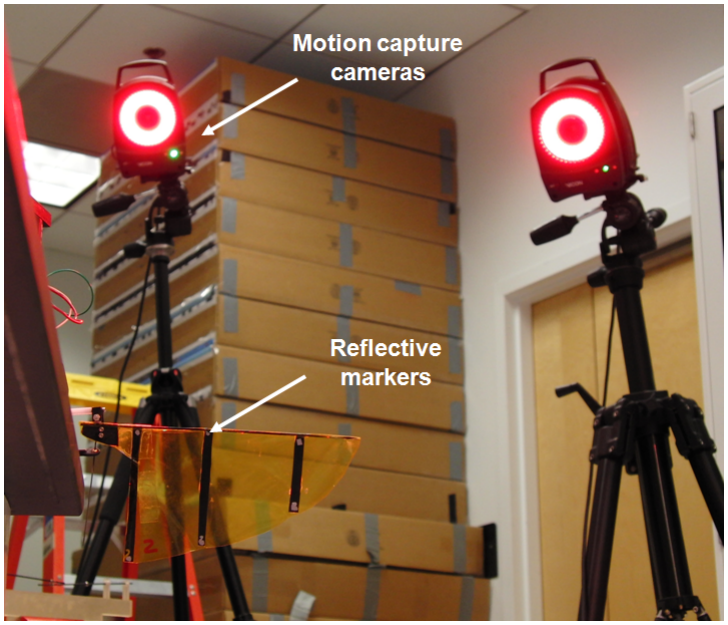

Figure 3.12: Experimental setup for wing motion tracking

These tests revealed that for this generic wing construction (Figure 3.8), the pitch angle variation that generated maximum lift was 90^o. This highlights the fact that it is feasible to build a flapping wing MAV using passive pitching produced

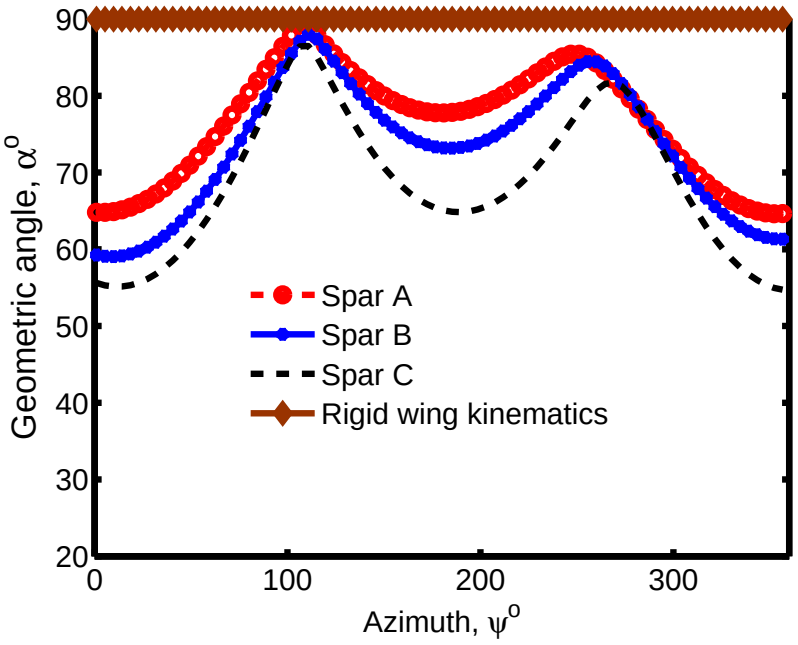

Figure 3.13: Wing X geometric angle variation at midstroke pitch angle of 90^o

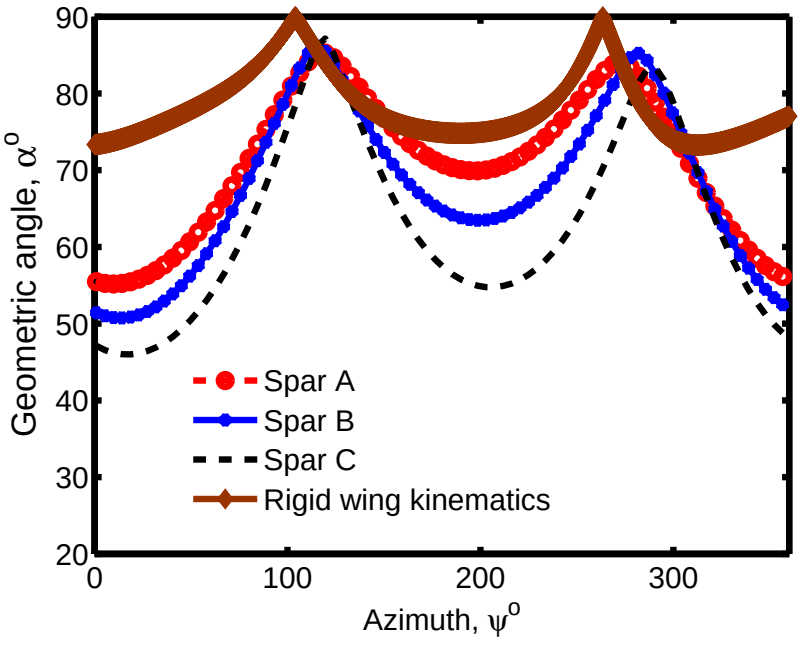

Figure 3.14: Wing X geometric angle variation at midstroke pitch angle of 75^o

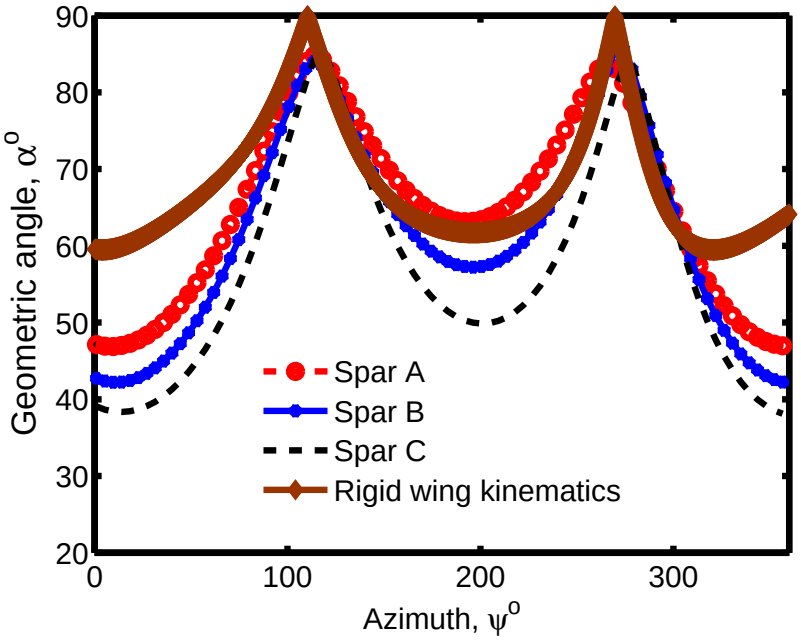

Figure 3.15: Wing X geometric angle variation at midstroke pitch angle of 65^o

by the wing, provided the wing flexibility is suitably tailored. This also eliminates the need for a complex active flap / pitching mechanism, since pitching could be achieved in a passive fashion. Thus for the remaining wing tested in this chapter, the rigid wing pitch angle was kept at 90^o.

3.7.2 Effect of Chordwise Stiffness

Since leading edge spar is torsionally stiff, the torsional deformation of the wing is directly related to the bending stiffness of the chordwise ribs. Therefore, it is important to investigate the effect of the stiffness of the chordwise ribs on lift production. Five different wings, A1, A2, A3, A4 and A5 were fabricated with rib thickness ranging from 0.15 mm to 0.75 mm. Since the width of the spars are kept the same, from wing A1 to A5, the bending stiffness of each rib would vary by a

factor of 243, whereas the mass of the ribs would only change by a factor of 5. Since all the wings used the same leading edge spar, the bending stiffness of the wings remained the same.

As shown in Figure 3.16, up to a frequency of 4 Hz, the wing A1 produced the maximum lift followed by the others. However, at around 7 Hz, there was a crossover in trend. Above this frequency, the wings A4 and A3 produced significantly higher lift followed by A5, A2 and A1. This is because of the fact that a wing which is torsionally more compliant will attain the optimum pitching kinematics at a lower frequency compared to a stiffer wing. Hence, the flapping frequency for the optimum wing pitching kinematics would be the lowest for wing A1, followed by A2 and then A3, A4 and A5.

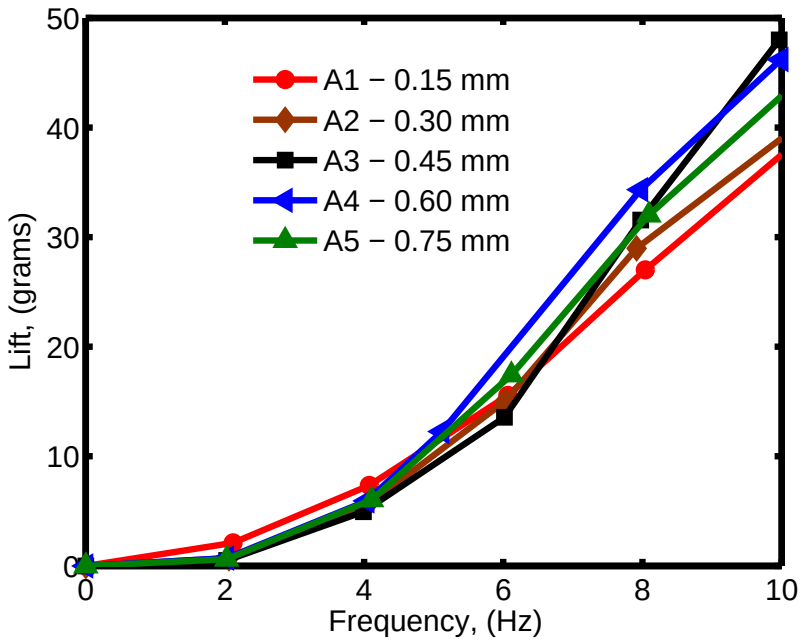

Figure 3.16: Lift variation with chordwise stiffness

The key conclusion from this test is that, when using passive pitching, as the

flapping frequency of the wing is increased, the increase in lift occurs because of two effects, namely: (1) the increase in wing dynamic pressure and (2) decrease in wing elastic twist (i.e., increase in geometric angle of attack). Here the first effect is always beneficial in augmenting the lift. The second effect is advantageous only till the wing attains the optimum pitching kinematics; thereafter an increase in the flapping frequency would push the wing to a lower pitch angle envelope and be detrimental to lift. This is why. the rate of increase of lift for wings A1 and A2 decrease beyond a certain frequency and the lift at 10 Hz is significantly lower than A3. Therefore, in order to obtain maximum lift, the stiffness of the ribs has to be tailored in such a way that the wing attains the optimum pitching kinematics at a moderately high flapping frequency (10 – 12 Hz).

3.7.3 Effect of Number of Ribs

Additional tests were conducted using wings with varying number of ribs with the same width and thickness. Wings F1 and G1 used 3 and 6 ribs respectively, and both had a thickness of 0.15 mm. Here the rib width was reduced by a factor of two from the baseline wing (A series). Figure 3.17 shows that the wing with 6 ribs produced higher lift than the 3 ribbed one. However, changing the number of ribs would also change the mass of the wing. Therefore, in Figure 3.17, a 3 ribbed wing with a rib width of 4.76 mm (A2) was compared with a wing with of 6 ribs, of rib width 2.38 mm ribs (G2). In this case the mass of the wings were the same. As shown in the figure, at lower frequencies (< 7 Hz), the wing G2 produced higher

lift and at higher frequencies A2 performed better.

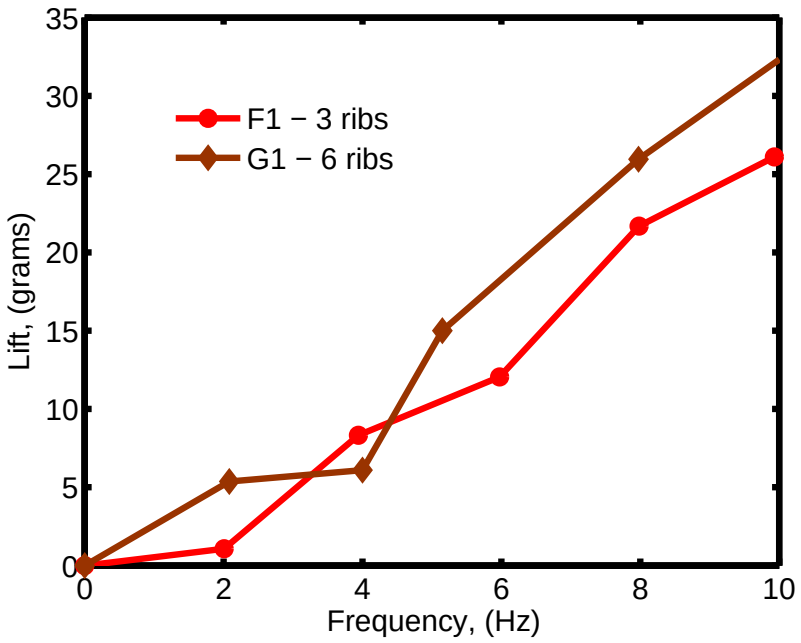

Figure 3.17: Lift variation with number of ribs

3.7.4 Effect of Film Thickness

Further, it is also important to investigate whether the wing skin thickness has any effect on the lift produced by the wings. Therefore, a wing $C1$ was fabricated, which has identical wing skeleton to wing $A1$, except that it uses a transparent 10 micron thick mylar skin, whereas the wing $A1$ uses the yellow 50 micron thick mylar. From Figure 3.19, it can be clearly seen that the wing A1 produced significantly higher lift than $C1$, showing that the wing skin thickness has a significant effect on the performance of the wing because it affects the overall wing stiffness and also the mass of the wing. This clearly shows that choosing the right film material is crucial to optimizing the lift of a flapping wing.

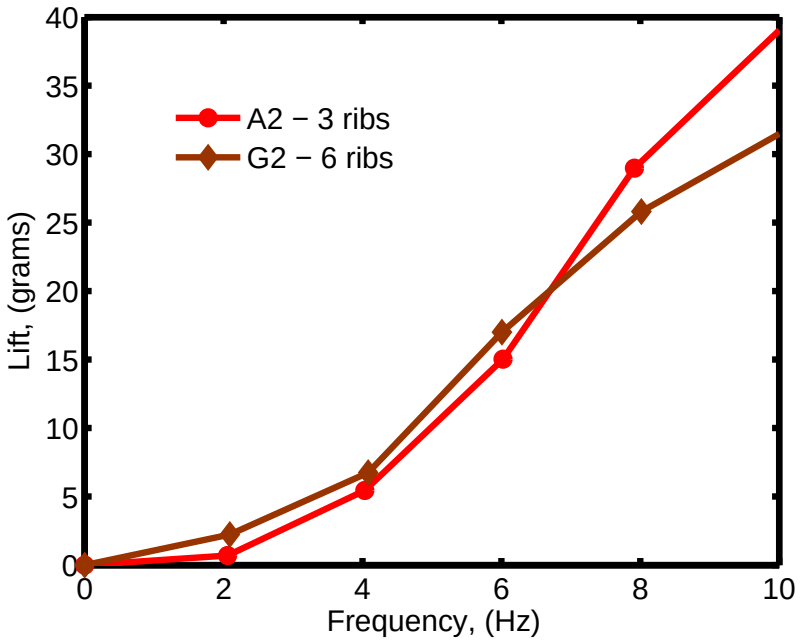

Figure 3.18: Lift variation with number of ribs

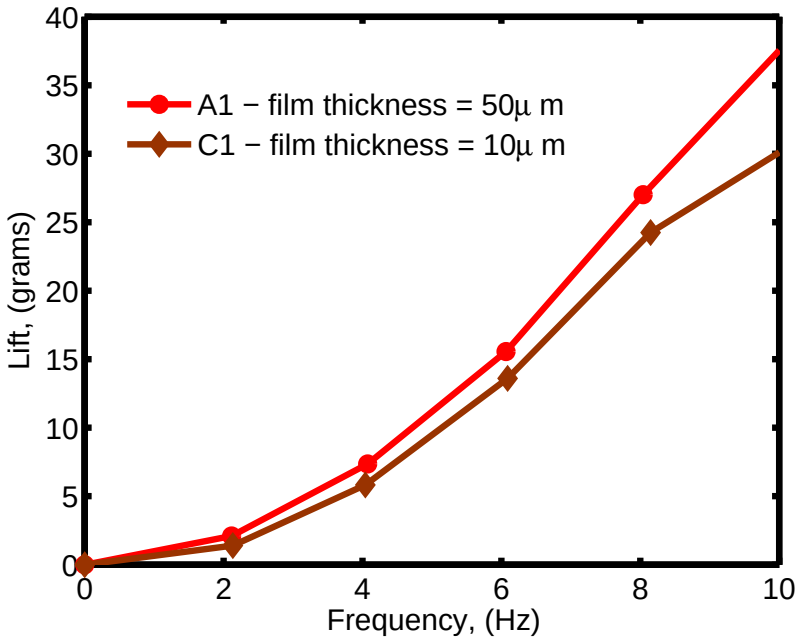

Figure 3.19: Lift variation with chordwise stiffness

3.7.5 Effect of Rib Angle

Tests were also performed using wing designs with different rib orientations. The wings tested were $A1$, $H70$, $H50$, and $H30$ (refer Figure 3.20), where the angle subtended by the two outboard ribs with the leading edge spar were 90^o, 70^o, 50^o and 30^o respectively. As shown in Figure 3.20, the lift did not vary much with the rib orientation for the 90^o, 70^o and 50^o cases upto 8 Hz, beyond this frequency, the 90^o orientation produced higher lift at 10 Hz. However, the wing with the 30^o rib angle produced much lower lift than the other three. The rib orientation directly affects the geometric bending-torsion coupling of the wing. However, from the above results, it is important to note that the average lift producing capability of the wing is not very sensitive to relatively large variations in rib orientations as long as the rib stiffness is kept constant.

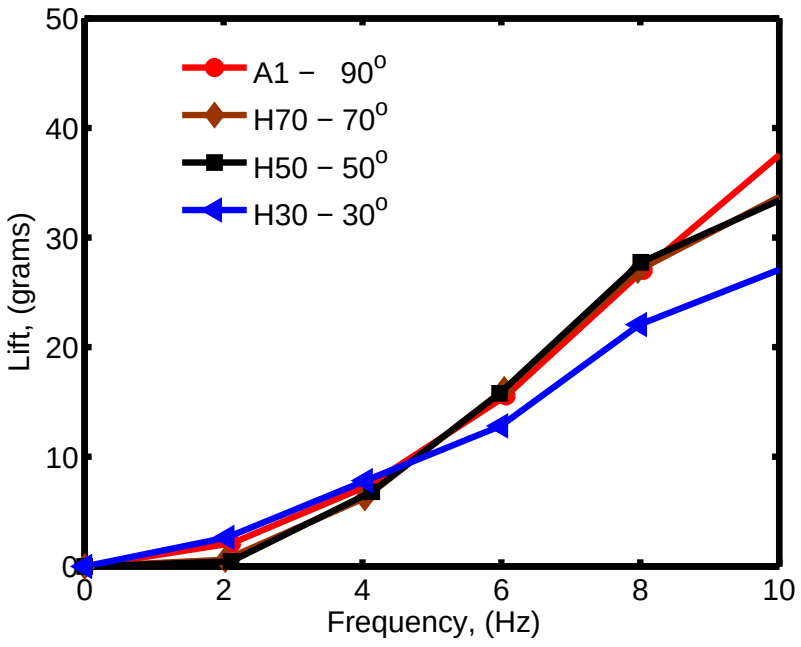

Figure 3.20: Lift variation with varying rib angle

One of the most interesting results of the prior section has been the attainment of high lift at relatively high pitch angles. This motivates a more qualitative approach to the flow field, where the goal is to visualize the presence of unsteady flow structures that are known to augment the lift of a flapping wing.

3.8 Flow Visualization

A flow visualization study was performed on Wing A2, to obtain qualitative data as the wing translates and rotates. This study was performed at a midstroke pitch of $\theta_m = 90^o$.

For this experiment, the flow was seeded using mineral oil fog and the flow field was captured at different phases of the flapping cycle using a stroboscope synchronized with flapping and a high resolution digital camera. Figures 3.21 to 3.24 shows the flow over Wing A2 through various instances during translation and rotation. Previous research has shown that a form of dynamic stall ensues during the translation phase of flapping and is observed in the form of a strong leading edge vortex(LEV) [10]. The hypothesis is that circulation of the LEV enhances the bound vortex of the wing and as a result can produce aerodynamic forces greater than those predicted by quasi-steady flow [11]. Even in the present experiment, a strong leading edge vortex is observed on the wing as shown in the figure. Traditionally, at high angles of attack on conventional airfoils, the LEV rapidly moves downstream and then sheds into the wake. As a result, the increase in lift from dynamic stall is seen only briefly, before lift plummets. However in flapping wing flight there is a

dominant span-wise flow that convects the vorticity towards the wing tip. Here it coalesces with the tip vortex and prevents the LEV from breaking away from the surface [12]. While the LEV is a dominant factor in lift augmentation, studies have shown that it is responsible only for 65 percent of the increased lift [11]. There are two other aerodynamic mechanisms that also play a significant role, namely rotational circulation and wake capture. During the rotational phase of the wing, additional lift is produced through rotational circulation which is analogous to the Magnus effect. This circulation is developed so as to maintain the rear stagnation point at the trailing edge, thus enforcing the Kutta condition [13]. During the translational and rotational phases, the wing moves through the wake generated from the previous stroke. It has been illustrated that this phenomenon increases the effective fluid velocity over each successive stroke, thus increasing the lift that is generated solely through translation. This continues until a steady state circulation is reached.

Figures 3.21 to 3.22 shows the wing flapping through the wake generated from the previous strokes. Figures 3.23 to 3.24 show a strong leading edge vortex along with spanwise flow. Various other secondary flow structures such as eddies and swirls can also be seen. While prior studies have predominantly focused on visualizing these unsteady phenomenon at Reynolds numbers of the order 150-200, this study illustrates their presence at Reynolds numbers of 38,000 which is more typical of a MAV.

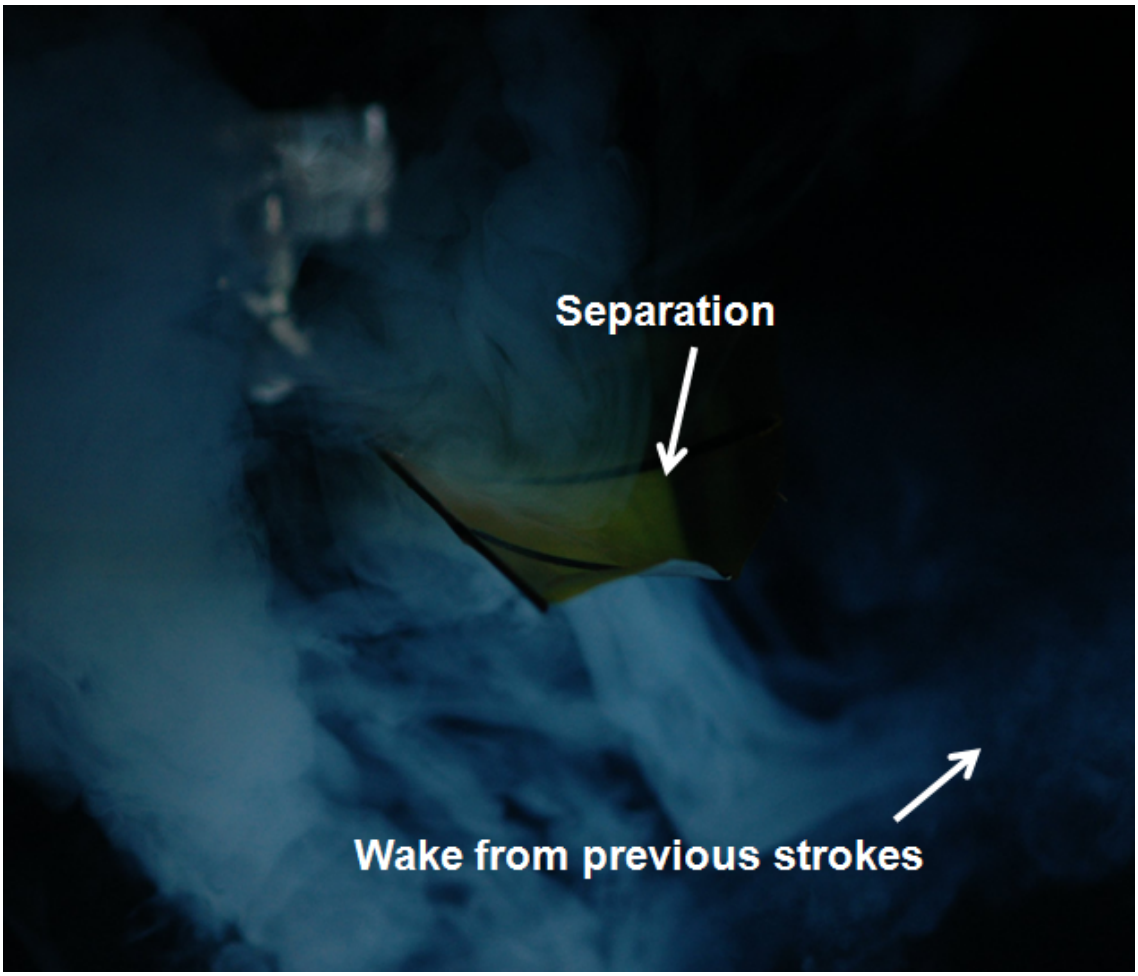

Figure 3.21: Flapping wing test rig

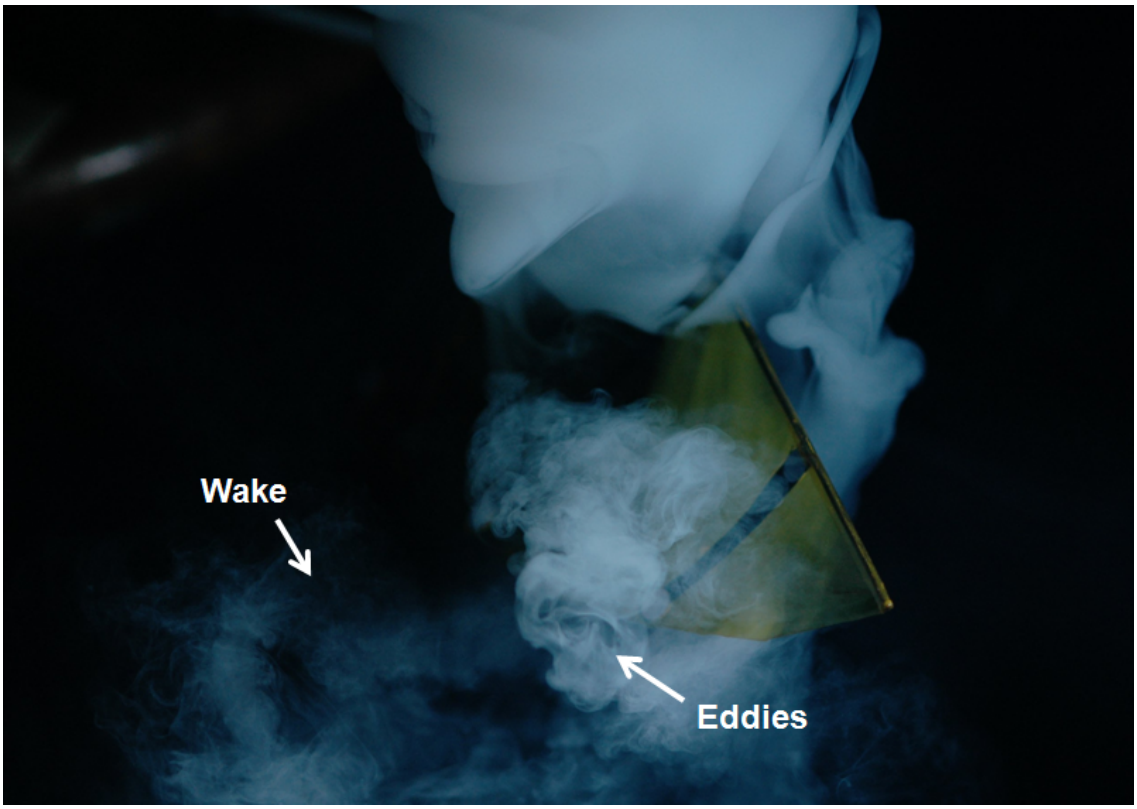

Figure 3.22: Flapping wing test rig

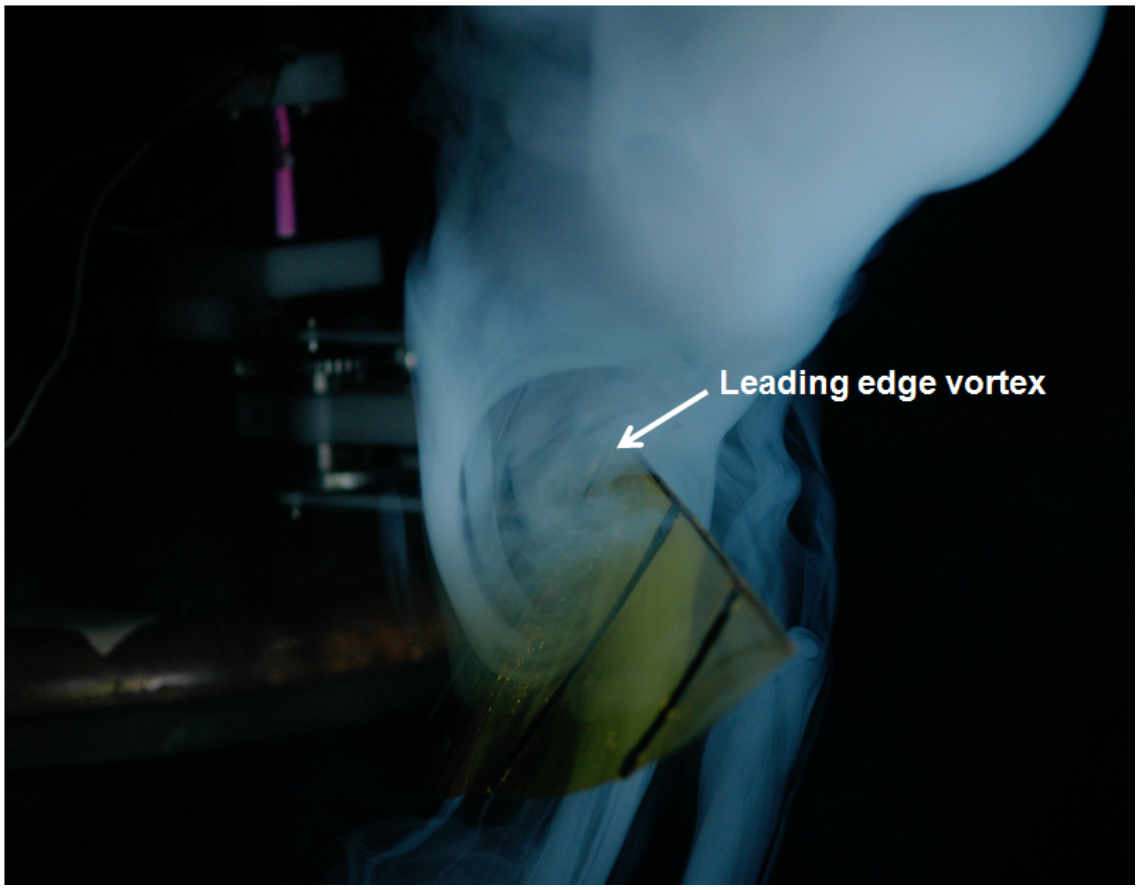

Figure 3.23: Flapping wing test rig

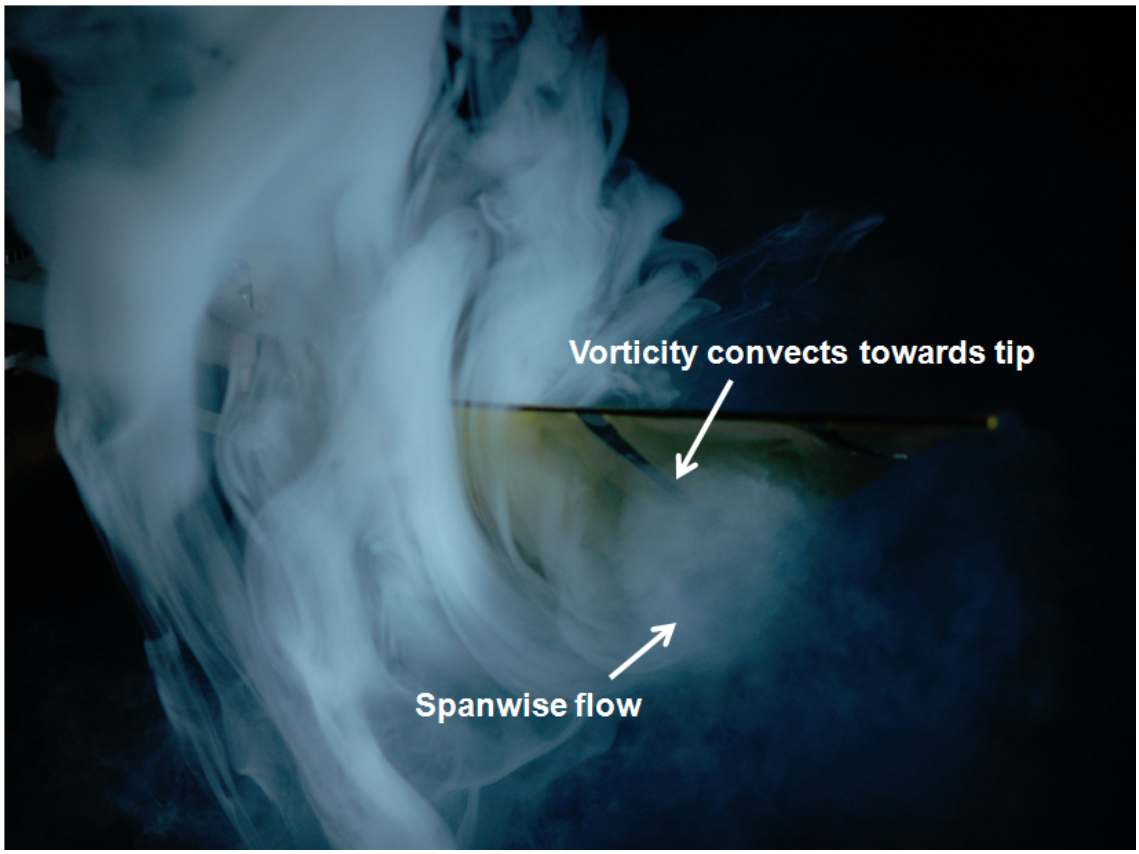

Figure 3.24: Flapping wing test rig

3.9 Power Results

While flapping at these high pitch angles at low Reynolds numbers leads to the augmentation of lift through unsteady mechanisms, there is also a significant increase in the overall drag of the system due to these unsteady phenomenon. This drag manifests itself from the perspective of an MAV in the form of high power consumption and low efficiencies. Thus a through insight into the power consumed as the wing flaps is required.

Using the special arrangement of the torque cell as shown in Figure 3.4, the power can be experimentally determined. The power measured using the torque and frequency measurements include the aerodynamic power of the wing (induced power, profile power and unsteady loses), the inertial power of the wing, parasitic power and the inertial power associated with the rest of the flapping mechanism (other than wings) and the balance associated losses. The power associated with the rest of the mechanism and balance associated losses are obtained by measuring the power consumed by the flapping mechanism in the absence of the wing. This is referred to as the tare power. The tare power is then subtracted from the total power measurements to obtain the aerodynamic and inertial power consumed by the wing (wing power). It is this power that is plotted for the different wings tested in Figures. 3.25-3.26.

Figures 3.25-3.26 plots the variation of wing power with flapping frequency for Wing Y and Wing X respectively. As mentioned earlier the only difference between Wings Y and X is the increase in the chordwise stiffness of the spars, by increasing

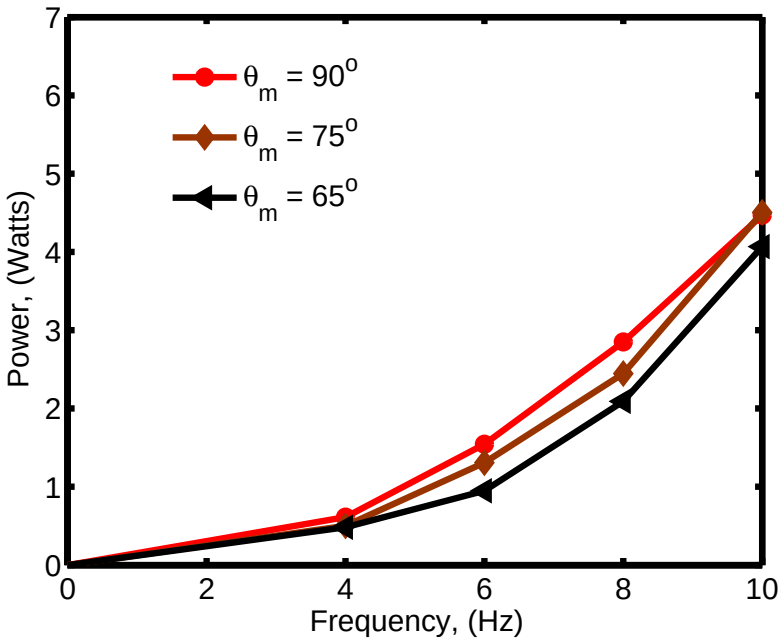

Figure 3.25: Power variation for Wing Y

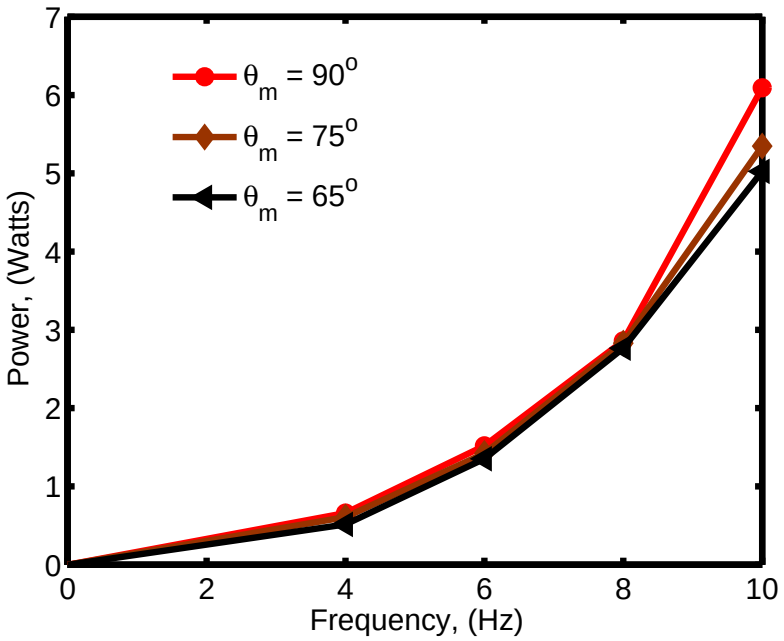

Figure 3.26: Power variation for Wing X

their thickness by a factor of two. The results show that the differences between the various pitching cases are minor. Overall maximum power is consumed by the wings when the midstroke pitch angle is 90^o.

3.10 Power Loading Results

The overall hover performance of an MAV system can be defined by the power loading, which the thrust produced per unit power. Thus, the higher the power loading the more efficient the hovering system. Figures 3.27-3.28 plot the power loading for Wings Y and X.

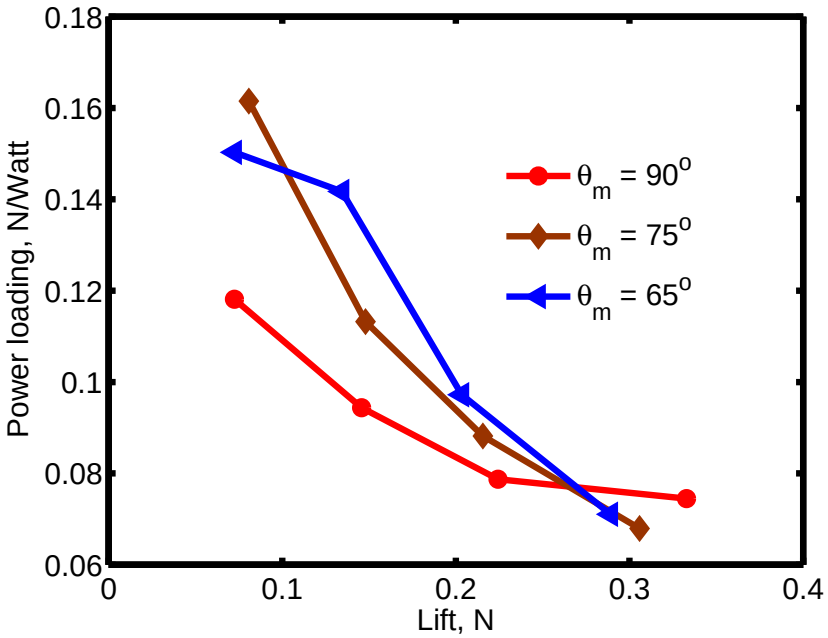

Figure 3.27: Power loading for Wing Y

For both wings the 90^o midstroke pitch case had the poorest power loading values, in part due to the large power consumption. A key point that is highlighted

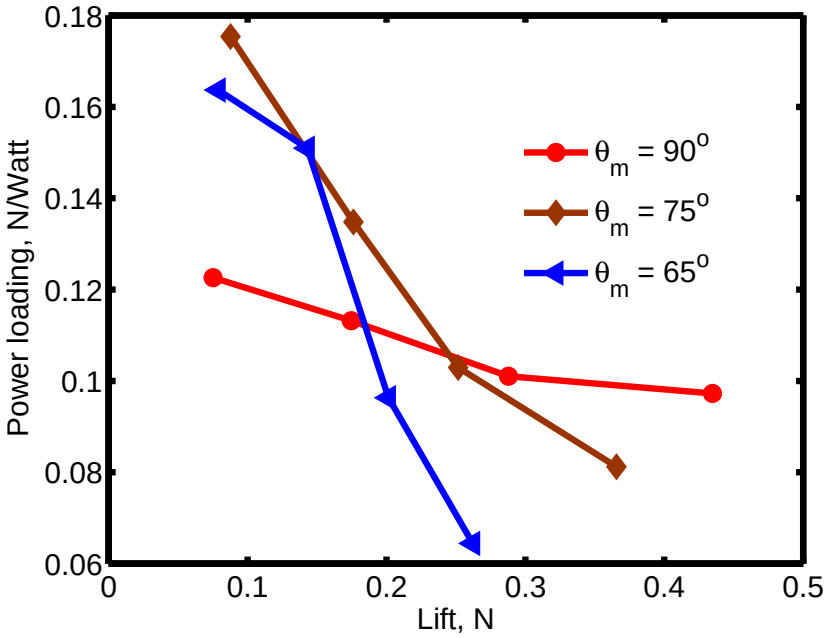

Figure 3.28: Power loading for Wing X

is the relative inefficiency of the 90^o pitch case. Maximum power loading for both the wings was seen for the 75^o midstroke case.

In Figure 3.29, the best power loading values for Wing X ($\theta_m = 65$) are compared to values of a conventional rotor of similar scale at the same disk loading. It can be clearly seen that the power loading for the flapping wing is significantly lower than that of a conventional rotor. This is because of the fact for a flapping wing, in addition to the aerodynamic power, a large component of power is utilized for accelerating and decelerating the wing during the flapping cycle. This inertial power can be a significant fraction of the total power depending on the mass of the wing. However, for a conventional rotor the inertial power is zero because the rotor operates at a constant rotational speed.

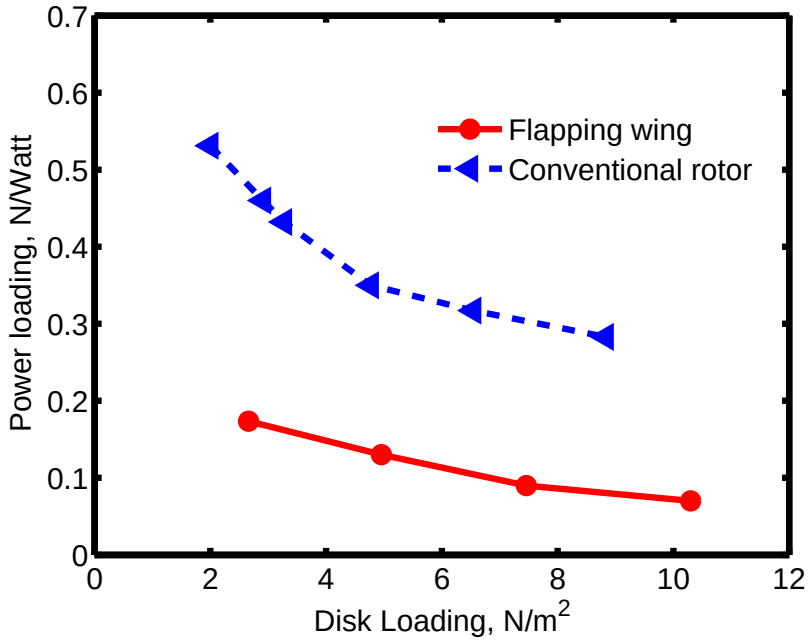

Figure 3.29: Comparison of power loading values

3.11 Conclusions

This study implemented a dual four bar mechanism in order to emulate insect-wing kinematics by incorporating the translational and rotational degrees of freedom. The mechanism featured an active pitching capability that was crucial in determining the optimized wing kinematic parameters. Various wing designs were systematically tested to obtain the lift and power measurements. Wing deformations at different spanwise loactions were obtained using a VICON® motion capture system. Specific conclusions derived from this work are:

1. Lift measurements were carried out at $\theta_m = 65^o$, 75^o and 90^o for various wings. It was observed that at low frequencies (4-6 Hz) the lift generated was identical. However for all wings tested at higher frequencies (8-10 Hz), the

90^o pitch angle case provided maximum lift, highlighting the fact that it is feasible to build a flapping wing MAV using passive pitching produced the wing flexibility is suitably tailored. However, the 90^o pitch angle case also consumed the maximum power. For most cases, the best power loading was obtained for the 65^o pitch angle. Varying the bending and torsional flexibility of the wings caused significant improvements in the lift and power loading.

2. A quantitative estimate of the wing deformation was obtained using the VICON® motion-capture tests which clearly showed that the actual geometric angles of these flexible wings are significantly lower than the pitch variation prescribed by the flapping mechanism.

3. The comprehensive parametric wing study revealed that the effect of chordwise stiffness was a significant property that tremendously affected lift production. The ribs has to be tailored in such a way that the wing attains the optimum pitching kinematics at a moderately high flapping frequency (10 - 12 Hz). The wing with a rib thickness of 0.45 mm produced maximum lift compared with wings of lower thicknesses. However, the variation of the rib angle did not significantly affect the performance till 50^o degrees; however, reducing the angle below this angle proved detrimental to the lift production. Increasing the number of ribs from 3 to 6 reduced the lift production at higher frequencies. Moving from a 10 μm thick wing skin to 50 μm skin increased the overall stiffness of the wing and also improved the lift producing capability.

4. Flow visualization studies conducted on the flapping mechanism, revealed the

presence of a strong leading edge vortex (LEV), at this high angle of attack. While typically seen at Reynolds numbers of the order 150-200, this study shows their presence at MAV scale Reynolds numbers of 38,000.

5. One of the most significant contributions of this study is the experimental measurement of motor power for a flapping wing system through a special arrangement of the torque cell. Power and lift measurements revealed that the power loading for the flapper is much lower than that of a conventional rotor.

Table 3.1: Characteristics of Wings Tested

Name	**Ribs**	**Width (mm)**	**Thick.(mm)**	**Angle(deg)**	**Fabric (μm)**	**Mass (gm)**
A1	3	4.76	0.15	90	50	1.3
A2	3	4.76	0.30	90	50	1.5
A3	3	4.76	0.45	90	50	1.8
A4	3	4.76	0.60	90	50	2.0
A5	3	4.76	0.75	90	50	2.3
C1	3	4.76	0.15	90	10	1.1
C2	3	4.76	0.30	90	10	1.2
C3	3	4.76	0.45	90	10	1.3
F1	3	2.38	0.15	90	50	1.31
F2	3	2.38	0.30	90	50	1.48
G1	6	2.38	0.15	90	50	1.23
G2	6	2.38	0.30	90	50	1.46
H30	3	4.76	0.30	30	50	1.17
H50	3	4.76	0.30	50	50	1.39
H70	3	4.76	0.30	70	50	1.41
X	3	4.76	0.30	70	50	1.41
Y	3	4.76	0.15	70	50	1.41

Chapter 4

Results and Analysis: Instantaneous Flappping Tests

4.1 Overview

The prior chapters have been focused on the average aerodynamic force produced while flapping. For the purpose of designing and developing a hover capable flapping wing micro air vehicle, a careful analysis of the average forces might be adequate. However, in order to understand the unsteady aerodynamics of flapping wing flight, knowledge of the instantaneous aerodynamic forces is required. In this chapter, a new state of the art flapping wing test rig is introduced, which is capable of obtaining these forces in hover.

All prior experiments conducted with the intent of investigating the complex aerodynamics of insect flight have been performed using instantaneous force measurements at extremely low Reynolds numbers [9]. Experiments at MAV scale Reynolds numbers have been limited and were carried out for simplified wing motions only [14]. It should be noted that while there is a shortage of instantaneous force measurements, there have been several flow visualization including particle image velocimetry studies and CFD studies, which show that many of the lift augmentation mechanisms seen on insects exists even at the MAV scale [28] [22] [30]. Even though there have been force measurements at insect-scale Reynolds numbers to corroborate the presence of unsteady aerodynamic phenomenon such as leading

edge vortices, wake capture and rotational circulation, limited force measurements exists at the MAV scale. For instance, Singh et. al [28] conducted studies on an MAV scale flapping mechanism with rigid and flexible wings and collected instantaneous force data using a strain gauge arrangement. However, the force data had both inertial and aerodynamic components making it difficult to ascertain the presence of unsteady aerodynamic phenomenon. In other words, there is a dearth of experimental studies at the MAV scale Reynolds numbers that provides instantaneous aerodynamic data for complex insect wing kinematics. The primary goal of the study discussed in this chapter is to fill this void by performing a comprehensive experimental study to measure the instantaneous aerodynamic forces on a rigid wing, somewhat different in terms of insect-wing kinematics.

This chapter will cover the results and analysis of three categories of experiments:

1. In-Plane Flapping Motion at Fixed Pitch
2. 3-D Flapping Motion with Dynamically Varying Pitch (Complete Insect Wing Kinematics)
3. Wind Tunnel Tests

Here flapping at fixed pitch is a single degree of freedom in-plane flapping motion at a constant pitch angle (no pitching kinematics). Lift and drag forces are obtained for a variety of pitch angles in this test. However, the 3-D flapping motion with dynamically changing pitch angle respresented a generalized insect-wing wing

kinematics, with all three degrees of freedom, which include in-plane flapping, out-of-plane motions (wing coning) and wing pitching.

Wind tunnel tests were carried out to provide an understanding of the aerodynamics of low aspect ratio wings at MAV scale Reynolds numbers. Here, values of the lift and drag forces are obtained for a range of Reynolds numbers, maintaining the same aspect ratio as the flapping tests. Results are compared to the unsteady C_l and C_d values obtained from the flapping tests. Another key reason for conducting the wind tunnel tests is because of the dearth of experimental data at low Reynolds numbers for high pitch angles. Since insects predominantly flap at high pitch angles, a knowledge of aerodynamic coefficients at these angles is necessary. Finally the chapter will conclude with flow visualization and particle image velocimetry measurements.

The wing utilized for all these tests was a rigid rectangular wing of aspect ratio, AR = 2.67, span of 8 inches and chord of 3 inches (Figure 4.1). To obtain the required stiffness, the wing was fabricated from carbon rods and unidirectional carbon fiber.

4.2 Experimental Setup

A flapping wing test rig was designed and constructed as shown in Figure 4.2. The present flapping mechanism incorporates all three degrees of freedom of insect wing kinematics (translation, rotation and stroke plane deviation) by using a dual-differential four-bar mechanism as was discussed in Chapter 2, and is conceptually

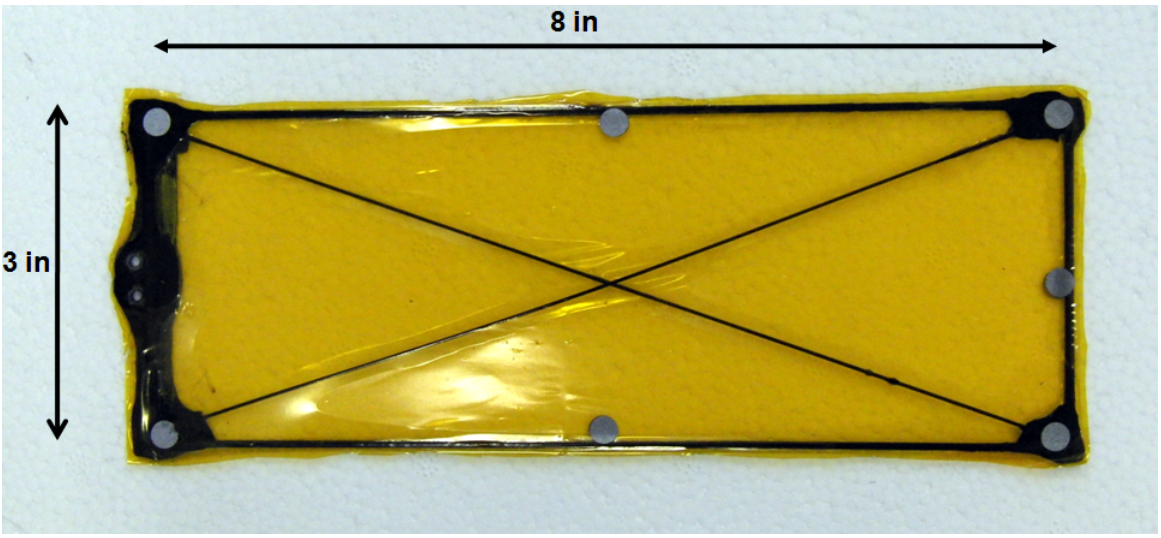

Figure 4.1: Wing used for translation tests

the same as the one used in Chapter 3. However unlike the prior setup that was built with the intent of being light-weight so it could be housed on an actual flapping wing MAV, this setup is designed to be strong and sturdy so as to prevent any unnecessary play and vibrations. As can be seen in Figure 4.2, all the linkages and the main structure are made from aluminum. The entire setup is placed on a steel hover stand in order to ensure that the wing flaps out of ground effect. A close up of the four bar linkages and gears is shown in Figure 4.3.

The gears are designed to have a large radii primarily to accommodate a range of stroke angles and to have a high rotational inertia. A high rotational inertia for the gears is crucial since it acts as a flywheel and leads to a smooth wing flapping motion. As a result, the gears are manufactured from stainless steel and have a radius of 1.5 inches. The gearing system has a 4:1 ratio. Coupled with the planetary gearbox in the motor, the system has a 16:1 gear ratio. Each gear has three concentric series of holes at three different radii from the center of rotation. The three radii correspond

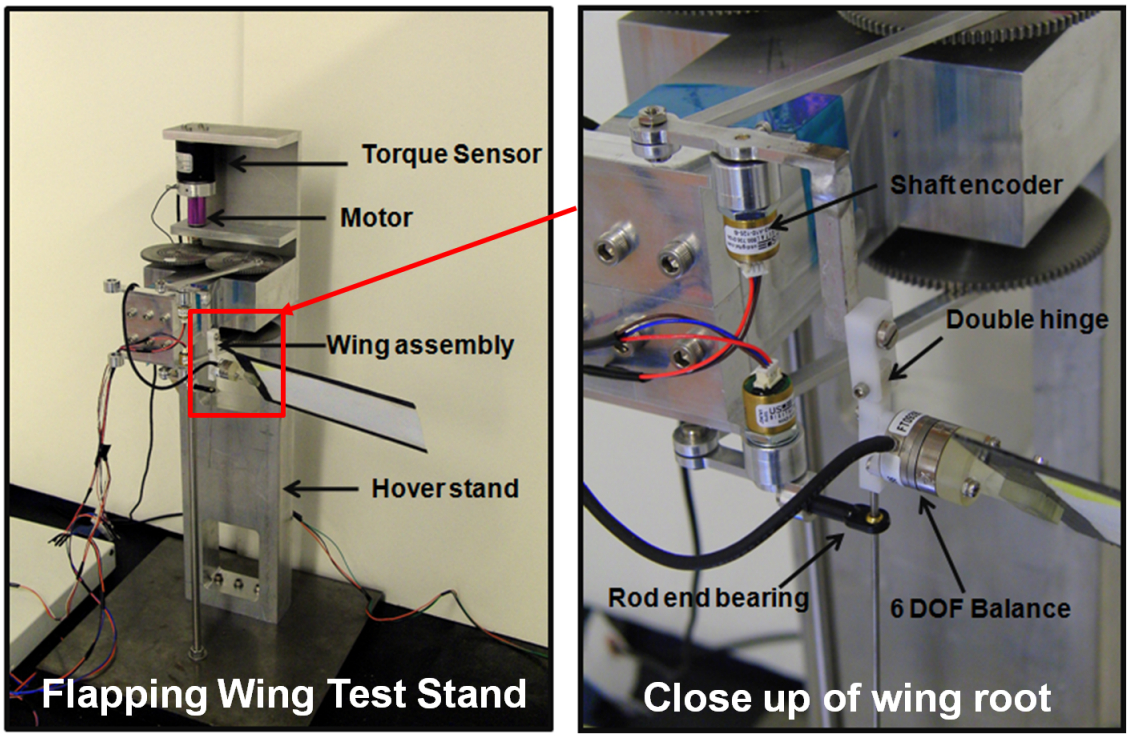

Figure 4.2: Flapping wing test rig

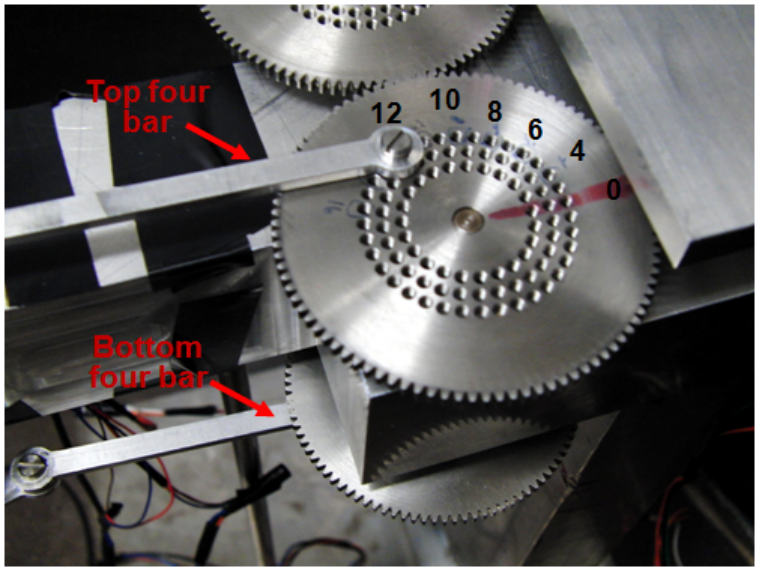

Figure 4.3: Close up of four bar mechanism

to different L_2 lengths, which gives the mechanism the ability to flap at different stroke amplitudes, while keeping all the other linkage lengths the same. The three different L_2 lengths are $0.52, 0.67$ and 0.815 inches. The other linkage lengths are : $L_1 = 5''$, $L_3 = 4.9''$ and $L_4 = 0.95''$. Utilizing these linkage combinations, stroke angles of 120^o, 100^o and 80^o can be generated for flapping actuation.

As explained in Chapters 2 and 3, changing the phase difference between the two four-bar mechanisms induces wing pitch and coning motions along with the flapping motion. By increasing the phase between the two four-bar mechanisms, the resulting pitch and coning angle magnitude can be increased. This is done by simply moving the linkage position on the gear to another hole on the same radial ring. These holes are numbered from 0 to 12. That is assuming the bottom linkage position does not change, moving the top linkage on the gear in the numbered holes will induce the phase difference. Hole number 0 corresponds to no pitch or coning variation (pure translation), and hole number 12 corresponds to the maximum pitch and coning variation in the stroke. The exact variation of these angles will be discussed in the upcoming sections.

To measure the wing forces, the flapping rig is equipped with a six component balance (ATI Nano-17) as can be seen from Figure 4.4. The balance is placed specifically at the wing root in order to capture only the wing forces. The resolution of the balance for the three forces is $1/160N$. The balance was positioned at the midchord of the wing. In order to track the position of the wing while flapping, two shaft encoders (USA Digital MA3) are placed to measure the azimuthal angles of the top and bottom linkages of the four-bar mechanism (Figure 4.2). The encoders

have an angular accuracy of 0.5 degrees and are capable of measuring a rotation of 360^o. The mechanism is also equipped with a Hall sensor to determine the flapping frequency. The Hall sensor is mounted on the setup such that through the course of one complete flapping cycle, it traverses eight magnets, thereby giving it a frequency accuracy of 0.125 Hz.

The force transducer utilized an IFPS box which had a cable running to a National Instruments USB DAQ device (NI USB-6251). Data from this device was transmitted to a computer with LabView. The LabView program collected raw voltages from the sensor during testing. These voltages were later post-processed with the ATI supplied calibration matrices to generate the observed forces and moments. It should be noted that applying the calibration while collecting the data directly in LabView leads to a time lag of 200-250 msec. This time lag was observed when the data from the shaft encoder and the force transducer were collected simultaneously and when the calibration was applied in real time. The torque sensor, shaft encoders and Hall sensors had voltage outputs connected to a National Instruments Signal Conditioning Block (NI SC-2345). This box housed four modules for the two encoders, one torque cell and one hall sensor. Data from the signal conditioning block was then sent to a USB DAQ device and then sent to the computer. A LabView program integrating both data from the force transducer and the encoders was utilized.

Due to the large inertial forces present while flapping in air, a custom vacuum chamber was designed and fabricated in order to isolate these inertial effects while flapping (Figure 4.5). Subtracting the instantaneous forces in vacuum from the

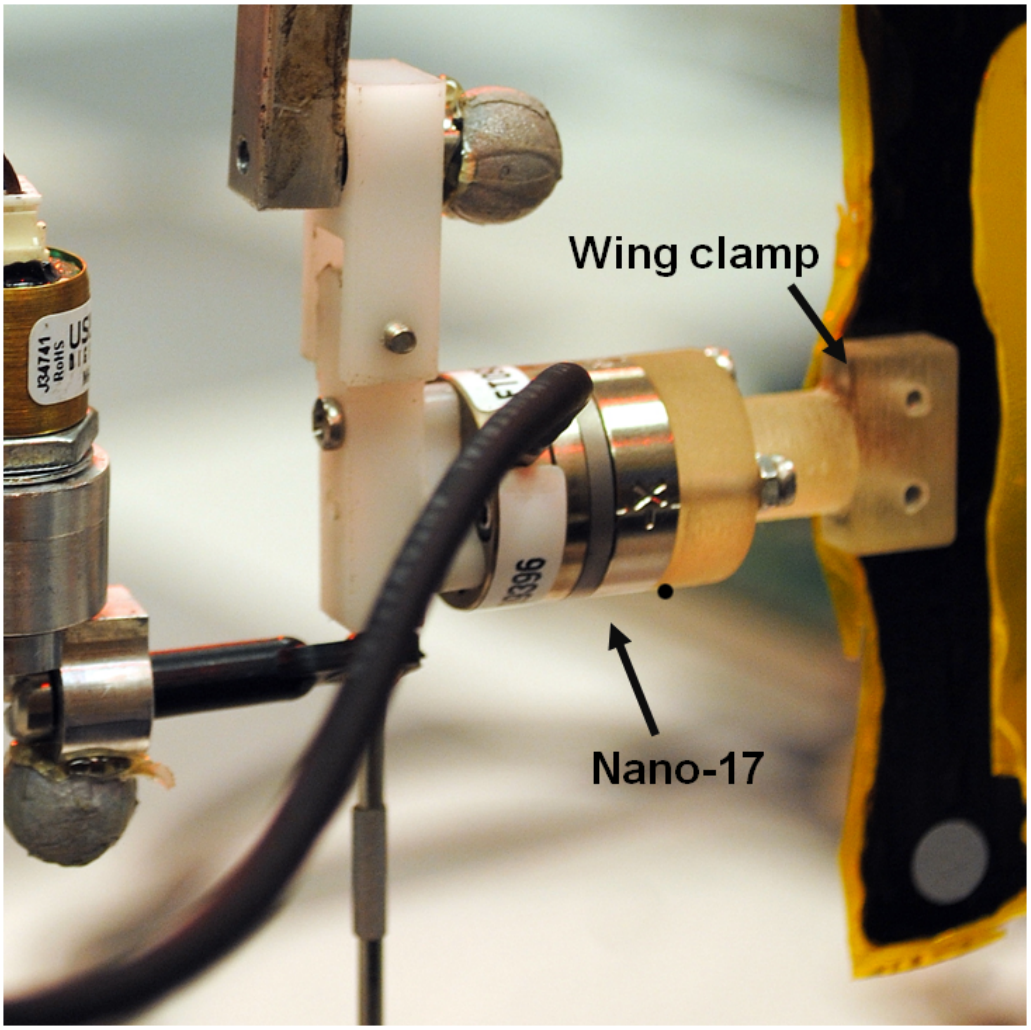

Figure 4.4: Close up of force transducer on wing

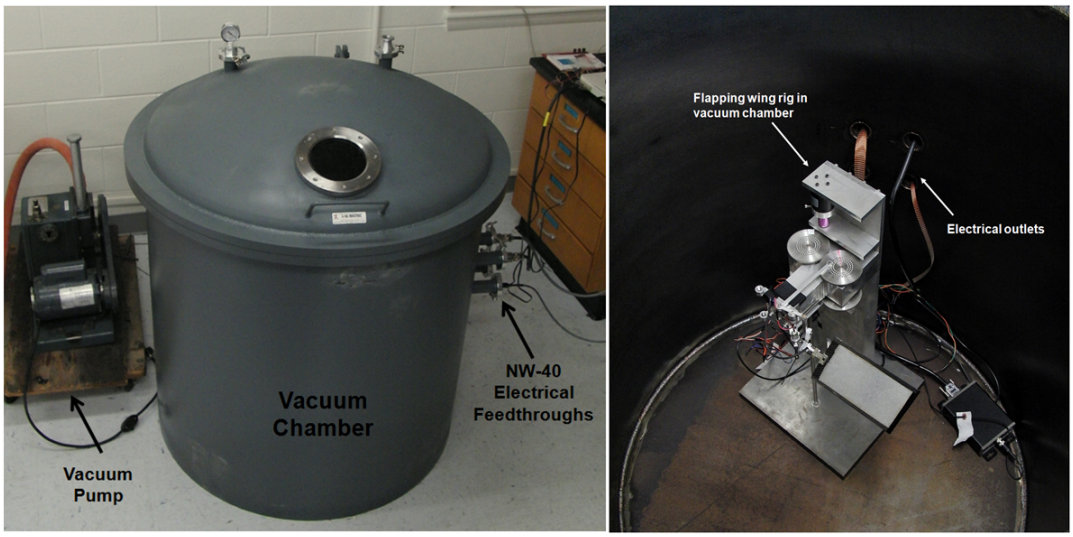

Figure 4.5: Flapping wing test rig in vacuum chamber

forces in air yield the pure aerodynamic forces acting on the wing. In order to ensure that the subtraction is cogent, the wing must be in the exact same location in both the air and vacuum experiments. In order to ensure that this condition always holds, the spatial position of the wing is estimated based on the angles measured from the two shaft encoders. Furthermore, it should be noted that this procedure of subtracting the inertial forces based on the vacuum chamber tests is valid only for a rigid wing. Detailed experimental studies and analysis were conducted in order to verify the accuracy of this technique. Thus for each test case, the wing was flapped in air and then in vacuum with the exact same prescribed kinematics. The subtraction of the resultant air and inertial forces yielded the net aerodynamic lift and drag. A graphical schematic of this process is outlined in Figure 4.6 and 4.7. All vacuum chamber tests were performed at 93.33 percent vacuum or a pressure of 28 in Hg.

Two sets of tests were conducted; one where the wing was flapping at a fixed

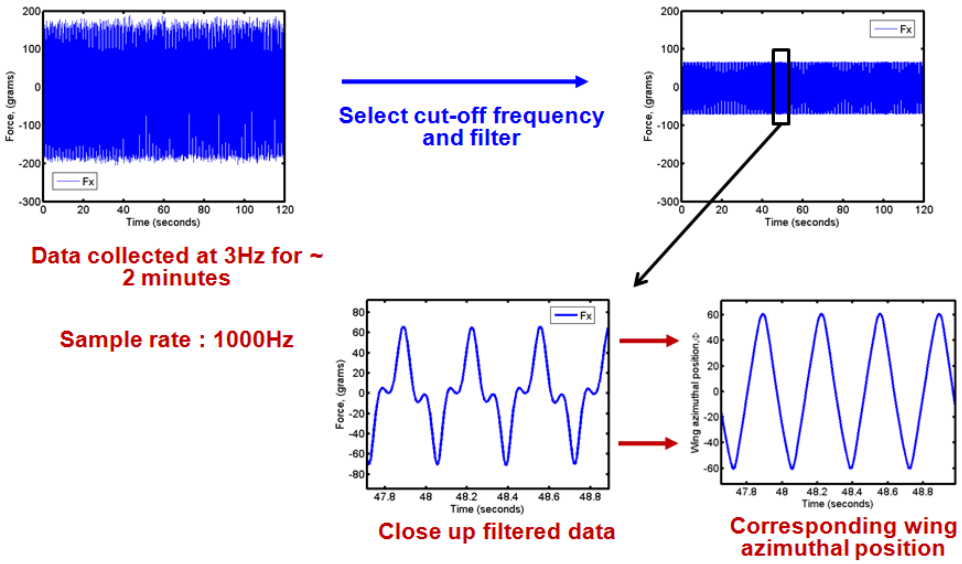

Figure 4.6: Data collection methodology

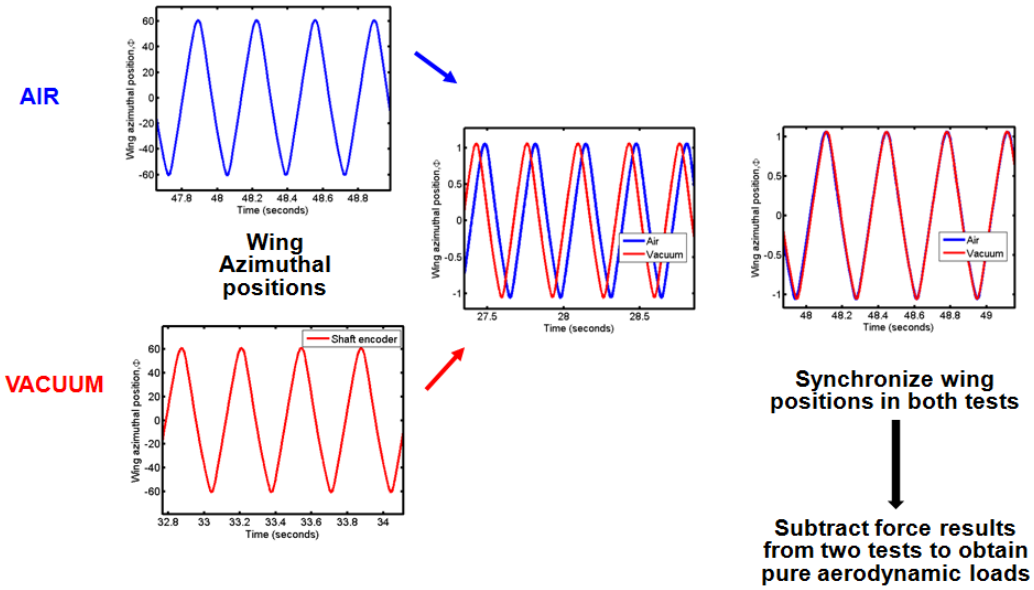

Figure 4.7: Inertial and air test subtraction methodology

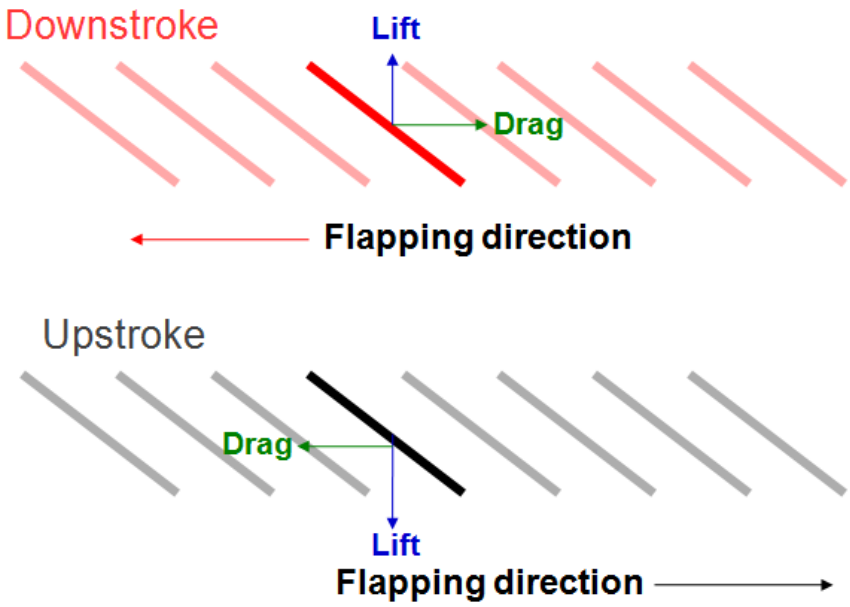

Figure 4.8: Schematic showing direction of forces for flapping with fixed pitch tests

pitch throughout the stroke, and the second where the wing was flapping with varying pitch and coning angles. Figures 4.8 and 4.9 represent the wing as a line for these two kinematics. It should be noted that while the first set permits only one degree of freedom (flapping), in the second set of tests the complete 3DOF wing kinematics (figure of eight flapping motion with wing pitching) is emulated. Here the combination of in-plane flapping and coning generate the figure of eight motion of the pitching axis generally seen in insect flight.

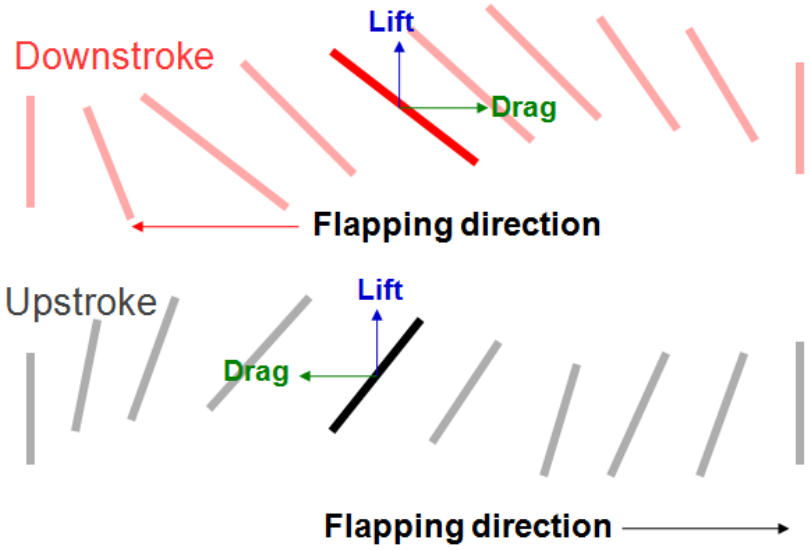

Figure 4.9: Schematic showing direction of forces for flapping varying pitch tests

4.3 Flapping at Fixed Pitch Results

4.3.1 Force and Power Measurements

As was illustrated earlier, the mechanism is capable of pure flapping motions when the top and bottom four bars are in phase with each other. Typically, for this configuration, the wing flaps at a fixed pitch of 90^o throughout the stroke. This pitch angle can be varied by changing the orientation of the wing clamp; which connects the wing to the force transducer. This requires a different wing clamping piece for each pitch angle. For the purposes of the flapping at fixed pitch tests, nine such parts were fabricated, which enabled the wing to attain translational pitch angles of 7^o, 9^o, 12^o, 15^o, 26^o, 35^o, 50^o, 65^o and 90^o. For all these translation pitch cases, the wing position and velocity were maintained. Their trajectories over the stroke are shown in Figure 4.10, 4.11 and 4.12.

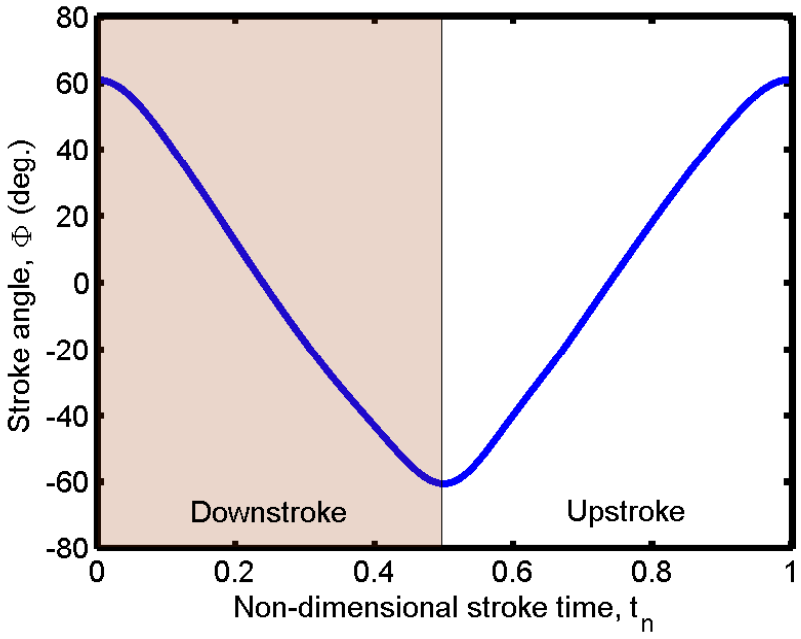

Figure 4.10: Wing angular position through the stroke

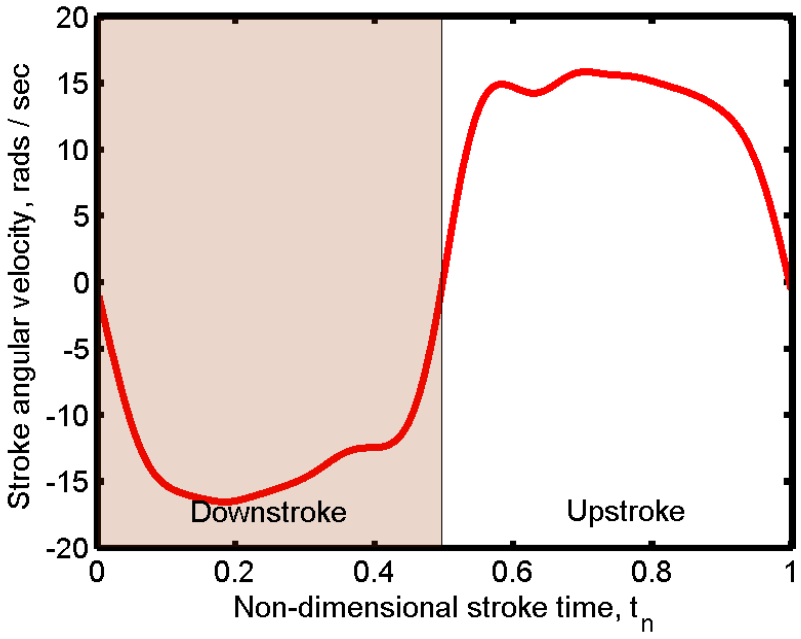

Figure 4.11: Wing angular velocity through the stroke

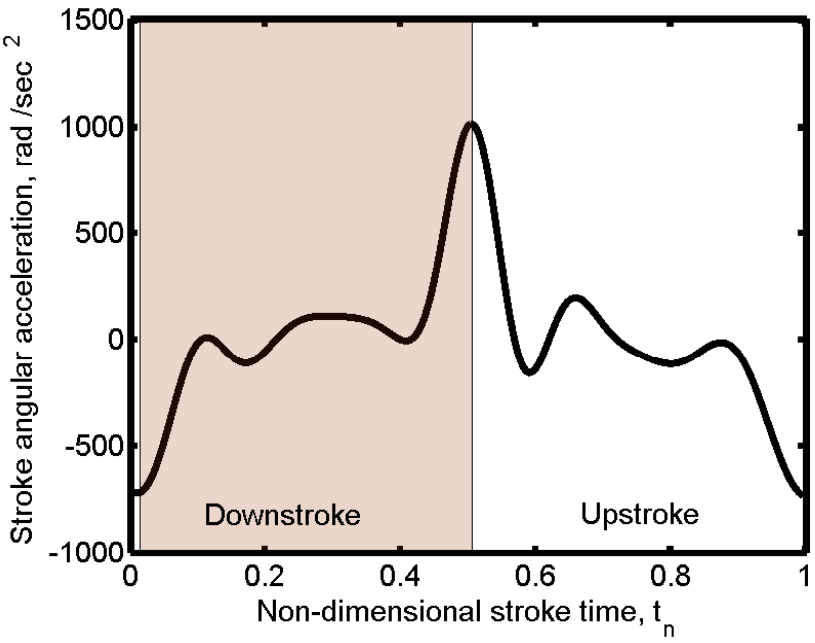

Figure 4.12: Wing angular acceleration through the stroke

The stroke amplitude (wing azimuthal position) was 120^o. Given the nature of the four bar mechanism (not purely harmonic), it should be noted that the upstroke and downstroke are not entirely symmetric. This asymmetry will be more pronounced in velocity and acceleration motions and reflected in force measurements as well. All cases were flapped at a flapping frequency of 3 Hz, which corresponds to a midstroke tip Reynolds number of 23,000. This frequency was maintained both in air and in vacuum, for the subtraction of the inertial force. Each experiment was conducted five times, and the results were averaged. As shown in Figure 4.13, the runs were highly repeatable. Data from all the sensors was collected at 1000 Hz for two minutes for each run.

The Cooley-Tukey Fast Fourier Transform (FFT) algorithm was used to obtain the various force harmonics and their respective amplitude contributions. This

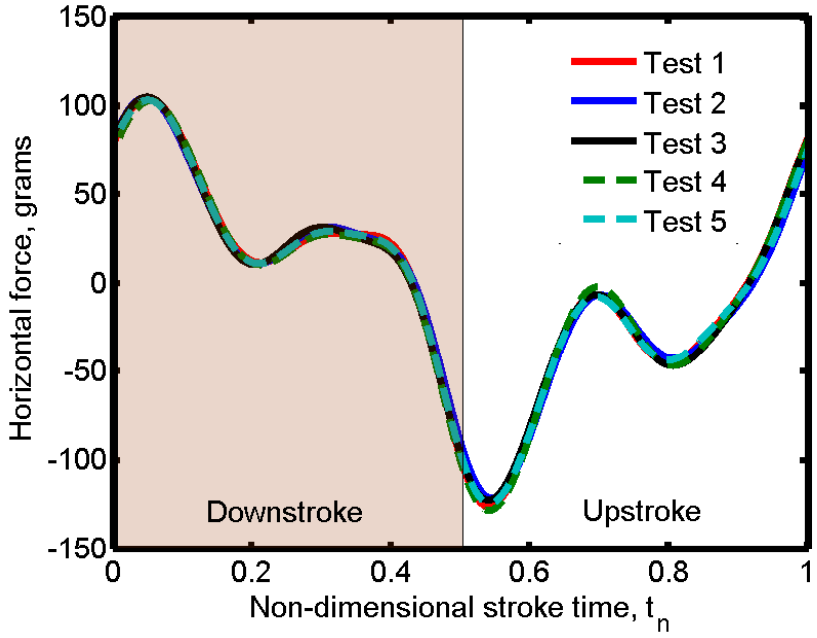

Figure 4.13: Horizontal force for five tests conducted for same prescribed kinematics

algorithm was also used on the stroke velocity, obtained by differentiating the stroke position obtained from the shaft encoder. The FFT of the wing position, velocity and acceleration for flapping at 3 Hz are shown in Figures 4.14, 4.15 and 4.16.

Since the aerodynamic forces are proportional to the velocity, it is important to to quantify the various velocity harmonics. From the graph in Figure 4.15, it can be seen that apart from the first harmonic there are minor contributions from the third (9 Hz) and fifth (15 Hz) harmonics. The angular velocity amplitude at higher harmonics are under two percent of the amplitude of the first harmonic and thus shall be ignored. Figure 4.16 plots the frequency contributions for the acceleration. Dominant 3/flap and 5/flap harmonics are seen. These will be reflected in the inertial forces as they directly proportional to the acceleration of the wing. In order to see how the first, third and fifth harmonics manifest in the forces, an FFT of

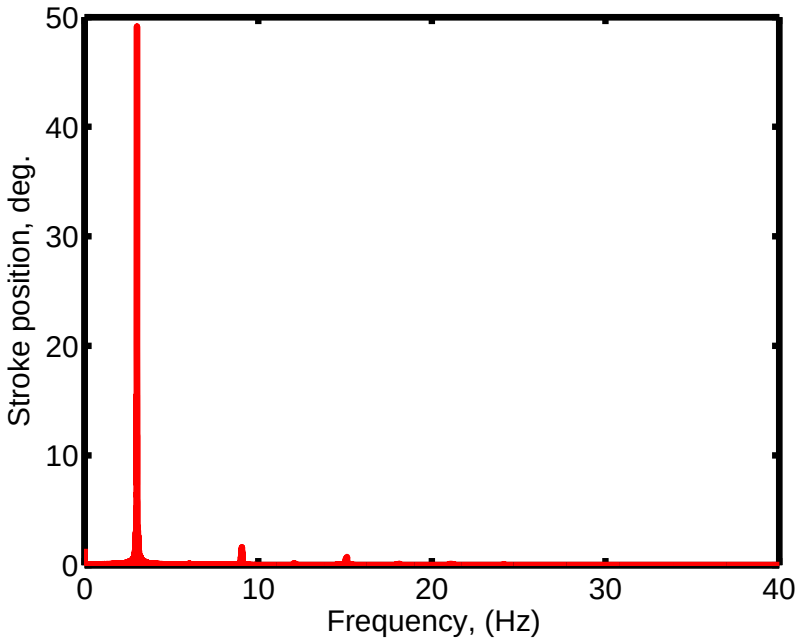

Figure 4.14: FFT of wing stroke position

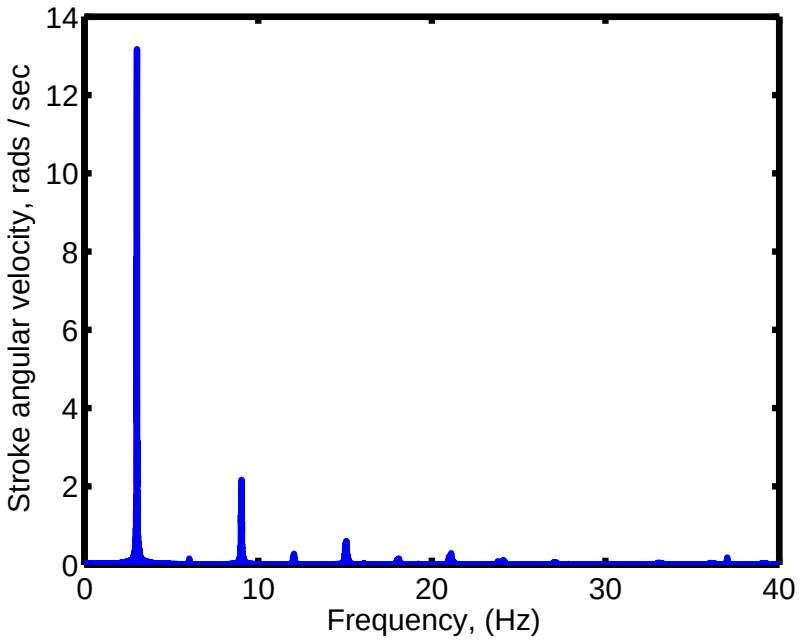

Figure 4.15: FFT of wing stroke velocity

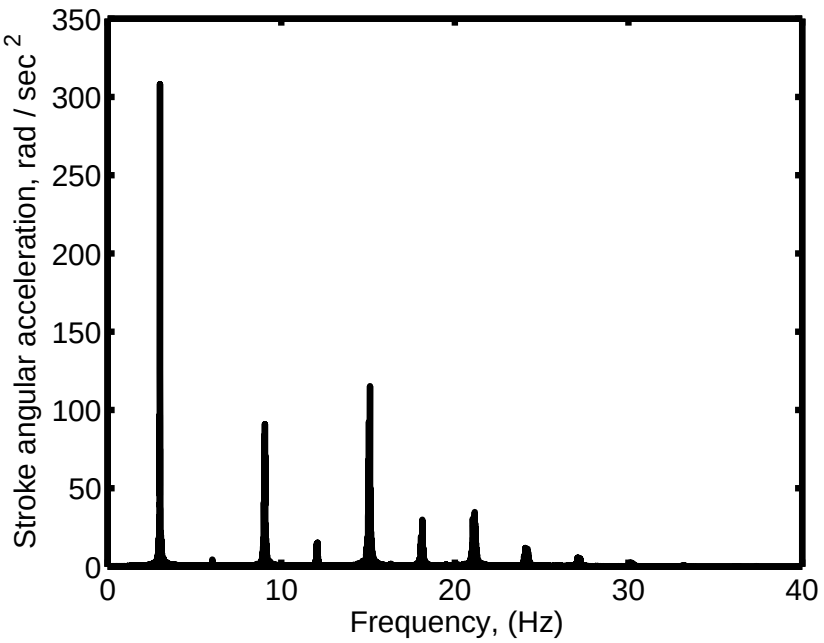

Figure 4.16: FFT of wing stroke acceleration

the forces was performed. This was performed for all test cases both in vacuum and in air. The subtraction of the force amplitudes from the air and vacuum tests for each frequency provided a spectral composition of the pure aerodynamic forces. While the most dominant aerodynamic contribution was from the 1/rev, there were also significant contributions from the 3/rev. The even harmonics (2/rev and 4/rev) had minor contributions to the net force amplitude. Figures 4.17 and 4.18 plot the frequency content of lift values in grams for a pitch angle of 15^o and 50^o respectively.

As can be seen from both plots at frequencies higher than 15 Hz, the net aerodynamic force amplitude is small especially for the lift force. A key point to note from these graphs is that apart from the fifth harmonic, the air force amplitude is always higher than the vacuum force. For all the tests conducted, it was observed that at 15 Hz the vacuum amplitude was always greater than the air amplitude.

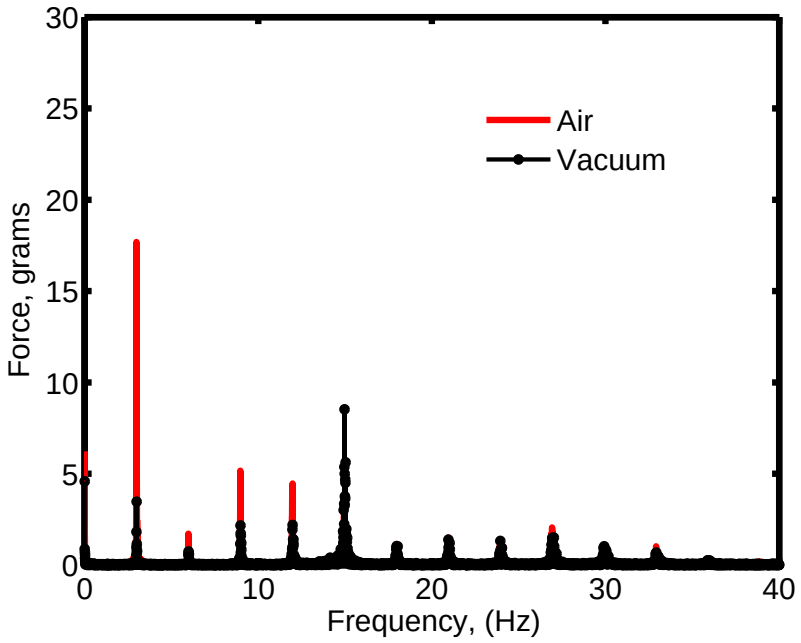

Figure 4.17: Vertical force harmonic content for a translation angle of 15^o

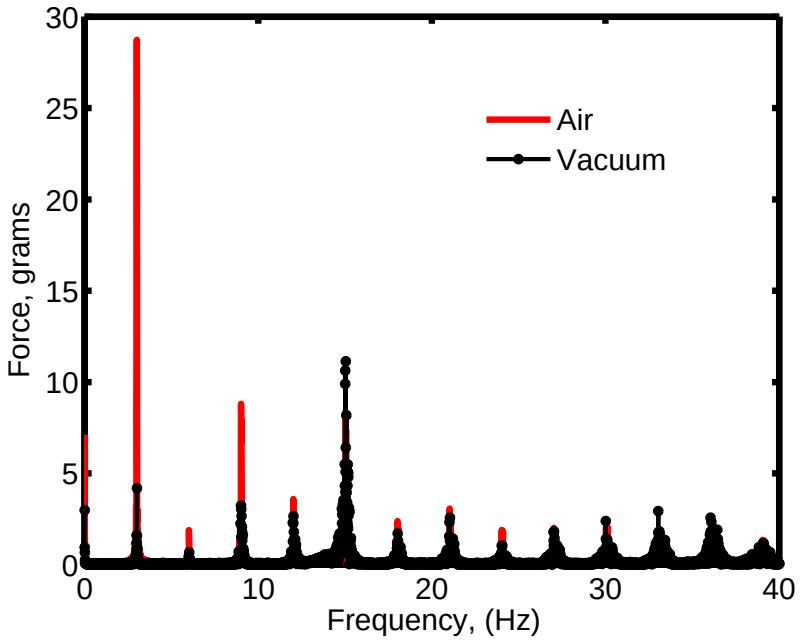

Figure 4.18: Vertical force harmonic content for a translation angle of 50^o

This indicates that the mode corresponding to the fifth harmonic is damped in air. Furthermore, the amplitude of the fifth harmonic in vacuum is significantly higher compared to all the other frequencies, which shows that the fifth harmonic corresponds to a wing structural mode excitation. Similar values of frequency-amplitude distribution were found for the drag force. Thus for all the test results shown below, the cut-off frequency of the forces was set to 15 Hz, so as to negate the inclusion of the structural mode.

Despite the inclusion of only the first five harmonics, the complexity of the data mandated a more simpler approach. As a result, the data was analyzed at a lower cut-off frequency of 7 Hz, thus capturing only the first two harmonics. This enabled a better understanding of the resultant data. The cut-off was performed using a sixth order Butterworth filter. The approach in this chapter will be to first analyze all the data at the lower cut-off frequency (7 Hz) for a rudimentary understanding of the forces, and then revisit the data at the higher cut-off frequency (15 Hz) for a more refined picture. Lift and drag forces with a cut-off at 7 Hz are plotted in Figure 4.19 and 4.20 respectively.

Figure 4.19 plots the lift variation over the entire flapping stroke as a function of the non-dimensional flapping cycle. In one cycle, the range t_n of 0 to 0.5 corresponds to the downstroke, and t_n of 0.5 to 1.0 refers to the upstroke. It is important to note that at the end of these ranges, the wing completes half a stroke and the velocity goes to zero before the wing translates (thereby changing direction) to the next stroke. Thus in the downstroke, the lift vector is pointing upwards, while in the upstroke, the direction of the lift vector is reversed and pointing downwards (see

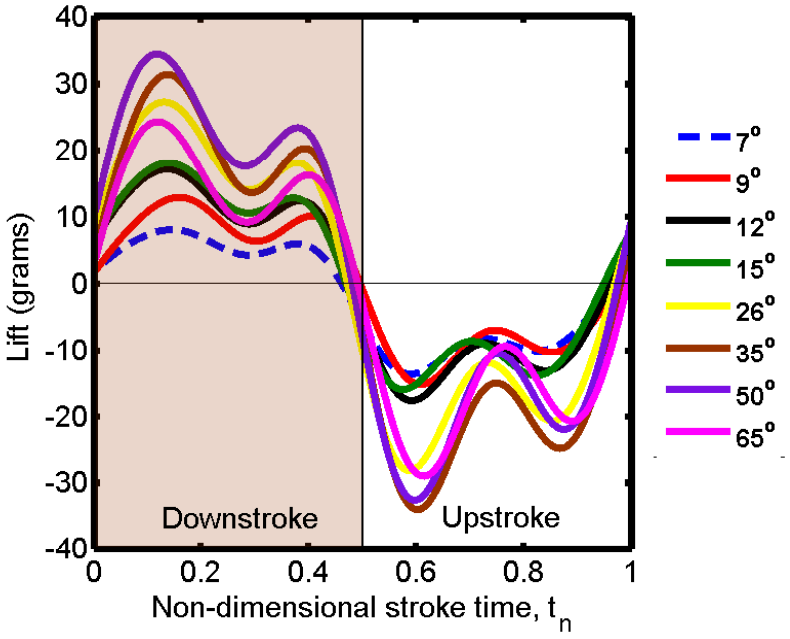

Figure 4.19: Lift variation over stroke

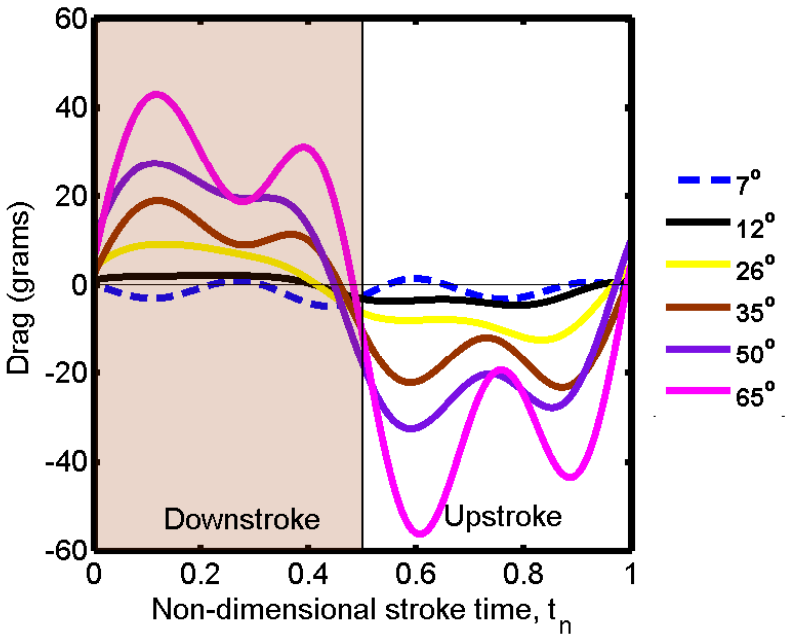

Figure 4.20: Drag variation over stroke

Figure 4.8). The values are different in the upstroke and downstroke because the velocity profiles are not exactly the same (see Figure 4.11)

Overall an increase in the translation pitch angle results in an increase in the lift till a pitch of 50^o (see Figure 4.19). The lift peaks at this angle, and decreases subsequently. At the end of the stroke, $t_n = 0.5$ and 1, lift values are seen to be small, thereby illustrating that the wake capture phenomenon is less dominant. The basic premise of the wake capture hypothesis is that the wing should produce an aerodynamic force once it has come to a complete rest after traversing through the halfstroke [9]. This is because even though the wing is still, the fluid around the wing has acquired a velocity due to the wake from the previous halfstroke. The lift at still-point conditions become large with increasing pitch angles. Overall the wake capture phenomenon appears less dominant. The drag variation over the stroke increases with an increase in the pitch angle (see Figure 4.20). As expected, maximum drag takes place at a pitch angle of 90^o. Lift and drag values are non-dimensionalized and shown in Figures 4.21-4.22. The non-dimensionalization was performed using:

$$C_L = \frac{2L}{\rho \int_{r_o}^{r_t} V(r)^2 c(r) dr} = \frac{2L}{\rho \dot{\Phi}^2 \int_{r_o}^{r_t} r^2 c(r) dr} \tag{4.1}$$

where r_o refers to the radial location at the wing root, and r_t corresponds to the wing tip. This treatment of the lift equation applied to flapping wings has been used extensively in literature [10],[9],[14]. From the equation and the kinematics, it can be inferred that the values of the aerodynamic coefficients at non-dimensional stroke times of $t_n = 0$, $t_n = 0.5$ and $t_n = 1.0$ tend to infinity, as the velocity at

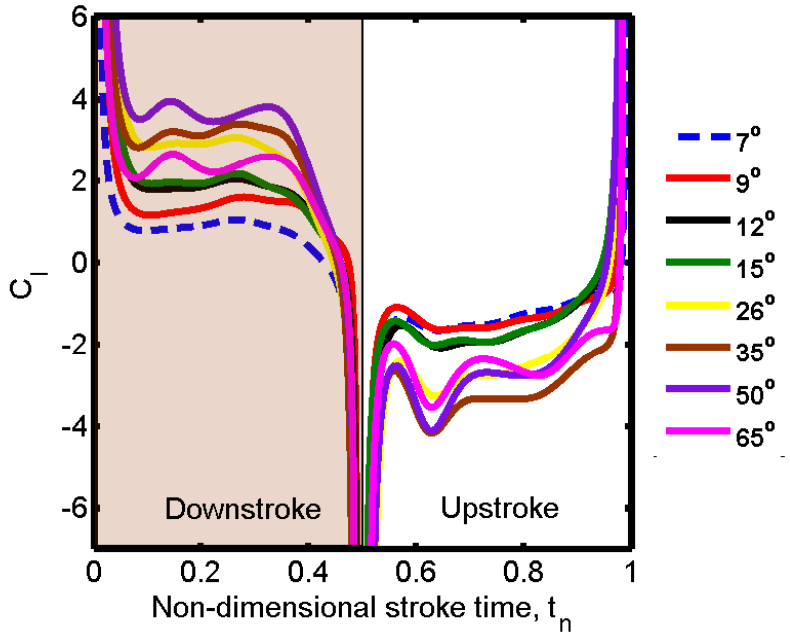

Figure 4.21: Lift coefficient for pure translation over stroke

these locations is zero. This non-physical solution can be ignored, but is presented in Figure 4.21 and 4.22 for completeness. It should be noted that the small values of lift which cause the non-physical solutions maybe attributed to small wake capture effects.

It is apparent from Figure 4.21, that the translational values of the lift coefficient are significantly higher than those observed with standard flat plates and airfoils. The same holds true for the drag coefficients (see 4.22). The maximum C_l observed is for a pitch angle of 50^o, while for C_d it is for 90^o. It is also interesting to note that there is a more dominant 2/flap force variation at higher pitch angles compared to low pitch angles. This maybe due to the inherent unsteadiness in the flow at these post-stall angles, however a detailed flow visualization is required for further insight.

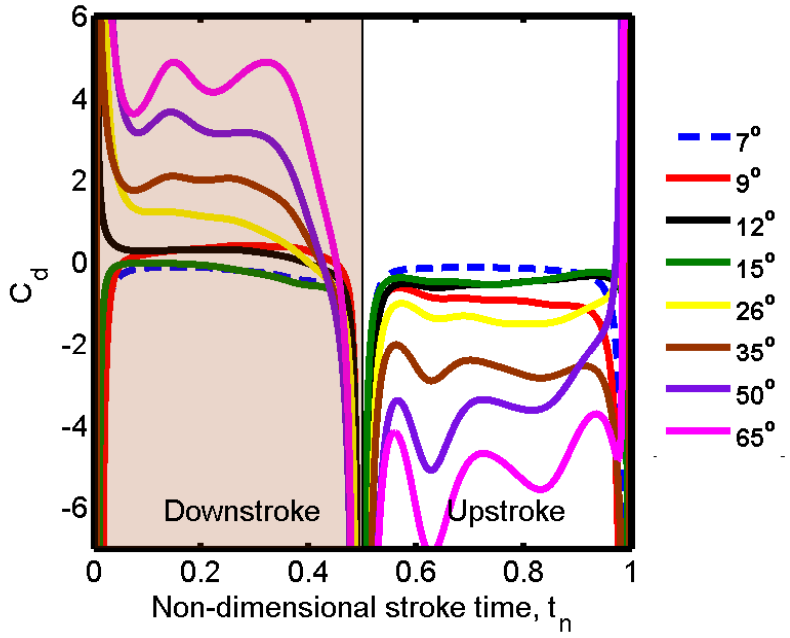

Figure 4.22: Drag coefficient for pure translation over stroke

Figure 4.23. plots the lift to drag ratio for different translation angles. Apart from the 7^o pitch case, all values of L/D lie between 0 to 5. It is interesting to note that at the start of the stroke (upstroke is shown here), there is an increase in the L/D till a t_n of around 0.7, after which there is a steady decline. It is evident that for high pitch angles; where insects operate, the lift to drag ratios are extremely low. Thus while a pure translation motion produces high values of C_l, the overall efficiency of this motion is poor since it is also characterized by high drag.

Along with the forces, data for the different moments were also collected from the force transducer at the wing root. The wing torque at the flapping axis was computed using the bending moment and the drag force. This was multiplied by the instantaneous velocity of the wing to yield the wing power consumption. Figure 4.24 plots the total flapping power variation in air over one stroke for a range of

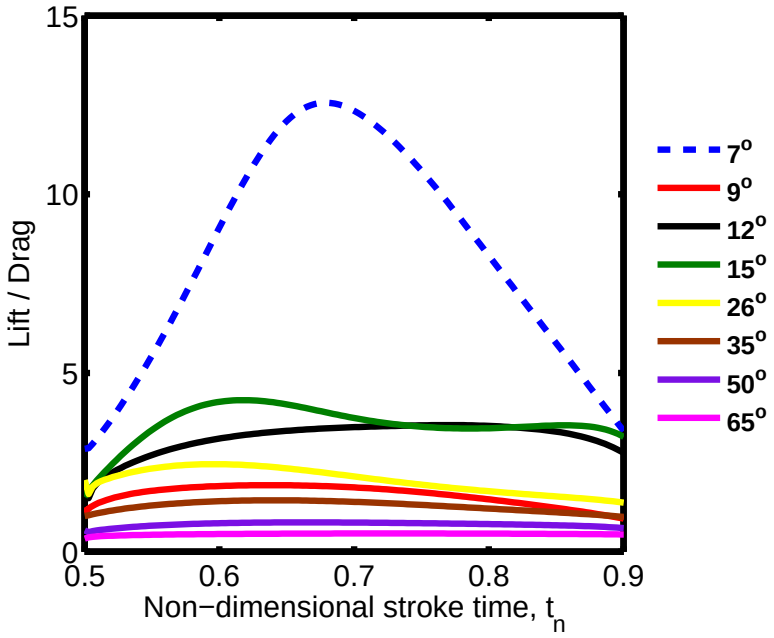

Figure 4.23: Lift to drag ratio in the upstroke

pitch angles. The inertial power, shown in Figure 4.25 is the power consumed when flapping in vacuum.

As is expected, the inertial power for all the tests is the same, as it is only dependent on wing acceleration and mass. Thus maximum power is consumed at the ends of the stroke, where the acceleration is maximum. The plot of the aerodynamic power is shown in Figure 4.26. It is simply the subtraction of the power consumed in vacuum from the power consumed when the wing is flapped in air.

The aerodynamic power increases with increasing pitch angle; and thus follows the same trend as the drag force. It reaches its maximum value at midstroke, where the velocity is maximum. Figure 4.27 plots the lift to aerodynamic power ratio for numerous pitch angles. For clarity, only the upstroke values are shown. Overall the lift to power values are well below 1 N/Watt, and tend to go close to 0.2 N/Watt

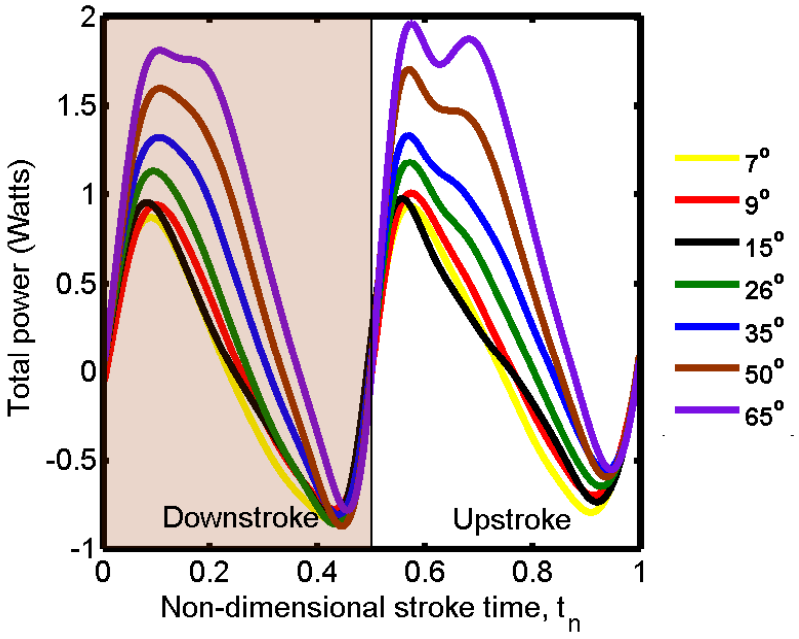

Figure 4.24: Total power over flapping stroke

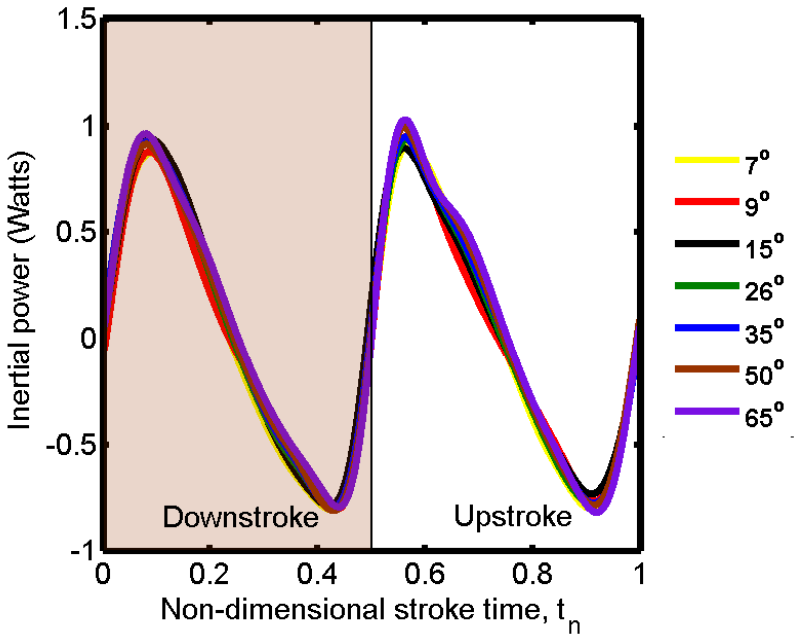

Figure 4.25: Inertial power over flapping stroke

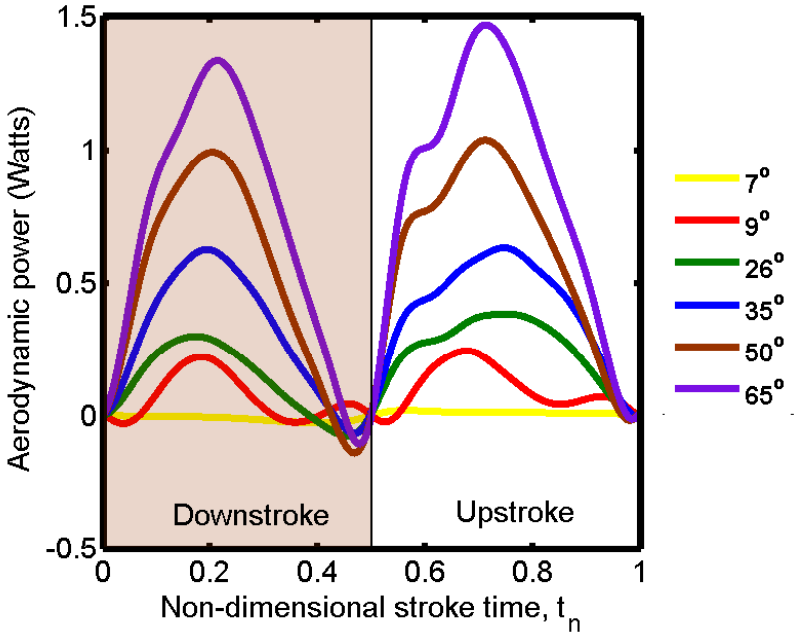

Figure 4.26: Aerodynamic power over flapping stroke

for high values of the pitch angle.

4.3.2 Flapping at Fixed Pitch Observations

Flapping within a single DOF kinematic framework for a variety of pitch angles yielded extremely high lift and drag coefficients as seen in this section. This manifested as low lift to drag ratios of the wing through the two halfstrokes. The question that these tests really bring to light is whether the high aerodynamic coefficients observed are a facet of unsteady aerodynamic mechanisms or steady fixed wing aerodynamics (effect of wing surface, aspect ratio and Reynolds number). In order to understand the reason for these results, wind tunnel tests were conducted.

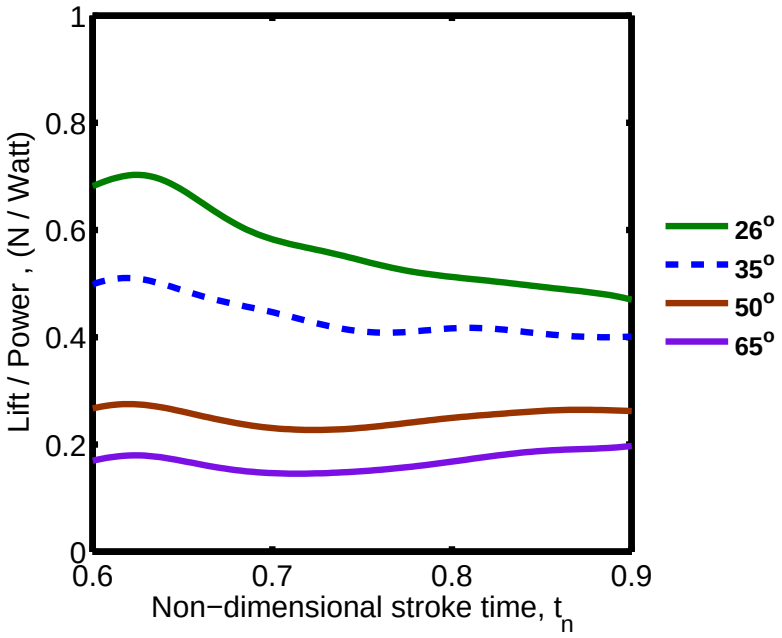

Figure 4.27: Lift to aerodynamic power ratios

4.3.3 Wind Tunnel Tests

Wind tunnel tests were conducted on the same wing used in the flapping experiments over a range of Reynolds numbers. The impetus being that this would provide steady static values of the aerodynamic coefficients, which would serve as a baseline when compared to the unsteady values of C_l and C_d generated while flapping with a fixed pitch.

The setup is shown in Figures 4.28 to 4.30, the wing is cantilevered at one end, clamped to a force transducer, thereby making the measured results three dimensional (tip vortex effects). The Reynolds number here is taken with respect to the chord length, that is:

$$Re = \frac{\rho V_\infty c}{\mu} \tag{4.2}$$

Here V_∞ is defined as the wind tunnel velocity, c is the chord length of the wing, ρ is the ambient air density and μ is the dynamic viscosity of the air [2]. Both temperature and pressure measurements were taken prior to each wind tunnel test run. The lift is defined to be perpendicular to the direction of the freestream velocity, and the drag is defined to be the aerodynamic force parallel to the direction of the flow. Unlike most experimental wind tunnel data where measurements are typically taken at low pitch angles (slightly beyond the first stall event), here pitch values are varied from 0^o to 90^o. The wing is a flat plate with the same aspect ratio and thickness to chord ratio as the one used in the flapping with fixed pitch cases.

To correlate the flapping at fixed pitch results and the wind tunnel test results, it is necessary to determine the Reynolds numbers experienced by the wing during the pure flapping experiment. Figure 4.31 shows the Reynolds number variation as a function of the stroke angle and the non-dimensional wing span. During a flap cycle, the maximum velocity occurs at the midstroke which corresponds to a stroke angle,(Φ) of 0^o. The maximum Reynolds number of 23,000 occurs at this stroke angle towards the tip of the wing. The Reynolds number at midstroke at 75 percent span is approximately 20,000. It is important to note that the four bar induced flapping is not entirely symmetric in both upstroke and downstroke. As a result, the velocity profiles in the upstroke and downstroke are not symmetric and this difference manifests in the Reynolds numbers as well. The velocity here is determined experimentally from the shaft encoder data. The azimuthal position obtained from the encoder is numerically differentiated in order to obtain the azimuthal velocity; which is multiplied by the spanwise radial distance.

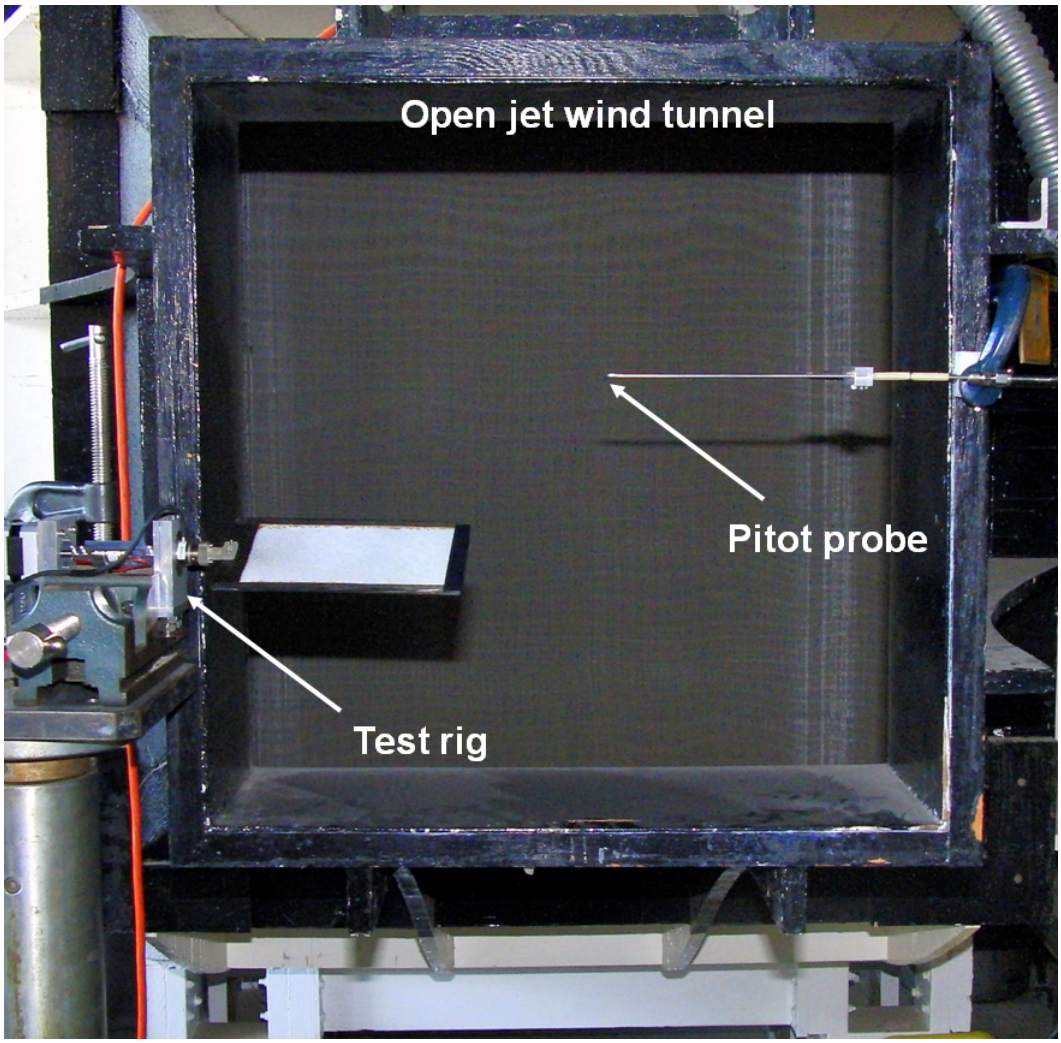

Figure 4.28: Wind tunnel test setup

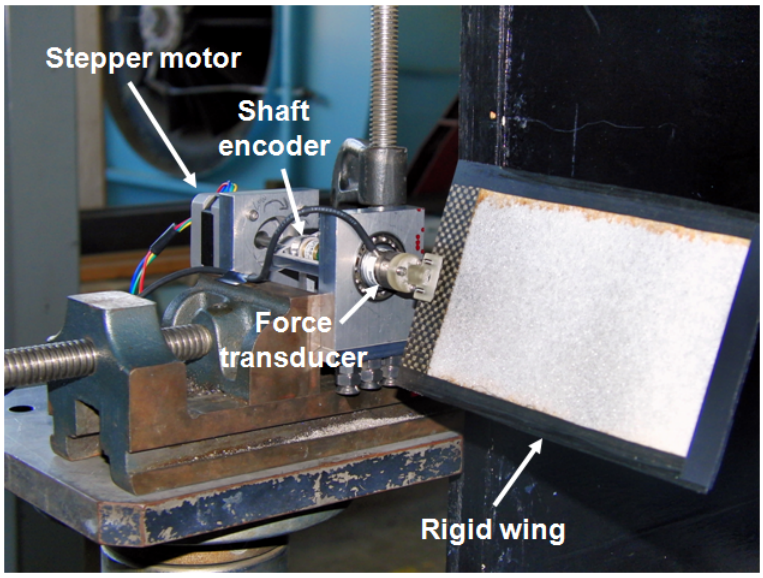

Figure 4.29: Wind tunnel test setup

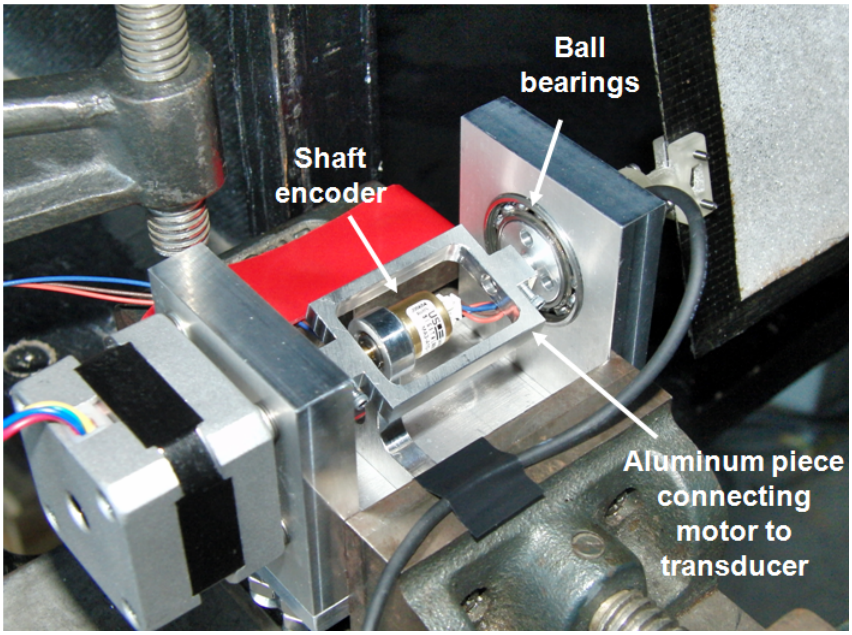

Figure 4.30: Close up of setup

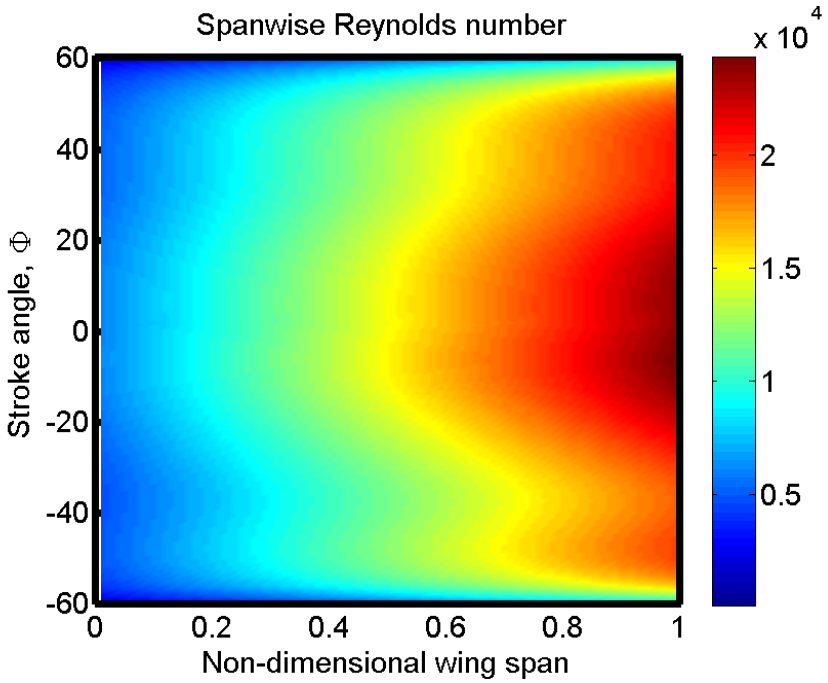

Figure 4.31: Reynolds number variation over stroke

Figures 4.32 and 4.33 plot the measured lift and drag coefficients at Reynolds number of 10,000 and 20,000, respectively. In both cases, the drag coefficient, shown as the red line, is seen to progressively increase with increasing pitch angle, attaining the maximum value at $\Theta = 90^o$. At $\Theta = 45^o$, the value of the drag coefficient is only slightly higher than the lift coefficient. This is because in the post stall condition, the pressure drag is resolved into normal and axial components. At a pitch angle of 45^o, the C_l and C_d due to pressure are essentially the same. The value of C_d is slightly higher than the C_l because of the small amount of skin friction drag present in C_d. The lift coefficient, shown by the blue line, increases steadily till $\Theta = 15^o$, where the flow seems to stall, leading to a reduction in lift thereafter. Increasing the pitch further, results in a maximum value of the lift coefficient at $\Theta = 45^o$. Through the range of pitch values from 45^o to 90^o a steady decline in the C_l is shown. The

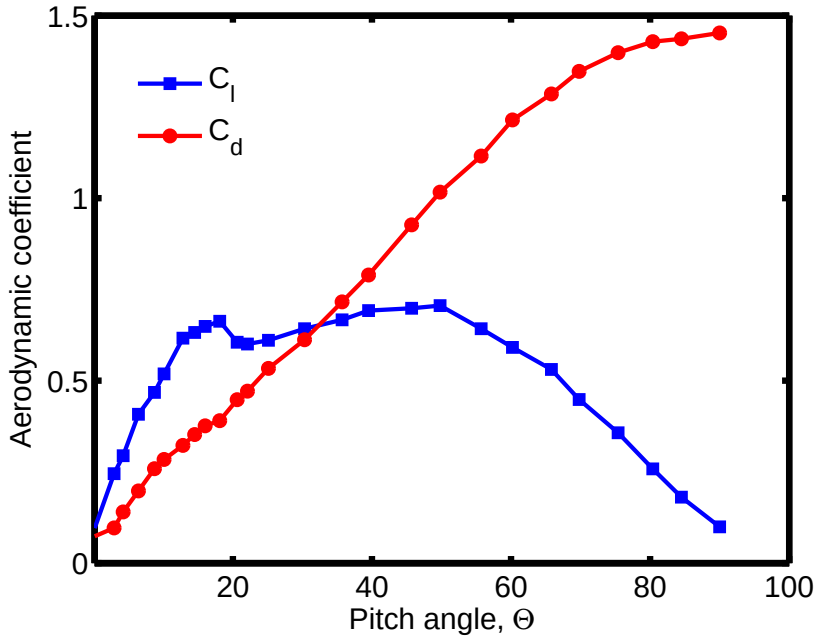

Figure 4.32: Wind tunnel data at Re 10,000

key feature of the plot is the gradual stall event at $\Theta = 15^o$.

Wind tunnel tests were conducted from $10,000$ to $60,000$. It was noticed that an increase in the Reynolds number leads to a decrease in the values of C_d and an minor increase in C_l. Figure 4.34 plots the variation of the drag coefficient with Reynolds numbers, showing this decrease. The greatest decrease in the drag coefficient was observed when varying the Reynolds number from 10,000 to 20,000. The lift coefficients at 10,000 and 60,000 are plotted in Figure 4.35. The maximum value of C_l before the second stall at Re 10000 is 0.65, while at Re 60000 it is 0.71.

Lift to drag ratios for the different cases are plotted in Figure 4.36. For all Reynolds numbers, maximum L/D occur at $\Theta = 7^o$. Thereafter, there is a subsequent decrease through all the range of pitch angles. Another important observation is the effect of Reynolds number on the maximum value of L/D ratio. At Re 10000,

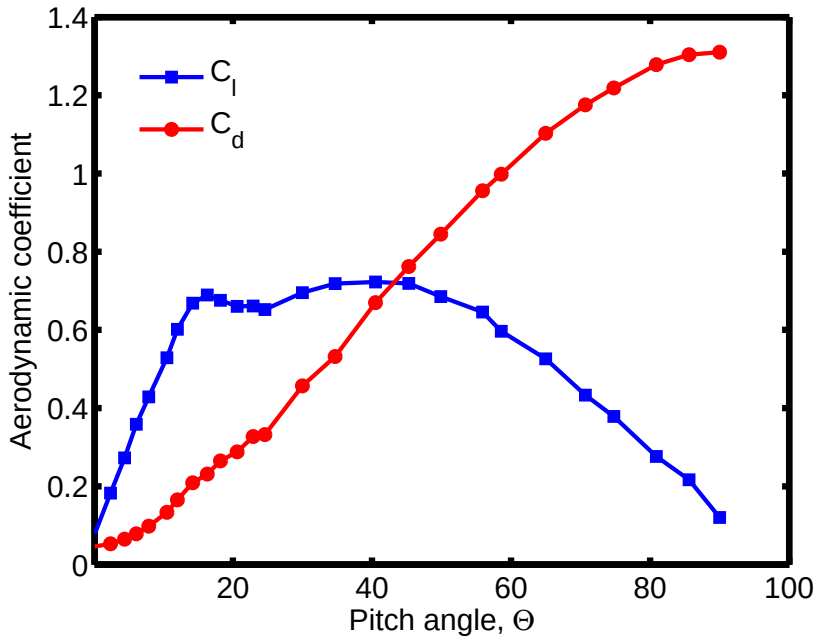

Figure 4.33: Wind tunnel data at Re 20,000

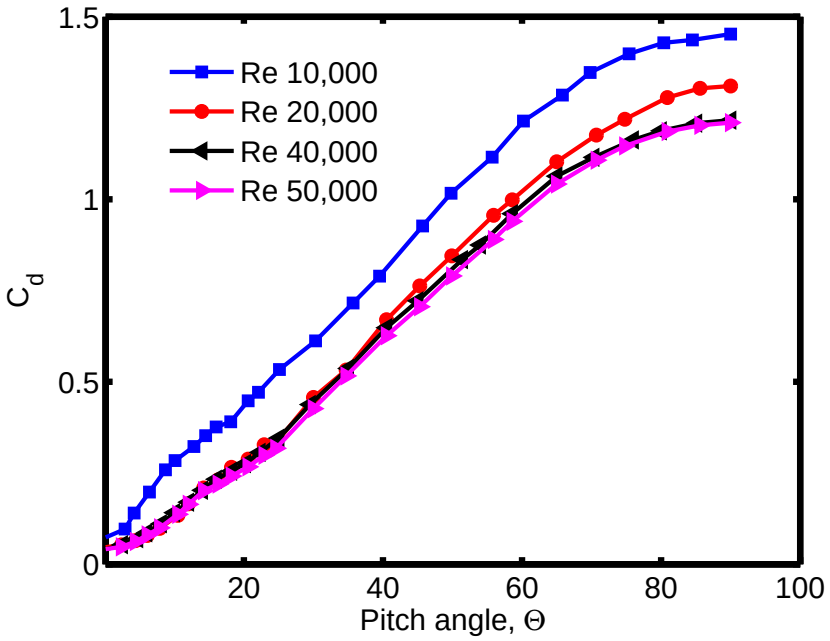

Figure 4.34: Drag coefficients over Reynolds numbers

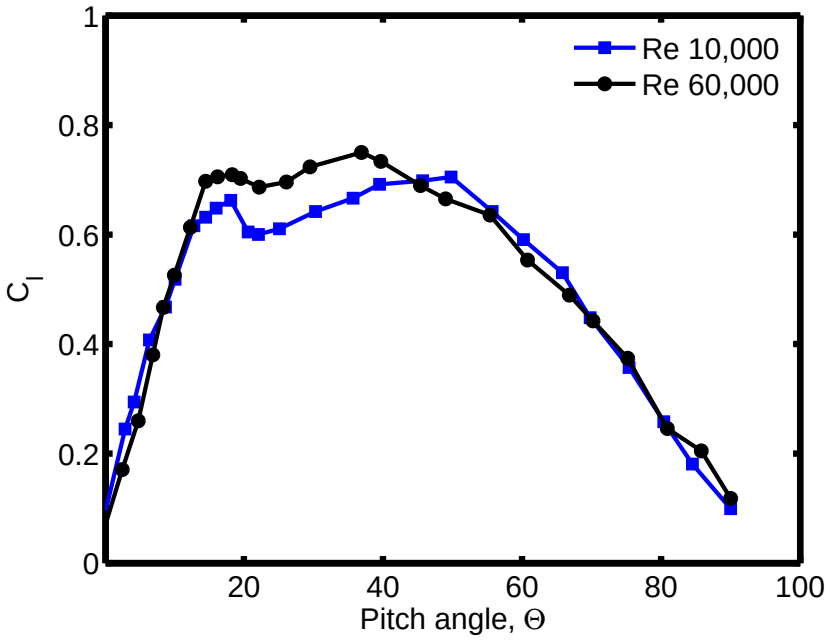

Figure 4.35: Lift coefficients for extreme Reynolds numbers

$(L/D)_{max}$ is 2.4 while at Re 60,000 it is is 7.7, illustrating that at MAV scale Renyolds numbers, the C_l/C_d is a very strong function of the Reynolds number.

A key feature of the wind tunnel tests results was the benign stall at $\Theta = 15^o$. Data from the current study was compared with similar results for flat plates from two other studies as shown in Figure 4.37 [26], [20]. The lack of values for higher pitch angles for both the other studies once again highlights one of the motivations of the present wind tunnel study. While Mueller's results are at a higher Reynolds number, the gradual lift stall is observed. Studies conducted for cambered plates show similar results [20]. The difference in lift coefficient values between Selig's infinite wing test and the current study are attributed to the effects of the tip vortex. The present study reports a more gradual and slightly higher stall pitch angle margin then the infinite wing case for the same Reynolds number. Mueller

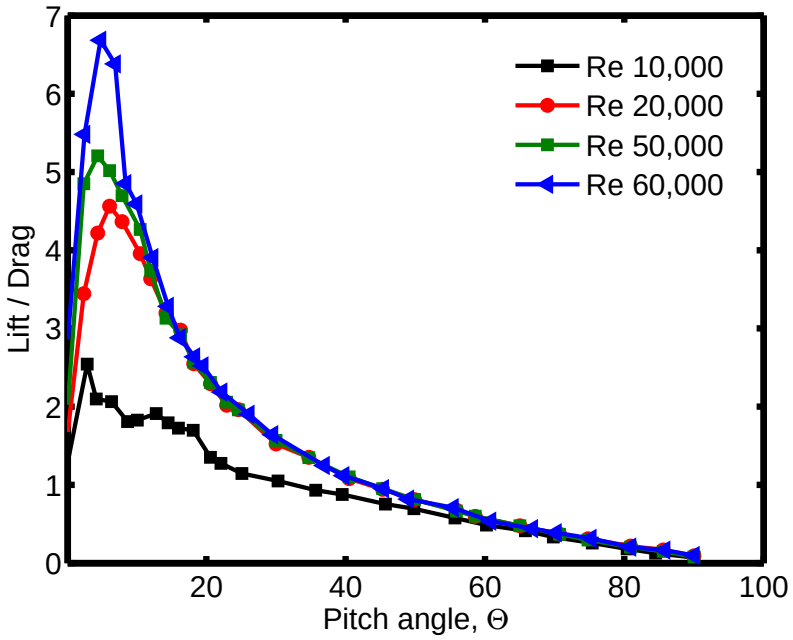

Figure 4.36: Lift to drag ratios

also noted a similar decrease in finite wing lift coefficients in his studies for a flat plate [20].

Figure 4.38 compares the mean lift coefficients for the flapping wing with fixed pitch cases with those of the static wind tunnel test at Re $20,000$. Mean values of the C_l for the flapping tests were determined and are plotted as discrete points. Overall, there is an over six times increase of the flapping C_l from the static values. It is interesting to note that the increase is greatest for pitch angles of 45^o and decreases subsequently. This may be the effect of the leading edge vortex, which is more dominant at higher pitch angles. However, only a qualitative look at the flow field can corroborate this. A first order Fourier series fit has been applied to the translation values as shown in the figure. This fit is given by the function:

$$C_l(\alpha^o) = 1.265 - 0.8477cos(0.04533\alpha^o) + 2.144sin(0.04533\alpha^o) \qquad (4.3)$$

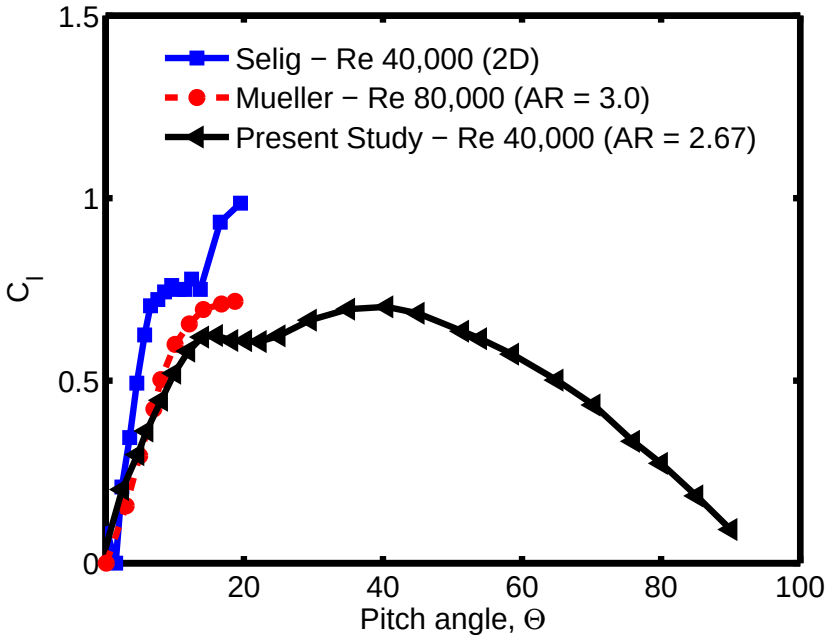

Figure 4.37: Comparison of similar wind tunnel experiments for a flat plate

This experimental fit will be utilized as a table lookup to understand the more complex aerodynamics of flapping with varying pitch cases. A similar Fourier series fit for the drag coefficient (see Figure 4.39) is given below:

$$C_d(\alpha^o) = 2.532 - 2.542cos(0.03741\alpha^o) + 0.03552sin(0.03741\alpha^o) \qquad (4.4)$$

4.3.4 Flow Visualization

Flow visualization studies were carried out using the flapping mechanism for a variety of translation pitch angles at 3 Hz. The main motivation for these tests was to qualitatively address the high unsteady lift and drag coefficients (compared to the static wind tunnel tests) seen in the pure flapping tests. Furthermore, a flapping with dynamically varying pitch case was also assessed to shed light on the nature

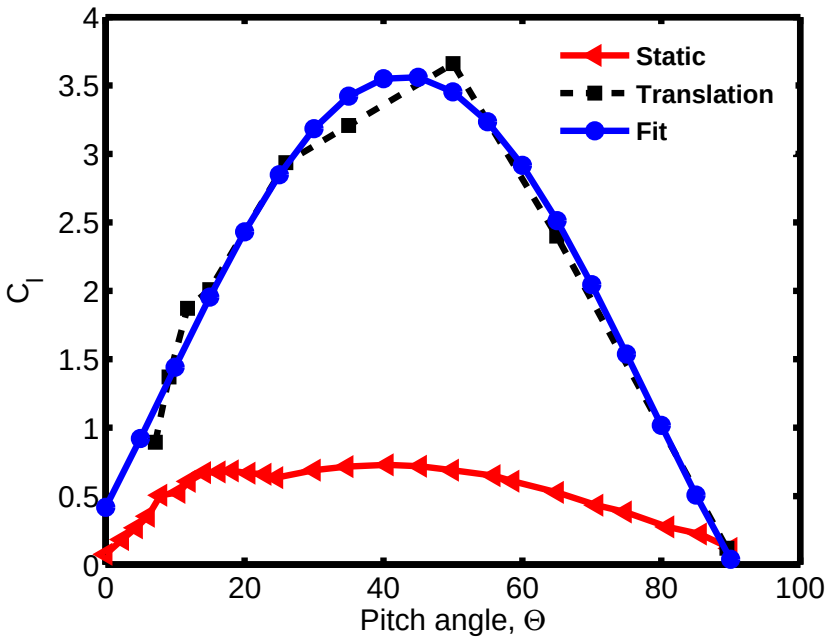

Figure 4.38: Lift coefficients at Re 20,000

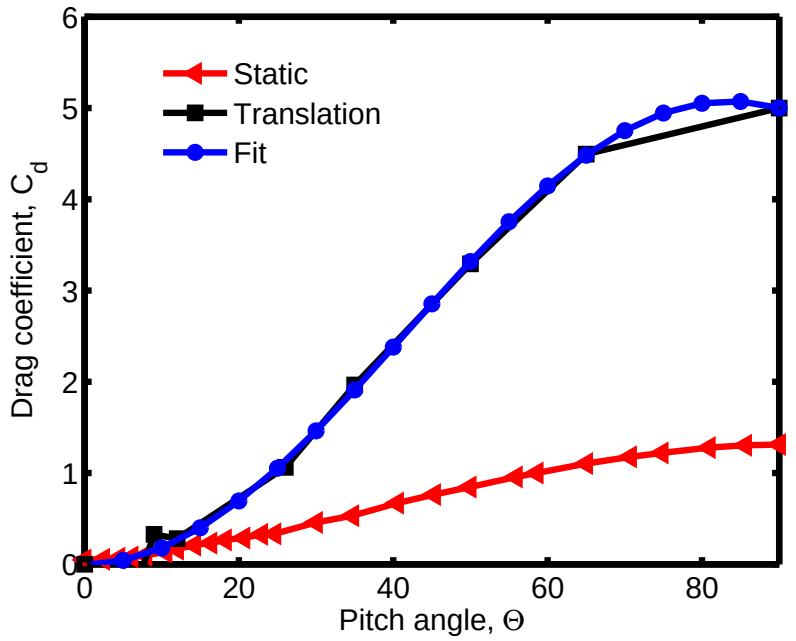

Figure 4.39: Drag coefficients at Re 20,000

of the complex flow field for these kind of wing kinematics. Specific interest was in the nature of the leading edge vortex, starting vortex and the presence of other flow structures that could cause an augmentation in lift.

A time resolved flow visualization technique was adopted. This methodology permits the temporal tracking of flow structures as the wing flaps through a complete cycle. The experimental setup is shown in Figure 4.40. Here the camera viewing axis is positioned orthogonal to the plane of the laser sheet. The flapping wing test rig was positioned such that the laser illuminated the mid-span location. The camera was placed at the midstroke location with respect to the stroke of the wing. For this purpose, a time resolved laser (Pegasus XR) and a high speed CMOS Nikon camera were used.

The flow was seeded with particles generated using high pressure nitrogen combined with a mineral oil solution. This mixture was then vaporized after being heated to its boiling point. The flow was seeded from both the top and the bottom through a honeycomb structure in order to ensure that there were no eddies present in the seeded flow. The high speed camera captured images of this flow at 500 frames per second. Flow visualization experiments were conducted for pitch angles of 7^o, 9^o, 15^o, 26^0, 50^o and 65^o. Figures 4.41 to 4.47 show the representative results. All images shown here were taken during the downstroke.

For low pitch angles, it was observed that the flow was relatively benign with the presence of small vortical structures at the leading edge and eddies at the trailing edge. No visible LEV was seen along the chord. Towards the tip, the eddies are generated by the merging of the viscous boundary layers present on the upper and

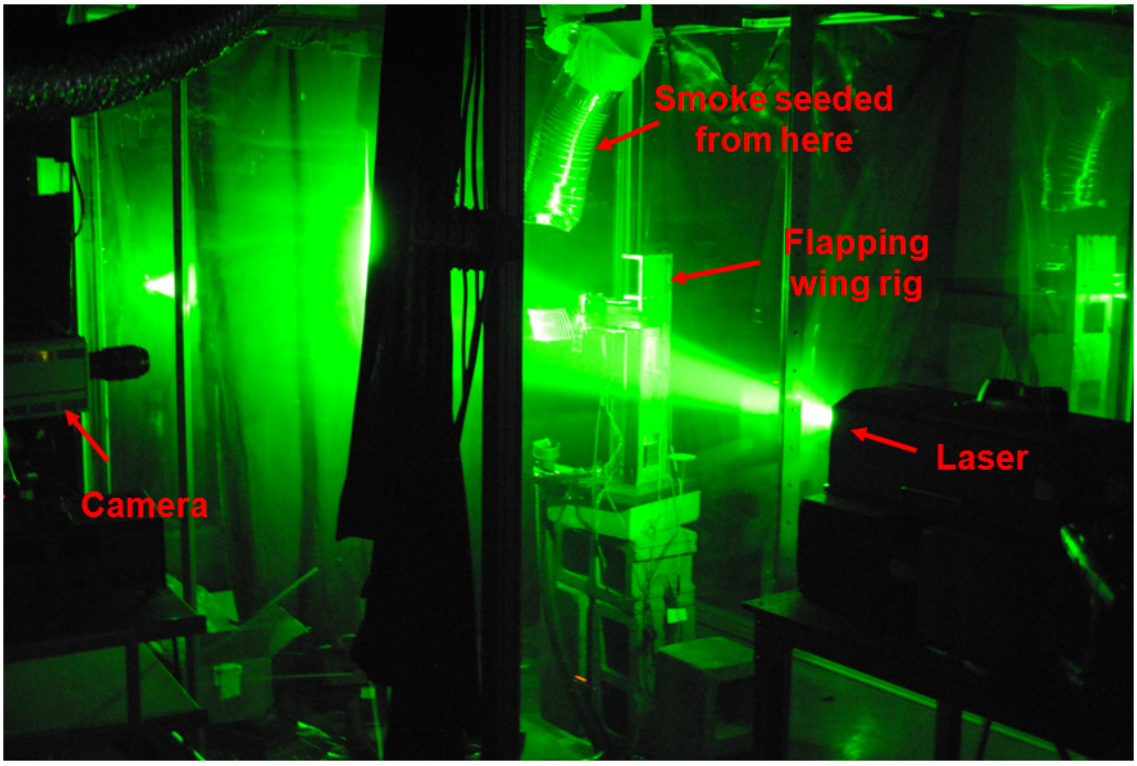

Figure 4.40: Flow visualization setup

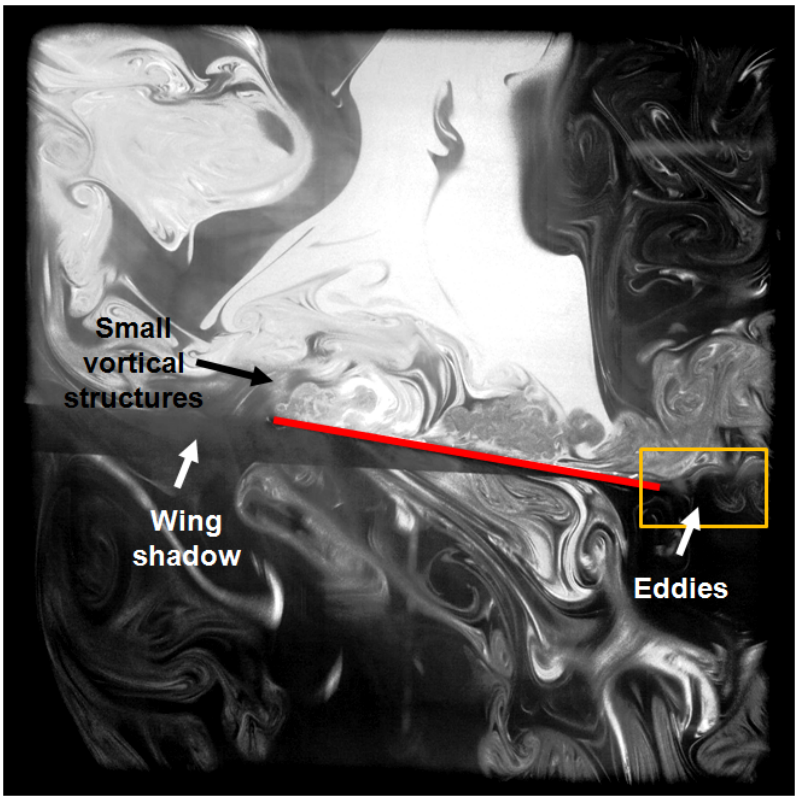

Figure 4.41: Flow visualization at mid-span, midstroke location for $\Theta = 7^o$ for translation flap motion at 3 Hz

Figure 4.42: Close up of trailing edge eddies in Figure 4.41

lower surfaces of the wing (see Figure 4.41). Figure 4.42 focuses on the eddies seen towards the trailing edge. Separation towards the tip occurs in the form of a Karman vortex street, as can be seen by the periodic swirling pattern of the vortices. The presence of a Von Karman vortex street is an interesting observation and one that has not been presented in earlier flapping wing flow visualization experiments [22], [31].

Figure 4.43 shows the flow structures present at a pitch angle of 15^o. Here there are a visible set of vortices along the chord of the wing. Ramasamy et. al observed a similar pattern on thin wings with sharp leading edges at a Reynolds number of $15,500$. Their conclusion was that the leading edge vortex is continually generated and shed into the trailed wake as the wing flaps through its stroke [22]. Thus in Figure 4.43, the secondary vortex seen at the midstroke location would invariably be the shed leading edge vortex of the wing at an earlier stroke position. Another interesting flow field development with an increase in the pitch angle, is the presence of a separated flow region between the secondary vortex core and the trailing edge wake.

A case where the flow is stalled is presented in Figure 4.44. There is an extremely large LEV that extends to around 50 percent of the chord. The vortex core for the LEV shown here is not visible and this maybe due to a strong spanwise flow component. That is, there are multiple LEVs present along the span of the wing, and these are spilled towards the tip due to the spanwise flow. The hypothesis of mutiple LEVs attaching and detaching still holds true here, as multiple vortical structures along the chord of the wing are seen.

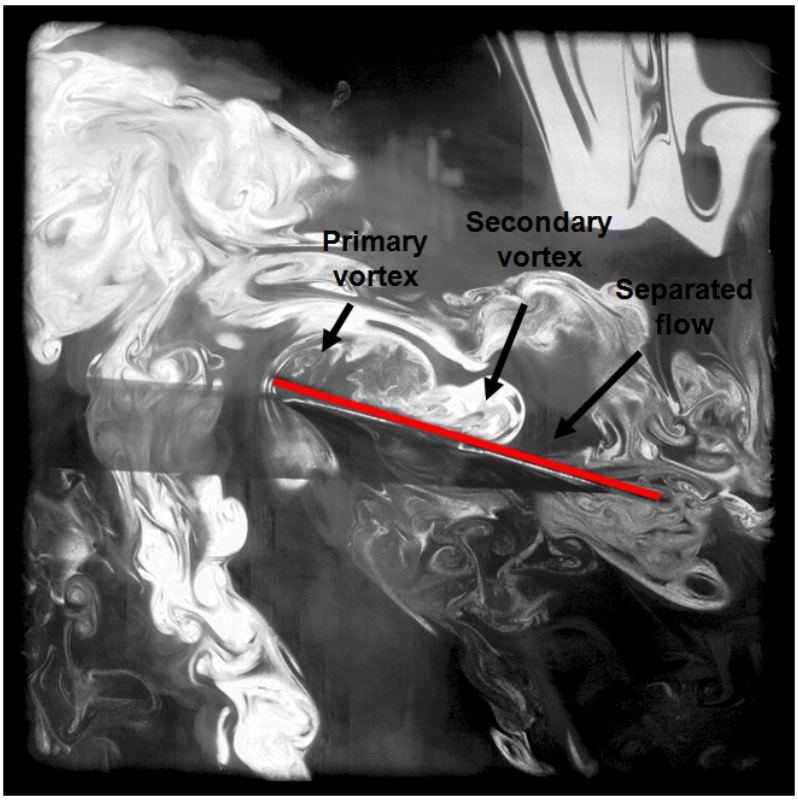

Figure 4.43: Flow visualization at mid-span, midstroke location for $\Theta = 15^o$ for translation flap motion at 3 Hz

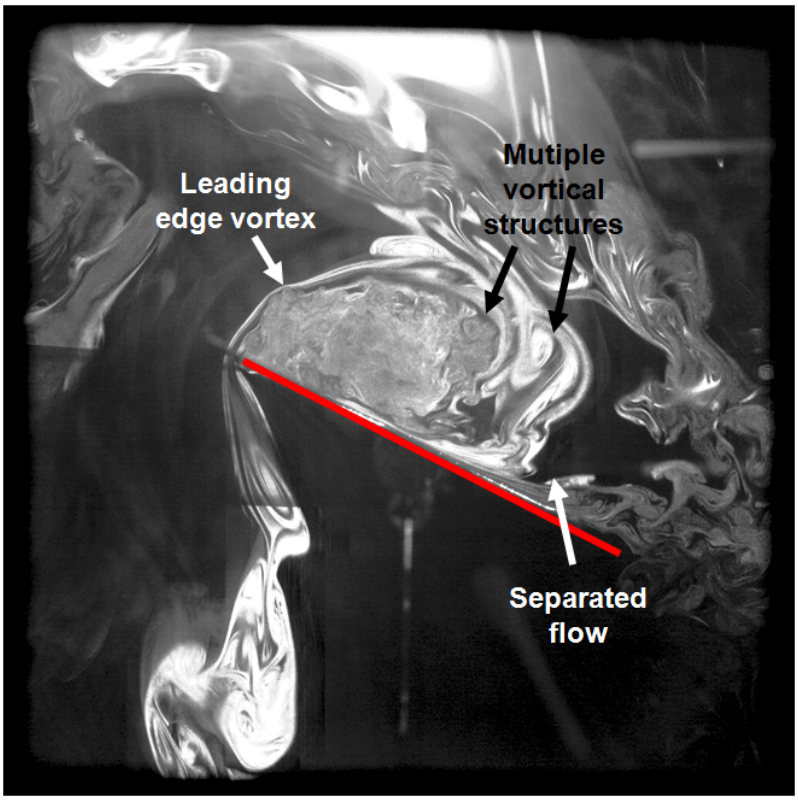

Figure 4.44: Flow visualization at mid-span, midstroke location for $\Theta = 26^o$ for translation flap motion at 3 Hz

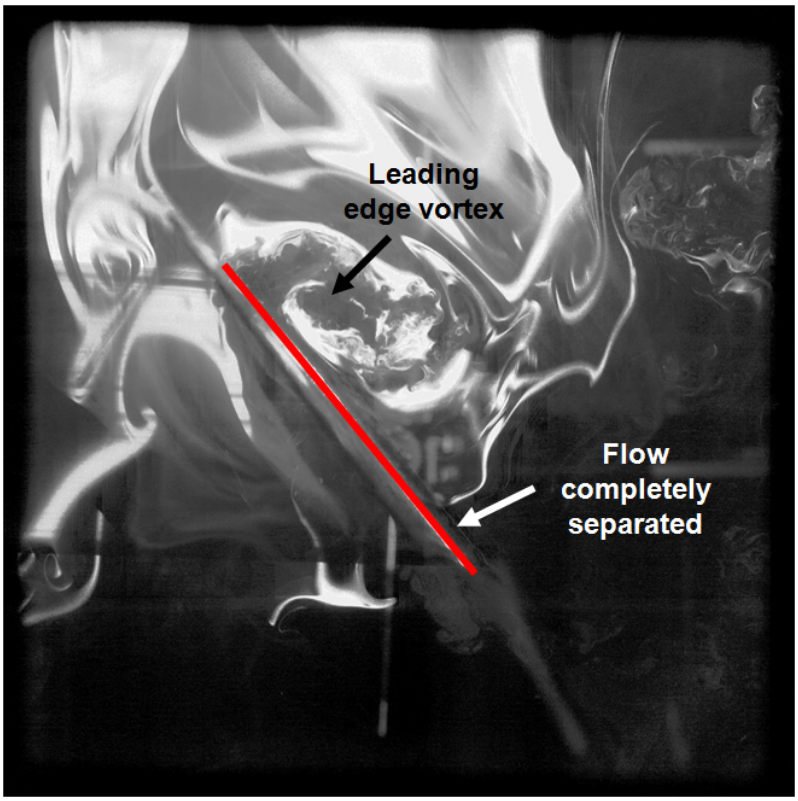

Figure 4.45: Flow visualization at mid-span, midstroke location for $\Theta = 50^o$ for translation flap motion at 3 Hz

Static and pure translation tests revealed that maximum lift was generated at a pitch angle of approximately 50^o. Figure 4.45 shows the complex flow structures responsible for the tremendous augmentation of lift at this angle. The LEV here is seen to be almost encompassing the entire chord length.

Figures 4.46 and 4.47 show representative images of the wing at a pitch of 65^o. While the first image is taken exactly at midstroke, the second one is taken a few milliseconds after midstroke in order to see how rapidly vortical flow structures develop. Both the images illustrate the presence of a leading edge vortex, that is smaller in size as compared to the one seen at 50^o. More importantly, while there

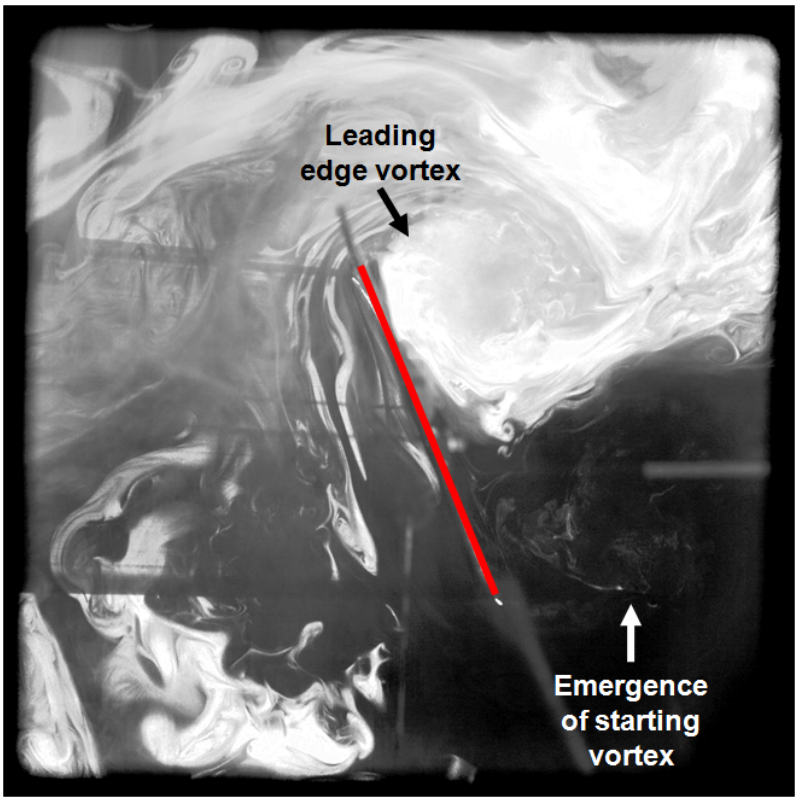

Figure 4.46: Flow visualization at mid-span, midstroke location for $\Theta = 65^o$ for translation flap motion at 3 Hz

is no vortical structure present near the trailing edge of the first image, within a few milliseconds a massive starting vortex has developed in the wake of the wing as shown in the second image.

The flow visualization studies clearly showed that the relatively large stable LEVs on the wing at high pitch angles is the reason for the large C_l and C_d values measured in the single degree of freedom flapping experiments. Overall, the presence of large LEVs were crucial in the identification of the unsteady aerodynamic phenomenon that tremendously augmented the lift values. The flow visualization study showed LEVs that encompassed the entire chord length for certain pitch angles.

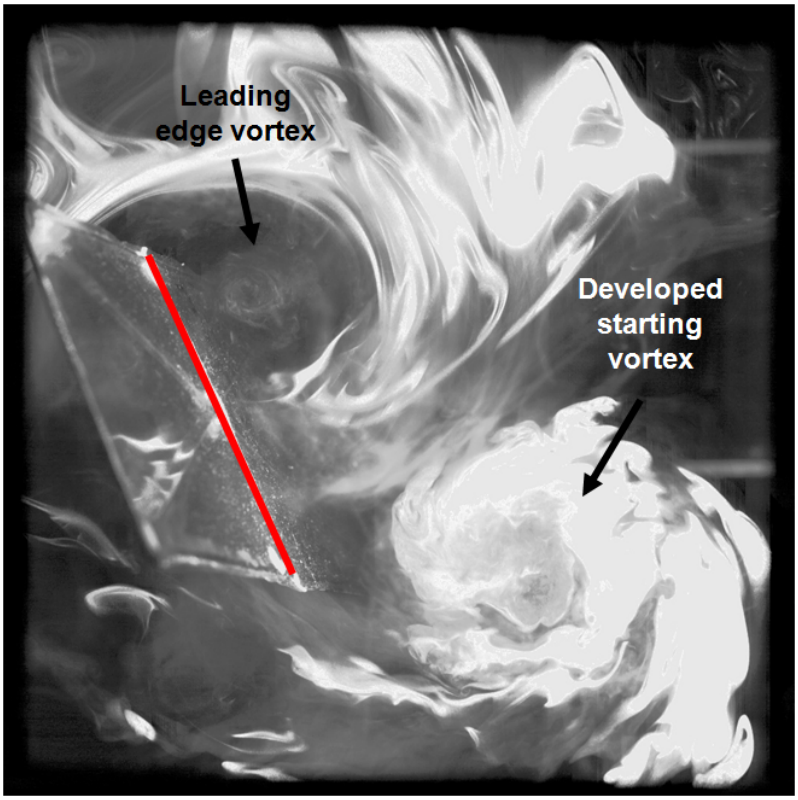

Figure 4.47: Flow visualization at mid-span, post midstroke location for $\Theta = 65^o$

The images also showed multiple discrete vortices at the top of the wing at different chord lengths. This is attributed to the periodic development, attachment and shedding of vortices at the leading edge. Given the unsteady flow field this may also explain the presence of higher harmonic aerodynamic forces as outlined earlier in this chapter. Before revisiting the force trajectories, a more quantitative approach to the flow field is needed.

4.3.5 Particle Image Velocimetry (PIV)

The main motivation for a particle image velocimetry study is to get quantitative information regarding the magnitude of the velocity and vorticity at different locations along the stroke. While the flow visualization studies provide an overall sense of the structures of the flow field, it is difficult to gauge the strengths and relative magnitudes of these structures. 2-D particle image velocimetry or 2-D PIV is a non-intrusive flow measurement technique that measures the planar velocity of particles within a given area. While the experimental setup is the same as that for flow visualization, the flow is seeded uniformly with submicron tracer particles, which serve to track the flow. The seeded flow is then illuminated twice within a small separation time. The camera is digitally synchronized with the laser to capture two successive images during this separation time interval.

The pair of images contains the pixel displacement of the particles for the separation time interval. This pixel displacement can be converted into millimetres using an appropriate calibration. A cross-correlation procedure is utilized to track

the movement of particles from one image to the other. This computes the magnitude and direction of the particles over the two frames. Once the pixel displacement is calculated, the velocity can be obtained. A more thorough review of the setup and cross-correlation technique details are available in reference [23].

The PIV study presented here was conducted for the single degree of freedom flapping case with a pitch angle of 65^0. Figures 4.48 to 4.51 plot the velocity vectors over the contour of the velocity magnitude at different instances during the downstroke. Since the camera and laser positions remained fixed, the wing is seen in some of the images to be a out of the laser plane. The wing as shown in these images is shown as a white rectangle. The velocity magnitude for all the plots varied from 0.5 m/sec to 8.5 m/sec. Overall, it was observed that before the wing reached the midstroke location (Figures 4.48 and 4.49), the region on the upper surface of the leading edge had the greatest area of high velocity magnitude. The direction of the velocity vectors here points towards the presence of only a single leading edge vortex. As the wing moves towards midstroke, the vortex seems to diffuse as the region of high velocity magnitude decreases relative to the chord length (Figures $4.50 - 4.51$). Additionally the formation of a starting vortex is reflected in the direction of the velocity vectors. As the wing leaves the midstroke position, the LEV has gone further down the chord, and the overall intensity of the vortex has decreased compared to the Figure 4.48.

While qualitative information from the PIV data provides an insight into the diminishing strength of the LEV as it approaches and leaves the midstroke position, quantitative information about the flow structures at midstroke can also be deter-

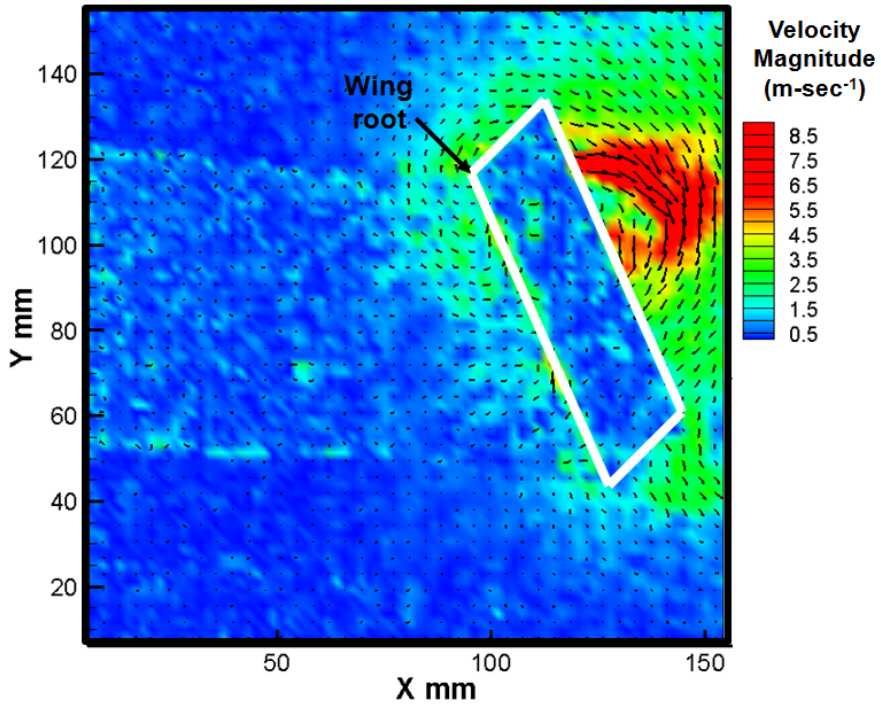

Figure 4.48: PIV data for wing at 65^0 pitch before onset of midstroke for translation flap motion

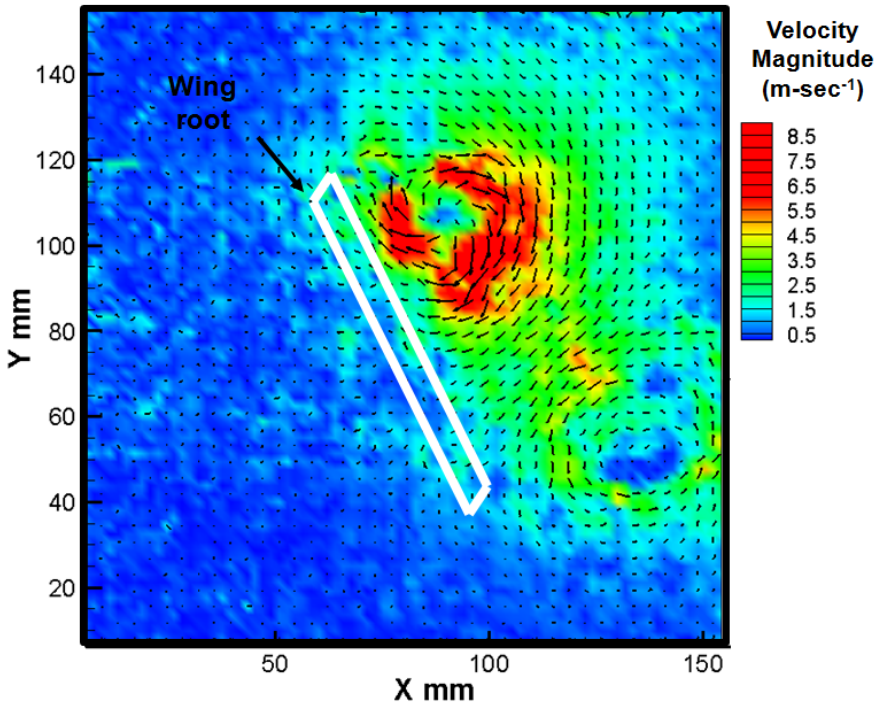

Figure 4.49: PIV data for wing at 65^0 pitch before onset of midstroke for translation flap motion

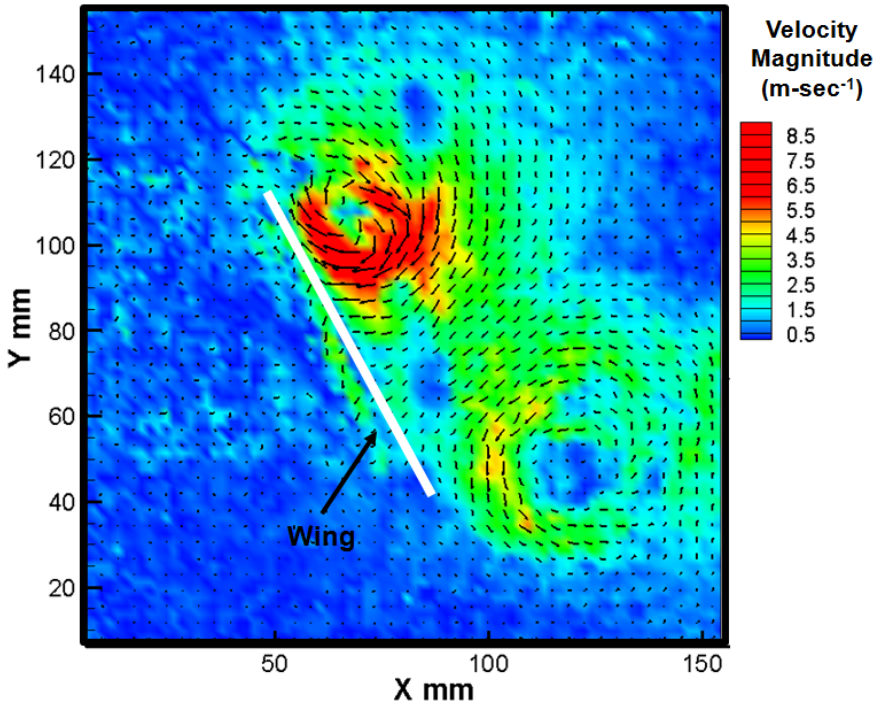

Figure 4.50: PIV data for wing at 65^0 at midstroke for translation flap motion

mined. The velocity vectors can be used to compute the bound circulation values using the circulation-box method, which can then be used to obtain a sectional lift coefficient via the Kutta-Joukowski theorem. It should be noted that this method can only be applied to the frame, where the chord is perfectly orthogonal to the camera (the wing is shown as a line) (see Figure 4.50). Other studies that have utilized such a method include [24], [22].

Figure 4.52 outlines the schematic of the circulation-box method. An integration contour around the wing is established that only encompasses bound flow structures, since the goal is to capture only the bound circulation. Thus, the starting vortex is intentionally not included. The bound circulation around the wing can

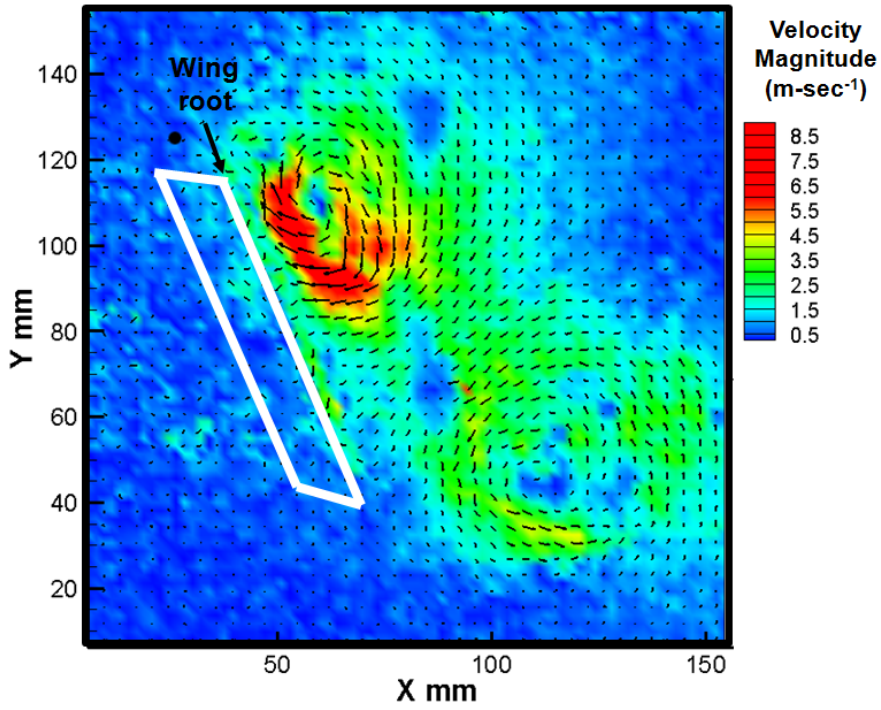

Figure 4.51: PIV data for wing at 65^0 post midstroke for translation flap motion

be computed by a numerical evaluation of the closed loop integral:

$$\Gamma_b = \oint_c V \cdot ds = \sum U \triangle x + V \triangle y \tag{4.5}$$

where U and V are the tangential velocities as shown in Figure 4.49. This integral is computed for various increasing sizes of contour boundaries till a steady state value of the bound circulation is reached. Figure 4.53 plots the bound circulation with respect to the areas of the integration contours chosen.

As seen from the graph, the value of the bound circulation was found to be $\Gamma_b = 0.2723 m^2/s$. Now, the sectional lift coefficient can be computed using:

$$c_l = \frac{\rho V_\infty \Gamma_b}{\frac{1}{2}\rho V_\infty^2 c} = \frac{2\Gamma_b}{V_\infty c} \tag{4.6}$$

where V_∞ is the freestream velocity at the midstroke for the midspan location and

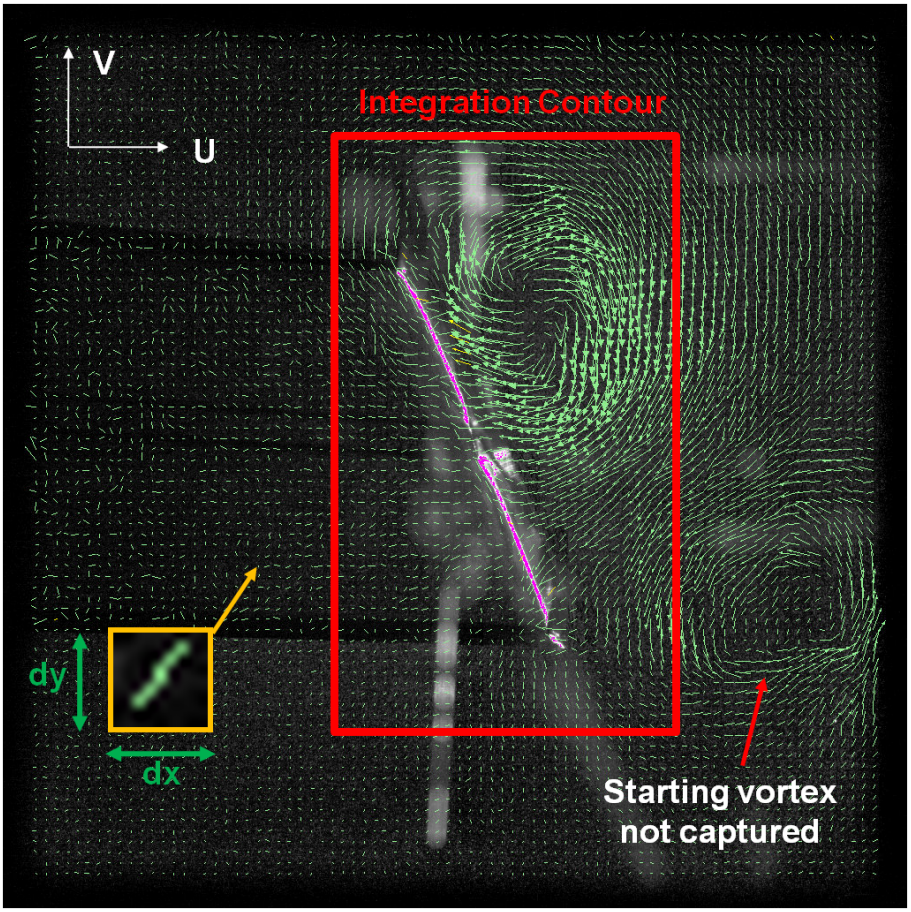

Figure 4.52: Schematic showing sample interrogation window

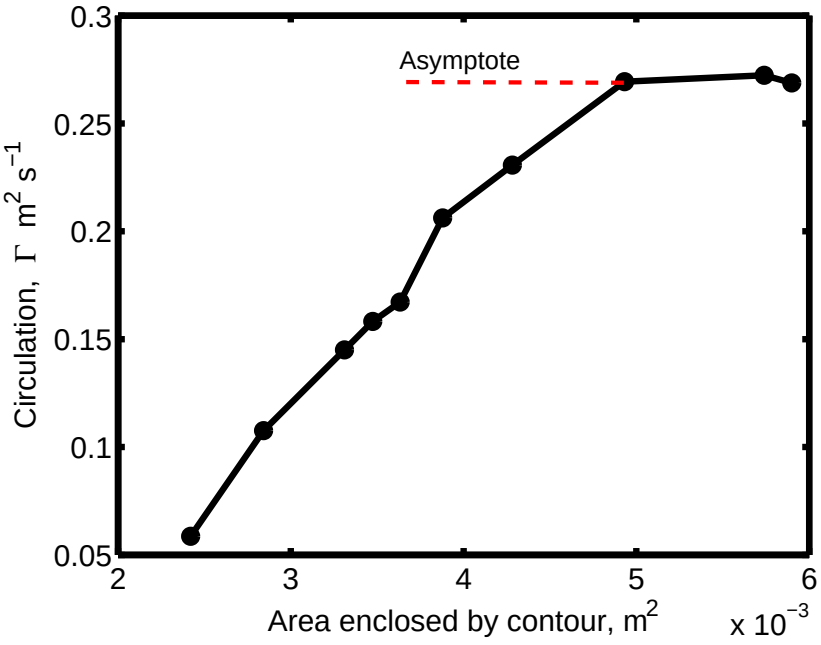

Figure 4.53: Integration process for estimate of sectional circulation for translation flap motion at 65^o

c is the chord length of the wing. The c_l was computed to be 2.803, which is comparatively high but within the range of lift coefficient (C_l) values obtained from the flapping with fixed pitch tests. Ramsey [24] in his work on an experimental insect-based flapping wing setup, reported similar high lift coefficients using the circulation-box approach. His methodology was extended to compute the bound circulation at multiple span locations, in order to compute the lift force via a spanwise integration of the sectional lift coefficients. He reported good correlation with the overall force that the wing was designed to produce at the flapping frequency. Thus the coefficient obtained in the present study via the circulation-box approach is a very good estimate of the sectional lift at midspan and reflects on the presence of unsteady aerodynamics that significantly augment lift values well in excess of

static wind tunnel data.

4.3.6 Higher Harmonic Force Contributions

As mentioned earlier, the translation force trajectories utilized a cut-off frequency of 7 Hz, thereby capturing only the first two force harmonics. Data was presented at this frequency for lucidity and to get a rudimentary understanding of the aerodynamics. Now the same data is analyzed again, but at cut-off frequency of 15 Hz. The purpose of this increase in the cut-off frequency is to capture various unsteady aerodynamic phenomena that were previously negated. More specifically, the aim of this section is to relate the instantaneous force measurements with the development, convection and shedding of the LEV as noted in the flow visualization and PIV study. In other words bring together the qualitative and quantitative results presented thus far. Figures 4.54 and 4.55 plot the aerodynamic coefficients for the different flapping at fixed pitch cases through the downstroke at a cut-off frequency of 15 Hz.

Results from the flow visualization and PIV studies showed that for all pitch angles (only 60^o for the PIV), the LEV was seen to have maximum strength a few miliseconds before reaching the midstroke location. Upon reaching the midstroke the LEV was seen to diffuse and start to shed down the chord. While the first vortex was shedding a second LEV was seen to form as the wing moved away from the camera and thus out of focus. Evidence for both the shedding and formation of multiple vortices can be seen Figures 4.43, 4.44 and 4.45.

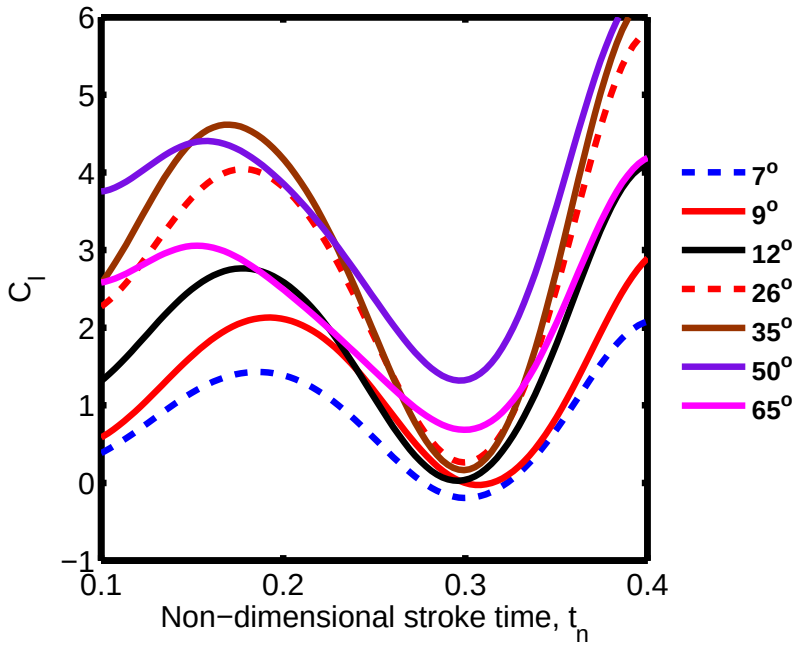

Figure 4.54: Higher harmonic lift coefficient in downstroke

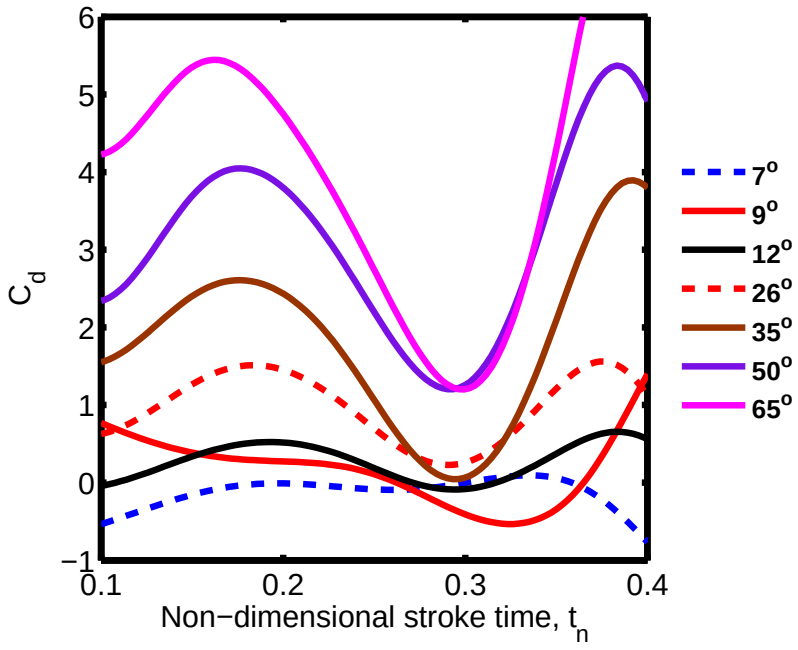

Figure 4.55: Higher harmonic drag coefficient in downstroke

The fluctuations in the lift coefficient (see Figure 4.54) maybe attributed to the development, convection and shedding of the LEV. That is the region from t_n of 0.1 to 0.2 may correspond to a the development of the LEV, region t_n of 0.2 to 0.3 may correspond to the convection and subsequent detachment, and region t_n of 0.3 to 0.4 correspond to the development of another vortex. However, given the complex nature of the flow field and the fact that the flow visualization and PIV studies were conducted only at midstroke and midspan, it is difficult to concretely prove this.

It is worth pointing out that for pitch angles 7^o and 9^o, at various instances in the downstroke, the values of the lift coefficient are negative. This implies that the effective angle of attack, at several locations along the wing is negative, which points at a high values of the inflow at various instances along the span as can be seen by:

$$\alpha = \theta - \phi = \theta - tan^{-1}\left(\frac{U_p}{U_T}\right) \tag{4.7}$$

That is values of the inflow velocity, U_p are high enough such that inflow angle, ϕ is greater than the pitch angle. For higher pitch angles, even though there is a significant drop in the lift coefficient at the same values of t_n, a positive lift coefficient is always maintained. Thus here, the inflow angle is significantly lower than the pitch of the wing.

Figure 4.55 plots the drag coefficient over the downstroke using a cut-off frequency of 15 Hz. While at higher pitch angles, the drag exhibit similar trends as lift with respect to when maximum and minimum values are reached, for low pitch

angles; 7^o and 9^o, the trends are rather different. This maybe attributed to the fact that at these low angles the skin friction drag is more dominant while at higher pitch angles the pressure drag dominates. It is interesting to note that the drag coefficient values at these low angles become negative, indicating that the wing is producing a forward force for a limited time in the downstroke.

4.4 3-D Flapping Motion With Dynamic Pitch Variation Results (Complete Insect Kinematics)

In the prior section, tests for flapping at a fixed pitch were conducted. A key observation of the study was the presence of high small aerodynamic coefficients attributed to the presence of large LEVs, and the aerodynamic forces at the ends of the stroke attributed to minor wake capture effects. This section seeks to investigate whether the inclusion of wing rotation and out of the plane wing motion (pitching axis traverses a figure of eight) within the kinematic framework presented thus far leads to an augmentation of the lift and drag forces. Figure 4.56 defines the three relevant angles involved in these tests; namely the coning angle (β), stroke angle (Φ) and pitch angle (θ). The wing is shown as a rectangular section.

Figures 4.57 and 4.58 provide alternate three dimensional views of the definition of these three angles. While these angles can be obtained through the kinematic relations presented in Chapter 2, a more direct approach of measuring these angles on the actual setup at the operating flapping frequency is pursued using a 3-D motion capture technique.

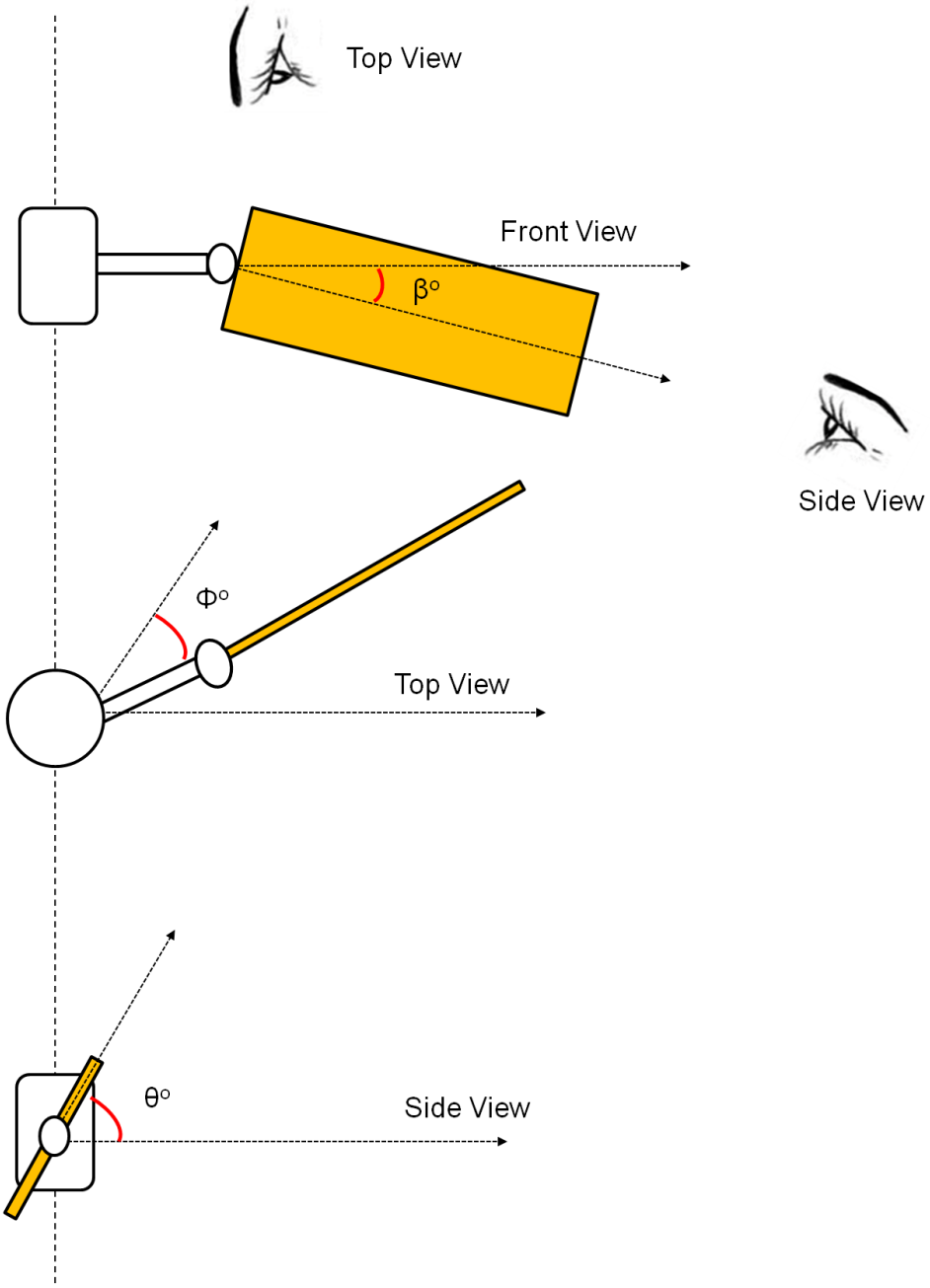

Figure 4.56: Schematic showing different kinematic angles

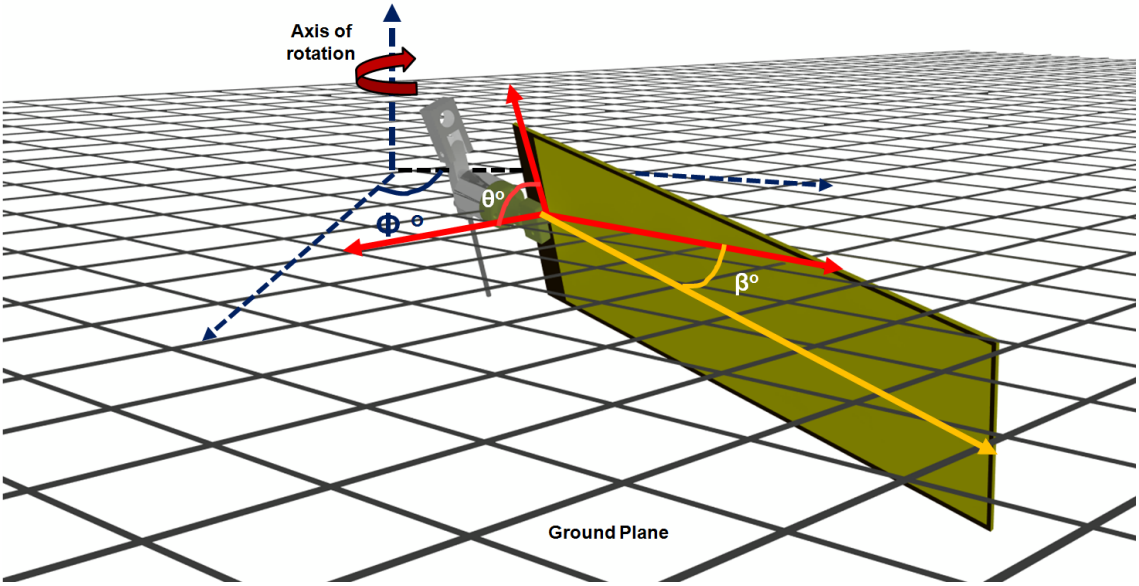

Figure 4.57: Isometric view of kinematic angles

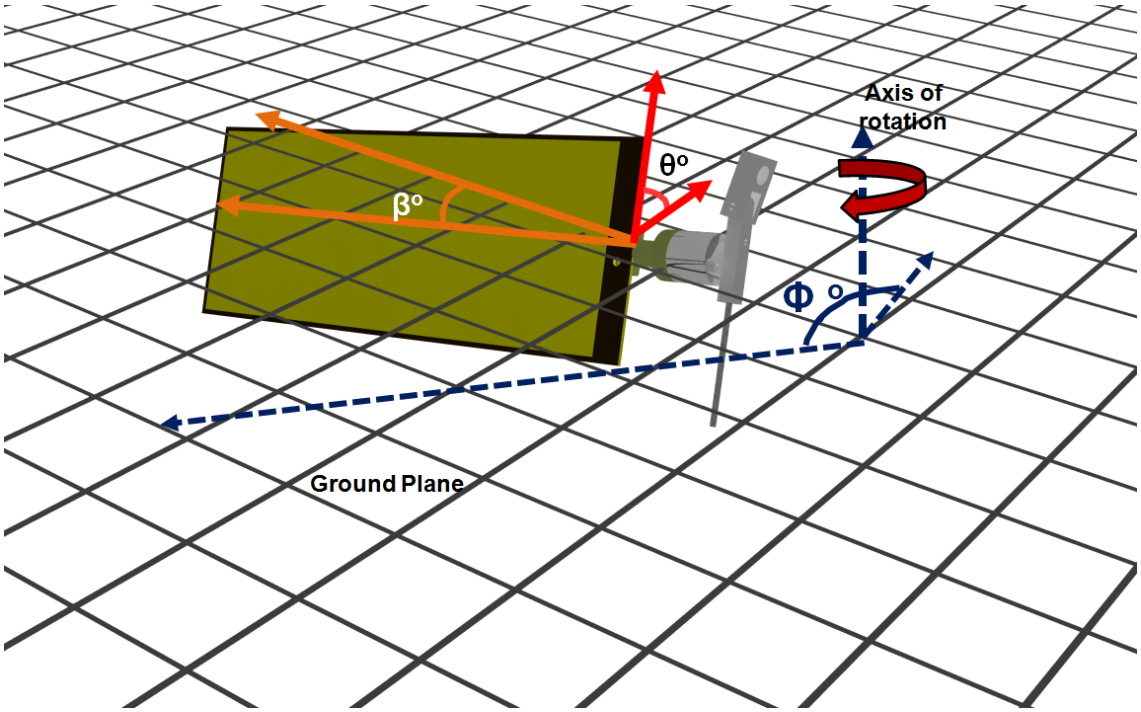

Figure 4.58: Top view projection of kinematic angles

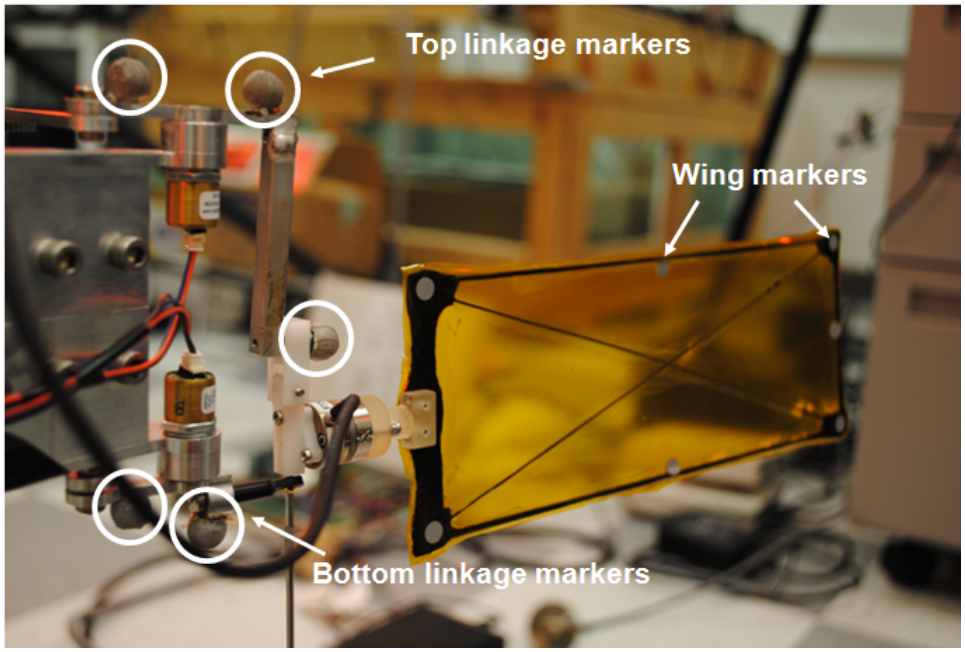

Figure 4.59: Flapping wing setup with motion capture equipment

4.4.1 Wing Kinematics

A motion capture system, VICON®, was used to capture the three kinematic angles (β, Φ, θ) as shown in Figures 4.57 and 4.58. The main motivation for this experiment is to be able to accurately measure the motion of the wing and the kinematic angles for a variety of pitching and coning combinations. Also, since the balance is undergoing the same kinematics as the wing, it is important to obtain the time history of the kinematic angles in order to transform the forces from the wing frame to the inertial frame.

Figure 4.59 shows the position of various markers on the flapping wing test setup used for this purpose. Data from VICON was taken at 500 Hz. This data was synchronized with data from the shaft encoders in order to be in phase with the force trajectories.

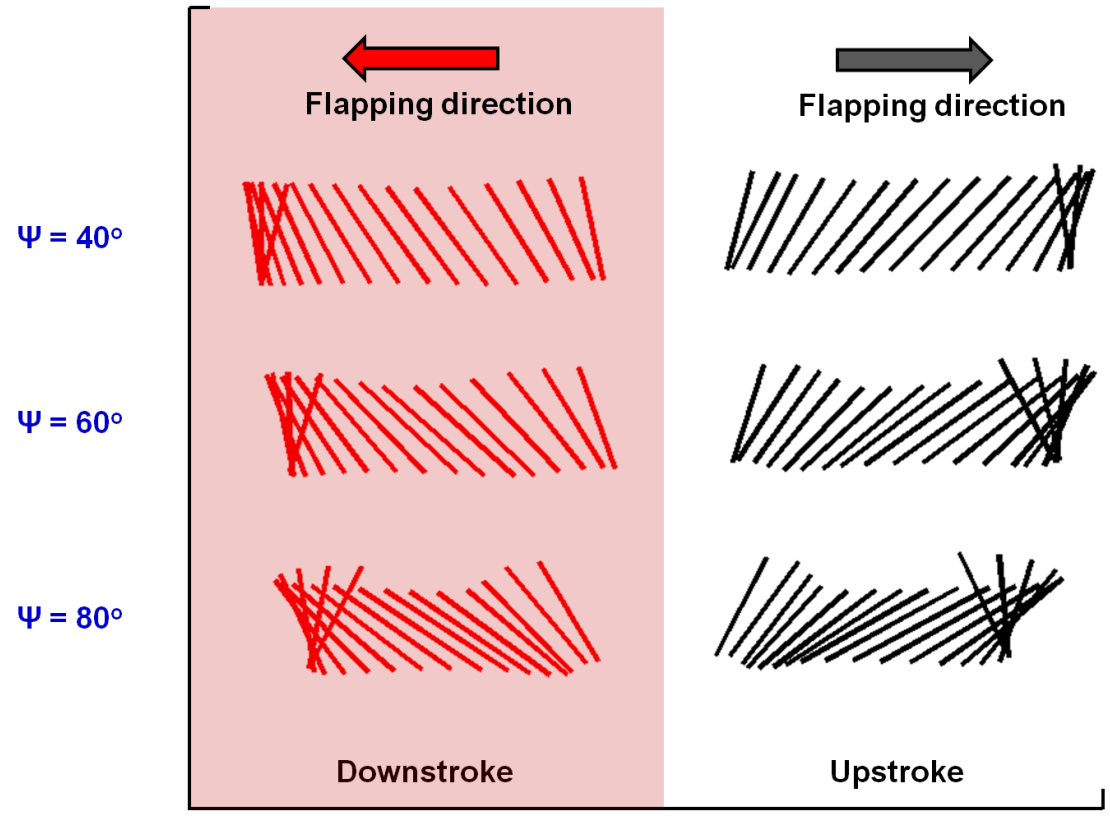

Figure 4.60: Schematic showing direction of forces for flapping with fixed pitch tests

As was mentioned in Chapter 2, the nature of the dual differential four-bar mechanism is such that as the phasing between the two four-bars is increased (which leads to the inclusion of more pitching and coning to the wing kinematics), the overall stroke amplitude seen by the wing decreases. Thus it is expected that for different flapping with pitch variation cases, the overall effective stroke amplitude is not a constant. In this study three such pitch and coning variations will be presented. These three variations correspond to phase angles of $\psi = 40^o$, $\psi = 60^o$, $\psi = 80^o$ respectively. Figure 4.60 plots the VICON® generated pitch angles at different instances of the stroke for the three variations. Here the position of the wing is shown as red (downstroke) and black (upstroke) lines on a two dimensional plane.

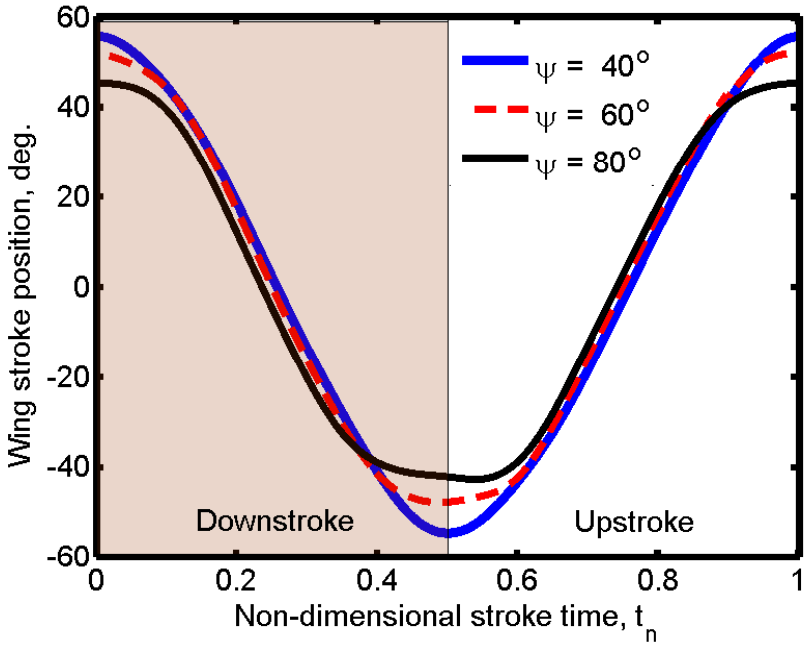

Figure 4.61: Wing stroke positions for different variations

There are three main points that should be noted from Figure 4.57. Firstly with increasing phase angle, the pitch angles progressively get lower. Secondly, the overall stroke length becomes shorter. That is, while the number of red and black lines are the same for all the variations, the stroke is more compressed. This was discussed in detail in Chapter 2. Finally, the third point is that for all variations, the wing attains a pitch of 90^o before the end of the halfstroke.

Figure 4.61 plot the position of the wing (based off its pitching axis) for the three different variations. Table 4.1 shows the stroke amplitude of the wing for each phase angle. There is a 22^o difference in the overall stroke angle between the $\psi = 40^o$ and $\psi = 80^o$ cases.

Figure 4.62 plots the wing angular velocities over the stroke. It should be noted that this angular velocity was obtained from the motion capture tests for the

Table 4.1: Comparison of stroke amplitudes for different phase angles

Phase, ψ^o	Stroke, Φ^o
40	110
60	100
80	87.3

pitching axis.

Pitch variations for flapping wing insects come under three broad categories based on the time and nature of wing rotation. These categories are symmetric rotation, advanced rotation and delayed rotation [9]. Figure 4.63 illustrates these three pitch variations as a function of the stroke. A symmetric rotation, (shown as the blue line in the figure) ensues when the wing reaches a pitch of 90^o at the end of each stroke. If the wing rotates to attain a pitch angle of 90^o before the end of the stroke, it is termed as an advanced rotation. It is expected that for a wing undergoing advanced rotation, there will be a positive peak in the lift force at the beginning of each half stroke [25]. Delayed rotation occurs when the wing starts to rotate after stroke reversal; that is the wing reaches a pitch angle of 90^o at the beginning of the next halfstroke. It is shown in Figure 4.63 (as the red line). This motion produces negative lift at the start of each halfstroke [9]. The wing in essence either has an augmentation or degradation in lift due to the wake generated from the previous stroke. Another unsteady aerodynamic phenomenon seen in flapping wing flight is lift due to rotational circulation. The rotation of the wing at the end

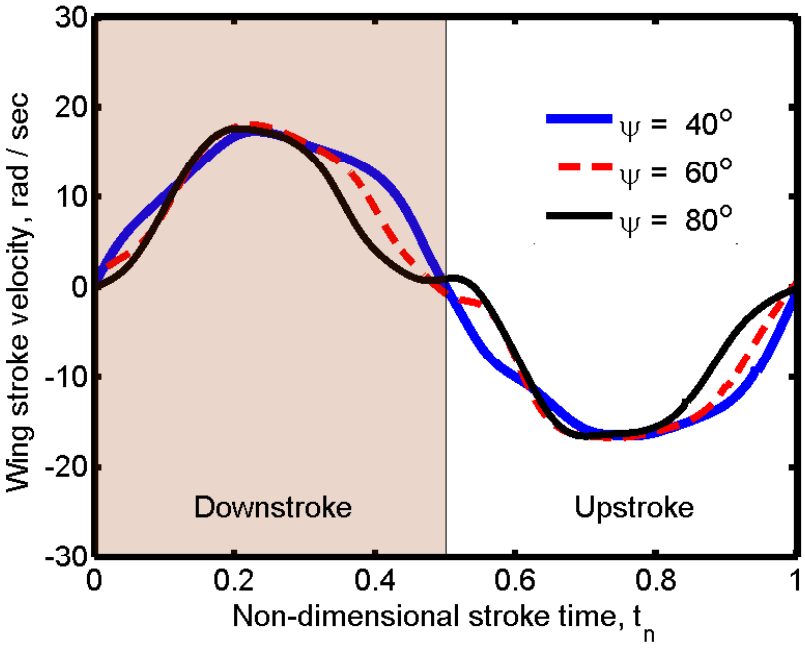

Figure 4.62: Wing angular velocity for different variations

of each halfstroke serves as a source of circulation quite similar to the Magnus effect on a baseball. The resulting rotational circulation that is generated is required so as to satisfy the Kutta condition at the trailing edge [31]. This circulation generates an upward vertical force.

The variation in pitch angles and coning angles for the flapping with varying pitch experiments conducted in this study are shown in Figures 4.64 and 4.65. These angular variations were obtained through the VICON® tests. With reference to the three categories of rotation illustrated in Figure 4.63, all pitch angle variations are inherently advanced. The coning angle for the different cases is presented in Figure 4.65.

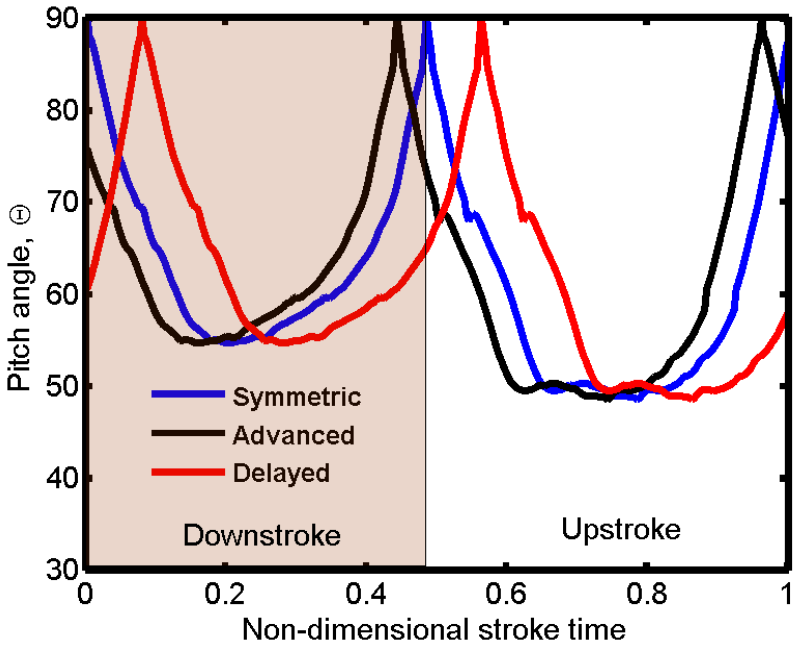

Figure 4.63: Classifications of different types of rotations

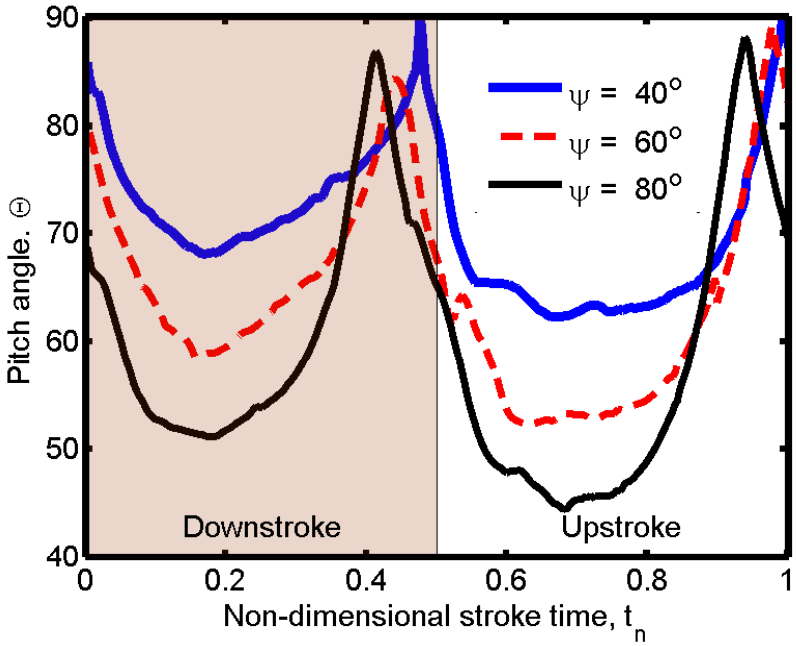

Figure 4.64: Pitching kinematics for different cases

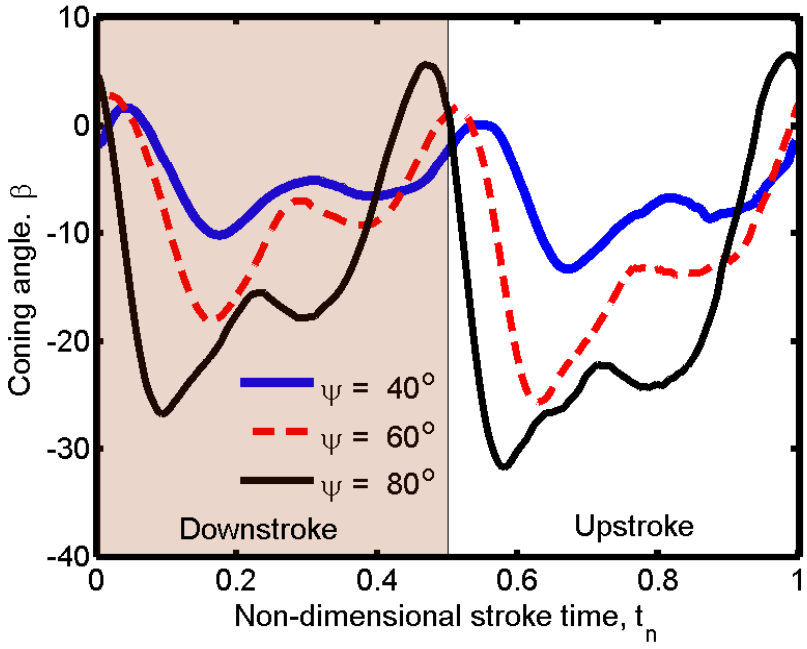

Figure 4.65: Coning kinematics for different cases

4.4.2 Aerodynamic Forces

Since the force transducer is connected to the wing root, it undergoes the same kinematics as the wing. In order to determine the lift and drag force from the wing normal and chordwise forces, coordinate transformations are required. Figure 4.66 shows the three distinct planes within the current kinematic framework.

Forces from the transducer are obtained in the blue plane known as the flapping, coned and pitched frame. Forces in this plane are transformed to those in the green plane known as the flapping and coned frame. This transformation is performed based on the pitch angle.

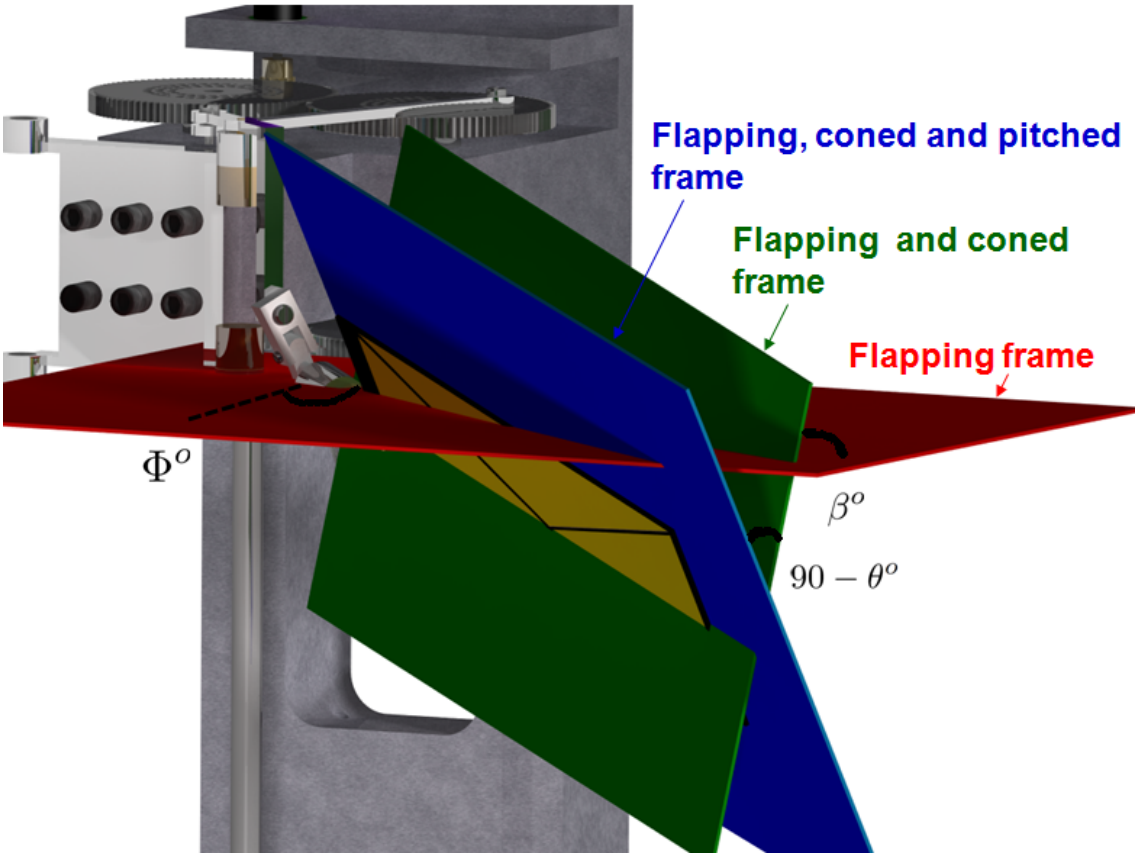

Figure 4.66: Definition of angles on flapping mechanism

$$\begin{bmatrix} L \\ D \\ S \end{bmatrix} = \begin{bmatrix} cos(\Theta) & sin(\Theta) & 0 \\ sin(\Theta) & -cos(\Theta) & 0 \\ 0 & 0 & 1 \end{bmatrix} \begin{bmatrix} F_{x_{TRANSDUCER}} \\ F_{y_{TRANSDUCER}} \\ F_{z_{TRANSDUCER}} \end{bmatrix} \tag{4.8}$$

where $F_{x_{TRANSDUCER}}$, $F_{y_{TRANSDUCER}}$ and $F_{z_{TRANSDUCER}}$ are the forces obtained from the force transducer at the wing root. Here the forces L, D, S are defined to be the lift, drag and spanwise forces. It is important to note that the flapping and coned frame moves the wing along the stroke and is not representative of the interial frame. While another coordinate transformation can be performed from the flapping and coned to the red flapping frame, this is not performed here. This is because, for our studies, we are interested in the forces in the flapping and coned frame because the velocity vector acts in this direction (see Figure 4.66). Figure 4.67 shows the varying direction of the lift and drag forces based on the direction of the incoming velocity with respect to the wing position. That is with respect to this frame, the lift acts perpendicular to the incoming velocity, the drag acts parallel and the spanwise force outward along the wing.

Lift variations for these kinematics flapping at 3 Hz are shown in Figures 4.68 to 4.70. These variations are denoted by the blue line. The red dashed line in the graphs labelled BET unsteady, is an analytical blade element theory based prediction of the lift. The values for the lift coefficients used here are taken from the Fourier series curve fit presented earlier for the pure translation data (see Figure 4.38). The velocity profiles and instantaneous wing pitch angles used are the same as the ones shown in Figure 4.63. Mathematically, from BET we have:

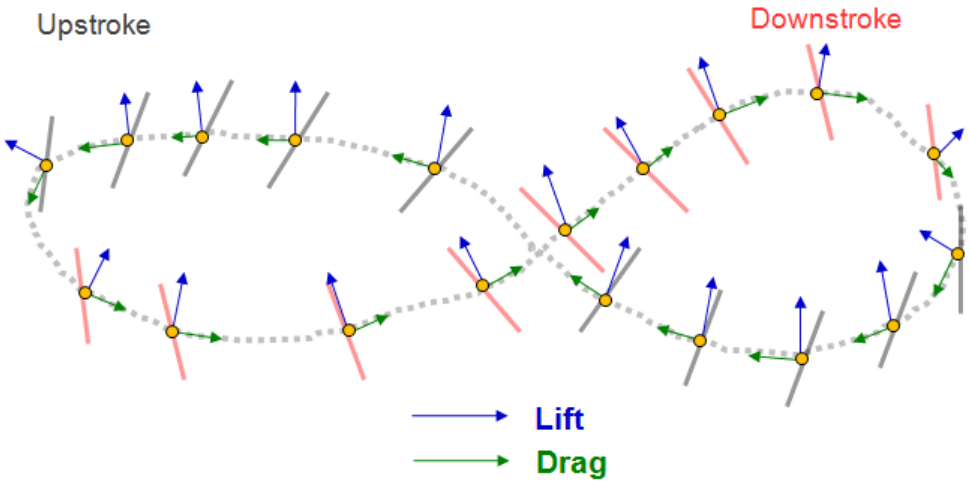

Figure 4.67: Definition of lift and drag vectors for flapping with varying pitch tests

$$L = \int_{r_o}^{r_f} \left(\frac{1}{2} \rho (\dot{\Phi}(r))^2 c(r) C_l(\alpha) \right) dy = \frac{1}{2} \rho \dot{\Phi}^2 \int_{r_o}^{r_f} \left(r^2 c(r) C_l(\alpha) \right) dy \tag{4.9}$$

where the integration limits r_o and r_f refer to the wing root and tip spatial locations. The lift coefficient function is defined as

$$C_l(\alpha^o) = 1.265 - 0.8477 cos(0.04533\alpha^o) + 2.144 sin(0.04533\alpha^o) \tag{4.10}$$

which is the Fourier series fit for the lift coefficient values for the flapping with fixed pitch tests. It should be noted that no inflow model is utilized here, thus the pitch angle is defined to be the angle of attack. The main impetus for presenting the BET based values here are to distinguish force peaks that arise from pure translation versus those that are a facet of rotational forces. Since BET does not incorporate any rotational kinematics, pitch rate terms and wake effects; it provides a baseline lift variation based entirely on the flapping kinematics. Thus by comparing the

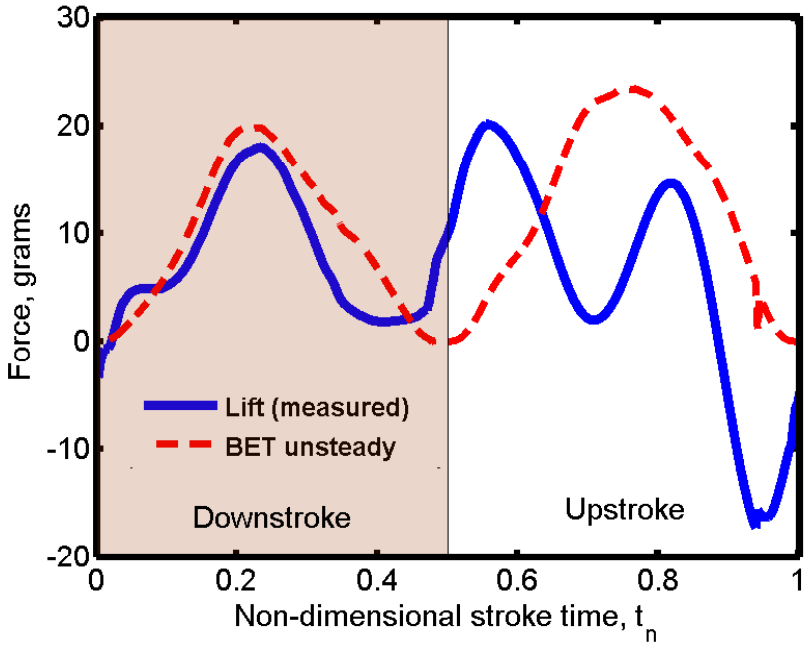

Figure 4.68: Lift variation for $\psi = 40^o$

measured lift values with those of the BET, inferences regarding these unsteady aerodynamic mechanisms can be made.

As can be seen for all force variations ($\psi = 40^0, 60^o$ and 80^o) BET predicts a maximum lift at approximately midstroke, with the lift attaining a value of zero at the end of each halfstroke. Interestingly, measured lift values, have three main peaks: two at the midstroke intervals and one at the end of each halfstroke. The force peaks due to translation occur at non-dimensional intervals from $t_n = 0.2$ to 0.4 and $t_n = 0.6$ to 0.8. At these periods, the lift generated from rotation is relatively lower than the unsteady BET values. This is expected as the lift coefficients from the pure translation tests are meant to serve as a upper limit on the translation force that can be generated. That is, in the flapping at fixed pitch tests, the flow has time over the entire stroke to stabilize. For the translation with rotation tests however,

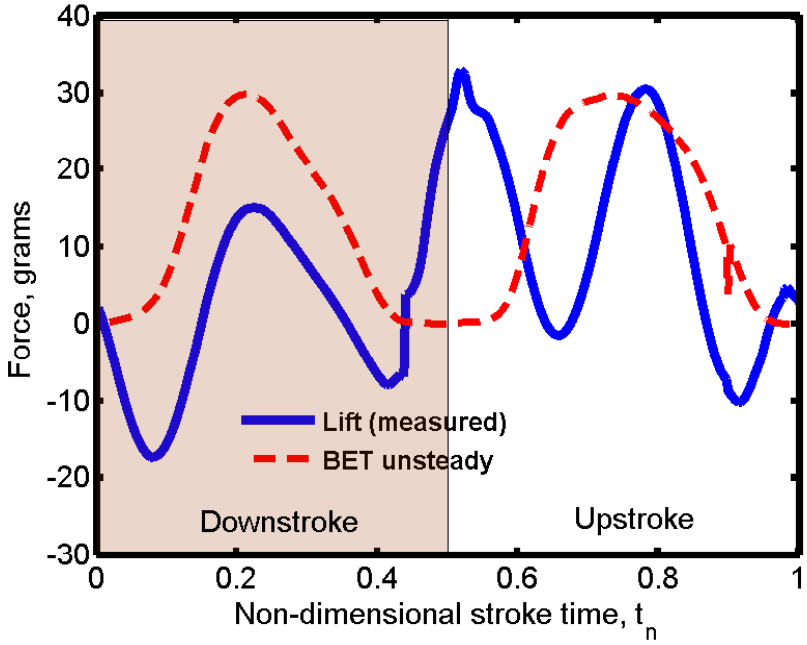

Figure 4.69: Lift variation for $\psi = 60^o$

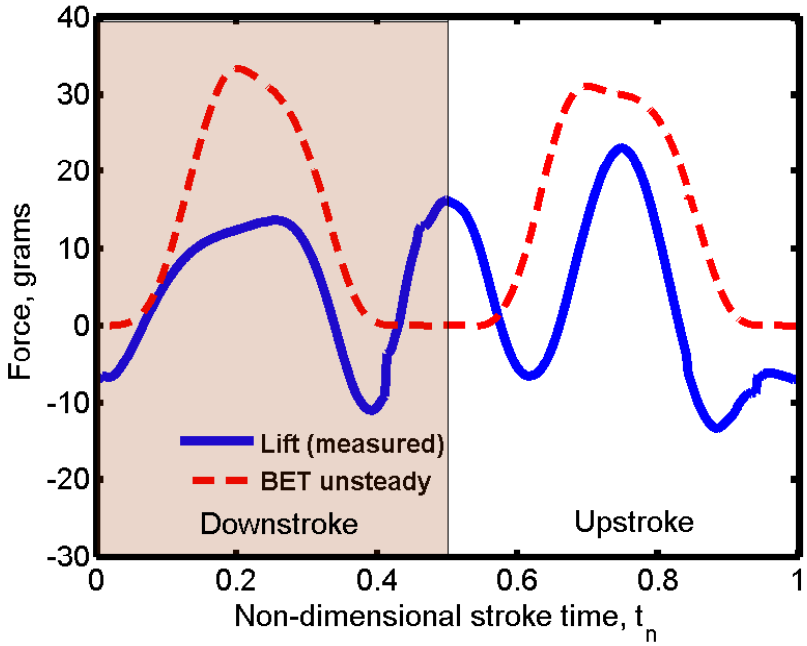

Figure 4.70: Lift variation for $\psi = 80^o$

the wing attains a certain pitch angle for only one instant during each halfstroke. Thus, the pitch rate is detrimental to the attainment of maximum possible lift at that particular pitch angle. For instance, in the downstrokes of the three position variations presented, the pitch rate is maximum for $\psi = 80^0$ and minimum for $\psi = 40^0$. Thus it is expected that that variation $\psi = 40^0$ will have the closest correlation with the BET lift values, and variation $\psi = 80^0$ will have the poorest matching.

As mentioned earlier, an additional third lift peak is present in the test data that is not captured in the BET prediction. The third peak that is seen to occur at a non-dimensional stroke time of roughly $t_n = 0.50$ to 0.55 for all the translation with rotation cases. In their work, Dickinson et. all showed that advanced rotation manifests itself as a positive lift peak at the end of each half stroke [9]. While there are significant differences in the kinematics between the present experiment and Dickinson's work, the underlying definition of advanced rotation is still valid. Figures 4.68 to 4.70 clearly illustrate that at the end of each halfstroke the lift peak is positive for the advanced rotation cases. In other words, even though the velocity of the wing at the end of the halfstroke is zero, the wing is still producing positive lift. Insects are known to utilize this unsteady aerodynamic phenomenon to generate a burst of lift towards the end of their strokes.

With respect to the experiments conducted in this study it is difficult to classify the exact nature of the observed rotational peak; which may be attributed to either wake capture, rotational circulation or both. The complex flow environment and nature of the lift variations makes it difficult to verify. However what can be said

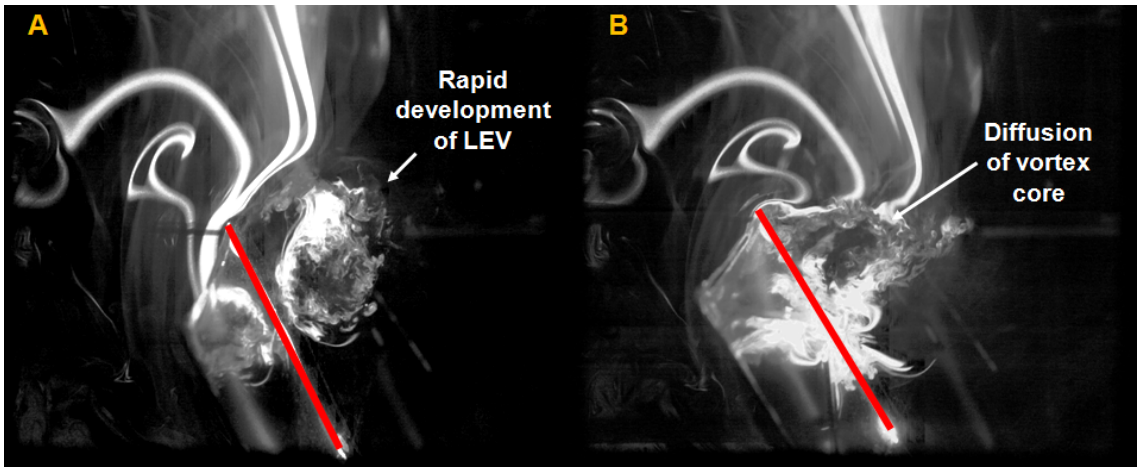

Figure 4.71: Flow visualization for Variation 6 at midstroke for downstroke flapping

is that there is a significant generation of force that is produced during rotation, that is comparable in magnitude to those produced for the during translation for the three cases.

4.4.3 Flow Visualization

In this section, flow visualization tests for the flapping with varying pitch will be discussed. Tests were conducted only on $\psi = 60^0$ at midstroke, at 3 Hz with the laser illuminating the midspan location. Representative results are shown in Figures 4.71 to 4.72.

As shown in Figure 4.71, as the wing approaches its midstroke location, there is a rapid development of a leading edge vortex (A), that diffuses in less than a chord length of travel (B). In Figure 4.72, a second LEV forms on the wing extending over the entire chord, even while the earlier vortex has still not completely shed from the wing surface (C). Finally as the wing starts to move out of the frame of the

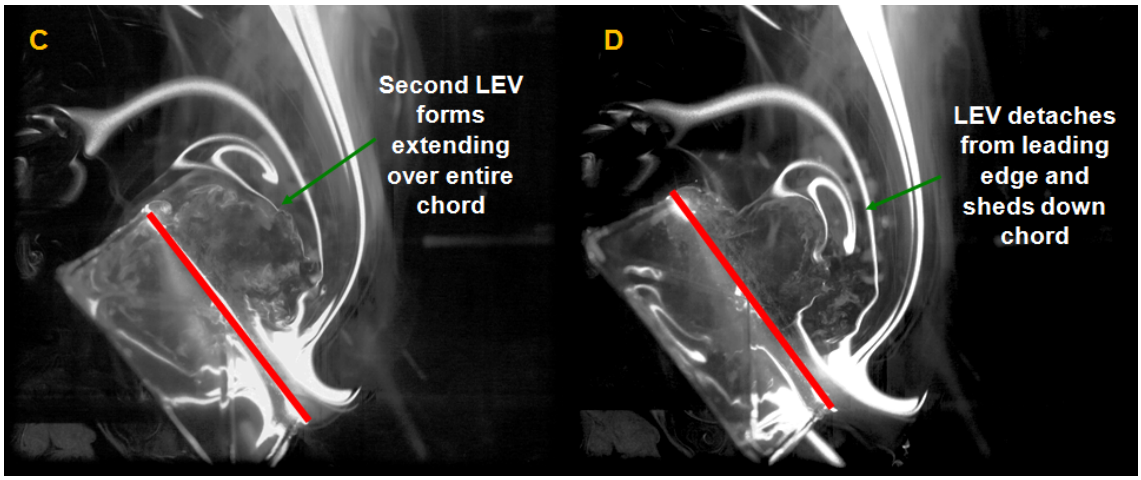

Figure 4.72: Flow visualization for Variation 6 at post midstroke for downstroke flapping

camera, the LEV detaches from the leading edge and sheds down the chord (D). A key observation for both the upstroke and downstroke motions was the rapid growth and shedding of the LEV, which was much quicker than the LEV behavior seen in the flapping with fixed pitch cases.

It is hypothesized that the pitch rate here played an important role in the rapid shedding of the leading edge vortex. In other words before the LEV could fully develop, it was forced to be separated from the leading edge due to the heightened pressure gradient induced by the rapid change in pitch. This might also explain why the overall lift generated by the 3-D flapping with dynamically varying pitch cases is lower than the 1-D flapping with fixed pitch. That is, the LEV does not get enough time to build up and is much more prone to separation and diffusion due to the pitch rate.

4.5 Conclusions

This chapter has focused on exploring the fundamental aerodynamics of a variety of flapping wing kinematics in an effort to understand the unsteady flow mechanisms insects adopt. The approach has been to dissect insect-based flapping flight at MAV-scale Reynolds numbers through three broad set of experiments. The experiments were static wind tunnel tests, single degree of freedom flapping (fixed pitch) and triple degree of freedom flapping (dynamically varying pitch and coning). The primary source of data has been from a six degree of freedom force transducer located at the wing root. Data from the transducer was substantiated with extensive flow visualization tests and a brief PIV study. The following are the main conclusions of this work.

1. A unique approach of determining pure aerodynamic forces while flapping at MAV scale Reynolds numbers was presented. For this purpose, a test rig was designed with a six DOF force transducer that used the same dual-differential four-bar mechanism discussed in Chapter 2. Wing testing was performed both in air and in vacuum while maintaining the same kinematics. A set of shaft encoders were utilized to make sure that the wing was at the same azimuthal location in both tests. Forces from the vacuum chamber tests were subtracted from those in the air tests using a synchronization procedure to yield the pure aerodynamic forces.

2. Single DOF flapping tests were conducted for pitch angles ranging from 7^o to 90^o and revealed extremely high lift and drag coefficients ranging from 1

to 4. Wind tunnel tests conducted at the same Reynolds numbers, using the same wing, showed that for the same pitch angles (tested in flapping), the aerodynamic coefficients were up to six times lower. This showed the extensive contribution of unsteady aerodynamic forces in simple single DOF flapping. It was hypothesized that this tremendous increase in lift and drag coefficients was due a strong LEV.

3. Flow visualization studies showed large LEVs being developed as the wing flapping through the midstroke. For higher pitch angles, these LEVs encompassed the entire chord of the wing. Other unique flow structures such as Von Karman streets were also observed towards the trailing edge, but only at lower pitch angles. It is conjectured that the LEVs were not stable, and periodically convected and shed as the wing completed a halfstroke. The convected LEVs were then replaced by secondary LEVs. It is believed that this cycle of vortex development, convection and shedding was responsible for the higher harmonic fluctuations observed in the lift and drag force coefficients over the stroke.

4. A 2-D PIV study was conducted for the wing flapping at a fixed pitch of 65^o at the midstroke, midspan location. A circulation box approach revealed a sectional lift coefficient of (c_l) 2.803 based on the bound circulation on the wing. The large LEV was the major flow structure contribution to this high value.

5. Power results from the single DOF flapping tests showed a relatively low lift

to power ratio for higher pitch angles. It is believed that this is because of the high induced and pressure drag at these angles. These results are significant as they truly quantify the aerodynamic inefficiency of pure flapping motions.

6. Three cases of 3 DOF flapping (dynamically varying pitch and coning) were explored. Lift measurements showed three force peaks over an entire stroke. A blade element theory model was formulated using the a table look up based on the mean values of the lift coefficient obtain from the single DOF flapping (fixed pitch) tests. While the model was able to account for two of the force peaks during translation, it did not predict the third one. This third peak was attributed to the unsteady effects of rotational circulation and wake capture.

7. The BET model also revealed that the two force peaks captured predicted higher values of lift than the actual experimental values. It was hypothesized that this discrepancy was due to the premature shedding of the LEV due to the increased pitch rate (compared to the single DOF tests). Flow visualization on a 3 DOF flapping case confirmed this hypothesis.

Chapter 5

Vehicle Design and Development

5.1 Overview

The present study culminates in an effort to develop a 120 gram hover-capable flapping wing micro air vehicle (MAV), which could be stabilized and controlled using the modulation of wing kinematics. While most studies aim to either to explore the aerodynamics using bulky complex setups or develop a light-weight micro air vehicle system, the main goal of this research has been to carry out both. In other words, bridge the divide between the experimental setup and the MAV, so both can be designed in a synergistic manner. More importantly, results from the experimental study can be applied to improve and understand the MAV approach. The flapping actuation system utilized in this chapter is conceptually identical to the one described in Chapter 2 and implemented in Chapters 3 and 4. In this chapter, the same mechanism is integrated into on a light-weight body. The wings used to propel the vehicle are the ones designed, fabricated and tested in Chapter 3. The optimized wing kinematics discussed earlier are used here.

Even though many researchers have attempted to build hover-capable flapping wing MAVs, only three of them are capable of untethered hover, most notably Mentor (SRI/ Toronto) and the Nano Scout (Aerovironment) [16], [36]. The first two vehicles fall in the same category as they rely on vane-type surfaces for control.

However, the Nano Scout flies similar to a true humming bird by using purely wing kinematics modulation for hover stability and control. The main disadvantage of the Mentor and Delfly is that they use four wings with fixed kinematics (no wing kinematics modulation) and incorporate vanes in the wing wake for stability and control. This may be one of the most practical and easy approaches to build a stable flapping-wing MAV. Insects and humming birds on the other hand are capable of performing remarkable aerial maneuvers primarily due to the large control forces and moments that they can generate by modulating their wing kinematics. Eliminating this capability from the design can severely impede the maneuvering ability of the vehicle.

This chapter seeks to bring to light the challenges involved in the mechanical design of a flapping wing MAV. Unsuccessful iterations and failed mechanisms will be touched upon in order to give the reader a sense why a certain configuration was selected. The main focus of this chapter is however the development of a control strategy for an insect-based flapping wing MAV using very similar control methodologies that insects and hummingbirds utilize. This is also the significant difference between the present approach and other similar studies.

5.2 Vehicle Iterations

The first generation fabricated MAV is shown in Figure 1. The mechanism is simply a light-weight version of the bench-top setup presented in Chapter 3. The MAV weighed 93 grams without the batteries. To keep the weight as low as pos-

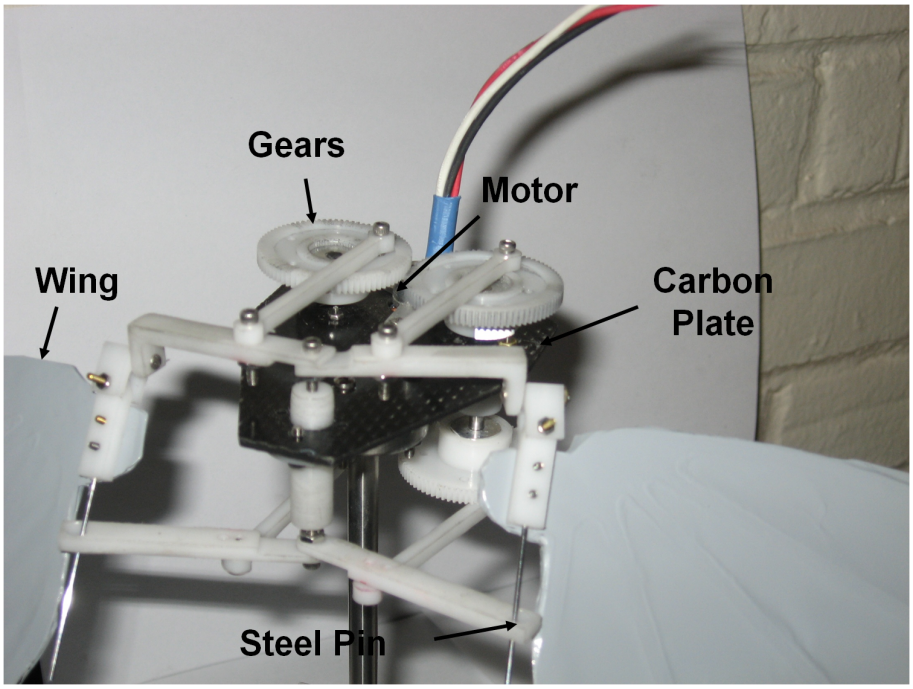

Figure 5.1: First generation hover capable FMAV concept

sible, most of the parts were fabricated out of Delrin and carbon fiber composite. The flapping mechanism for the MAV was constructed using the optimized parameters obtained from the experimental study described in Chapter 3. The Motor used for this MAV was an AXI Gold 2204 outrunner brushless motor (weighing 25 grams), with a maximum input power rating of 75 W. It was attached to the carbon base-plate, along with the flywheel setup. The two wings were flapped using two independent sets of four-bar mechanisms, each having a set of two flywheels. However, both the four-bar mechanisms were driven by the same motor. The advantage of having two flywheels sets is that the wings can flap in phase with each other. The disadvantage of such a model is the weight due to two additional flywheels.

Upon testing, numerous problems and issues with mechanism came to light. Since all the oscillatory loads were finally transferred to just one carbon base-plate,

excessive vibrations of the plate were observed. These vibrations caused numerous mechanical problems such as the flywheel gears and the motor gears were moving vertically relative to each other causing the gears to wear off. For the wings that were tested on this MAV, it was noticed that the power output of the motor was not sufficient to generate the 100 grams of lift required. In other words before the MAV could produce enough thrust to lift itself off, the motor would stall. The main reason for this may be the fact that these wings were too heavy and the small motor was inadequate to provide the power at high frequencies. All these problems prevented the flapper from reaching its desired frequency of 12 Hz. The previous bench-top setups did not come across power or vibration issues because it was built sturdy (no weight constraint) and used a powerful motor. Doubtlessly, one has to face these issues while moving from a bench-top test setup to a light-weight flight capable version and these issues become extremely challenging to resolve with large oscillatory loads as in the case of flapping wings. Given these inherent problems, it was thought best to start with a new design. Details of this new design are presented below (Figure 2).

In the new flapping wing MAV, the two sets of flywheels were replaced by just one consisting of two sets of four bar mechanisms to reduce the weight. This introduces a phase difference between the two wings and thereby affects the instantaneous forces produced by the MAV. However, this is not an issue for a tethered hovering MAV (where all the degrees of freedom, except the vertical degree of freedom are constrained), which was the intent of this investigation. In the present version, two carbon base plates were used. Each of them had half the thickness of

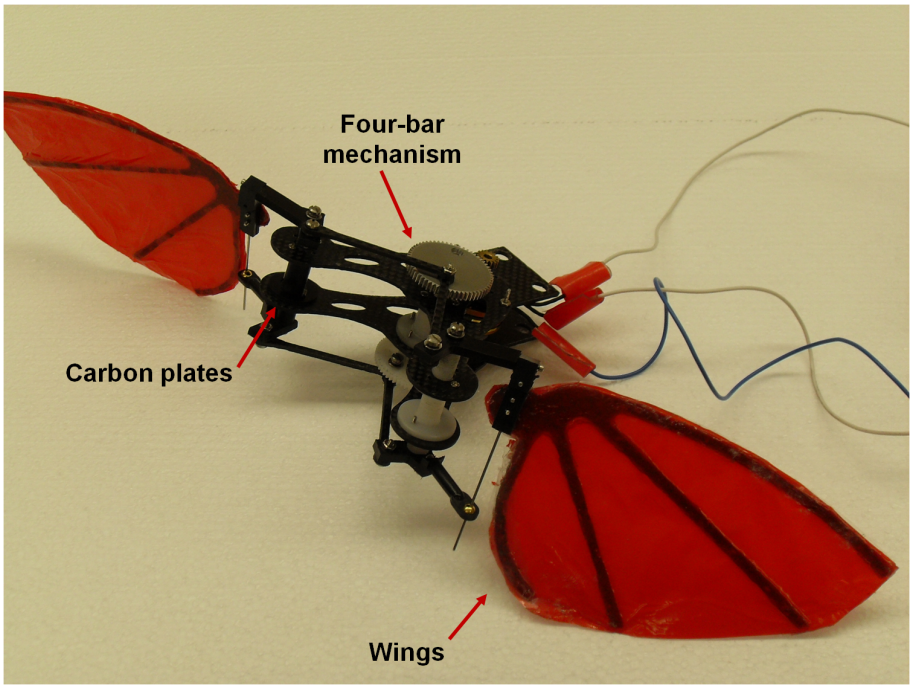

Figure 5.2: Second generation hover-capable FMAV

the previous one, (to keep the weight same), but were separated by a distance to improve the overall structural stiffness and thereby reduce vibrations.

At high frequencies, inertial forces coupled with aeroelastic forces caused the wings to bend, and thereby amplify their flapping amplitude. Therefore, the four-bar mechanisms had to be appropriately placed so that both the wings do not interfere with each other or with any part of the mechanism during their flapping cycle. Another modification that was introduced into the older MAV version was with regard to the steel pin which was cantilevered on one end and free on the other. The wing was attached to this. At high frequencies, it was found that the pin had too much play and there was an asymmetry between consecutive downstroke and upstroke motions. In order to reduce this problem, a rod-end bearing was utilized in the present MAV, as is shown in Figure 5.2. Furthermore the AXI Motor was

replaced with a Welgard C28/26/12 motor rated for 140 Watts.

Due to weight constraints as well as problems with excessive vibration, this second generation design was not ideal. The introduction of two carbon plates in the second generation compared to one in the first did not yield the desired advantages. There was also the associated weight penalty of the delrin columns that were utilized in clamping the two carbon plates together. Additionally the new motor was heavier compared to the one utilized on the second generation MAV. A third generation flapping wing MAV was designed subsequently, and its details are presented below.

5.3 Third Generation MAV

Figure 5.3 shows the third generation flapping wing MAV. The vehicle body was manufactured using a rapid prototyping technique as it permitted overall design flexibility in terms of the size and placement of on-board components. The wings along with a corresponding four bar mechanism were attached to the body. The total electrical power consumed by two wings at 12 Hz was measured to be around 57 Watts. Therefore, a 75 Watts outrunner motor weighing 25 grams was used to drive the flapping mechanism (see Figure 5.3). A gear ratio of 7:1 was used so that the motor operates at the peak efficiency rpm. The mass of the entire vehicle with all the components was 56 grams. The MAV was then tethered between two vertical steel guide-rods as shown in Figure 5.4. Upon flapping at about 10 Hz, tethered hover was achieved.

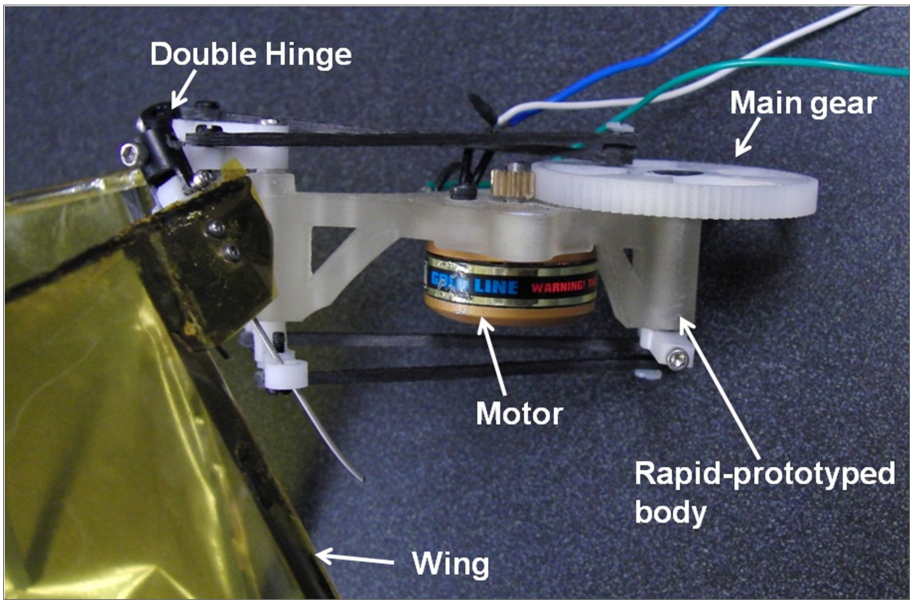

Figure 5.3: First generation hover capable FMAV concept

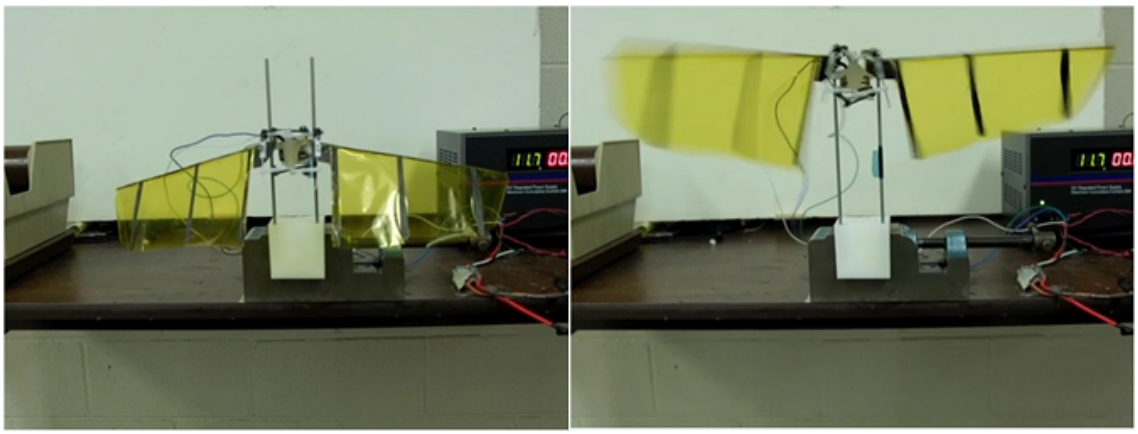

Figure 5.4: Third generation flapper achieving tethered hover

This demonstrated the flight worthiness of this flapping concept, even though the MAV weighed only 56 grams as it did not have control mechanisms and the battery pack. However, since the wings produced a total lift of almost 110 grams, there was still a 54 gram weight allowance for batteries and the required actuators/electronics for control.

5.4 Control Mechanism Design

Numerous control methodologies were thought of, designed and then implemented on a complete vehicle concept. Figures 5.5 to 5.7 illustrate the design of these concepts. Each of these mechanisms was designed using the same four bar-based mechanism in the tethered vehicle, however the control strategy implemented was different. All these designs were unsuccessful in being able to generate the required control actuation. However as can be seen from the iterations, the mechanisms developed were much more simple, and went from a direct wing actuation, to an indirect four-bar linkage variation.

The final mechanism is presented in Figure 5.8. The basic operating principle of the present control mechanism is to generate the pitch, roll, and yaw moments by being able to independently tilt the flapping plane of each wing longitudinally and laterally and also move the mean flapping area fore and aft.

As shown in Figures 5.8 to 5.10, the key component of the control mechanism is a steel rod (control rod) which forms the flapping hinge for the wing. Tilting the control rod would therefore tilt the flapping hinge, which in turn tilts the flapping

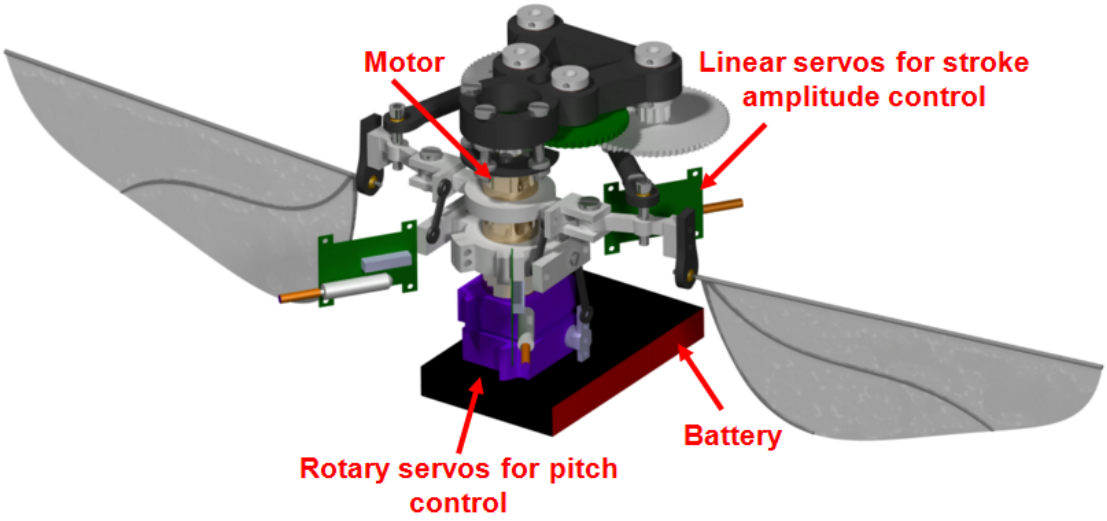

Figure 5.5: First generation controlled mechanism design

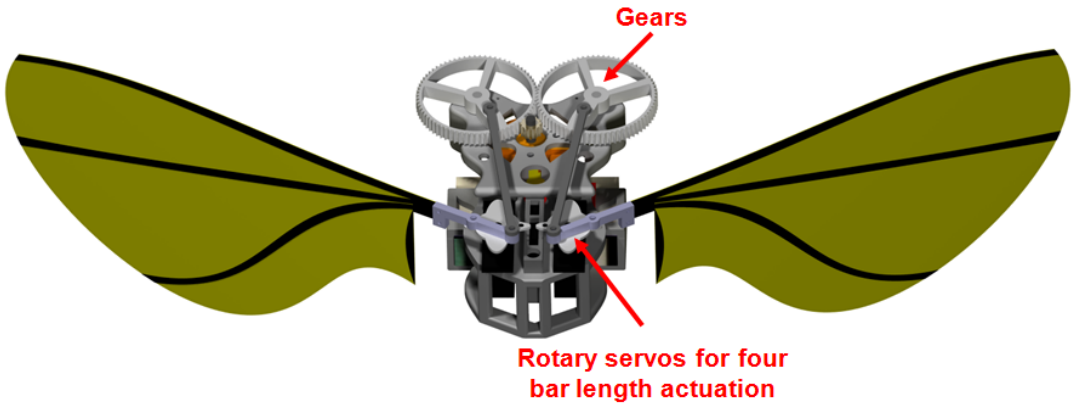

Figure 5.6: Second generation controlled mechanism design

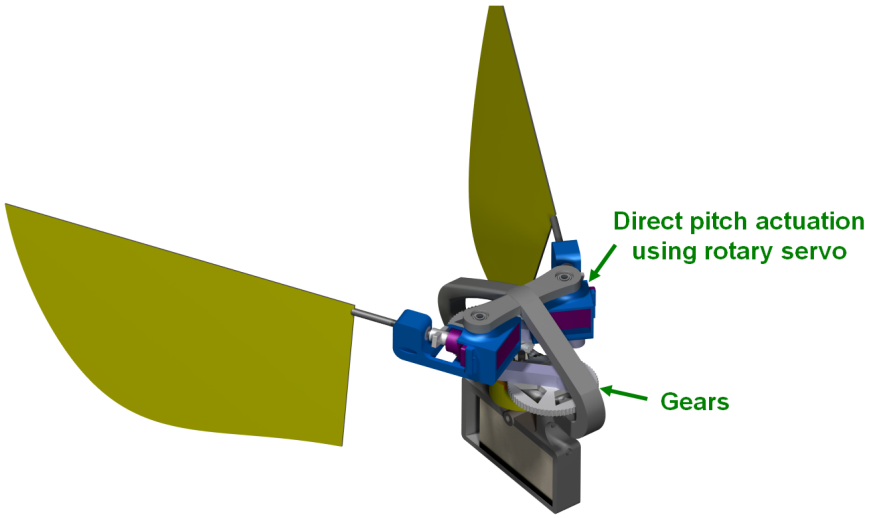

Figure 5.7: Third generation controlled mechanism design

plane. Now, depending on the direction in which the rod is tilted, the flapping plane could be either tilted longitudinally or laterally. Tilting the rod also changes one of the linkage lengths of the four-bar mechanism which would shift the mean flapping area forward and backward. The tilting of the flapping plane in three-dimensions would require the capability to independently tilt the control rod in two mutually perpendicular directions. This is performed using two rotary actuators (servos) placed below the wing and mutually orthogonal with respect to each other (Figures 5.9 and 5.10). As shown in Figure 5.9, the control rod is gripped by the two servo arms, where the rod passes through a slot in the servo arm so that servos can independently tilt the rod without constraining each others motion. To facilitate tilting, the control rod is placed through a ball link at the top. Also, a change in the angle subtended by the rod, will lead to an out of plane motion, making the four bar mechanism no longer planar. In order to permit this extra degree of freedom,

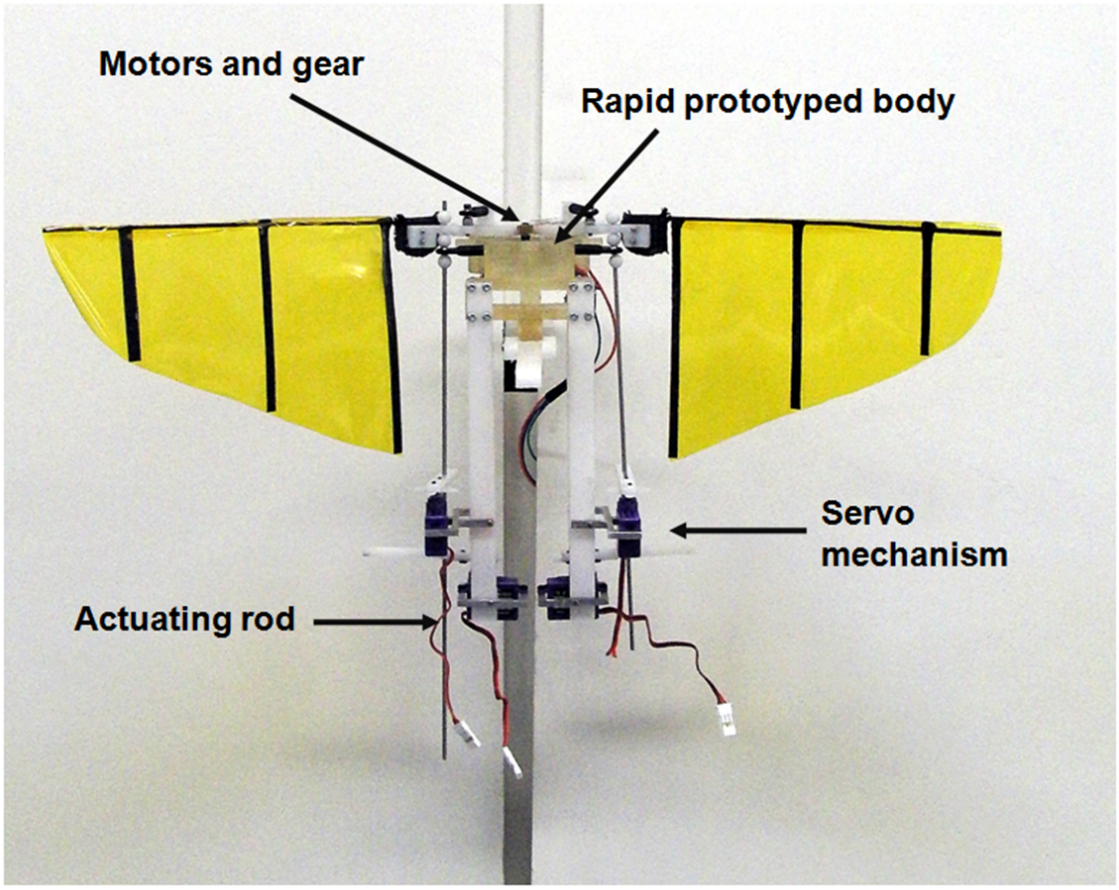

Figure 5.8: Final flapping wing mechanism with actuation

two of the linkages used rod end bearings instead of planar radial bearings.

5.5 Control Strategy

To obtain a qualitative understanding of the extent and effect of the collective and individual actuation of the four servos, a model of the mechanism was developed as shown in Figure 5.11. In this model, the control rod is constrained at five different points. The location of these points is not arbitrary, but dictated by the permissible control rod motions. The point that corresponds to the center of this mapping is

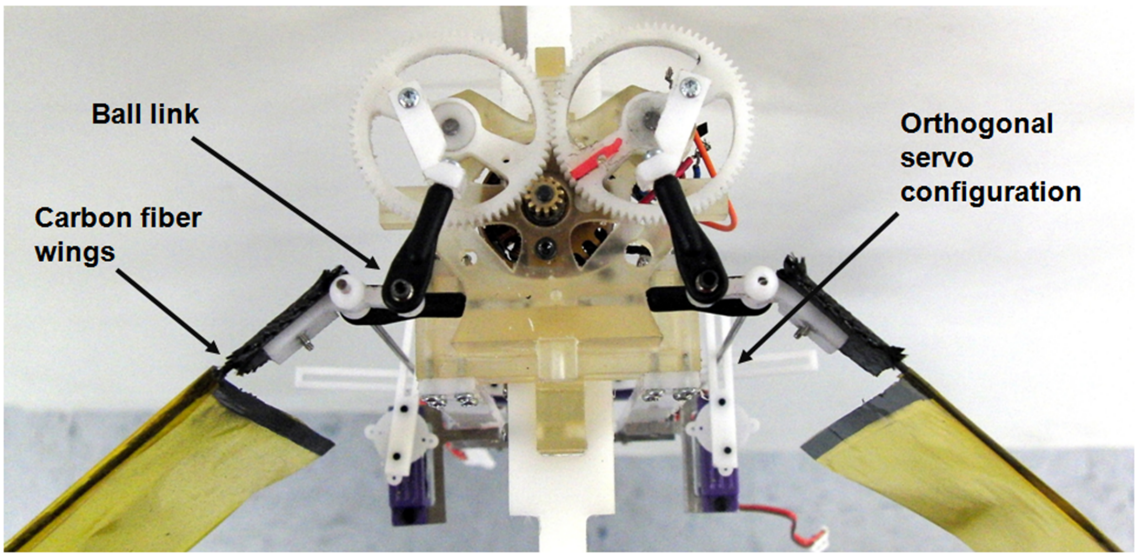

Figure 5.9: Top view of controlled mechanism

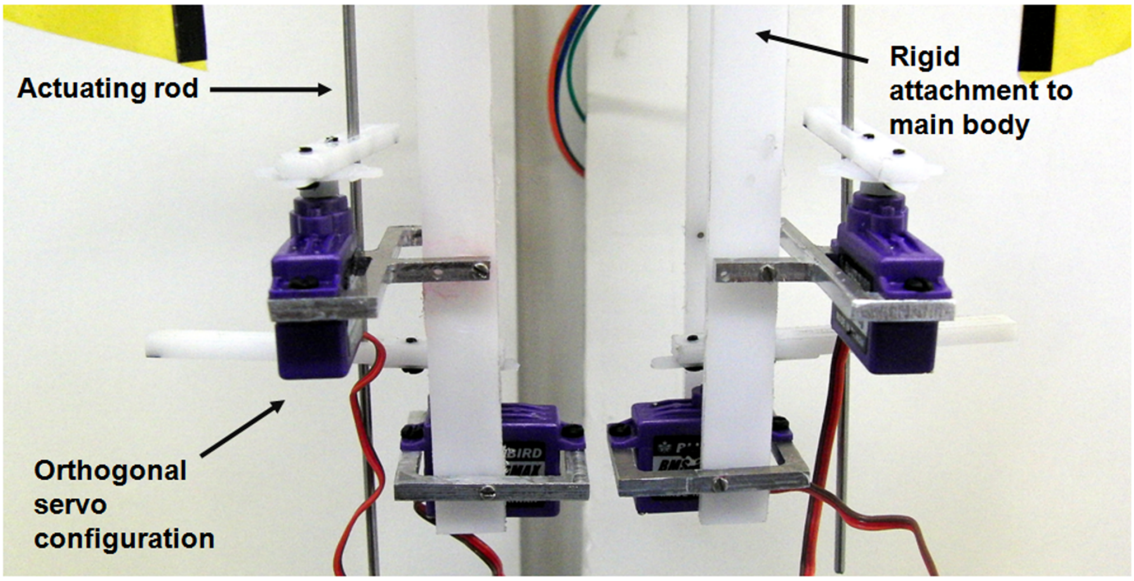

Figure 5.10: Close up of actuators

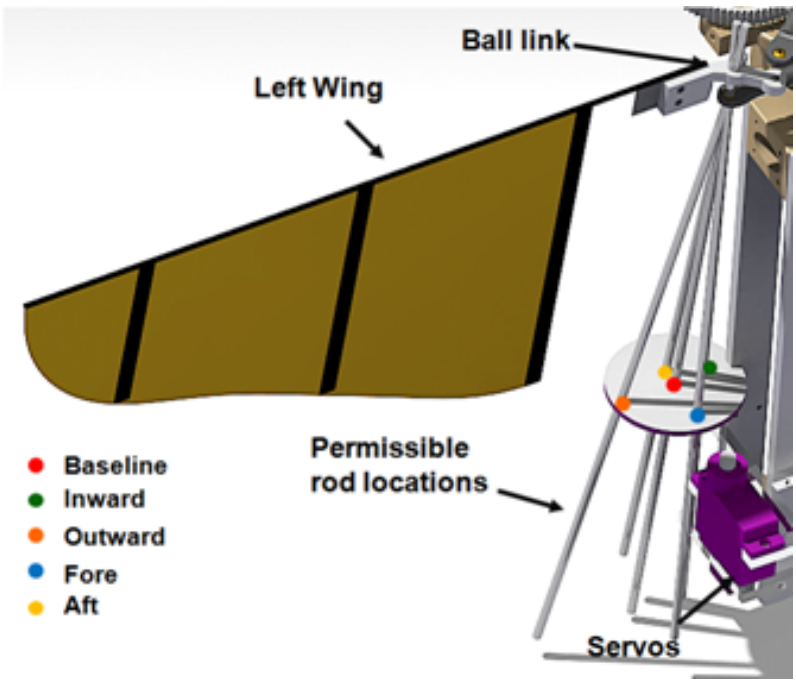

Figure 5.11: Kinematic model with permissible rod locations

referred to as the baseline case. From here the rod can be moved inwards, outwards, forwards or aft. This motion induces three effects on the mechanism, namely:

- Fore and aft shift of mean flapping area
- Longitudinal tilt of the flapping plane
- Lateral tilt of the flapping plane

These variations in the wing kinematics are inherently coupled. For instance, moving the control rod forward tends to push the mean flapping area backwards and tilt the flapping plane longitudinally backward. Similarly moving it backwards shifts the mean flapping area towards the front and tilts the flapping plane longitudinally upward. Exploiting the sensitivity of the position and angle subtended by the control rod, for small perturbations, large aerodynamic moments can be generated. Since

we have the ability to vary the wing kinematics in both a symmetric and differential manner, we developed a rudimentary outline for generating attitude stability in the form of pitch, roll and yaw control moments. The definition of these moments and their corresponding axes are shown in Figure 5.12 (A) and (B).

Pitch Control: The pitch can be modulated by varying the location of the mean flapping area (see Figure 5.12) which in turn moves the net center of lift. As shown in Figure 5.12 (C-D), when the mean is shifted backwards, the center of lift also moves closer to the rear of the vehicle thereby generating a nose-down pitching moment. Likewise when the mean is shifted forwards, the corresponding movement of the center of lift will yield a nose-up pitching moment. In our mechanism this shift in the mean flapping area is achieved by moving the control rod longitudinally (fore and aft motions). This will also induce a tilt in the flapping plane that varies the moment generated by the mean shift. This coupling effect will be explained in detail in the upcoming section.

Roll Control: A roll moment is induced by differential lateral tilting of the flapping planes. Figure 5.13 illustrates this effect. Figure 5.13(A) shows the baseline case along with the corresponding roll, pitch and yaw axes. In 5.13 (B), through the actuation of the rod, the flapping plane on the right side tilts laterally upwards, thereby inducing a counter clockwise rolling moment. In 5.13(C) the rolling moment is clockwise as the flapping plane on the left hand side as it is tilted laterally rightwards.

Yaw Control: The mechanism should be able to generate yaw moments by differentially tilting the flapping plane. As shown in Figure 5.14, a yaw moment is

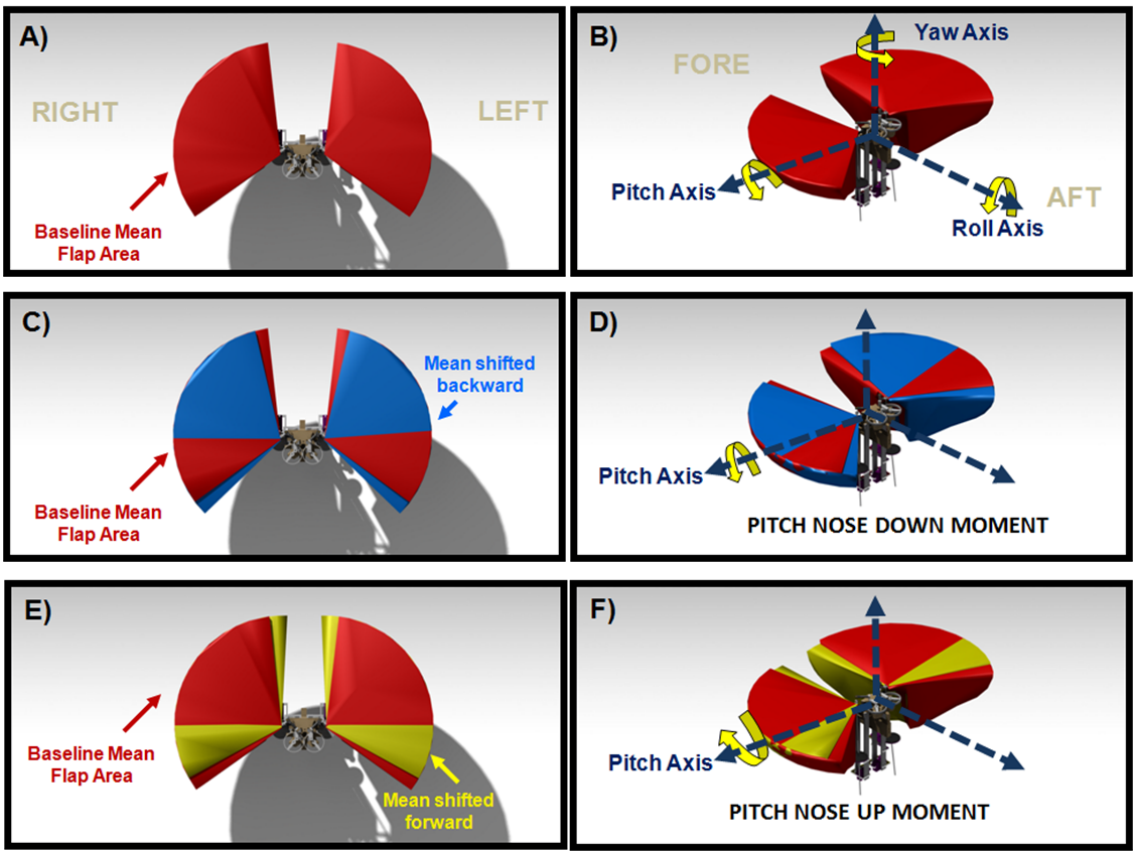

Figure 5.12: Simulated pitching kinematics for flapping wing mechanism

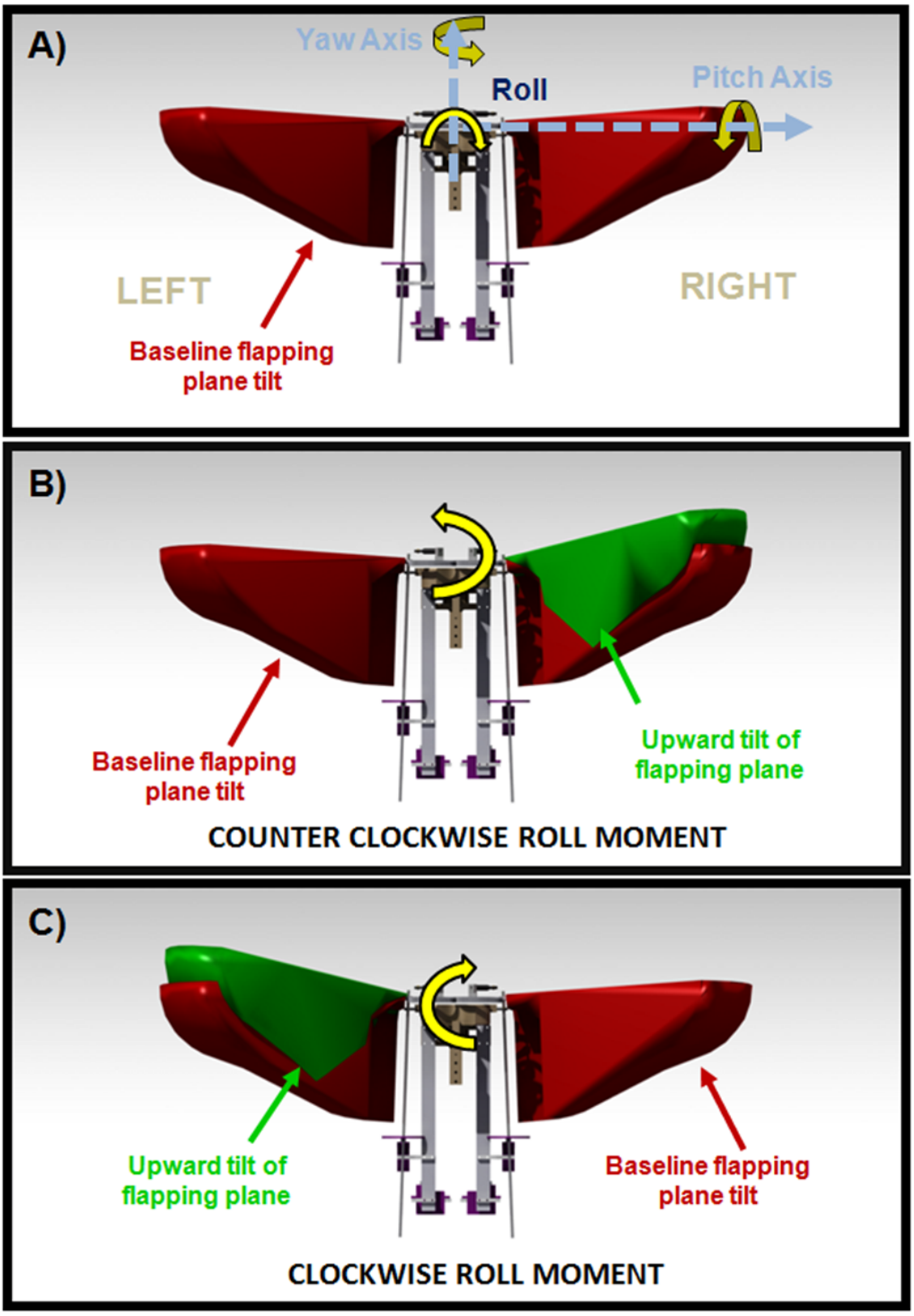

Figure 5.13: Simulated roll kinematics for flapping wing mechanism

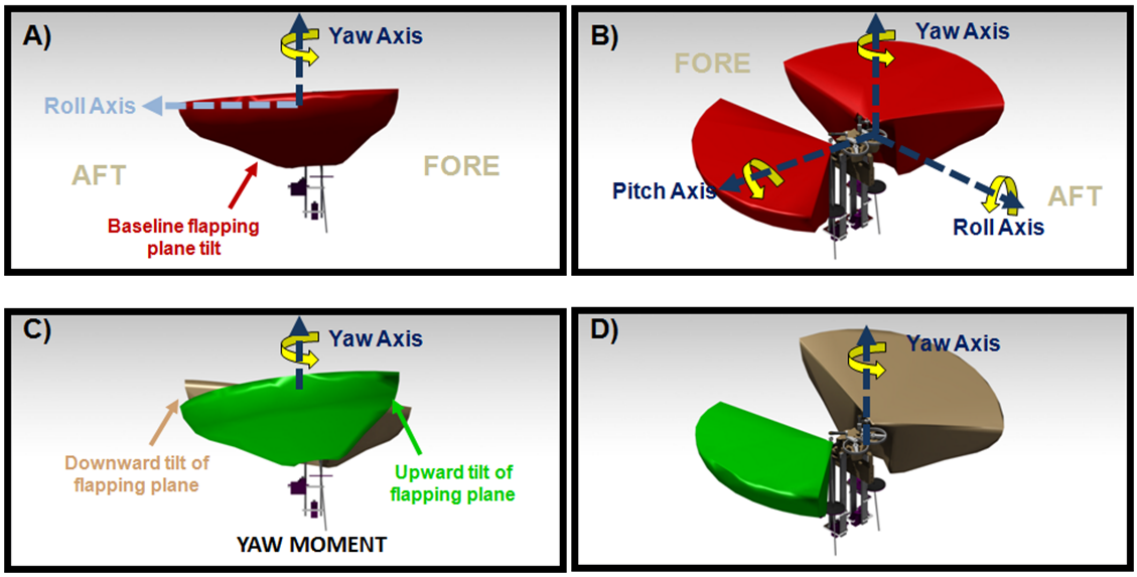

Figure 5.14: Simulated yaw kinematics for flapping wing mechanism

generated when the flapping plane of one wing is tilted fore and the other wing is tilted aft. The details of the wing kinematics of the actual test setup for different control rod motions will be illustrated in the next section using a motion tracking system.

5.6 Motion Capture Tests

Having demonstrated the capability of the present control strategy to generate sufficient pitch, roll, and yaw moments, it is important to obtain a quantitative understanding of how the control rod motion affects the wing kinematics. A VICON® motion tracking system was employed to capture the control rod dynamics and the resulting wing kinematics on the present setup. Ten reflective markers were placed on each wing, three on each rib and one at the wing tip along with three additional reflective markers on each control rod (Figure 5.15). This would verify whether the

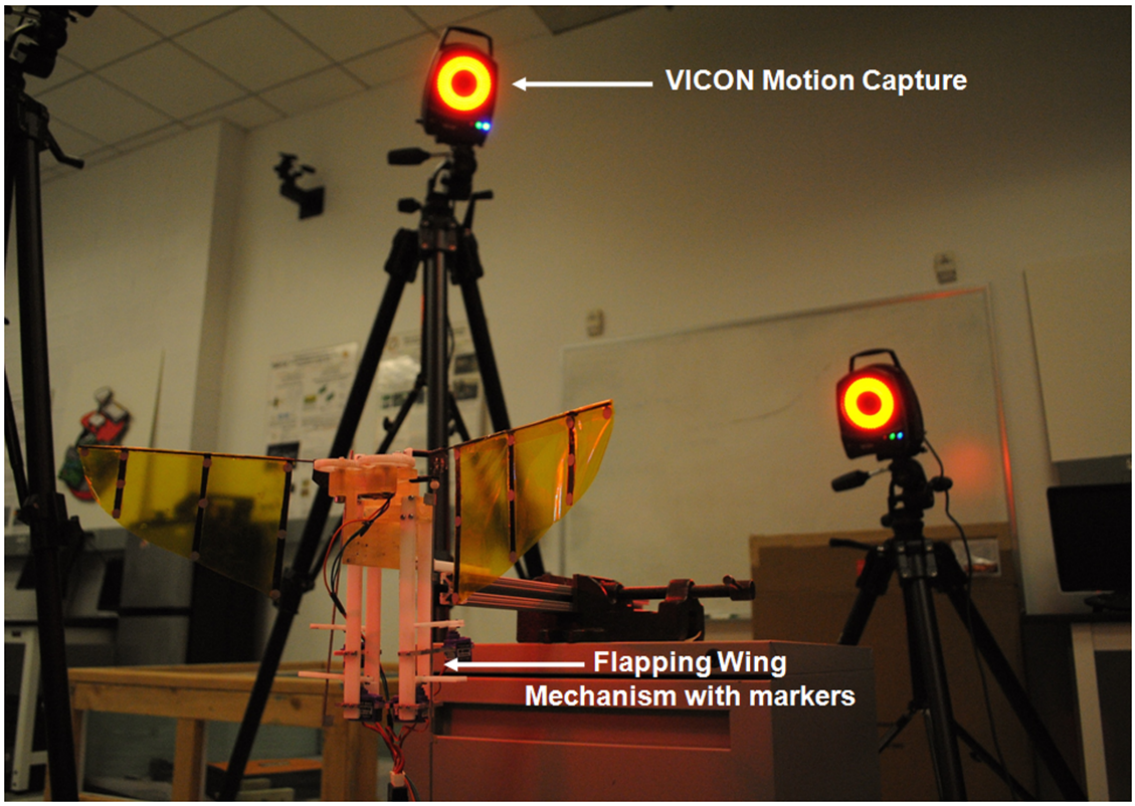

Figure 5.15: Controlled mechanism undergoing motion tracking experiments

behavior of actual control mechanism is similar to the one predicted by the kinematic analysis in the previous section (Figs. 5.12-5.14). The same control inputs used to generate pitch, roll and yaw moments in the single axis tests were used for the VICON® tests. The mechanism was rigidly clamped in order to prevent any associated body dynamics. The VICON® system data collection rate was set at 700 Hz. A third order Butterworth filter with a 12 Hz cut-off frequency was applied to the data in order to eliminate 2/flap and higher wing deformations, as we are interested only in the rigid kinematics. Tests were conducted for each case (pitch, roll, and yaw) with multiple actuation cycles.

Figure 5.16 shows the global coordinate system of the wing kinematics for

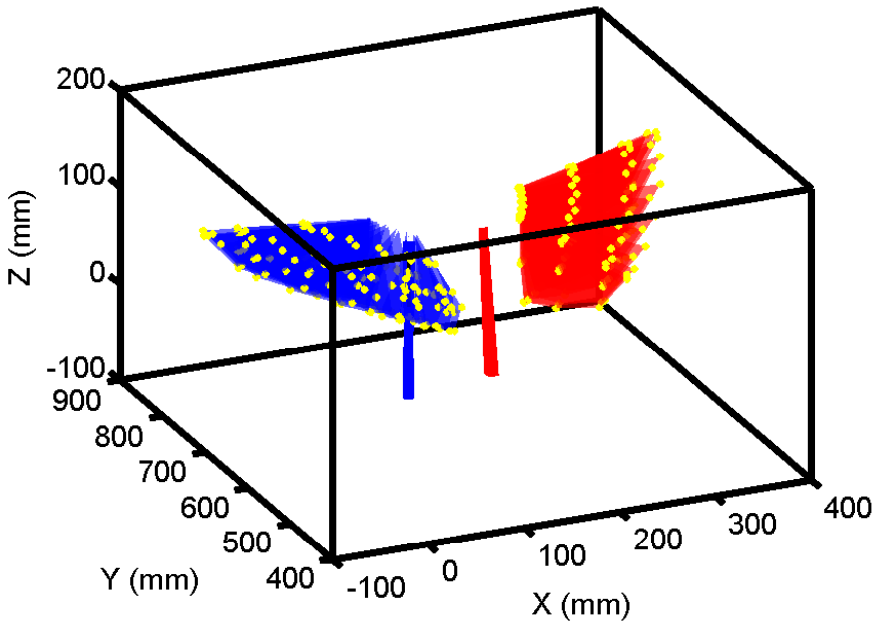

Figure 5.16: Global coordinate system for motion capture tests

one flap cycle. The left wing and its corresponding actuation rod is blue and the right wing and its rod is red. The yellow dots on the wings denote the position of the actual markers in VICON. The wing is re-constructed using the markers and a triangulation algorithm.

Pitch: The rod dynamics for the pitch test are shown in Figure 5.17. The mean displacements of the bottom marker of both rods in all three directions are plotted. For this particular test, the servos were actuated through five cycles over a period of eight seconds. Here an actuation cycle refers to the movement of the marker on the rods from the baseline position at zero to its peak displacement (either positive or negative) and back to zero. From the graph, we note that maximum displacement for pitch actuation on both rods occurs along the Y-axis. In other words, to generate the pitching moments, the rod moves fore and aft longitudinally. Also, it can be seen

that both the rods are actuated in phase for pitching. The resulting wing kinematics are plotted in Figures 5.18 to 5.21. Figures 5.18 and 5.19, respectively, show the side view and top view of the wing kinematics for producing a nose up pitching moment. The wing kinematics corresponds to the control rod position at 3 seconds in Figure 5.17. A nose-up pitching moment would be induced because the mean flapping area is shifted forward as shown in Figure 5.19. However, the forward shift in flapping area is produced when the control rod is tilted aft, which would produce a forward tilt of the flapping plane (Figure 5.19) thus producing a small nose-down pitching moment. This effectively tilts the resultant lift vector forwards. While these two moments act effectively against each other, the dominant moment is the nose-up moment caused by the mean shift in the flapping area. Similarly, Figures 5.20 and 5.21 show the wing kinematics for inducing a nose down pitching moment because in this case, the mean flapping area is shifted backward (Figure. 20) and the flapping plane is tilted forward (Figure. 21). The wing kinematics corresponds to the control rod position at 4 seconds in Figure. 21. This result corroborates with our kinematic model, which stats that for pitch, no lateral movement in the position of the rod is required.

Roll: The roll kinematics are plotted in Figures 5.22 to 5.24. Figure 5.22 shows the mean control rod displacement for bottom marker along all the three axes in five actuation cycles. Figures 5.23 and 5.24 plot the wing kinematics as viewed from the front for the control rod position at approximately 17 seconds and 15 seconds, respectively. Unlike the pitching moment, which had large displacements in the Y-direction, for a roll moment, the control rod has to move either inward or outward.

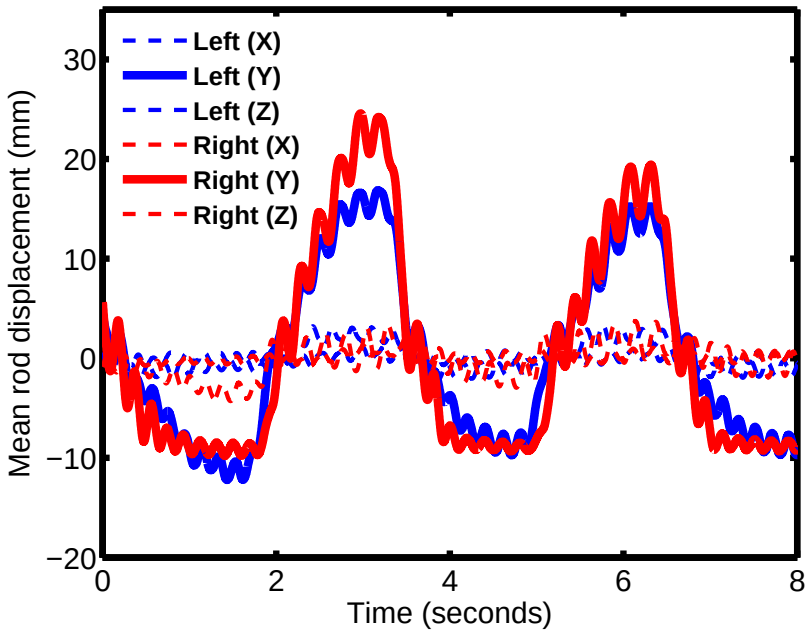

Figure 5.17: Mean rod displacement for all three axes for pitch

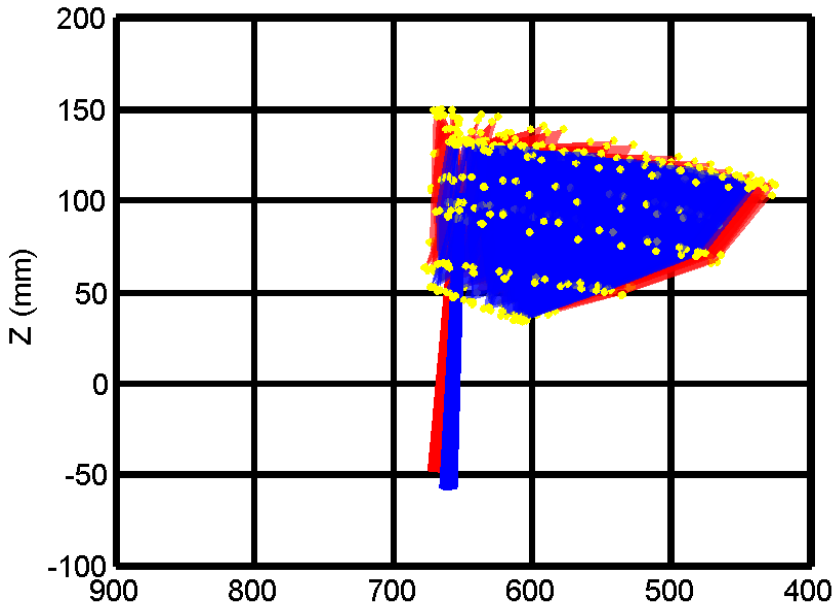

Figure 5.18: Side view of pitch actuation at 3 seconds

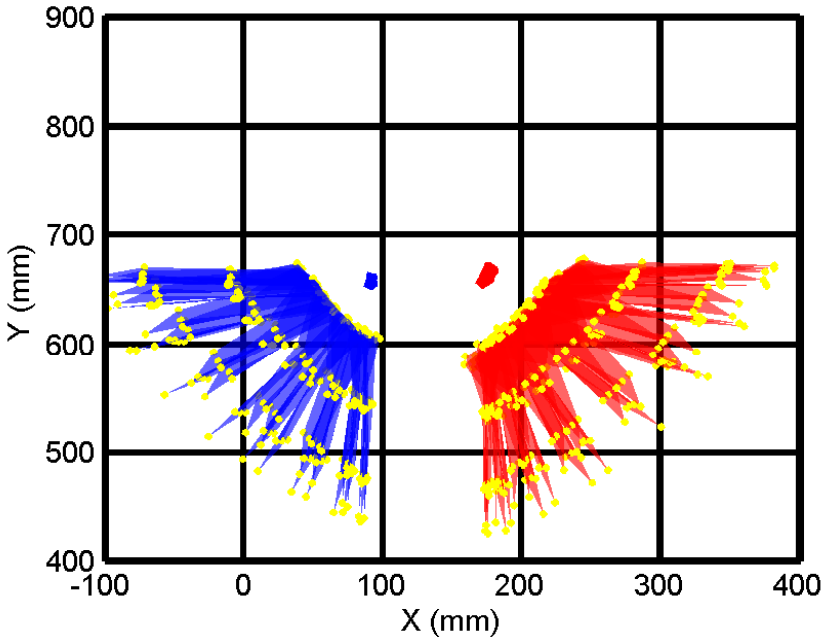

Figure 5.19: Top view of pitch actuation at 3 seconds

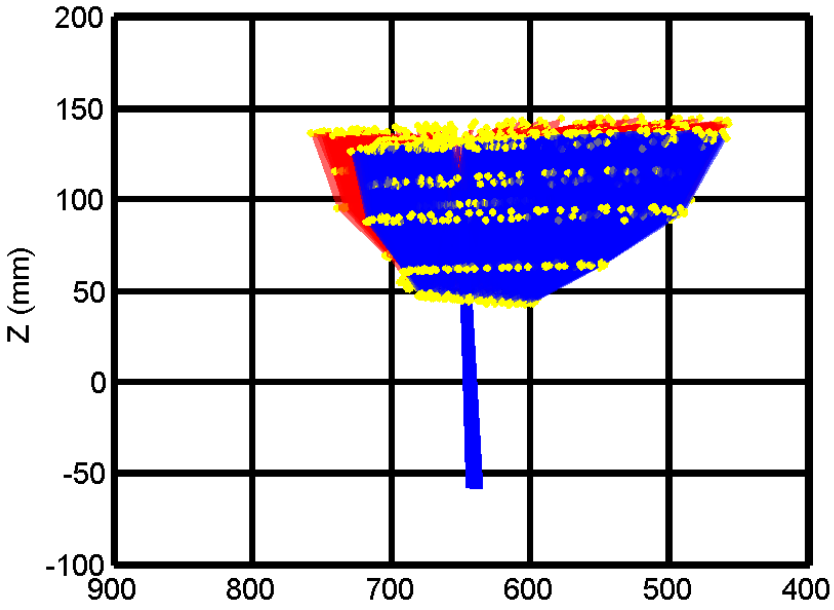

Figure 5.20: Side view of pitch actuation at 4 seconds

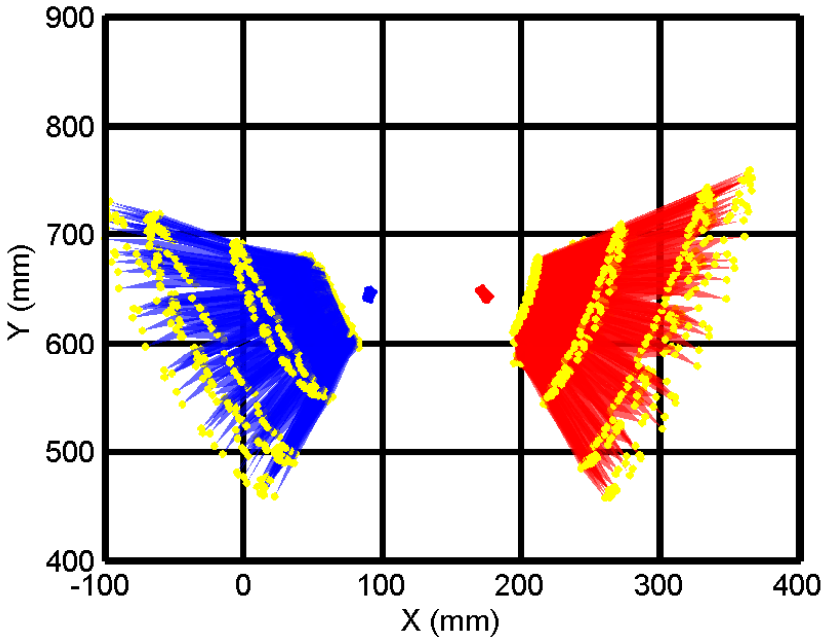

Figure 5.21: Top view of pitch actuation at 4 seconds

As shown in Figure 5.22, the excursions in the other two directions are smaller compared to those in X-direction. The two rods move laterally and differentially in order to generate this moment. In the present mechanism the outward movement of the control rod was significantly higher than the inward movement; therefore, the upward tilt of the flapping plane is much more prominent than the downward tilt. An outward movement of the red rod (right hand side) in Figure 5.23 leads to an upward tilt of the flapping plane as predicted by the simulation. When the blue rod (left hand side) is tilted outwards the effect is that the flapping plane on the left hand side is tilted upwards, leading to a roll right moment as seen in Figure 34.

Yaw: The yawing moment as mentioned before is achieved by a differential fore and aft tilt of the flapping planes for the wings. The mean control rod displacement for all three axes is plotted in Figure 5.25, and maximum displacement to generate a

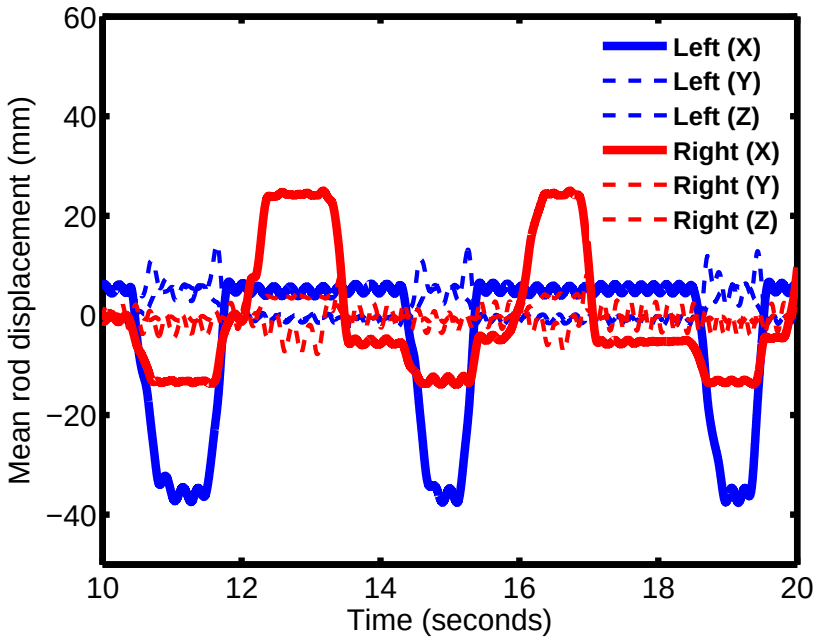

Figure 5.22: Mean rod displacement for all three axes for roll

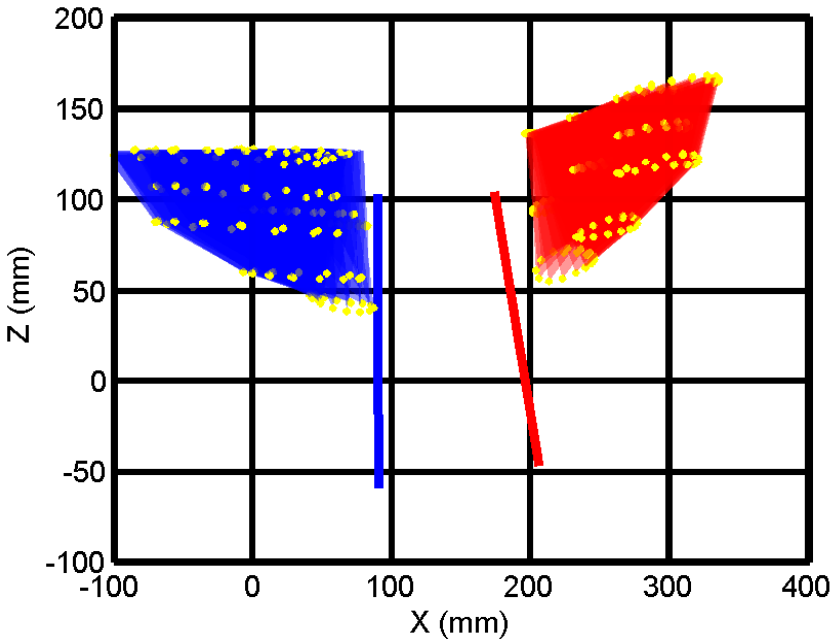

Figure 5.23: Front view of clockwise roll actuation

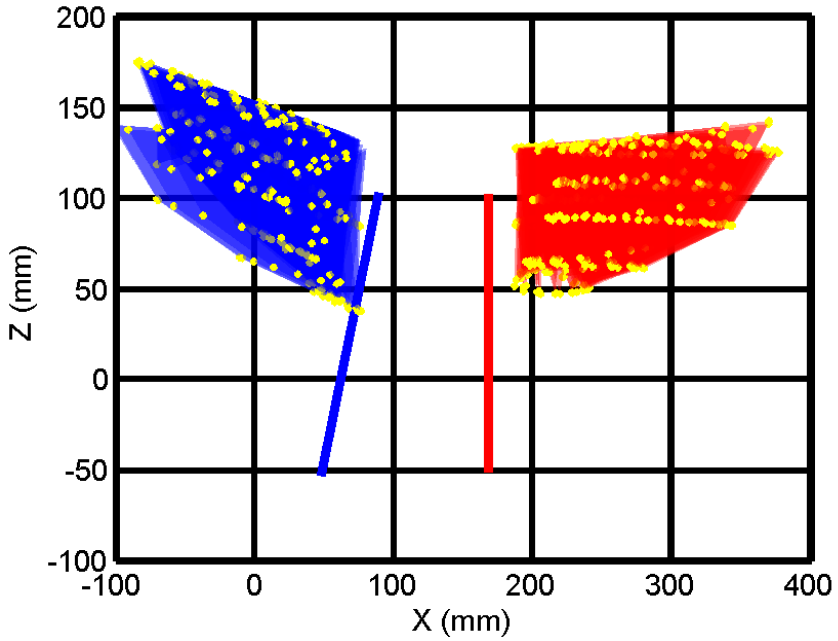

Figure 5.24: Front view of counter-clockwise roll actuation

yawing moment is in the Y-axis. Also, it can be seen that, for yaw, the control rods tilt in the opposite directions. Figure 5.26 plots the side view of the wing kinematics in yaw, for a clockwise motion as seen from the top. As shown in Figure 5.14 for creating a clockwise yawing moment the left flap plane has to tilt forward and the right flap plane has to tilt backward. Similarly, a counter-clockwise yaw moment is shown in Figure 5.27. Here the planes are tilted in the opposite manner as Figure 5.26.

5.7 Demonstration of Control Strategy

The VICON tests clearly show that the present control mechanism can modulate the wing kinematics in the same way as predicted by the kinematic model.

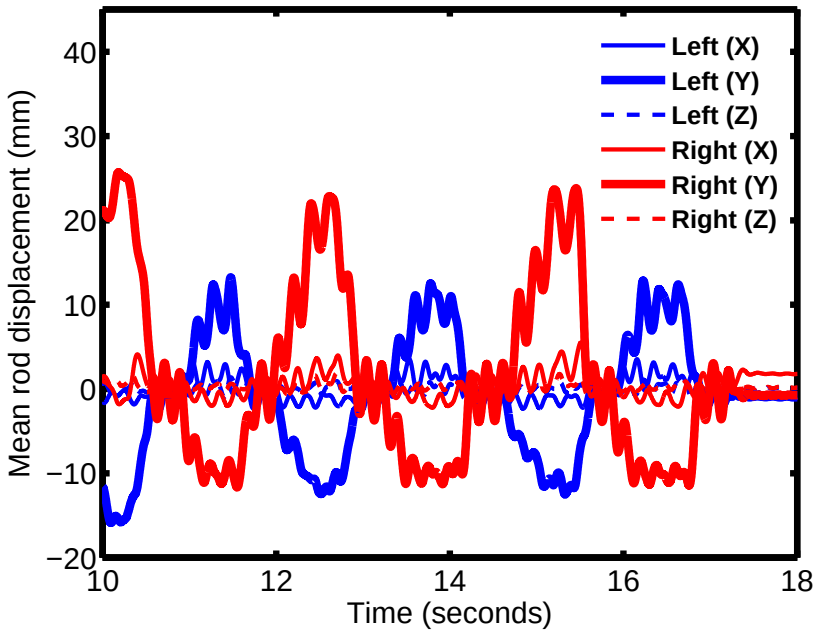

Figure 5.25: Mean rod displacement for all three axes for yaw

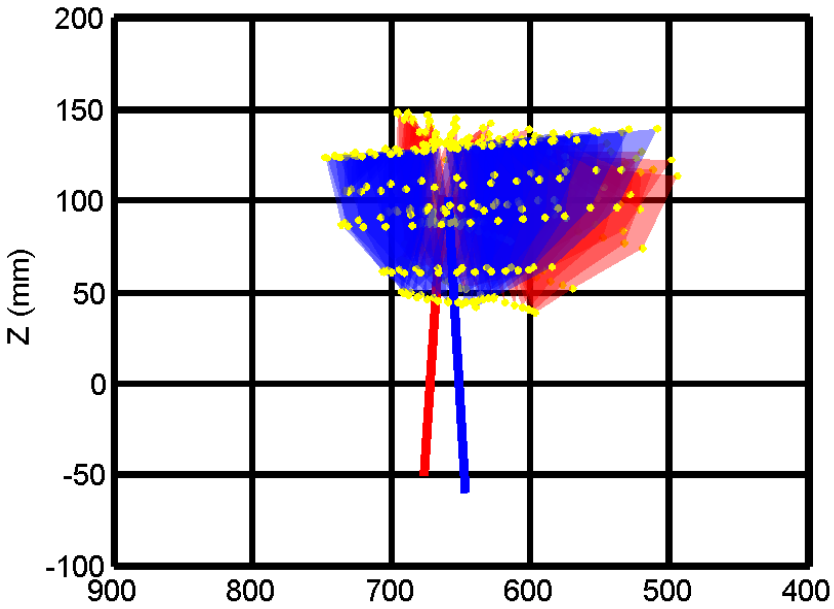

Figure 5.26: Front view of counter clockwise yaw actuation

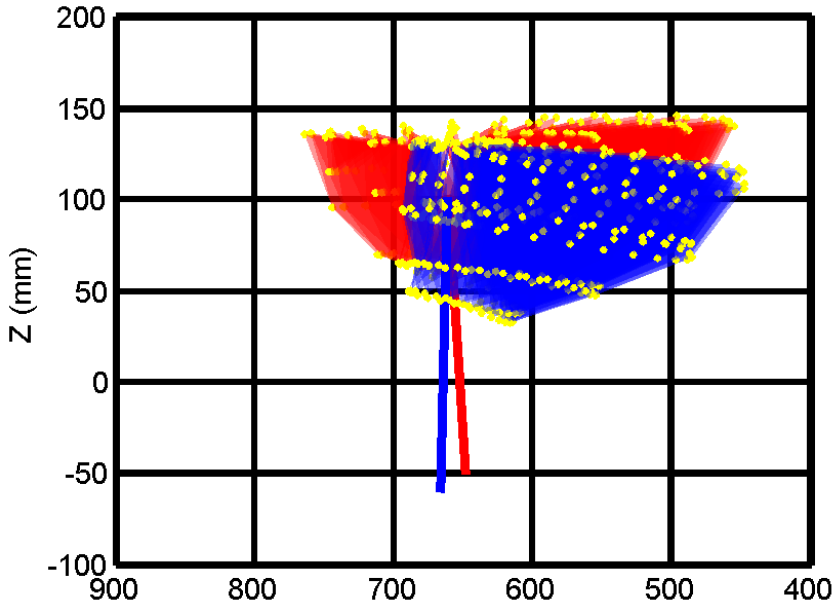

Figure 5.27: Front view of clockwise yaw actuation

However, it is important to experimentally demonstrate that this wing kinematics modulation technique can generate sufficient moments to induce pitch, roll and yaw motions on the actual vehicle. For this, a setup was build which is capable of providing the vehicle independent pitch, roll and yaw degrees of freedom. Single axis tests were conducted for each degree of freedom by providing the respective control inputs. Figures 5.28 to 5.30 show the different test stands and the flapper with control mechanism performing pitch, roll and yaw motions. The mechanism generated these control moments at flapping frequencies of 7 Hz and upwards. A general observation was that the mechanism was more responsive to control inputs and had greater control authority at higher frequencies. A closer look at the position of the rods does validate our original control strategy. Figure 5.28 captures two frames from a video that shows pitch up and pitch down motions. This was pro-

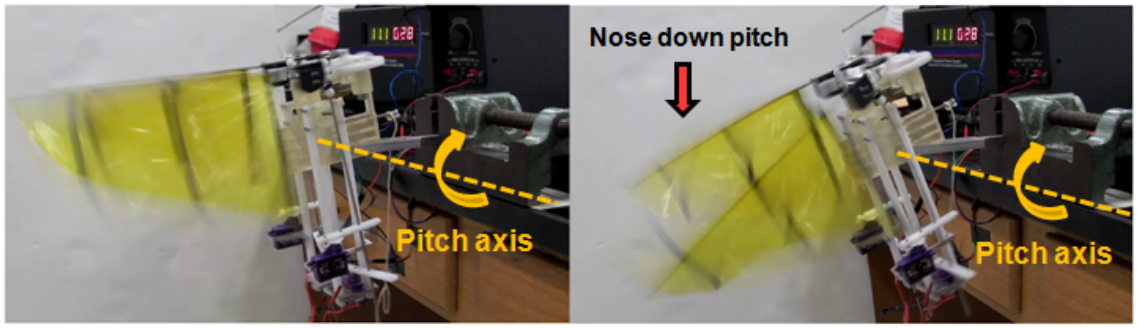

Figure 5.28: Flapping wing mechanism demonstrating pitch

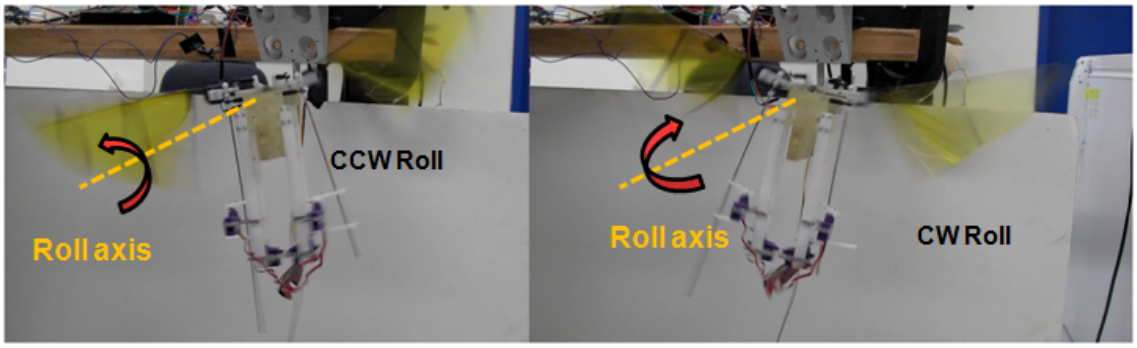

Figure 5.29: Flapping wing mechanism demonstrating roll

duced by the symmetric fore and aft motion of the control rod using the respective servos. Figure 5.29 shows two frames of the mechanism producing roll moments. The position of the control rods in both pictures shows an inward and outward differential actuation, which leads to a differential tilt in the left and right flapping plane as discussed earlier. Figure 5.30 captures the mechanism demonstrating yaw, which was produced by the differential fore and aft tilting of the control rods, which would generate a differential fore-aft tilting of the flapping planes generating a yaw moment.

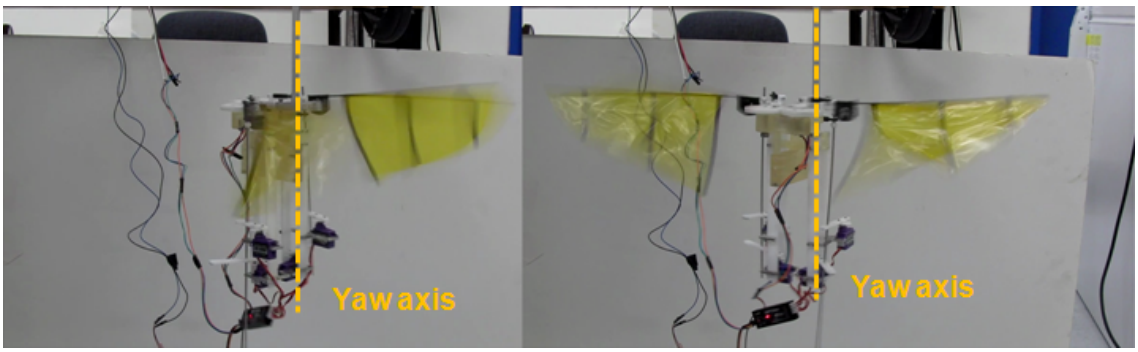

Figure 5.30: Flapping wing mechanism demonstrating yaw

5.8 Final Vehicle Assembly

The final fully assembled vehicle is shown in Figure 5.28. Significant weight has been reduced from the mechanism utilized in the control strategy demonstration experiments. Compared to the old body which weighed 41 grams, the new rapid prototyped body weighed only 10 grams. The servo mounting assembly which is manufactured from 0.0325 inch carbon fiber weighed only 14 grams compared to the earlier setup made from delrin which weighed close to 35 grams. The mechanism has been fitted with a 2.5 GHz receiver in addition to a 30 gram battery, positioned at the base of the vehicle in order to bring the vehicle's center of gravity down. The total weight of the vehicle is 122 grams.

5.9 Conclusions

This chapter has been focused on extending the dual-differential four bar mechanism to an actual flapping wing micro air vehicle. In this study, two optimized wings were implemented on a tethered vehicle weighing 56 grams without any on

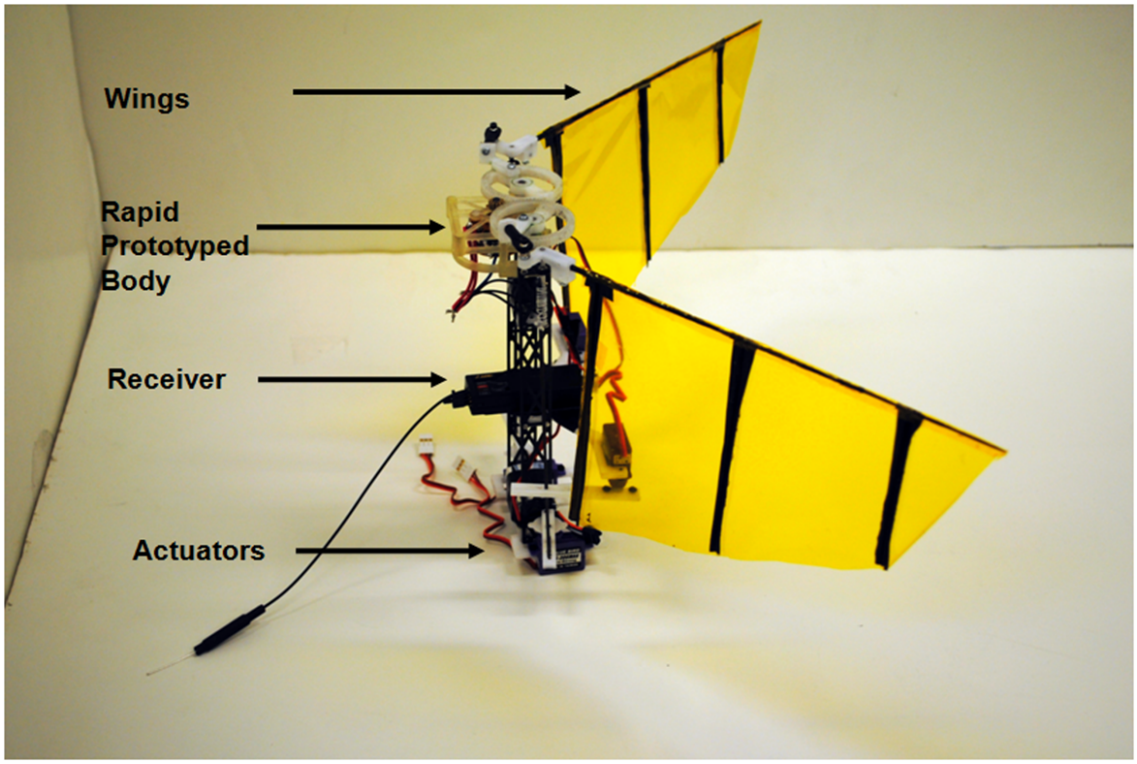

Figure 5.31: Fully assembled vehicle

board control system. This vehicle successfully demonstrated tethered hover.

The most significant contribution of this study has been the design and implementation of a control strategy utilizing wing kinematics modulation for vehicle attitude control. A kinematic model of the proposed mechanism was simulated and basic strategies for achieving pitch, roll and yaw moments were formulated.

Exact kinematics of both the wings in response to various actuator motions (control inputs) were measured using a VICON® motion capture system. This was used to validate the simulated kinematics for achieving roll, pitch and yaw moments.

The ability of present control strategy to create the required pitch, roll and yaw kinematics was demonstrated. This clearly shows that the present methodology is able to produce sufficient attitude stabilization moments, for a flapping MAV in hover. A new lighter vehicle was designed so as to house this control mechanism at a lower weight penalty.

Chapter 8

Concluding Remarks

8.1 Overview

This work has explored biomimetic insect flapping wing aerodynamics and controls using three distinct experimental approaches. The first approach was to focus on time averaged aerodynamic force and power measurements for a series of flexible wings. These wings were aeroelastically tailored to be light and produce significant amount of lift. This translated into the second approach, where an actual flapping wing micro air vehicle was designed and built. The vehicle demonstrated tethered hover and pitch, roll and yaw control. The third approach was to explore the aerodynamics more rigorously at MAV-scale Reynolds numbers through instantaneous rigid wing tests. These tests utilized a state of the art six degree of freedom balance along with a vacuum chamber for inertial force subtraction. Below are some of the important contributions of this study:

8.2 Important Contributions

8.2.1 Flapping Mechanism

A simple concept was introduced capable of emulating all three degrees of freedom of insect kinematics. The mechanism demonstrated the ability to generate

these complex kinematics on rigid wings. The mechanism was designed to be simple and flap at high frequencies.

8.2.2 Time Averaged Flexible Wing Tests

The mechanism featured an active pitching capability that was crucial in determining the optimized wing kinematic parameters. Numerous wing designs were systematically tested to obtain the lift and power measurements. Wing deformations at different spanwise loactions were obtained using a VICON® motion capture system. Lift and power values were collected for the wings over a range of frequencies. Overall it was found that wing torsional stiffness was the most important parameter affecting wing performance.

The optimized wing produced a maximum lift of roughly 60 grams at a flapping frequency of 10 Hz.

One of the most significant contributions of this study was the experimental measurement of motor power for a flapping wing system through a special arrangement of the torque cell. Measurements revealed that the power loading for the flapper is significantly lower than that of a conventional rotor.

8.2.3 Instantaneous Rigid Wing Tests

Wing testing was performed both in air and in vacuum while maintaining the same kinematics in order to obtain the pure aerodynamic forces while flapping. A set of shaft encoders were utilized to make sure that the wing was at the same azimuthal

location in both tests. Forces from the vacuum chamber tests were subtracted from those in the air tests using a synchronization procedure to yield the pure aerodynamic forces.

Extremely high values of C_l and C_d (3-4) were observed for flapping the wing at a fixed pitch. These values were found to be well in excess of those predicted by wind tunnel tests for the same wing. Flow visualization and PIV studies showed that this maybe primarily due to the presence of large leading edge vortices. Tests results also pointed towards the presence of minor wake capture phenomenon.

3-D flapping tests were conducted, which incorporated wing pitching and coning motions (in addition to flapping). Comparisons of the force trajectories with a standard blade element theory formulation revealed the presence of lift due to rotational circulation towards the ends of the halfstrokes.

Overall this study has also addressed the lack of experimental instantaneous aerodynamic forces for insect-based wing motions at MAV scale Reynolds numbers. Moreover force data has been substantiated with PIV and flow visualization results.

8.2.4 Vehicle Design and Development

In this study, two optimized wings were implemented on a tethered vehicle weighing 56 grams without any on board control system. This vehicle successfully demonstrated tethered hover. A simple control strategy was formulated and implemented on the flapping wing vehicle and it successfully demonstrated pitch, roll and yaw control.

8.3 Remarks for Future Work

This thesis is a small step towards the development of a fully autonomous, hover-capable flapping wing micro air vehicle. While this research has covered three approaches, there are several directions along which further research can be carried out.

1. More time averaged experimental studies can be conducted towards an optimized wing design. Metrics such as wing planform, aspect ratio and different wing kinematics can be tested. The present study only utilized mylar films for wing construction, however more advanced light weight materials can also be used on the wings.

2. A study of rigid wings with different aspect ratios keeping the same tip mid-stroke Reynolds number should be conducted. Lift and drag coefficients should be compared in order to determine how the tip vortex affects these parameters.

3. Detailed computational fluid dynamics studies can be performed using the instantaneous rigid wing data obtained in the experiments. Furthermore, data from the PIV and flow visualization can be compared with those generated via CFD.

4. Progress towards free flight tests utilizing the vehicle that was designed and developed should continue, utilizing the control strategies presented in this work.

Bibliography

[1] *Aerovironment : Nano*, Website, www.avinc.com/nano. Accessed September 2, 2011

[2] Anderson, J.D., *Fundamentals of Aerodynamics*, McGraw-Hill Series, 2005

[3] Ansari, et. al., *Insectlike Flapping Wings in the Hover Part 1: Effect of Wing Kinematics*, Journal of Aircraft, Vol. 45, No. 6., November - December 2008

[4] Aono, et.al., *A Computational and Experimental Study of Flexible Flapping Wing Aerodynamics*, AIAA Aerospace Sciences Meeting, 4-7 January, 2010, Orlando, Florida

[5] Bradshaw, N., Lentink, D.,*Aerodynamic and Structural Dynamic Identification of a Flapping wing Micro Air Vehicle*, 26th AIAA Applied Aerodynamics Conference, Honolulu, Hawaii, 18-21 August 2008,

[6] Briggs, L.J., *Effect of spin and speed on the lateral deflection of a baseball; and the Magnus effect on smooth spheres*, American Journal of Physics, 27: 589-96, 1959.

[7] Chopra, I., *Hovering Micro Air Vehicles : Challenges and Opportunities*, Proceedings of the American Helicopter Society Specialists' Conference, International Forum on Rotorcraft Multidisciplinary Technology, October 15-17, 2007, Seoul, Korea

[8] *DelFly* Website, http://www.delfly.nl/?site=DIImenu=lang=nl, Accessed September 2, 2011.

[9] Dickinson, M.H., Lehmann F.O., Sane, S.P., *Wing Rotation and the Aerodynamic Basis of Insect Flight*, Science, 284, 1954 (1999)

[10] Ellington, C.P, et.al, *Leading-edge vortices in insect flight*, Nature, Vol 384, December 1996

[11] Fry, S.N., Sayaman, R., Dickinson, M.H.,*The Aerodynamics of Free-Flight Maneuvers in Drosophlia*, Science, 300, 495(2003)

[12] Grasmeyer, J.M., Keennon, M.T., *Development of the Black Widow Micro Air Vehicle*, American Institute of Aeronautics and Astronautics, 2001

[13] *A hawk moth (Manduca sexta) hovering*, Hendrick Lab, Movies. Web. 8 Jan 2010. ¡http://www.unc.edu/ thedrick/movies.html¿

[14] Jones, A.R., Babinsky, H., *Leading Edge Vortex Development on a Waving Wing at Reynolds Numbers Between 10,000 and 60,000*, 49th AIAA Aerospace Sciences Meeting, 4-7 January, 2011, Orlando, Florida

[15] Keennon et al. *Air Vehicle Flight Mechanism and Control Method*, United States Patent Application Publication, US/2010/0308160, December 9th, 2010

[16] Keennon, M., *Tailless Flapping Wing Flight : Progression of propulsion and control developments from initial tests to fully controlled free flight* Aerovironment, Film, www.youtube.com/watch?v=Cov7-XWUa18, July 1, 2009

[17] Leishman, J. G.,*Principles of Helicopter Aerodynamics*, 2nd ed., Cambridge University Press, New York, NY, 2006.

[18] Magnus, G., *Über die Abweichung der Geschosse*, Abhandlungen der Königlichen Akademie der Wissenschaften zu Berlin, 1853

[19] Mehta, R.D., *Aerodynamics of Sports Balls*, Annual Review of Fluid Mechanics, 17 : 151-89, 1985.

[20] Pelletier,A., Mueller, T.J.,*Low Reynolds Number Aerodynamics of Low-Aspect-Ratio, Thin/Flat/Cambered-Plate Wings*, Journal of Aircraft, Vol.37, No.5, September - October 2000

[21] Perez-Arancibia, N., et. al *First controlled vertical flight of a biologically inspired microrobot*, Bioinspiration and Biomimetics, 6(2011)

[22] Ramasamy, M., Leishman, J.G., *Phase-Locked Particle Image Velocimetry Measurements of a Flapping Wing*, Journal of Aircraft, Vol. 43, No. 6, November - December 2006.

[23] Ramasamy, M., Johnson, B., Leishman, J.G., *Understanding the Aerodynamic Efficiency of a Hovering Micro-Rotor*, Journal of the American Helicopter Society, July 2008.

[24] Ramsey, J.R.,*Flow Field and Performance Measurements of a Flapping-Wing Device Using Particle Image Velocimetry*, Master of Science Thesis, University of Maryland, 2011

[25] Sane, S.P., *The aerodynamics of insect flight*, The Journal of Experimental Biology, 206, 4191-4208, 2003

[26] Selig, S.M., Deters, R.W., Williamson, G.A., *Wind Tunnel Testing Airfoils at Low Reynolds Numbers*, 49th AIAA Aerospace Sciences Meeting, 4-7 January, 2011, Orlando, Florida

[27] Shyy, W., Lian, Y., Tang, J., Viieru, D., Liu, H., *Aerodynamics of Low Reynolds Number Flyers* Cambridge University Press, 2009

[28] Singh, B., Chopra, I., *Wing Design and Optimization for a Flapping Wing Micro Air Vehicle*, American Helicopter Society Annual Forum, June 7-10, 2004, Baltimore, Maryland

[29] Singh, B., *Dynamics and Aeroelasticity of Hover Capable Flapping Wings : Experiments and Analysis*, Doctor of Philosophy Thesis, University of Maryland, 2006

[30] Tang, J., Viieru, D., and Shyy, W., *Effects of Reynolds Number, Reduced Frequency and Flapping Kinematics on Hovering Aerodynamics,* 45th AIAA Aerospace Sciences Meeting and Exhibit, AIAA 2007-129, Reno, NV, January 811, 2007.

[31] Tarascio, T.J., Ramasamy, M., Chopra, I., Leishman, J.G., *Flow Visualization of Micro Air vehicle Scaled Insect-Based Flapping Wings*, Journal of Aircraft, Vol.42, No.2, March - April 2005.

[32] *The Flight of Birds and Insects* The American Naturalist, Vol. 5, No. 1 (Mar., 1871) pp.29-33

[33] Tobalske, B.W., *Biomechanics of bird flight*, The Journal of Experimental Biology, 210, 3135-3146, 2007

[34] Usherwood, J.R., Ellington, C.P., *The aerodynamics of revolving wings I. Model hawkmoth wings*, The Journal of Experimental Biology, 205, 1547 - 1564, 2002

[35] Walker, J. A., *Rotational Lift: Something Different or More of the Same?* , Journal of Experimental Biology, Vol. 205, 2002, pp. 3783 3792.

[36] Zdunich, P., et. al *Development and Testing of the Mentor Flapping-Wing Micro Air Vehicle*, Journal of Aircraft, Vol. 44, No. 5, September-October 2007